UCRL-TH-215351

LAWRENCE
LIVERMORE
NATIONAL
LABORATORY

Neutron Capture and the Production of 60-Fe in Stellar Environments

K. Kelley

September 14, 2005

Neutron Capture and the Production of ^{60}Fe in Stellar Environments

By

KEVIN KELLEY
B.S. (University of California, Davis) 2001
M.S. (University of California, Davis) 2002

DISSERTATION

Submitted in partial satisfaction of the requirements for the degree of

DOCTOR OF PHILOSOPHY

in

Physics

in the

OFFICE OF GRADUATE STUDIES

of the

UNIVERSITY OF CALIFORNIA

DAVIS

Approved:

Committee in Charge

2005

Dedication

I would like to dedicate this thesis to my parents, Richard and Mary Kelley, who taught me the values of hard work and perseverance; to my children Meghan and Anthony, who keep me young at heart; and most of all, to my dear wife Kimberlee, whose patience, love, and support have always been valuable beyond measure.

Acknowledgments

My most sincere appreciation goes to Dr. Robert Hoffman, who first introduced me to the field of nuclear astrophysics, and whose counsel, direction, and support in this work have been indispensable. Also, I owe a debt of gratitude to Dr. Jack Gunion, who has graciously accepted the delay of other research goals in support of this work. I wish to thank Dr. Frank Dietrich for many discussions regarding the physics of nuclear reactions.

My regards go as well to the A- and N-Divisions at Lawrence Livermore National Laboratory and to the SciDAC Center for Supernovae Research of the U.S. Department of Energy Office of Science, who have provided financial support for this endeavor.

Last of all I wish to thank Dr. Rob Hoffman, Dr. Jack Gunion, and Dr. Paul Brady for serving on the dissertation committee for this work. I also acknowledge Joshua Molgaard who provided assistance in the editing of the text.

Disclaimer

This document was prepared as an account of work sponsored by an agency of the United States Government. Neither the United States Government nor the University of California nor any of their employees, makes any warranty, express or implied, or assumes any legal liability or responsibility for the accuracy, completeness, or usefulness of any information, apparatus, product, or process disclosed, or represents that its use would not infringe privately owned rights. Reference herein to any specific commercial product, process, or service by trade name, trademark, manufacturer, or otherwise, does not necessarily constitute or imply its endorsement, recommendation, or favoring by the United States Government or the University of California. The views and opinions of authors expressed herein do not necessarily state or reflect those of the United States Government or the University of California, and shall not be used for advertising or product endorsement purposes.

Auspices Statement

This work was supported in part by the Deparment of Energy (DOE) Program for Scientific Discovery through Advanced Computing (SciDAC; DE-FC02-01ER41176). Portions of this work were performed under the auspices of the U.S. Department of Energy by the University of California Lawrence Livermore National Laboratory under contract W-7405-ENG-48.

Abstract

The observation of gamma rays associated with the decay of ^{26}Al and ^{60}Fe can provide important information regarding ongoing nucleosynthesis in our galaxy. The half-lives of these radioisotopes (7.2×10^5 y and 1.5×10^6 y, respectively) are long compared to the interval between synthesis events such as supernovae, so they build up in a steady state in the interstellar medium (centered on the galactic plane, where massive stars reside), yet short enough that gamma radiation from their decay may be detected. Additionally, these half-lifes are short compared to the period of galactic revolution, so that observable abundances remain in the proximity of their production sites.

Predicted abundances of ^{26}Al and ^{60}Fe vary widely between several calculations in the last decade. In 2004, the first observation of the gamma ray flux from ^{60}Fe decay was reported, with a ^{60}Fe/^{26}Al flux ratio in good agreement with nucleosynthesis modeling from 1995. However, recent calculations that include well motivated updates to the stellar and nuclear physics, predict a flux ratio as much as six times higher than the observed value. It is desirable to understand the discrepancy between the latest calculation, which in principle should have been more accurate, and the observation.

In the present study, the uncertainties related to two key nuclear aspects of this problem, namely the neutron capture reaction rates for ^{59,60}Fe, are investigated. New reaction rates are modeled using local systematics as opposed to the global systematics used in previous studies. Comparisons to experimental data are made whenever possible. The sensitivity of the reaction rates to various input quantities is gauged, and estimates regarding the total uncertainty in the reaction rates are made. The resulting rates and uncertainties are used in parameterized single-zone nucleosynthesis calculations using hydrodynamic conditions typical of those found in more complex stellar models. Finally, the sensitivity of the abundance of ^{60}Fe to the reaction rates is discussed.

Contents

1 Introduction **1**

1.1 The Significance of ^{60}Fe 2

1.2 Previous Galactic Chemical Evolution Studies 6

1.3 Signals for ^{60}Fe 10

1.4 Primary Nuclear Uncertainties 13

2 Nuclear Reaction Mechanisms **18**

2.1 Direct Reactions 22

2.1.1 Elastic and Inelastic Scattering 22

2.1.2 Nucleon Transfer Reactions 25

2.2 Compound Nuclear Reactions 27

2.2.1 Early Models of Compound Nuclear Reactions 28

2.2.2 The Hauser-Feshbach Model 31

2.2.3 Width Fluctuation Correlations 36

2.2.4 Decay of Continuum States 37

2.3 Pre-equilibrium Reactions 39

2.4 The STAPRE Code 43

3 Nuclear Structure Data **46**

3.1 Ground State Spins and Parities 46

3.2 Masses and Separation Energies 47

3.3 Discrete Levels 49

4 Nuclear Level Densities **54**

4.1 Theoretical Foundations of the Nuclear Level Density 54

4.1.1 The Fermi Gas State Density 54

4.1.2 The Backshift 58

4.1.3 Spin Cut-off Parameter 61
4.1.4 The Level Density Parameter 62
4.1.5 Shell Effects and the Level Density Parameter 63
4.1.6 Level Densities below the Neutron Binding Energy 64
4.1.7 Fitting the Level Density Formulae to Spectroscopic States . 66
4.2 Past Approaches to the Level Density 68
4.2.1 Woosley et al. (1978) 68
4.2.2 Rauscher, Thielemann, and Kratz (1997) 71
4.2.3 Hartree-Fock BCS 74
4.3 Local Systematics for Level Density Parameters 77

5 Transmission Coefficients 88
5.1 Particle Transmission Coefficients 88
5.1.1 Neutron and Proton Transmission Coefficients 90
5.1.2 Alpha Particle Transmission Coefficients 100
5.1.3 Deuteron Transmission Coefficients 101
5.2 Photon Transmission Coefficients 102
5.2.1 Previous treatments 107
5.2.2 Photon Strength Functions Based on Local Systematics . . . 110
5.2.3 Average Radiation Widths 117

6 Cross Sections Modeled with Local Systematics 121
6.1 Normalizing Capture Cross Sections 121
6.2 Neutron Capture Cross Sections 128
6.3 Maxwellian-Averaged Capture Cross Sections 133
6.4 Results for ^{59}Fe and ^{60}Fe Capture Cross Sections 137
6.5 Other Reactions with Stable Targets 138
6.6 Direct Reaction Contributions 152

7 Reaction Rate Sensitivities **158**

7.1 Uncertainties in Systematic Input Parameters 159

7.1.1 Asymptotic Level Density Parameter 159

7.1.2 GDR Parameters 160

7.1.3 Normalization of the γ-ray Transmission Coefficient 160

7.1.4 Collective Uncertainties Arising from Local Systematics . . . 161

7.2 Variations in Input Parameter Prescriptions 162

7.2.1 Level Density Prescription and Discrete Levels 163

7.2.2 Neutron Transmission Coefficients 164

7.2.3 Width Fluctuation Correlation 165

7.2.4 GDR parameters 166

7.2.5 E1 and M1 Strength Functions 166

7.2.6 Collective Variations 168

8 Parameterized Single-Zone Nucleosynthesis **170**

8.1 Nuclear Reaction Networks 170

8.2 Thermodynamic Conditions of Burning Stages 172

8.3 Fitting Reaction Rates to Parameterized Forms 176

8.4 Nuclear Burning Stages 182

8.5 Analysis of Resulting ^{26}Al and ^{60}Fe Abundances 196

8.6 A Result From KEPLER 208

9 Summary and Conclusions **211**

A Ground State Nuclear Properties **215**

B Discrete Levels and Branching Ratios **218**

C Neutron Resonance Data **255**

D Experimental GDR Parameters **257**

E Level Density Parameters **258**

F Initial Solar Seeds for Hydrogen Burning **262**

List of Figures

1 Electron capture decay of ^{26}Al to ^{26}Mg 4

2 β^- decay chain of ^{60}Fe to ^{60}Ni 5

3 Production of ^{26}Al and ^{60}Fe in a $25M_\odot$ solar metallicity star 9

4 ^{26}Al and ^{60}Fe yields 11

5 Measured total neutron cross section on ^{55}Mn 21

6 Pre-equilibrium fraction for neutrons and protons incident on ^{56}Fe . 43

7 Cumulative number of levels in $^{55-56}$Mn and $^{55-56}$Fe 59

8 Calculated resonance spacings from WFHZ level densities 71

9 Integrated level density at E_{cut} using WFHZ inputs 72

10 Calculated resonance spacings from RTK level densities 73

11 Integrated level density at E_{cut} using RTK inputs 74

12 Calculated resonance spacings using HF-BCS level densities 75

13 Integrated level density at E_{cut} using HF-BCS level densities 76

14 The local level density systematic 80

15 Calculated resonance spacings from our local level density systematic 81

16 Select constant temperature fits to discrete level spectra 84

17 Integrated level density at E_{cut} using our preferred inputs 85

18 Sample proton transmission coefficients 91

19 Sample neutron transmission coefficients 92

20 Modeled total neutron cross sections compared to measurements . . 93

21 Modeled S-wave strength functions 96

22 Modeled P-wave strength functions 96

23 Modeled potential scattering radii 97

24 Neutron transmission coefficient ratios for ^{59}Fe 98

25 Neutron transmission coefficient ratios for ^{60}Fe 99

26 Sample alpha particle transmission coefficients 101
27 Systematics for E1 GDR energies 111
28 Systematics for E1 GDR widths 112
29 Systematics for E1 GDR peak cross sections 113
30 Systematics for average S-wave radiation widths 116
31 Secondary photon transmission coefficient normalization systematics 126
32 Modeled neutron capture cross sections compared to measurements 130
33 Modeled neutron capture MACS compared to recommended values 134
34 Modeled neutron capture cross sections for ^{59,60}Fe targets 137
35 Ratio of ^{59,60}Fe neutron capture cross sections 139
36 Modeled (n,p) cross sections compared to measurements 141
37 Modeled (n,α) cross sections compared to measurements 145
38 Modeled (n,d) cross sections compared to measurements 147
39 Modeled (n,np)+(n,pn) cross sections compared to measurements . 148
40 Modeled (n,2n) cross sections compared to measurements 150
41 Modeled (p,n) cross sections compared to measurements 152
42 Direct reaction contributions to neutron capture by ^{56}Fe and ^{58}Fe . 155
43 Uncertainties in (n,γ) rates arising from the level density systematic 159
44 Uncertainties in (n,γ) rates arising from the normalization of T_γ . . 161
45 Collective uncertainties associated with systematics 162
46 Variations in (n,γ) rates arising from the choice of level density . . . 163
47 Variations in (n,γ) rates with other local systematics 163
48 Variations in (n,γ) rates from the choice of optical potential 165
49 Variations in (n,γ) rates from with the inclusion of WFC 165
50 Variations in (n,γ) rates arising from the choice of GDR parameters 166
51 Variations in (n,γ) rates arising from E1 and M1 strength functions 167
52 Variations in (n,γ) rates with the inclusion of the E1 enhancement . 167

53 Collective variation of (n,γ) rates based on input choices 168
54 ^{26}Al production using WFHZ based rate sets 198
55 ^{26}Al production using RT based rate sets 199
56 ^{26}Al production using WFHZ and RT rate sets 200
57 ^{60}Fe production using WFHZ based rate sets 202
58 ^{60}Fe production using RT based rate sets 203
59 ^{60}Fe production using WFHZ and RT rate sets 204
60 ^{60}Fe/^{26}Al production ratio using WFHZ based rate sets 206
61 ^{60}Fe/^{26}Al production ratio using RT based rate sets 207

List of Tables

1 Select ground state spins and parities in various modeling efforts . . 47

2 Select binding energies adopted in various modeling efforts 50

3 Discrete level schemes for ^{60}Fe 51

4 Discrete level schemes for ^{61}Fe 52

5 Local level density systematic trials 79

6 Modeled average S-wave radiation widths 118

7 Modeled 30 keV neutron capture MACS 123

8 Modeled radiation widths (including secondary normalization) . . . 127

9 Modeled neutron capture MACS (including secondary normalization) 128

10 Stellar enhancement factors for ^{59}Fe(n,γ)^{60}Fe and ^{60}Fe(n,γ)^{61}Fe . . 179

11 Sensitivity of ^{60}Fe production to inclusion of stellar enhancement factors 180

12 Fitting constants for parameterized neutron capture rates 181

13 Isotopes included in reaction networks 183

14 ^{26}Al and ^{60}Fe from hydrostatic hydrogen burning 184

15 ^{26}Al and ^{60}Fe from hydrostatic helium burning 186

16 ^{26}Al and ^{60}Fe from explosive helium burning 187

17 ^{26}Al and ^{60}Fe from hydrostatic carbon burning 189

18 ^{26}Al and ^{60}Fe from explosive carbon burning 190

19 ^{26}Al and ^{60}Fe from hydrostatic neon burning 193

20 ^{26}Al and ^{60}Fe from explosive neon burning 194

21 ^{26}Al and ^{60}Fe from hydrostatic and explosive oxygen burning 197

22 Adopted ground state nuclear properties 215

23 Adopted discrete levels 218

24 Experimental neutron resonance data 255

25 Experimental GDR parameters 257

26 Local systematic level density parameters 258

27 Initial composition for hydrogen burning 262

1 Introduction

A natural place to begin a discussion about the uncertainties related to the production of a radioisotope such as ^{60}Fe is to address three questions:

1. What is so important about this particular isotope?
2. What do we already know about it?
3. Why should we bother researching it further?

In short, ^{60}Fe is important for two reasons. First, its half-life is long compared to the interval between synthesis events, so that a flux of gamma rays arising from its decay may be steadily observable. Additionally, its half-life is short compared to the period of galactic rotation, so that any ^{60}Fe abundance will remain in the proximity of its production site. This ideal half life allows ^{60}Fe to serve as an indicator of ongoing nucleosynthesis. Second, since its abundance is observable, collected astrophysical data pertaining to ^{60}Fe can constrain stellar models.

Much research regarding ^{60}Fe has been carried out in the last decade. In 1995, a detailed Galactic chemical evolution (GCE) survey predicted the abundances of ^{26}Al and ^{60}Fe, as well as the flux ratio of gamma rays produced in their decays [34, 36]. At the time of the survey, gamma ray line emission from ^{26}Al existing in the interstellar medium had been observed, but gamma rays from ^{60}Fe decay had not. This non-observation was not surprising, since the GCE survey put the total flux for ^{60}Fe below the detection threshold of the COMPTEL instrument that detected ^{26}Al. Within the past year and a half, other instruments have recorded a signal for ^{60}Fe decay, with a ^{60}Fe/^{26}Al flux ratio consistent with the 1995 modeled value [10, 30].

In the decade since the 1995 survey, improvements have been made to both the nuclear physics and the stellar models. When the calculations are carried out using

the new reaction rates and models [25], the predicted flux ratio increases by roughly a factor of four–no longer in agreement with the observation. Worse yet, the new prediction would indicate that gamma rays from ^{60}Fe *should* have been observed by the COMPTEL instrument.

This brings us to the third question regarding the motivation for further research. The current discrepancy between the predicted and observed ^{60}Fe/^{26}Al flux ratios has three possible sources: (1) the observations are flawed, (2) the reaction rates relevant to the production of ^{60}Fe are incorrect, or (3) the stellar models are in some way incorrect or incomplete. The first source seems highly unlikely, since concurrent observations from two independent sources are in excellent agreement with each other [10, 31]. It is far more likely that the discrepancy comes from either the nuclear or stellar physics. By thoroughly investigating the uncertainties in the nuclear side of the problem, we will be able to either resolve the issue or at least narrow the problem down to another aspect of stellar evolution.

The remainder of this section will explore these issues in greater detail.

1.1 The Significance of ^{60}Fe

Most of the information we can collect from our galaxy and beyond is limited to the electromagnetic radiation we can observe from ground and satellite based detectors. We generally cannot collect elements produced in astrophysical events, such as gamma-ray bursts or supernovae, and bring them back to a laboratory for analysis, although some data has been gathered from meteorites [2, 15, 20]. Rather, our information regarding the chemical composition of our galaxy comes primarily from the spectroscopy of the electromagnetic radiation they produce. In the case of radioisotopes, this radiation comes primarily from decay.

The average lifetime of massive stars ($8M_\odot$ and above) is on the order of one million years, and the typical frequency of major nucleosynthesis events within our

galaxy, such as supernovae, is on the order of a few per century [5]. If the lifetime of a given radioisotope is short compared to this interval, its associated gamma ray line flux may only be observed for a short period of time following a synthesis event. Given the low frequency of these events, significant observation of short lived isotopes becomes unlikely if not impossible. Additionally, a single synthesis event such as a supernova may not produce an observable quantity of the isotope. Rather, it is the gradual buildup of a particular species in the interstellar medium that results in an observable steady-state abundance. Any isotope that would yield an observable gamma ray flux must have a mean lifetime considerably longer than the interval between synthesis events.

On the other hand, if the lifetime of the isotope is too long, its decay may still escape detection. Radioactive decays would be rare, and the flux of gamma rays associated with those decays ends up lower than the detection threshold of the observing instrument. So candidate radioisotopes for observable decay flux must be long-lived, but not too long-lived.

Such nuclear species are intrinsically valuable in astrophysics, in that we can compare the predictions of stellar evolution models to observation and refine our models. Additionally, a half life that lends a particular species to gamma ray observation is short compared to the period of galactic rotation, which is on the order of 240 million years. Any abundance of the radioisotope will decay before moving far from its production site. Thus one can identify the stellar populations responsible for its production, and the isotope can serve as a "tracer" of ongoing nucleosynthesis [21].

There are only a handful of radioisotopes that have such a lifetime and are produced in abundances sufficient to enable observation. Two of the more important are ^{26}Al and ^{60}Fe. Prior to 2004, ^{26}Al ($t_{1/2} = 7.17 \times 10^5$ y [35]) had been the only one of the two observed. ^{26}Al decays via electron capture to the first excited state of

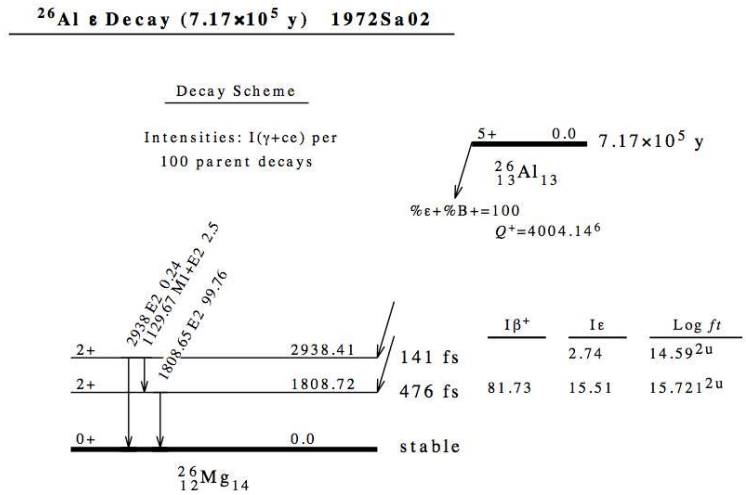

Figure 1: Electron capture decay of ^{26}Al to ^{26}Mg. The signature 1809 keV gamma ray is produced as the first excited state in ^{26}Mg decays to the ground state.

^{26}Mg. The ^{26}Mg decays to the ground state by emitting a 1809 keV gamma ray (see Figure 1, obtained from [19]). This line flux associated with the decay of ^{26}Al was first observed with the HEAO-3 experiment in 1979 [18]. In 1993, the COMPTEL detector aboard the Compton Gamma Ray Observatory provided an all-sky map of the 1809 keV flux [9]. The flux comes primarily from the galactic plane, strongest at the galactic center. There are additional hot spots, which have been correlated with spiral arms and known supernovae remnants. This distribution seems to rule out novae and low mass stars as producers of ^{26}Al, and suggests that ^{26}Al may be produced primarily in massive stars, particularly Type-II supernovae (SNII), Wolf-Rayet stars, or Asymptotic Giant Branch (AGB) stars. [21, 23]. The total observed flux of 1809 keV gamma rays suggests an abundance of roughly $2M_{\odot}$ of ^{26}Al in our galaxy [23].

It is unclear whether the origins of ^{26}Al lie in the winds of massive stars or the explosions of SNII. The present observational data on ^{26}Al cannot discern between these two possible origins.

The half life of ^{60}Fe ($t_{1/2} = 1.5 \times 10^6$ y [35]) is similar to that of ^{26}Al, and

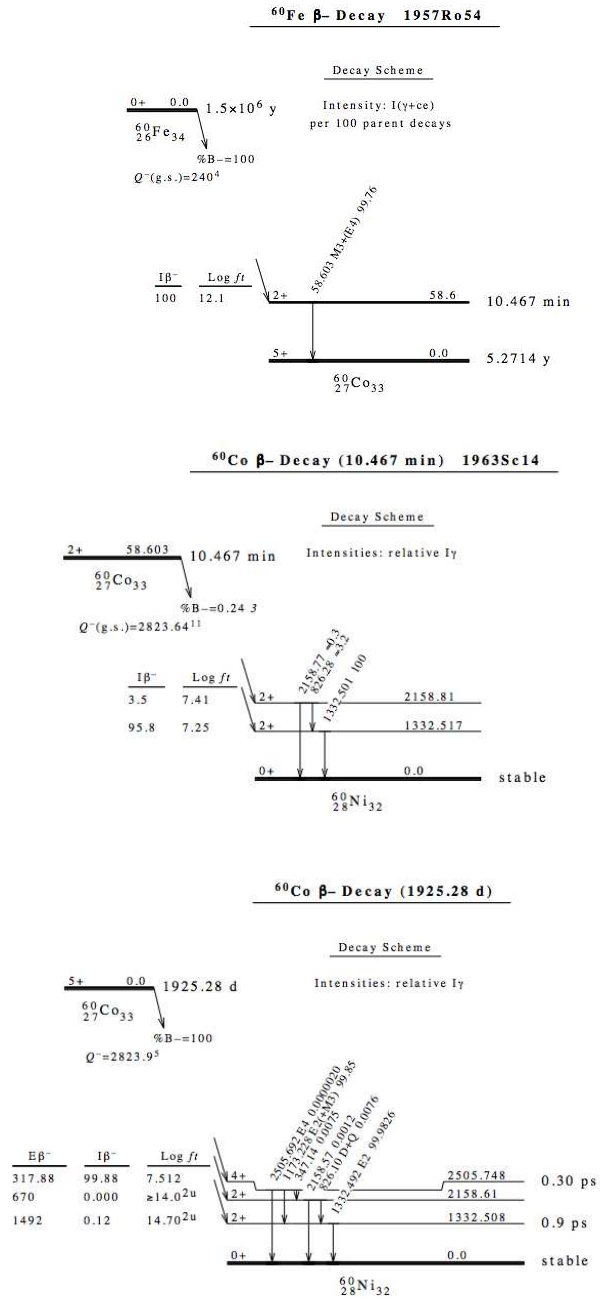

Figure 2: β^- decay chain of ^{60}Fe to ^{60}Ni. ^{60}Fe first decays to the ground or first excited state of ^{60}Co, both of which decay rapidly to the first three excited states of ^{60}Ni. The signature 1173 keV and 1332 keV gamma rays are emitted as the excited states of ^{60}Ni decay to the ground state.

the decay flux from ^{60}Fe should also be observable, provided that it is produced in sufficient quantities. The signature 1173 keV and 1332 keV gamma rays associated

with the β^- decay of ^{60}Fe arise from the subsequent β^- decay of the daughter nucleus ^{60}Co ($t_{1/2}$ = 1925 d [35]) (see Figure 2). The lifetime of ^{60}Co is short enough that any amount produced in a synthesis event will decay long before ^{60}Fe decay becomes appreciable. It has been shown [8] that ^{60}Fe can be produced in abundance in massive stars evolving as supernovae. However, the production of ^{60}Fe occurs primarily during the advanced stages of the evolution of the star, and deep inside the stellar interior. Unlike ^{26}Al, the stellar winds of a Wolf-Rayet star would not eject ^{60}Fe. An observation of the relative fluxes of decay emission lines from ^{26}Al and ^{60}Fe can therefore provide insight regarding the source of not only ^{60}Fe, but ^{26}Al as well. For instance, if the distribution of ^{60}Fe in the galactic plane is very similar to that of ^{26}Al, i.e. primarily in the galactic center, spiral arms, and hot spots correlating to SNII events, it would imply that ^{60}Fe and ^{26}Al are produced by the same sources, favoring the SNII origin of ^{26}Al [22].

It is apparent that the observation of ^{60}Fe abundance via gamma rays produced in its decay can provide very important information relative to ongoing nucleosynthesis in our galaxy. It is therefore important to understand, to the greatest extent possible, the details regarding the origin of both radioisotopes.

1.2 Previous Galactic Chemical Evolution Studies

Several groups have carried out nucleosynthesis calculations and provided an estimate of the ^{60}Fe/^{26}Al line flux ratio. The present review will cover only two of these studies in detail, namely those of Timmes *et al.* [33] (hereafter TWHHWM95) and Rauscher *et al.* [25] (hereafter RHHW02). We restrict ourselves to these particular studies primarily because the differences between them are limited to the nuclear reaction rates and minor adjustments to the stellar evolution code. Certain other studies have not been included in this analysis because they either start with He pre-supernovae cores [32] or omit neutrino induced reactions [16], which are important

in the synthesis of ^{26}Al.

Nucleosynthesis in 1995

The ^{26}Al and ^{60}Fe steady-state abundances in TWHHWM95 are based on the stellar yields of Woosley and Weaver [36]. The strength of this particular stellar-chemical evolution survey lies in its predicted abundances of stable isotopes, which compare favorably with observed abundances [1], generally to within a factor of two [34]. This agreement was obtained without any artificial tuning of the parameters in the model. The details of the nuclear physics employed will be presented in detail in Sections 3-5. It is useful at this point to briefly discuss the stellar physics involved.

The TWHHWM95 survey employed several stellar models, with masses ranging from 11-40 $M_\odot$ and initial metallicities of 0, 10^{-4}, 0.01, 0.1, and 1 $Z_\odot$. In each case, the explosion was simulated using a simple piston. The parameterization of the piston and explosion energies were varied. Mass loss was not accounted for. These models used a reaction network of 200 isotopes ranging from hydrogen to germanium. The nuclear reaction rates were based on several sources [3, 6, 7, 28, 37]. A tabulation of the reaction rates is provided by Hoffman [11]. Weak rates were included, as were neutrino induced reactions which have a significant effect on r-process nucleosynthesis [38]. For more details on these stellar models see [36].

An exponential disk was assumed for the mass distribution of the galaxy, and the disk was divided into several radial zones (as opposed to a hydrodynamic treatment). Sources of nucleosynthesis included primordial contributions, stellar birth, infall, intermediate to low-mass stars, Type Ia supernovae (SNIa), and Type II supernovae (SNII). For more details on the chemical evolution model, see [34].

TWHHWM95 predicted that massive stars could account for all of the observed ^{26}Al abundance (although with a somewhat large uncertainty) with a spatial distribution consistent with that observed by the COMPTEL instrument. It was

produced in SNII in the hydrogen and neon-oxygen burning shells, in both pre- and post-explosive supernova processes (see Figure 3, from [33]). During the explosion, the ^{26}Al in the hydrogen shell is ejected unmodified. The ^{26}Al in the hydrogen shell may also be ejected in the winds of more massive stars. The synthesis of ^{26}Al in the neon-oxygen burning shell is significantly enhanced by the ν-process (i.e. neutrino induced nuclear reactions), which can be seen in Figure 3.

The abundance of ^{60}Fe also predicted in TWHHWM95 comes from pre- and post-explosive processes, primarily in the neon-oxygen shell, but also at the base of the helium shell. There is a noticeable absence of ^{60}Fe in the hydrogen envelope, and hence ^{60}Fe will not be ejected in stellar winds. Otherwise, ^{60}Fe and ^{26}Al are produced in the same locations in the stellar interior, and one would expect their galactic distributions to also be similar, provided that SNII are the primary source of ^{26}Al in the interstellar medium.

The steady-state abundances of ^{26}Al and ^{60}Fe in TWHHWM95 were $2.0 \pm 1.0\ M_\odot$ and $0.74 \pm 0.4\ M_\odot$, respectively, with a total abundance of $2.2 \pm 1.1\ M_\odot$ of ^{26}Al and $1.7 \pm 0.9\ M_\odot$ of ^{60}Fe. The predicted steady-state abundance of ^{26}Al, compared with the COMPTEL observed abundance of $2M_\odot$, supports the hypothesis that most ^{26}Al is produced in massive stars, but with a rather large uncertainty. These abundances of ^{26}Al and ^{60}Fe result in a ^{60}Fe/^{26}Al flux ratio of 0.16. This puts the expected flux from ^{60}Fe below the detection threshold of the COMPTEL instrument, but within the threshold of modern instruments such as the INTEGRAL satellite [10].

Nucleosynthesis in 2002

In the decade since TWHHWM95, well motivated improvements have been made to the stellar models and reaction networks of Woosley, et al. Many of these improvements were adopted in a limited study conducted in 2002 by Rauscher *et al.*

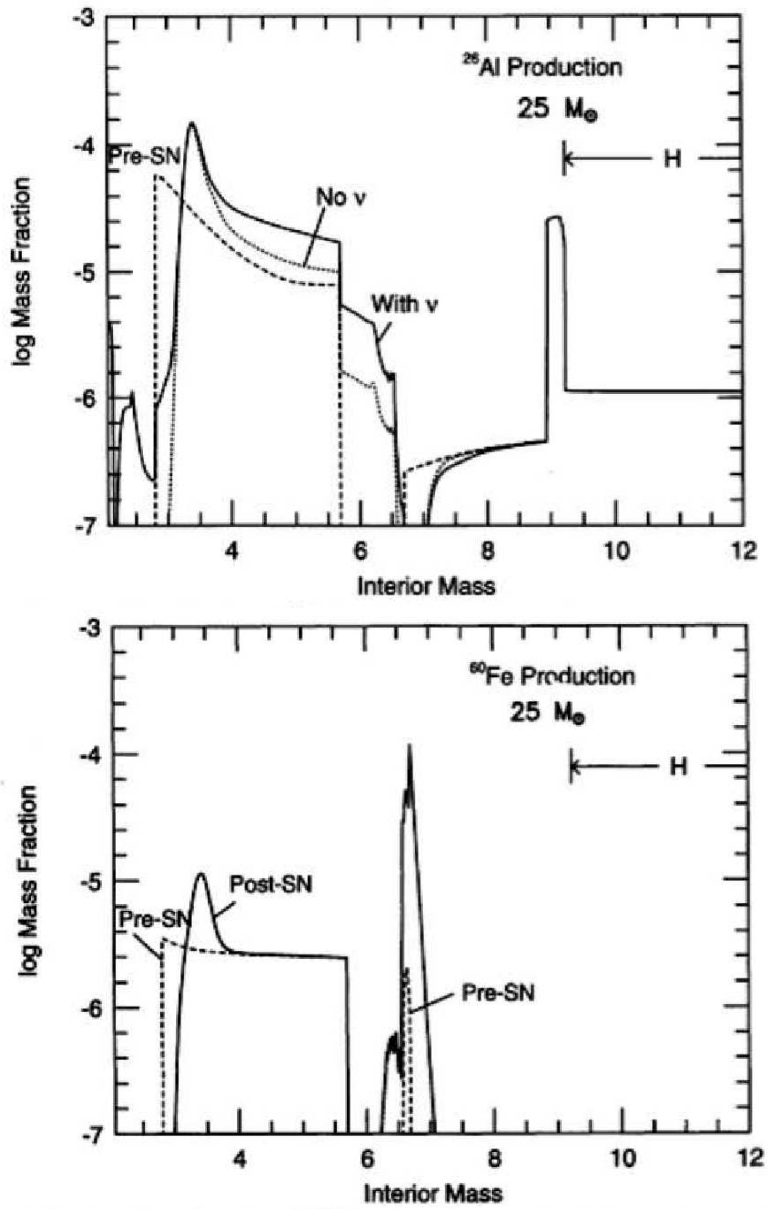

Figure 3: Production of ^{26}Al and ^{60}Fe as a function of interior mass in a $25M_{\odot}$ solar metallicity star (from Timmes, et al., ApJ **449** (1995), 204).

[25] (hereafter RHHW02).

Most of the underlying physics in RHHW02 is identical to that found in TWHHWM95, with a few notable exceptions. The most critical change in the stellar model was the inclusion of mass loss, which had been completely neglected in TWHHWM95. Other changes included the adoption of new opacities below 10^8K,

updated neutrino losses, and the suppression of convective overshooting.

The reaction network used in RHHW02 is strikingly different from that of TWHHWM95. First of all, the network is much larger. The old survey only included a few hundred isotopes from hydrogen to germanium. RHHW02 utilizes an adaptive network, where isotopes are added or removed as needed to account for all significant nuclear flows, including up to 4679 isotopes from hydrogen to astatine. A typical 15 $M_\odot$ star might employ in excess of 2400 of these isotopes. The reaction rates were also subject to significant updates. The light isotope rates were based initially on Caughlan and Fowler [6], but included many updates [12, 14]. More significant for ^{60}Fe production are the modifications to the Hauser-Feshbach rates affecting intermediate mass to heavy nuclei, which had been completely revamped to account for the wealth of experimental data available after 1980 [24, 26, 27]. The details of the Hauser-Feshbach calculations will be presented in Sections 3-5.

RHHW02 predicts an ^{26}Al abundance roughly half that of TWHHWM95 for a $25M_\odot$ star (see Figure 4, data found in [33, 25]). The ^{60}Fe abundance was several times larger than that of the previous study. For other stars, the clear trend is a smaller production of ^{26}Al and a larger production of ^{60}Fe. When convolved with an initial mass function, these yields predict an ^{60}Fe/^{26}Al flux ratio nearly four times greater than the value of 0.16 predicted by TWHHWM95 [22].

1.3 Signals for ^{60}Fe

In 2004, the first observation of ^{60}Fe gamma ray line flux was reported from the Reuven Ramaty High Energy Solar Spectroscopic Imager (RHESSI) satellite, launched in 2002 [17]. Although intended to perform imaging and spectroscopy of solar flares, its lack of shielding allows for the detection of gamma rays from all directions, and the gamma ray line flux from the inner galaxy, where most of the ^{26}Al resides according to the COMPTEL all sky map [9], can be obtained using the Earth as

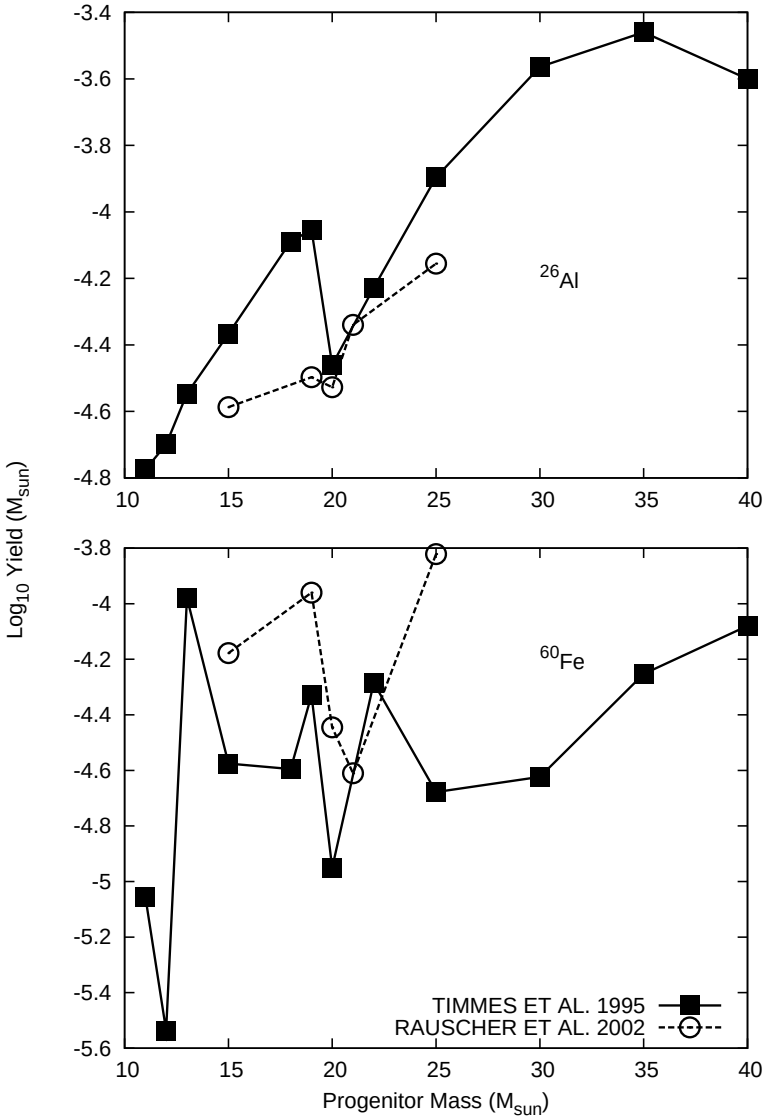

Figure 4: ^{26}Al and ^{60}Fe yields. Solid black squares (connected with solid lines) represent yields from TWHHWM95 and open circles (connected with dashed lines) represent yields from RHHW02.

an occulter [29]. Using this method, the RHESSI satellite measured a total flux of 1809 keV gamma rays (which arise from ^{26}Al decay) of $(5.71 \pm 0.54) \times 10^{-4}$ photons cm^{-2} s^{-1}. This result is consistent with previous measurements [18, 9]. Additionally, a signal was recorded for the 1173 keV and 1332 keV emission lines from ^{60}Fe decay with a combined flux of approximately 16% of that the 1809 keV line [30], in perfect agreement with the prediction of TWHHWM95. Recently, the

measured fluxes have been revised. The total 1809 keV flux is now reported at $(3.89 \pm 0.36) \times 10^{-4}$ photons cm^{-2} s^{-1}, and the combined 1173 keV and 1332 keV fluxes at $(3.6 \pm 1.4) \times 10^{-5}$ photons cm^{-2} s^{-1} [31]. This corresponds to a flux ratio of 0.093, so that the prediction of TWHHWM95 is still in reasonable agreement with observation.

Confirmation of this result has recently come from the INTEGRAL satellite, which has measured an 1809 keV flux of $(3.4 \pm 0.2) \times 10^{-4}$ photons cm^{-2} s^{-1} and a combined 1173 keV and 1332 keV flux of $(3.7 \pm 1.1) \times 10^{-5}$ photons cm^{-2} s^{-1}, corresponding to a ^{60}Fe/^{26}Al flux ratio of 0.11±0.03 [10] Eventually, the INTEGRAL mission will provide an all sky map of the distribution of ^{26}Al and ^{60}Fe.

The agreement between the TWHHWM95 prediction and observations from RHESSI and INTEGRAL, combined with the stark discrepancy between the observations and the RHHW02 prediction, is rather disconcerting. First of all, the well motivated improvements made in the stellar physics (inclusion of mass loss, improved opacities, neutrino flows, etc...) and in the nuclear physics (considerably larger reaction network, reaction rates updated to reflect experimental data available after 1980) would suggest that the more recent calculation should be more reliable. Additionally, if SNII are the primary source of steady-state ^{26}Al and one believes the result of RHHW02, the flux of 1173 and 1332 keV gamma rays should have been observed in the COMPTEL experiment.

It seems that we must draw one of the following four conclusions:

1. The observations are incorrect. Perhaps the data or the analysis was flawed. This scenario seems highly unlikely, since the two observations are independent yet agree so well.

2. The improvements made to the stellar model in RHHW02 were incorrect. A likely suspect here could be mass loss, since its inclusion marks the most

significant change from the models employed by TWHHWM95.

3. The reaction rates in RHHW02 are incorrect. The most likely candidates are discussed later. At the present time, a systematic comparison of the rates used in TWHHWM95 and RHHW02 has not been carried out , although such comparisons have been made between several of the TWHHWM95 rates and a set similar to RHHW02 [13].

4. The stellar-chemical models and nuclear physics are both reasonably correct, and the observation simply indicates that SNII are not the primary source of ^{26}Al in the interstellar medium.

To safely draw any one of these four conclusions, the other three need to be ruled out. Herein lies the primary motivation for the present work. A re-evaluation of the reaction rates directly responsible for the production of ^{60}Fe will allow us to either pinpoint the nuclear physics as the sole cause of the discrepancy between RHHW02 and observation, determine how much of the discrepancy is due to nuclear aspects, or eliminate the reaction rates as a suspect altogether. Pending the results of this investigation, it may subsequently become necessary to examine the stellar physics in detail.

1.4 Primary Nuclear Uncertainties

The following are the primary nuclear uncertainties relevant to ^{60}Fe.

1. ^{12}C(α,γ)^{16}O: The primary effect of this reaction, as it applies to the production of ^{60}Fe, is that it controls the structure and presence of the helium shell in which a significant portion of the ^{60}Fe is formed (see Figure 4). The ^{12}C target is stable, and numerous experiments have attempted to measure the cross section. However, the reaction proceeds through two sub-threshold resonances

whose widths must be determined indirectly [39], so measuring this cross section is difficult. Direct measurements have only been made down to energies 940 keV, while the reaction energies typical in the helium shell are on the order of 300 keV and below. Hence, we must rely on modeled or extrapolated rates. TWHHWM95 adopted the ^{12}C(α,γ)^{16}O rate provided by Caughlan and Fowler [6], but with an additional multiplicative factor of 1.7 to account for other aspects of stellar structure beyond the scope of this work. A more recent evaluation [4], multiplied by a factor of 1.2, is adopted in RHHW02.

In this study, we will not investigate the uncertainties related to this particular reaction rate. These uncertainties would affect many aspects of the stellar evolution. An accurate analysis of the sensitivity of ^{60}Fe abundances to ^{12}C(α,γ)^{16}O may be quite difficult. Furthermore, if this rate was significantly in error, other aspects of the stellar evolution would also be in error, including the abundances of stable isotopes which were reproduced in a most satisfactory manner in the 1995 GCE survey. It was for these reasons that the cited multiplicative factors were introduced, and we can be reasonably confident that the ^{12}C(α,γ)^{16}O rate currently in use is accurate.

2. ^{22}Ne(α,n)^{25}Mg: This reaction is an important neutron source in the neon-oxygen shell. The ^{22}Ne target is also stable, and the cross section has been measured. Uncertainties in the cross section can be more readily (and more accurately) pinned down by experiment than by theory. In any case, the production of ^{60}Fe appears to have only a minor sensitivity to variations in this rate.

3. Weak decay rates for ^{59,60}Fe and ^{60}Co: This refers not just to the lifetime of the radioisotopes as measured in the laboratory, but a temperature-dependent decay rate more appropriate for astrophysical application. These rates affect

the amount of ^{59}Fe seed available for neutron capture producing ^{60}Fe and the flux of 1173 and 1332 keV gamma rays. In the present work we do not consider the uncertainties in these rates, but adopt the rates used by [36] and [27].

4. ^{59}Fe(n,γ)^{60}Fe and ^{60}Fe(n,γ)^{61}Fe. These reactions comprise the primary production and destruction channels for ^{60}Fe. Unlike the other strong rates listed thus far, the target nuclei for these reactions are unstable. The cross sections cannot be measured with modern experimental techniques, and therefore must be modeled. Since the compound nuclei involved in these reactions lie off stability, there can be large uncertainties in the parameters that serve as inputs to the models. The rates used for these capture reactions in TWHHWM95 and RHHW02 are quite different. If nuclear physics is playing a significant role in the discrepancy between the yields of the two studies, the ^{59,60}Fe capture cross sections are prime suspects. It is these reactions that we explore in the remainder of this thesis.

In Section 2 we provide a review of the reaction mechanisms which play a role in neutron capture, as well as a discussion of the formalism relevant to modeling the reactions. In Sections 3-5 we consider the various quantities that serve as inputs to the calculations, including a detailed review of the models used in developing the reaction rates of TWHHWM95 and RHHW02. In these three sections we also develop a procedure for determining systematically input quantities that are not measured. The systematics are based on data available in the local isotopic region, as opposed to a global approach used in previous efforts. We investigate the quality and reliability of the systematic input parameters. In Section 6 we compare cross sections calculated from our model inputs to those from previous efforts and available measurements. This is done to establish the accuracy of each modeling effort in the local region of interest. In Section 7 an investigation is made into the sensi-

tivity of the ^{59}Fe(n,γ)^{60}Fe and ^{60}Fe(n,γ)^{61}Fe rates to the various input quantities. In Section 8 we explore the sensitivity of ^{26}Al and ^{60}Fe synthesis to variations in the reaction rates using parameterized single-zone models. Conclusions follow.

References

[1] Anders, E. & Grevesse, N. 1989, Geochim. Cosmochim. Acta, **53**, 197

[2] Anders, E. & Zinner, E. 1993, Meteorites **28**, 49i0

[3] Bao, Z.Y., and Käppeler, F. 1986, At. Data Nucl. Data Tables, **36**, 411

[4] Buchmann, L. 1996, ApJ **468**, 127

[5] Cappellaro, E., Turatto, M., Benetti, S., Tsvetkov, D.Y., Bartunov, O.S. & Makarova, I.N. 1993, A&A **273**, 383

[6] Caughlan, G.R. & Fowler, W.A. 1988, At. Data Nucl. Data Tables, **40**, 283

[7] Caughlan, G.R., Fowler, W.A., Harris, M.J. & Zimmerman, B.A. 1985, At. Data Nucl. Data Tables, **32**, 197

[8] Clayton, D.D. 1982 , in Essays in Nuclear Astrophysics, ed. C. Barnes et al. (Cambridge:CUP), 401

[9] Diehl, R. et al. 1993, A&AS **97**, 181

[10] Harris, M.J. 2005, A&A **433**, L49

[11] Hoffman, R.D. 1994, unpublished

[12] Hoffman, R.D., Woosley, S.E. & Weaver, T.A. 2001, ApJ **549**, 1085

[13] Hoffman, R.D., Woosley, S.E., Weaver, T.A., Rauscher, T., & Thielemann, F.-K., 1999, ApJ **521**, 735

[14] Iliadis, C., D'Auria, J., Sumner, S., Thompson, W. & Weischer, M. 2001, ApJS **134**, 151

[15] Lee, T., Papanastassiou, D.A., & Wasserburg, G.J. 1977, ApJ **211**, 107

[16] Limongi, M. & Chieffi, A. 2003, ApJ **592**, 404

[17] Lin, R.P., et al. 2002, SoPh **210**, 61

[18] Mahoney, W., Ling, J.C., Jacobsen, A.S., & Lingenfelter, R.E. 1982, ApJ **262**, 742

[19] Nuclear Data Sheets, 2005 (http://www.nndc.bnl.gov/nds)

[20] Ott, U. 1993, Nature **365**, 25

[21] Prantzos, N. 1993, ApJ **405**, 55

[22] Prantzos, N. 2004, A&A **420**, 1033

[23] Prantzos, N., & Diehl, R. 1996, Phys. Rep. **267**, 1

[24] Rauscher, T., Thielemann, F.-K. & Kratz, K.-L. 1997, Phys. Rev. C **56**, 1613.

[25] Rauscher, T., Heger, A., Hoffman, R.D. & Woosley, S.E. 2002, ApJ **576**, 323

[26] Rauscher, T. & Thielemann, F.-K. 2000, At. Data Nucl. Data Tables **75**, 1

[27] Rauscher, T. & Thielemann, F.-K. 2001, At. Data Nucl. Data Tables **79**, 47

[28] Sargood, D.G. 1982, Phys. Rep. **93**, 61

[29] Smith, D.M. 2003, ApJL **589**, 55

[30] Smith, D.M. 2004, New Astr. Rev. **48**, 87

[31] Smith, D.M. 2004, in The INTEGRAL Universe, ed. V. Schönfelder, G.G. Licht & C. Winkler (Noordwljki:ESA), ESA Spec. Publ. 552, 45

[32] Thielemann, K.-F., Nomoto, K. & Hashimoto, M. 1996, ApJ **460**, 408

[33] Timmes, F.X., Woosley, S.E., Hartmann, D.H., Hoffman, R.D., Weaver, T.A., & Matteucci, F. 1995, ApJ **449**, 204

[34] Timmes, F. X., Woosley, S. E., & Weaver, T. A. 1995, ApJS **98** , 617

[35] Tuli, J.K. 2000, Nucl. Wallet Cards (New York: Brookhaven Natl. Labs.)

[36] Woosley, S.E., & Weaver, T.A. 1995, ApJS **101**, 181

[37] Woosley, S.E., Fowler, W.A., Holmes, J.A. & Zimmerman, B.A. 1978, At. Data Nucl. Data Tables, **22**, 371

[38] Woosley, S.E., Wilson, J.R., Mathews, G.J., Hoffman, R.D. & Meyer, B.S. 1994, ApJ **433**, 229

[39] Woosley, S.E., Heger, A. & Weaver, T.A. 2002, Rev. Mod. Phys. **74**, 1015

2 Nuclear Reaction Mechanisms

The strength of a given reaction is best described in terms of a cross section. In particular, the differential cross section $d\sigma/d\Omega$ is defined as the rate at which the outgoing particle is scattered into the solid angle $d\Omega$, divided by the flux of incoming particles given as the number of incident particles per unit area per unit time. The cross section σ is obtained by integrating $d\sigma/d\Omega$ over the 4π solid angle. The resulting quantity is a function of energy (or velocity), and has units of area. Hence the name "cross section". The reaction rates used in nucleosynthesis calculations are a convolution of the cross section with a velocity distribution of incident particles $\Phi(v)$:

$$N_A \langle \sigma v \rangle = \int_0^\infty \sigma(v)\ v\ \Phi(v)\ dv\ . \tag{1}$$

In stellar environments, $\Phi(v)$ is assumed to be Maxwellian. The integral in this expression can easily be handled numerically, and the process of calculating reaction rates reduces to calculating the associated cross sections.

When one is considering nucleosynthetic processes, all possible nuclear flows likely to occur in stellar environments must be taken into account. The (possibly radioactive) residual of a given reaction subsequently becomes a target for additional reactions. Thus, nucleosynthesis calculations typically involve a large network of stable and radioactive isotopes, with multiple reactions for each isotope. Ideally, the cross sections would be measured in the laboratory. However, at the present date, cross sections have primarily been measured for stable targets. Most radionuclides have too short a lifetime to fabricate a target and perform the experiment. Those which are longer lived generally cannot be produced and collected in sufficient abundances. There are only a handful of exceptions, such as ^{99}Tc ($t_{1/2} = 2.1 \times 10^5$ yr). Currently research is being conducted into radioactive beam experiments, which may open the doors to measuring cross sections for radioactive targets [24]. Also,

there is an effort to measure these cross sections indirectly using surrogate reaction techniques [9]. In any event, the time when all the rates for a reaction network will be measured is many decades away, and then only if such measurements prove feasible. For the time being, a large number of cross sections must be supplied by theory. Such is the case with the ^{59}Fe(n,γ)^{60}Fe and ^{60}Fe(n,γ)^{61}Fe reactions, which we have established as the most probable source of nuclear uncertainties in the production of ^{60}Fe. In this section, we describe the theory and methods required for modeling these cross sections.

Before modeling cross sections, one must first understand the mechanisms by which nuclear reactions take place. Consider a target nucleus $\mathcal{I}$ in state μ interacting with an incident particle j. There are essentially two basic ways the interaction can occur. First, j may interact directly with one or a few of the nucleons in $\mathcal{I}$. For example, j may "knock out" one of the nucleons in $\mathcal{I}$ and take its place. It is also possible for j to radiate energy in the form of a gamma ray and fall into a bound state of the nucleus $\mathcal{I} + j$. If j is a composite particle, such as a deuteron, this type of radiative capture may only occur for one of its constituents in a "stripping" reaction. These reactions involving only a few nucleons are referred to collectively as "direct reactions". They occur in the time it takes the projectile to traverse the nuclear field (generally on the order of $\sim 10^{-22}$ seconds), and the outgoing particles tend to be forward peaked.

Second, the reaction may proceed by the absorption of j into $\mathcal{I}$, where collisions with the various constituent nucleons of $\mathcal{I}$ will disseminate the excess kinetic energy throughout the nucleus. The pair form an intermediate "compound nucleus" in statistical equilibrium. The excess excitation energy in the compound nucleus is subsequently shed via the emission of particles and radiation. Such reactions are called compound nuclear reactions, and occur on time scales of $\sim 10^{-15} - 10^{-18}$ seconds, considerably longer than those of direct reactions. Also, the process of

equilibration causes the compound nuclear state to essentially "forget" how it was formed (with the exception that energy, angular momentum, and parity are conserved), and the outgoing particles are emitted more or less isotropically. Deviations from isotropic distributions may occur with angular momentum cutoffs, in which case the distribution will remain symmetric. Thus, by observing the angular distribution of outgoing particles, one can infer which reaction mechanism is dominant.

During the course of equilibration, it is possible for a sufficient amount of excitation energy to be localized onto a single nucleon that it can escape the nuclear field. This emission happens prior to the compound nucleus obtaining statistical equilibrium. Such reactions are referred to as "pre-equilibrium" reactions, and comprise a third reaction mechanism.

The remainder of this section will briefly summarize the processes of direct and pre-equilibrium reactions, which turn out to be of only minor importance in this study. The dominant reaction mechanism in the present work is the compound nuclear mechanism, and we will review it in considerable detail.

Before proceeding with these in-depth discussions, we should introduce a few concepts that apply equally to all types of reactions. The first is the notion of the so-called "Q-value". The total mass of a system typically changes during the course of a nuclear reaction. This change in mass is accompanied by an increase or decrease in the excess energy available to the system. The Q-value of the reaction $\mathcal{I} + j \longrightarrow \mathcal{L} + k$, designated Q_{jk}, is defined as the increase in energy associated with the reaction. Q_{jk} may take on positive or negative values, depending on the masses of the reactants and products. The method of calculating these Q-values will be discussed in Section 3.

Nuclear reactions proceed through "resonances", which can be described in terms of "virtual" quasi-stationary energy levels in the target/projectile system [3]. Many of these resonances, especially those associated with single particle and collective

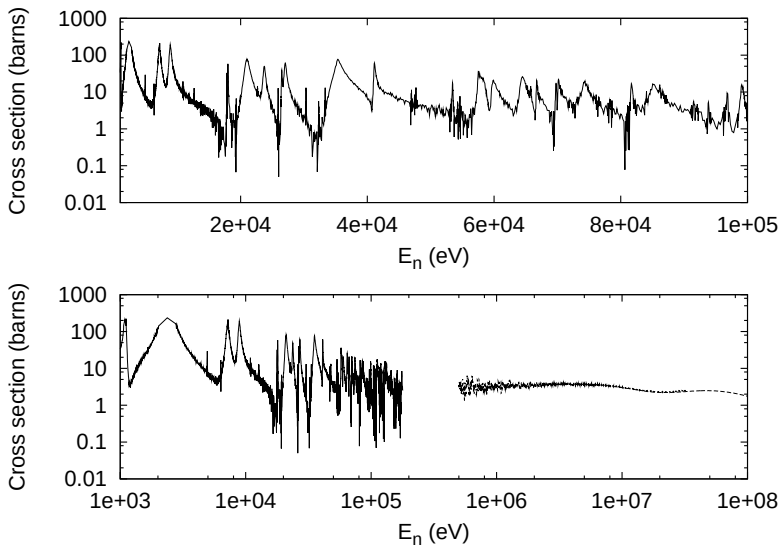

Figure 5: Measured total neutron cross section on ^{55}Mn. Structure arising from individual resonances is clearly seen below 10^6 eV of incident energy.

excitations, are quite narrow, with widths typically on the order of tens of eV. At high excitation energies the spacing between these resonances becomes small compared to their width, and the interaction can be accurately described with energy-averaged quantities, such as transmission coefficients derived from an optical potential.

Individual resonances provide structure to some cross sections at low incident particle energies. An example of such a resonance structure, found in the total neutron cross section on ^{55}Mg, can be seen in Figure 5. The data below 500 keV incident energy is taken from [15], and the higher energy data is taken from [1] and [4]. For the sake of clarity, errorbars have been omitted. Individual resonances are responsible for the "noisy" structure seen below 1 MeV. At higher energies (above 1 MeV) the resonances begin to overlap, the interaction from individual resonances begins to be replaced by an "average" behavior, and the cross section varies smoothly with energy.

One can model direct reactions between resonances by making use of a real nuclear potential. However, the modeling of compound nuclear reactions relies heavily

on the use of energy averaged transmission coefficients, and cannot reproduce resonant structure. Thus the validity of compound nuclear modeling is questionable at very low energies where the effects of individual resonances can be seen. At best, such calculations can yield an average behavior.

2.1 Direct Reactions

Direct reactions involve only one or a few of the nucleons in the target. They proceed through single resonances, as opposed to compound nuclear reactions which populate energy levels according to their statistical weights. As such, direct reactions connect the initial and final states via a definite structural relationship, and provide a powerful probe into nuclear structure [13].

In the specific region of the isotopic plane and at energies of interest to us, the direct reaction contributions to most reactions are quite small compared to the compound nuclear and pre-equilibrium components. We are usually able to safely ignore the direct reaction component to a cross section for incident neutron energies below a few tens of MeV. However, in cases where sub-threshold resonances with large spectroscopic factors exist, the contribution may be more significant [22]. In Section 6.6 we investigate the importance of direct reaction contributions to neutron capture on a few iron targets. Based on the results, we justify the neglect of direct reactions in our modeling effort. For completeness, we provide this brief description of the formalism involved in direct reaction modeling. This discussion will also introduce some concepts needed in understanding compound nuclear reactions.

2.1.1 Elastic and Inelastic Scattering

The simplest direct process is "shape" elastic scattering, where the incident particle interacts with the nucleus as a whole without gaining or losing energy. The target is represented by a potential V which may be either a real or complex optical

potential. The projectile spin and Coulomb repulsion can be accounted for by including appropriate terms in the scattering potential. At large distances from the target, the incident particle is represented by a plane wave (traveling in the direction of the azimuthal axis by convention), and the refracted particle by a spherical wave, so that the asymptotic wavefunction is of the form

$$\psi(r,\theta) \sim \exp(ikz) + \frac{f(\theta)}{r}\exp(ikr) \ . \tag{2}$$

Here k is the wavenumber given by $k = \sqrt{(}2mE)/\hbar$, and $f(\theta)$ is the scattering amplitude which describes the angular dependence of the scattered wave (azimuthal symmetry is maintained). These scattering amplitudes are found by solving the Schrödinger equation using the potential V. The differential cross section is related to the scattering amplitude by

$$\frac{d\sigma_{el.}}{d\Omega} = \left|f(\theta)\right|^2 \tag{3}$$

and the total elastic scattering cross section is obtained by integrating over solid angles.

This wavefunction may be decomposed into partial waves:

$$\psi(r,\theta) = \sum_l \frac{\phi_l(r)}{r} P_l(\cos\ \theta) \tag{4}$$

where $P_l(\cos\ \theta)$ are Legendre polynomials. This expansion allows the Schrödinger equation to be separated into radial and angular parts. The resulting radial wave equation may be numerically integrated to obtain the radial wavefunctions $\phi_l(r)$. All of the information obtained from solving the wave equations can be conveniently contained in the (complex) phase shift δ_l, defined as the difference in the phase of the asymptotic wave in the presence and absence of the scattering potential V. The

δ_l are a function of the incident energy, and since each δ_l is associated with a unique $P_l(\cos\ \theta)$, they contain all of the information regarding the angular and energy dependence of the scattering. The scattering amplitude can be expressed in terms of the phase shifts:

$$f(\theta) = \frac{1}{2ik}\sum_l (2l+1)\left[\exp(2i\delta_l) - 1\right] P_l(\cos\ \theta)\ . \tag{5}$$

Putting this expression into Equation 3 and integrating over the angles, one finds

$$\sigma_{el.} = \frac{4\pi}{k^2}\sum_l (2l+1)\Big|1 - \exp(2i\delta_l)\Big|^2\ . \tag{6}$$

Even though the partial expansion involves an infinite number of partial waves, only a few will contribute appreciably to the cross section, and the sum can generally be cut off after a finite number of l waves. Evaluation of the elastic cross section is thus reduced to numerically determining a handful of phase shifts [13].

Another useful quantity is the transmission coefficient, defined as

$$T_l = 1 - \Big|\exp(2i\delta_l)\Big|^2\ . \tag{7}$$

As its name suggests, the transmission coefficient is related to the probability that the partial wave l will be absorbed into the potential. The absorption cross section is then given by

$$\sigma_{abs.} = \frac{\pi}{k^2}\sum_l (2l+1)T_l\ . \tag{8}$$

This quantity will be useful in our discussion of compound nuclear reactions.

Inelastic scattering is treated similar to elastic scattering in that the projectile interacts with the nucleus as a whole, but with energy being transferred between the target and incident particle. Efforts to model inelastic scattering considering

only the transfer of energy between the incident particle and a single nucleon tend to underestimate the cross section, indicating that the transferred energy can excite collective motions in the target. Reactions involving these collective states must be modeled using a coupled-channel formalism. One decomposes the wavefunction of the system into bound state wavefunctions of the nuclear potential. The bound state wavefunctions are then decomposed into spherical harmonics, and the expansion coefficients are obtained by solving the Schrödinger equation. The angular and radial portions of the wavefunction can be separated, similar to the elastic scattering case described above. This yields a set of coupled equations describing the wavefunction in all the elastic and inelastic channels, which can be solved to find the radial components of the partial wavefunctions. The phase shifts are subsequently formed, and the cross section can be determined accordingly.

To perform a coupled channel calculation, one needs to properly describe the vibrational or rotational nature of the collective nuclear states. In practice, one must limit the number of inelastic channels (corresponding to final states of the residual nucleus) to a few of the lowest energy excitations.

2.1.2 Nucleon Transfer Reactions

In our study, we are not so much interested in the scattering of the projectile, but rather the absorption of it. Direct reactions where one or more nucleons are stripped from or picked up by the projectile are called nucleon transfer reactions. Neutron capture is an example of such a reaction–the neutron is transferred to the target.

Nucleon transfer is usually modeled in the context of the distorted wave Born approximation (DWBA). In this approximation, a first order perturbation theory is applied to determine the reaction amplitude. The differential cross section is given by

$$\frac{d\sigma}{d\Omega} = \frac{m_i k_i}{m_f k_f} \left| M(\vec{k_i}, \vec{k_f}) \right|^2 \tag{9}$$

where

$$M(\vec{k_i}, \vec{k_f}) = \frac{m_f}{2\pi\hbar^2} \left\langle \psi_f(\vec{k_f}) \middle| H' \middle| \psi_i(\vec{k_i}) \right\rangle \ . \tag{10}$$

In these expressions $\vec{k_i}$ and $\vec{k_f}$ are the wavevectors associated with the projectile and outgoing particle, and m_i and m_f are their masses. The perturbation Hamiltonian H' is defined as the difference between the total Hamiltonian of the system and the Hamiltonian of either the initial or final asymptotic states. The initial wavefunction ψ_i may be expressed as a product of the wavefunction of the target ψ_T, the wavefunction for the relative motion of the projectile with respect to the target $\psi_p(\vec{k_i})$, and if the projectile is a composite particle (such as a deuteron) the internal wavefunction of the projectile ϕ_p. The final state wavefunction can be expressed similarly using the residual and outgoing particle. Hence, the matrix element becomes

$$M(\vec{k_i}, \vec{k_f}) = \frac{m_f}{2\pi\hbar^2} \left\langle \psi_R \psi_o(\vec{k_f}) \middle| H' \middle| \psi_p(\vec{k_i}) \phi_p \psi_T \right\rangle \ . \tag{11}$$

The wavefunction of the residual ψ_R, can be written in terms of the the target ψ_T and the captured particle ψ_c as

$$\psi_R = \sum_{JL} \sqrt{S_{JL}} \psi_T \phi_c \ . \tag{12}$$

The sum extends over total and orbital angular momenta of the transferred particle. S_{JL} is the spectroscopic factor associated with the "emptiness" of the final state. For select targets S_{JL} can be measured in stripping reactions. Otherwise it may be estimated from nuclear models.

Integration over the coordinates of the target wavefunction, after making this substitution, reduces the matrix element to

$$M(\vec{k_i}, \vec{k_f}) = \frac{m_f}{2\pi\hbar^2} \sum_{JL} \sqrt{S_{JL}} \left\langle \phi_c \psi_o(\vec{k_f}) \middle| H' \middle| \psi_p(\vec{k_i}) \phi_p \right\rangle \ . \tag{13}$$

The $\psi_p(\vec{k_i})$ and $\psi_o(\vec{k_f})$ are the same wavefunctions that would appear in elastic scattering of the projectile/target and residual/outgoing pairs, respectively. An analysis of elastic scattering must therefore precede the modeling of nucleon transfer reactions. Further approximations allow one to treat $H'\phi_p$ as a delta function of the coordinates of the constituents. The remaining wavefunction ϕ_c is an eigenfunction of the potential with the depth adjusted to give the state JL at the appropriate energy.

This formalism for nucleon transfer reactions only accounts for the capture of the incident nucleon to a single particle state. As with inelastic scattering, a complete treatment must also account for capture that excites collective states. This is often referred to as semi-direct capture, and modeling it requires using the coupled-channel formalism in conjunction with the DWBA.

In our brief study of direct capture in Section 6.6, we use the CUPIDO code, which entails both direct and semidirect capture [8]. This code also uses the complete "current" Hamiltonian used to describe the interaction between the nuclear and electromagnetic field rather than the popular density approximation. The only external inputs required in modeling direct capture are the optical potential (presented in Section 5) and the spectroscopic properties of the resonances, which we obtain from experimental databases. Since we are not investigating direct reactions beyond demonstrating their negligible size in relation to compound nuclear reactions (see Section 6.6), we will elaborate no further on direct reaction mechanisms. Rather, we turn our attention to the more important compound nuclear mechanisms.

2.2 Compound Nuclear Reactions

Statistical reaction theory dates back to 1936 when Bohr first proposed that a collision between a neutron and a heavy nucleus could result in the formation of

an intermediate state known as a compound nucleus [2]. The compound nucleus exhibits "remarkable stability" and is sufficiently long lived that the nucleons reach statistical equilibrium. Bohr further suggested that the compound nucleus would decay either by the emission of radiation or particles, and that these competing decay modes would have no "immediate connexion (Sp) with the first stage of the encounter". This latter idea, that the compound nucleus essentially "forgets" how it was formed, is commonly known as the Bohr independence hypothesis or "nuclear amnesia". The excess energy is eventually shed via the emission of particles or radiation, similar to the evaporation of molecules from the surface of a liquid.

The independence hypothesis has been the subject of numerous experimental tests. There have been attempts to form a compound nuclear state at a given excitation energy from two separate incident channels, such as the formation of ^{51}Cr from ^{50}Cr plus neutron or ^{50}V plus proton, and subsequently measure the ratio of decay probabilities into the various exit channels. If the independence hypothesis is correct the ratios of decay probabilities should be the same for both incident channels. Such measurements have been made for intermediate mass and heavy nuclei, and support the independence hypothesis [14, 7, 29, 21]. These measurements typically involve incident energies ranging from 10 to 40 MeV.

There is also experimental evidence that suggests the independence hypothesis loses validity at higher energies [10, 11]. This can be easily understood within the framework of pre-equilibrium emission. With greater excitation energies it is more likely that enough energy will be localized in a single nucleon that it can escape the nuclear potential, and less likely that a compound nucleus will be formed.

2.2.1 Early Models of Compound Nuclear Reactions

The first working theory of compound nuclear reactions based on Bohr's hypothesis was developed by Weisskopf and Ewing [27]. A cross section σ_{jk}, which proceeds

through incident channel j and exit channel k, may be expressed as

$$\sigma_{jk} = \sigma_j P_k \tag{14}$$

where σ_j is the cross section for the formation of the compound nucleus through channel j (the absorption cross section), and P_k is the probability that the compound nucleus will decay through channel k. Suppose that we wish to consider an incident channel of energy E and an exit channel to states of energy between E' and $E' + dE'$. The formation of the compound nucleus will exhibit a dependence on the incident energy, while the probability of decay via specific exit channels will depend on both the incident and outgoing energies. This latter dependence on the incident energy is not in violation of the independence hypothesis: the incident energy is needed only to supply excitation energy to the compound nucleus. Explicitly including the energy dependence, Equation 14 reads

$$\sigma_{jk}(E, E')dE' = \sigma_j(E) P_k(E, E')dE' \ . \tag{15}$$

The decay probability P_k is related to both the decay width $\Gamma_k(E, E')$ and the density of states in the residual nucleus ($\rho_k(U' = E - E' - B_k)$, where B_k is the binding energy of the residual). In particular, the probability will be given by the product of the decay width and level density divided by the sum of all other possible decay channels k'', i.e.

$$\sigma_{jk}(E, E')dE' = \sigma_j(E) \frac{\Gamma_k(E, E')\rho_k(U')dE'}{\sum_{k''} \int_0^{E-Q_{jk''}} \Gamma_{k''}(E, E'')\rho_{k''}(U'')dE''} \ . \tag{16}$$

$Q_{jk''}$ is the Q-value of the reaction involving the incident channel j and exit channel k''. The integration in the denominator accounts for all possible states in the residual formed by the emission of k''.

At this point we may invoke the reciprocity theorem, which relates a cross section for a given reaction to it's inverse:

$$\lambda\!\!\!^{-2}_k \sigma_{jk} = \lambda\!\!\!^{-2}_j \sigma_{\hat{k}\hat{j}} \ . \tag{17}$$

Hats on subscripts refer to time reversed states. The quantity $\lambda\!\!\!^{-}_i$ is related to the wave number k_i:

$$\begin{aligned} \lambda\!\!\!^{-}_i &= \frac{1}{k_i} \\ &= \left(\frac{2}{\hbar^2} m_u \hat{A}_i E_i\right)^{-\frac{1}{2}} \ . \end{aligned} \tag{18}$$

Here, m_u is 931.5 MeV/c^2, $\hat{A}_i$ is the reduced mass of particle i in atomic units, and E_i is the center of mass energy. This expression, when combined with Equations 15, 16, and 17 implies that the decay width Γ_k is proportional to $m_u \hat{A}_k E_k \sigma_k$, i.e. the decay width for the exit channel k may be expressed in terms of the cross section for forming the compound nucleus via incident channel k. Additionally, we note that the level densities should be augmented by a statistical weight $g_k = 2J_k + 1$ to account for the magnetic quantum states associated with spin J_k. This leads us to the Weisskopf-Ewing formula

$$\sigma_{jk}(E, E')dE' = \sigma_j(E) \frac{g_k \hat{A}_k E' \sigma_k(E') \rho_k(U') dE'}{\sum_{k''} g_{k''} \hat{A}_{k''} \int_0^{E-Q''} E'' \sigma_{k''}(E'') \rho_{k''}(U'') dE''} \tag{19}$$

where the absorption cross sections $\sigma_i(E)$ are generally expressed in terms of transmission coefficients as in Equation 8, i.e.

$$\sigma_j(E) = \pi \lambda\!\!\!^{-2}_j T_j(E) \ . \tag{20}$$

These transmission coefficients are generally obtained from an optical potential,

and are energy averaged. As such, they only describe the absorption accurately in regions where resonance structure is absent. Hence, the Weisskopf-Ewing model cannot reproduce resonant structure in a cross section.

The simple Weisskopf-Ewing model suffers from two primary weaknesses. First, it neglects the conservation of angular momentum. Second, it only describes reactions involving a continuum of states, as expressed in terms of an empirical level density. Despite these weaknesses, this model can still be useful in determining quantities such as level density parameters (when used in conjunction with measured cross sections) and the magnitudes of total cross sections [13].

2.2.2 The Hauser-Feshbach Model

To include angular momentum conservation and discrete nuclear structure with the independence hypothesis, we begin by considering a target nucleus $\mathcal{I}$ in state μ (with spin and parity given by J^μ and Π^μ). A compound nucleus of spin J and parity Π is formed via the incident channel j with energy E and subsequently decays through the exit channel k with energy E', leaving us with a residual nucleus $\mathcal{L}$ in state ν. The incident and outgoing energies E and E' are related. In particular

$$E' = E + Q_{ij}^{\mu\nu} \tag{21}$$

where we have defined

$$Q_{ij}^{\mu\nu} = Q_{ij} + E^\mu - E^\nu \ . \tag{22}$$

The quantities E^μ and E^ν are the energies corresponding to the states μ and ν.

Suppose that j can be described via an incident plane wave. This wave can be separated into angular momentum components by means of the partial wave expansion (Equation 4). Consider now the lth partial wave in this expansion (with angular momentum l). The cross section for the formation of the compound nucleus

for this particular l wave is given by

$$\sigma_j^{\mu}(E) = \pi \lambda\!\!\!^{-2}_j (2l+1) T_{jil}^{J\Pi}(E) \tag{23}$$

where $T_{jil}^{J\Pi}(E)$ is the transmission function for particle j (having energy E) into $\mathcal{I}^{\mu}$ via partial wave l. The incident channel spin $i = J^j + J^{\mu}$ couples with the angular momentum l to given the compound nucleus angular momentum J.

The independence hypothesis (Equation 14) tells us that the cross section for this reaction, proceeding through this incident l wave, will be equal to the formation cross section given in Equation 23 multiplied by the probability that the compound nucleus will decay through channel k with energy E'. Similar to the Weisskopf-Ewing model, the decay probabilities are related to the compound nucleus formation cross sections for the channel k. In particular, we can combine Equations 14 and 23 to find

$$\sigma_{jk}(E) = \pi \lambda\!\!\!^{-2}_j (2l+1) T_{jil}^{J\Pi}(E) P_k(E, E') \tag{24}$$

and similarly

$$\sigma_{\hat{k}\hat{j}}(E') = \pi \lambda\!\!\!^{-2}_k (2l'+1) T_{\hat{k}i'l'}^{J\Pi}(E') P_{\hat{j}}(E, E') \ . \tag{25}$$

Multiplying the first of these expressions by $\lambda\!\!\!^{-2}_k$ and the second by $\lambda\!\!\!^{-2}_j$, we may invoke reciprocity (Equation 17) to find

$$T_{jil}^{J\Pi}(E) P_k(E, E') = T_{\hat{k}i'l'}^{J\Pi}(E') P_{\hat{j}}(E, E') \ . \tag{26}$$

Hence the decay probability for channel k (P_k) is proportional to the transmission function for the time reversed channel. The possible decay probabilities must sum to unity, so that P_k may be written as $P_k / \sum_{k''} P_{k''}$. Replacing the decay probabilities with their transmission functions, the constants of proportionality will cancel,

leaving us with

$$P_k = \frac{T^{J\Pi}_{\hat{k}i'l'}(E')}{\sum_{k'',i'',l''}\sum_{\nu''=0}^{\nu''_{max}} T^{J\Pi}_{k''i''l''}(E^{\nu''})} \tag{27}$$

where the sum over states in the denominator is cut of at ν''_{max}, the highest level whose energy is below the maximum excitation energy available to the channel k''. The exit channel spin $i' = J^k + J^\nu$ (and $i'' = J^{k''} + J^{\nu''}$ in the denominator) and exiting partial wave l' (l'') must couple to give J, the spin of the compound nuclear state.

We may now write the cross section for the reaction $\mathcal{I}^\mu + j \rightarrow \mathcal{L}^\nu + k$ proceeding through the absorption of the lth partial wave of j into a compound nuclear state of spin J in terms of the transmission functions:

$$\sigma^{\mu\nu}_{jkl}(E) = \pi\lambda\!\!\!^{-2}_j(2l+1)T^{J\Pi}_{jil}(E)\frac{T^{J\Pi}_{\hat{k}i'l'}(E')}{\sum_{k'',i'',l''}\sum_{\nu''=0}^{\nu''_{max}} T^{J\Pi}_{k''i''l''}(E^{\nu''})} \ . \tag{28}$$

The partial waves l' and l'' are subject to the constraints originating from the coupling of incident and outgoing channel spins (containing the spins of the target and residual) and the total angular momentum of the compound system, J. Conservation of angular momentum has now been explicitly accounted for, as well as the individual levels in the target, compound nucleus, and residual. Equation 28 gives the cross section proceeding from a specific state in the target to a specific state in the residual via a specific l wave and state of the compound nucleus. In practice, such a cross section cannot be measured, in that experiments involve unpolarized beams consisting of many l waves, and detectors do not measure the spins of outgoing particles.

The laboratory cross section can be obtained by averaging Equation 28 over initial spins and summing over final spins. Since the spins of the target and residual are fixed (recall that we are considering specific states μ and ν), these sums may be expressed in terms of the channel spins. Additionally, we must sum over all possible

l waves and total angular momenta J and parity Π in the compound nucleus. The averaging over initial spins can be achieved by inserting the probabilities that J^μ and J^j will couple to give a particular i and subsequently that j and l will couple to give J. Such coupling probabilities are given by

$$P(a+b \to c) = \frac{2c+1}{(2a+1)(2b+1)} \ . \tag{29}$$

In total, we have

$$\bar{\sigma}^{\mu\nu}_{jk}(E) = \sum_{i,i',l,l',J,\Pi} \frac{2i+1}{(2J^\mu+1)(2J^j+1)} \frac{2J+1}{(2i+1)(2l+1)} \sigma^{\mu\nu}_{jkl}(E) \ . \tag{30}$$

The factors of $(2i+1)$ cancel, and the factor of $(2l+1)$ will cancel with that in $\sigma^{\mu\nu}_{jkl}(E)$. This leaves us with

$$\bar{\sigma}^{\mu\nu}_{jk}(E) = \sum_{i,i',l,l',J,\Pi} \frac{2J+1}{(2J^\mu+1)(2J^j+1)} \pi \lambda\!\!\!^{-2}_j T^{J\Pi}_{jil}(E) \frac{T^{J\Pi}_{\hat{k}i'l'}(E')}{\sum_{k'',i'',l''} \sum_{\nu''=0}^{\nu''_{max}} T^{J\Pi}_{k''i''l''}(E^{\nu''})} \ . \tag{31}$$

We abbreviate $(2J^a+1)$ with g_a. Moving several constant factors outside of the sum, we obtain an expression for the total spin-averaged cross section of the compound nuclear reaction $\mathcal{I}^\mu + j \to \mathcal{L}^\nu + k$:

$$\bar{\sigma}^{\mu\nu}_{jk}(E) = \frac{\pi \lambda\!\!\!^{-2}_j}{g_\mu g_j} \sum_{i,i',l,l',J,\Pi} g_J T^{J\Pi}_{jil}(E) \frac{T^{J\Pi}_{\hat{k}i'l'}(E+Q^{\mu\nu}_{jk})}{\sum_{k'',i'',l''} \sum_{\nu''=0}^{\nu''_{max}} T^{J\Pi}_{k''i''l''}(E^{\nu''})} \ . \tag{32}$$

This model was first developed in 1952 by Hauser and Feshbach [16], and is appropriately known as the Hauser-Feshbach model. It is similar to the Weisskopf-Ewing model, except that provisions have been made to ensure the conservation of angular momentum. It additionally considers specific states in the target and residual, as well as individual states in the compound nucleus.

It is now necessary to say a few more words regarding the denominator of Equa-

tion 32. In particular, we note that the sum extends over all energetically accessible discrete states ν''. However, the excitation energy for an exit channel k'' often exceeds the energy of the highest discrete state for which the relevant spins and parities are known (typically 1-3 MeV). In such situations, one must employ an empirical spin- and parity-dependent level density $\rho(E, J, \Pi)$. The summation over discrete states may then be replaced with

$$\sum_{\nu''=0}^{\nu''_{max}} T^{J\Pi}_{k''i''l''}(E^{\nu''}) \quad \rightarrow$$
$$\sum_{\nu''=0}^{\omega} T^{J\Pi}_{k''i''l''}(E^{\nu''}) + \sum_{J'\Pi'} \int_{E_\omega}^{E_{max}} T^{J\Pi}_{k''i''l''}(\epsilon)\rho(E + Q_{jk''} - \epsilon, J', \Pi')d\epsilon \ . \qquad (33)$$

Here, ω is the highest level up to which the spins and parities are known and E_{max} is the maximum excitation energy available ($E_{max} = E + E^{\mu} + Q_{jk''}$). More will be said regarding the level density in Section 4.

We should also note at this point that the transmission coefficient is treated in a different manner for photons. An outgoing photon is described in terms of its multipolarity rather than by an l wave with a channel spin. Additionally, we express the photon transmission coefficient in terms of the transition energy ϵ_γ In particular, we should rewrite Equation 32 as

$$\text{Particle Out}: \quad \bar{\sigma}^{\mu\nu}_{jk}(E) = \frac{\pi \lambda\!\!\!^{-2}_j}{g_\mu g_j} \sum_{i,i',l,l',J,\Pi} g_J T^{J\Pi}_{jil}(E) \frac{T^{J\Pi}_{ki'l'}(E + Q^{\mu\nu}_{jk})}{T_{tot}}$$
$$\text{Photon Out}: \quad \bar{\sigma}^{\mu\nu}_{jk}(E) = \frac{\pi \lambda\!\!\!^{-2}_j}{g_\mu g_j} \sum_{i,l,X,L,J,\Pi} g_J T^{J\Pi}_{jil}(E) \frac{T^{J\Pi}_{\gamma XL}(\epsilon^{\nu}_{\gamma})}{T_{tot}} \qquad (34)$$

where

$$T_{tot} = \sum_{k'',i'',l''} \left[\sum_{\nu''=0}^{\omega} T^{J\Pi}_{k''i''l''}(E^{\nu''}) + \sum_{J'\Pi'} \int_{E_\omega}^{E_{max}} T^{J\Pi}_{k''i''l''}(\epsilon)\rho(E^{k''}_{exc} - \epsilon, J', \Pi')d\epsilon \right] +$$
$$\sum_{X'',L''} \left[\sum_{\nu''=0}^{\omega} T^{J\Pi}_{\gamma X''L''}(\epsilon^{\nu''}_{\gamma}) + \sum_{J'\Pi'} \int_{0}^{\epsilon^{\omega}_{\gamma}} T^{J\Pi}_{\gamma X''L''}(\epsilon)\rho(E^{\gamma}_{exc} - \epsilon, J', \Pi')d\epsilon \right] \ . \qquad (35)$$

In this equation, E_{max} is defined as before and $E_{exc}^{k''}$ is the excitation energy for the channel k'', given by $E_{exc}^{k''} = E + E^{\mu} + Q_{jk''}$.

In heavier nuclei where the fissility, defined as 0.0205 Z^2/A, is large enough, we must consider fission as a possible exit channel. In such cases, T_{tot} would need to be modified accordingly. In the isotopic region of interest in the present work (the iron group), fission probabilities are low ($\leq 2\%$) and may be neglected.

2.2.3 Width Fluctuation Correlations

Equations 34 and 35 neglect to account for possible correlations in the wavefunctions of the incident and outgoing waves in the elastic channel. These so-called width fluctuation correlations cause an enhancement of the elastic scattering and a corresponding decrease in the cross sections of other channels [23].

Width fluctuation correlations are generally taken into account with an additional multiplicative factor in the Hauser-Feshbach formula, i.e. Equation 28 becomes

$$\sigma_{jk}^{\mu\nu}(E) = \pi \lambda\!\!\!^{-}{}_j^2 (2l+1) T_{jil}^{J\Pi}(E) \frac{T_{\hat{k}i'l'}^{J\Pi}(E')}{\sum_{k'',i'',l''} \sum_{\nu''=0}^{\nu''_{max}} T_{k''i''l''}^{J\Pi}(E^{\nu''})} W_{jk} \ . \tag{36}$$

A reasonably complete expression for W_{jk} can be obtained through the Gaussian orthogonal ensemble (GOE) [26]. However, this approach requires the evaluation of a triple integral, and is numerically expensive. The correlations are usually evaluated with some sort of approximation. The method developed by Moldauer [20] has been particularly popular, and this is the model we adopt in our calculations. There are also other approximation schemes, such as the HRTW method [18]. Both approximation schemes yield somewhat similar results, although the Moldauer approach is consistently closer to the full GOE treatment [17].

The Moldauer approximation yields

$$W_{jk} = \left(1 + \frac{2\delta_{jk}}{v_k}\right) \int_0^\infty dt \prod_f \left(1 + \frac{2t}{v_f} \frac{\langle \Gamma_f \rangle}{\langle \Gamma_{tot} \rangle}\right)^{\left(\frac{v_f}{2} + \delta_{fj} + \delta_{fk}\right)} . \tag{37}$$

In this expression, the various v_i are the degrees of freedom associated with a χ^2 random distribution of partial widths. The partial widths themselves (Γ_k) are proportional to the transmission coefficients and level spacings. The product is over all possible exit channels. Gaussian quadrature can be efficiently employed to evaluate the integral.

Since the compound elastic cross section decreases rapidly above a few MeV, width fluctuation correlations are generally only significant for incident energies below 1 MeV.

2.2.4 Decay of Continuum States

The cross section given in Equation 34 is still not, in practice, measurable in the laboratory. In an experiment designed to measure a cross section, the beam of incident particles may excite several states in the residual nucleus, many of which rapidly decay. Due to the frequency of events, it is not possible to reconstruct which particular state was formed. What *can* be measured is the total cross section ultimately ending up in the ground state and, if they exist, any long lived isomers in the residual nucleus.

In the case where all excited states eventually decay to the ground state, the measurable laboratory cross section can be obtained from Equation 34 by simply summing over all energetically accessible states in the residual. This is done by replacing the $T^{J\Pi}_{ki'l'}$ in Equation 34 with a sum over the transmission coefficients, including the continuum as described by the level density formula, as in Equation 33. However, when isomers are present, the process is more complicated and requires

a detailed knowledge of how the various states in the residual decay.

The necessary information is found in the gamma decay branching ratios, which can be measured. The branching ratio $\Gamma_\gamma^{\nu\nu'}$ is the probability that a state ν will decay to a state ν'. The absence of branching ratios for state ν would imply that the state is stable, and hence one may account for long-lived isomers by assuming all the branching ratios for the isomeric state are zero With this information, one can model the gamma ray cascade in detail and determine how often a given state will decay to the ground state or isomers.

Branching ratio data is only available for a few of the lowest lying discrete levels. For residuals in a continuum state, the branching ratios can be estimated in terms of transmission functions. In particular, for a transition energy ϵ_γ from a continuum state at energy E to a state at energy E',

$$\Gamma_\gamma(\epsilon_\gamma) = \frac{\sum_{X,L} T_{\gamma XL}(\epsilon_\gamma)}{\sum_{J',\Pi',X',L'} \left[\sum_{\nu''=0}^{\omega} T_{\gamma X'L'}(\epsilon_\gamma i^{\nu''}) + \int_0^{E-E^\omega} T_{\gamma X'L'}(\epsilon_\gamma)\rho(E-\epsilon_\gamma, J', \Pi')d\epsilon_\gamma\right]} \ . \tag{38}$$

Even with this approximation, a portion of the cross section will occasionally remain in the continuum after the gamma cascade is modeled. When this occurs, we distribute the continuum cross section to the ground and isomeric states, weighting the distribution by spins. If the spin of a possible final state (either the ground state or an isomer) is J, the amount of continuum cross section distributed to that state is given by

$$\sigma_{cont\to J} = \frac{2J+1}{\sum_{J'}(2J'+1)}\sigma_{cont} \tag{39}$$

where σ_{cont} is the amount of cross section left in the continuum (typically less than 1% of the activation cross section). The sum is over the ground state and isomers.

This completes our description of the statistical model used in our modeling effort. As mentioned previously, the compound nuclear mechanism is dominant

over other reaction mechanisms in the mass and energy ranges of interest to us, and we could safely model our cross sections using only the Hauser-Feshbach model with width fluctuation correlations.

2.3 Pre-equilibrium Reactions

Pre-equilibrium emission of particles from the compound nucleus occurs when enough energy is localized in a single particle during equilibration, allowing it to escape the nuclear field. The escaping particle can either be a single nucleon or a composite, such as an alpha cluster. This generally requires a large excitation energy, and hence pre-equilibrium processes only become significant above ∼10 MeV incident energy. For astrophysical purposes, we only need to consider incident energies up to ∼10 MeV, so pre-equilibrium could be safely ignored. However, in our study we model cross sections up to 20 MeV to aid in the evaluation of input parameters. We have therefore included pre-equilibrium in our modeling effort, and a brief description of the model used is appropriate.

We adopt a simple exciton model in our calculations [6]. In this model, the system of target plus projectile equilibrates through a series of two-body collisions. Emission of particles is allowed from all intermediate states, which are characterized only by the number of particle and hole degrees of freedom ($\mathcal{P}$ and $\mathcal{H}$, respectively). These particle and hole states are created and annihilated in pairs, so that the state of the system may be equivalently expressed in terms of the exciton number $\mathcal{N} = \mathcal{P} + \mathcal{H}$.

We assume that upon absorption of the projectile, the compound system is in a state consisting of two particles and one hole ($\mathcal{P}_0 = 2$, $\mathcal{H}_0 = 1$). The initial population probabilities of states with exciton number $\mathcal{N}$ may be expressed in terms of a delta function

$$b_0(\mathcal{N}) = \delta_{\mathcal{N}\mathcal{N}_0} \; . = \delta_{\mathcal{P}\mathcal{P}_0}\delta_{\mathcal{H}\mathcal{H}_0} \tag{40}$$

The occupation of these states after $m+1$ internal transitions is given by

$$b_{m+1}(\mathcal{N}) = b_m(\mathcal{N}+2)\frac{\lambda_-(\mathcal{N}+2)}{\lambda(\mathcal{N}+2)} + b_m(\mathcal{N})\frac{\lambda_0(\mathcal{N})}{\lambda(\mathcal{N})} + b_m(\mathcal{N}-2)\frac{\lambda_+(\mathcal{N}-2)}{\lambda(\mathcal{N}-2)} \ . \quad (41)$$

In this expression, $\lambda_+(\mathcal{N})$ is the average rate of transitions resulting in a change of exciton number by +2. The rates $\lambda_0(\mathcal{N})$ and $\lambda_-(\mathcal{N})$ correspond to transitions resulting in a change of exciton number by 0 or -2. The denominator $\lambda(\mathcal{N})$ is the total transition rate, given by

$$\lambda(\mathcal{N}) = \lambda_+(\mathcal{N}) + \lambda_0(\mathcal{N}) + \lambda_-(\mathcal{N}) + \lambda^e(\mathcal{N}) \quad (42)$$

where $\lambda^e(\mathcal{N})$ is the rate of emission of particles. This quantity is in turn given by

$$\lambda^e(\mathcal{N}) = \sum_j \int d\epsilon_j \lambda_j^e(\mathcal{N}, \epsilon_j) \quad (43)$$

where $\lambda_j^e(\mathcal{N}, \epsilon_j)$ is the emission rate for particle j with kinetic energy ϵ_j. The sum extends over all particles for which pre-equilibrium emission is considered. The occupation numbers are determined iteratively, beginning with the initial configuration. After a maximum number of transitions M, defined by

$$\left| \frac{b_{M-1}(\mathcal{N})}{b_M(\mathcal{N})} - \frac{\sum_{\mathcal{N}'} b_{M-1}(\mathcal{N}')}{\sum_{\mathcal{N}'} b_M(\mathcal{N}')} \right| \leq 0.01 \frac{\sum_{\mathcal{N}'} b_{M-1}(\mathcal{N}')}{\sum_{\mathcal{N}'} b_M(\mathcal{N}')} \quad (44)$$

for all $\mathcal{N}$, the system is assumed to be in equilibrium. The pre-equilibrium contribution to the cross section is then given by

$$\frac{d\sigma_{jk}}{dE} = \sigma_j(E) \sum_{m=0}^{M} \sum_{\mathcal{N}} b_m(\mathcal{N}) \frac{\lambda_k^e(\mathcal{N}, E)}{\lambda(\mathcal{N})} \quad (45)$$

which can be integrated to find the total pre-equilibrium cross section. It is also

useful to define the pre-equilibrium fraction, which expresses the fraction of the reaction cross section that undergoes pre-equilibrium processes. This is given by

$$\mathcal{F} = \sum_{m=0}^{M} \sum_{\mathcal{N}} b_m(\mathcal{N}) \frac{\lambda^e(\mathcal{N}, E)}{\lambda(\mathcal{N})} \ . \tag{46}$$

A large pre-equilibrium fraction indicates that pre-equilibrium processes are significant.

The internal transition rates are a function of excitation energy, and are given by [5]

$$\begin{aligned} \lambda_+(\mathcal{N}) &= \frac{2\pi}{\hbar}\left|M\right|^2 \frac{g(gE - C_{\mathcal{P}+1,\mathcal{H}+1})^2}{\mathcal{P}+\mathcal{H}+1} \\ \lambda_0(\mathcal{N}) &= \frac{2\pi}{\hbar}\left|M\right|^2 g(gE - C_{\mathcal{P},\mathcal{H}})(\mathcal{P}+\mathcal{H}-1) \\ \lambda_-(\mathcal{N}) &= \frac{2\pi}{\hbar}\left|M\right|^2 g\mathcal{P}\mathcal{H}(\mathcal{P}+\mathcal{H}-2) \end{aligned} \tag{47}$$

where

$$C_{\mathcal{P},\mathcal{H}} = \frac{1}{2}(\mathcal{P}^2 + \mathcal{H}^2) \ . \tag{48}$$

The parameter g is related to the Fermi-gas level density parameter a (discussed in Section 4) by $g = 6a/\pi^2$. In our implementation of the exciton model, we assume $a = A/8$. The average effective matrix element $\left|M\right|^2$ is given by

$$\left|M\right|^2 = \frac{\mathrm{FM}}{A^3 E} \ . \tag{49}$$

Here, A is the mass number and E the excitation energy of the compound system. The parameter FM is chosen empirically to match measured cross section data. In this region of interest, FM = 200 provides a satisfactory fit. Sensitivity to this parameter will be explored in Section 7.

This leads us to the particle emission rates. For neutrons and protons, we employ

the rates suggested by [12], which are

$$\lambda_j^e(\mathcal{N}, \epsilon_j) = \frac{2J_j + 1}{\pi^2 \hbar^3} \hat{m}_j \epsilon_j \sigma_j(\epsilon_j) \frac{\mathcal{N} \pm 1}{\mathcal{N}} \frac{w(\mathcal{P} - 1, \mathcal{H}, E - S_j - \epsilon_j)}{w(\mathcal{P}, \mathcal{H}, E)} \tag{50}$$

where the "+" is used when the incident and emitted nucleon are of the same type. The quantities $\hat{m}_j$ and J_j are the reduced mass and spin of the exit particle, and $\sigma_j(\epsilon_j)$ is the absorption cross section for particle j incident on the residual with kinetic energy ϵ_j. S_j is the separation energy of particle j from the compound nucleus. The $w(\mathcal{P}, \mathcal{H}, E)$ is the density of of states for $\mathcal{P}$ particles and $\mathcal{H}$ holes at energy E, given by [28]

$$w(\mathcal{P}, \mathcal{H}, E) = \frac{g\left[g(E - \Delta) - A_{\mathcal{P},\mathcal{H}}\right]^{\mathcal{P}+\mathcal{H}-1}}{\mathcal{P}!\mathcal{H}!(\mathcal{P} + \mathcal{H} - 1)!} \tag{51}$$

with

$$A_{\mathcal{P},\mathcal{H}} = \frac{1}{4}(\mathcal{P}^2 + \mathcal{H}^2 + \mathcal{P} - 3\mathcal{H}) \ . \tag{52}$$

In our implementation, $\Delta = 0$.

We also include possible alpha particle emission, with the rate given by [19]

$$\lambda_\alpha^e(\mathcal{N}, \epsilon_\alpha) = \frac{1}{\pi^2 \hbar^3} \hat{m}_\alpha \epsilon_\alpha \sigma_\alpha(\epsilon_\alpha) \ . \frac{\Phi K_{\mathcal{N}-1}^\alpha w(\mathcal{P} - 1, \mathcal{H}, E - S_\alpha - \epsilon_\alpha)}{\Phi K_{\mathcal{N}}^\alpha w(\mathcal{P}, \mathcal{H}, E) + (1 - \Phi)\Phi K_{\mathcal{N}}^\nu w(\mathcal{P}, \mathcal{H}, E)} \tag{53}$$

The various K factors appearing in this expression are constants given in [19], and Φ is the alpha cluster preformation probability, which we take to be 0.5.

This completes our description of the implementation of pre-equilibrium in this work. In Figure 6 we plot the pre-equilibrium fraction defined in Equation 46 for protons and neutrons incident on ^{59,60}Fe. As expected, the pre-equilibrium fraction is small at low energies, accounting for only 10% of the decay of the ^{57}Fe compound nucleus. The fraction is easily negligible below 1 MeV, where the neutron capture

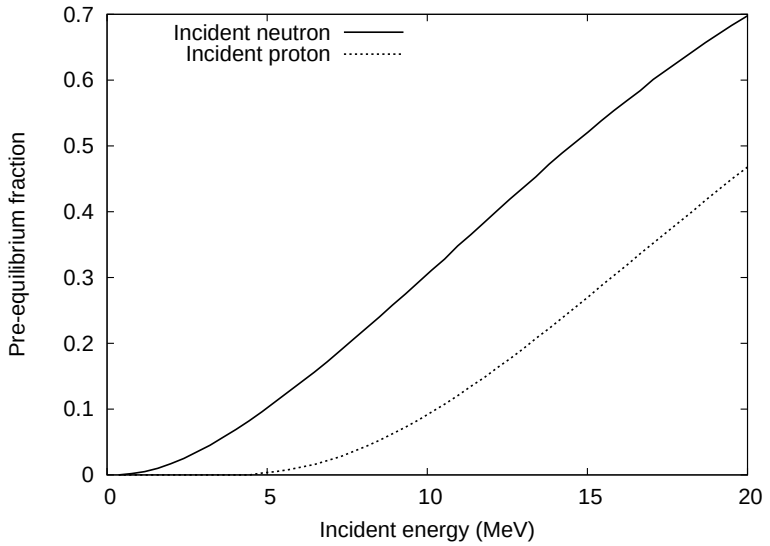

Figure 6: Pre-equilibrium fraction for neutrons (solid line) and protons (dotted line) incident on ^{56}Fe.

cross sections are most significant. Above 10 MeV, pre-equilibrium accounts for as much as 30-70% of the reaction cross section. Since the transition and emission rates (Equations 47, 50, and 53) depend only on the mass number of the target, the pre-equilibrium fractions for other isotopes in this region will be similar.

2.4 The STAPRE Code

In our modeling efforts, we adopt the STAPRE-H95 code [25]. This code embodies the Hauser-Feshbach model and the pre-equilibrium treatment described above. Pre-equilibrium emission is considered only for the first compound nucleus. Direct reactions are not included, but have been calculated separately for a few select capture reactions using the CUPIDO code [8].

A few reactions we have modeled, including (n,2n), (p,2n), and (n,np), include the emission of multiple particles. Such multistep emission is handled in the STAPRE code by means of sequential evaporation, where the cross section for emission from the first compound nucleus replaces the absorption cross section in the Hauser-Feshbach model. Decay of the resulting second compound nucleus is

then treated within the framework of the statistical model in the usual way. Sequential evaporation requires the specification of the particle emission sequence, i.e. an (n,np) reaction is treated differently than an (n,pn) reaction. The order of particle emission cannot be determined in experiments, and hence measured (n,np) cross sections should be compared with the sum of (n,np) and (n,pn) calculations.

Versions of the STAPRE code are widely available. However, we have made significant modifications, particularly to level density and transmission coefficient subroutines. These modifications have been made to expand the capability of the code with regards to the inclusion of modern treatments of level density parameters and the E1 and M1 photon strength functions.

References

[1] Abfalterer, W.P., Bateman, F.B., Dietrich, F.S., Finlay, R.W., Haight, R.C., & Morgan, G.L., 2001, Phys. Rev. **C63**, 044608.

[2] Bohr, N., 1936, Nature **137**, 344.

[3] Breit, G., & Wigner, E., 1936, Phys. Rev. **49**, 519.

[4] Cierjacks, S., Forti, P., Kopsch, D., Kropp, L.,Nebe, J, & Unseld, H., 1969, Kernforschungszentrum Karlsruhe Reports, **1000**, 6902.

[5] Cline, C.K., 1972, Nuc. Phys. **A195**, 353.

[6] Cline, C.K., & Blann, M., 1971, Nuc. Phys. **A172**, 225.

[7] D'Auria, J.M., Fluss, M.J., Herzog, G., Kowalski, L., Miller, J.M., & Reedy, D.C., 1968, Phys. Rev. **174**, 1409.

[8] Dietrich, F.S. 2004, private communication

[9] Escher, J., Ahle, L., Bernstein, L., Church, J.A., Dietrich, F., Forssen, C., and Hoffman, R. Surrogate nuclear reactions and the origin of the heavy elements, UCRL-PROC-205320

[10] Gadioli, E., 1976, Nuklonika **21**, 385.

[11] Gadioli, E., Gadioli Erba, E., Parker, D., & Asher, J., 1985, Phys. Rev. **C32**, 1214.

[12] Gadioli, E., Gadioli Erba, E., Parker, D., & Sona, P.G., 1973, Nuc. Phys. **A217**, 589.

[13] Gadioli, E. & Hodgson, P.E., 1992, Pre-Equilibrium Nuclear Reactions (Oxford: Clarendon Press)

[14] Ghosal, S.N., 1950, Phys. Rev. **80**, 939.

[15] Harvey, J.A., & Hockaday, M., from Experimental Nuclear Reaction Data File, Brookhaven National Laboratory, US Dept. of Energy, http://www.nndc.bnl.gov/nndc/exfor/

[16] Hauser, W., & Feshbach, H., 1952, Phys. Rev. **87**, 366.

[17] Hilaire, S., Lagrange, Ch., & Koning, A. J. 2003, Ann. of Phys. **306**, 209

[18] Hofmann, H.M., Richert, J, Tepel, J. W. & Weidenmuller, H.A. 1975, Ann. of Phys. **90**, 403

[19] Milazzo-Colli, L., and Braga-Marcazzan, G.M., 1973, Nuc. Phys. **A210**, 297

[20] Moldauer, P.A., 1976, Phys. Rev. **C14** 764.

[21] Montgomery, D.M., & Porile, N.T., 1970, Phys. Rev. **C2**, 595.

[22] Rauscher, T., & Guber, K.H., 2002, Phys. Rev. **C66**, 028802.

[23] Satchler, G.R., 1963, Phys. Lett. **7**, 55.

[24] Savard, G. "The U.S. Rare Isotope Accelerator Project," Proc. 2001 Particle Accelerator Conf., June 18-22, Chicago, IL, 2001, p. 561. http://accelconf.web.cern.ch/AccelConf/p01/PAPERS/ROPA002.PDF

[25] Uhl, M., & Strohmaier, B. IRK-Vienna Report IRK-76/01 1976 (Upd. 1978)

[26] Verbaarschot, J.J.M., Weidenmüller, H.A., & Zirnbauer, M.R., 1985, Phys. Rep. **129**, 367.

[27] Weisskopf, V.F., & Ewing, P.H., 1940, Phys. Rev **57**, 472.

[28] Williams, F.C., 1971, Nuc. Phys. **A166**, 231.

[29] Wong, P., Daly, S., & Porile, N.T., 1970, Nuc. Phys. **A151**, 549.

3 Nuclear Structure Data

The Hauser-Feshbach model requires as input the spins and parities of the ground state and excited states of the various compound nuclei involved in the reaction, which enter into the statistical factors of Equation 32 and the selection rules of Equations 34 and 35. Also required are the binding and separation energies, which come into the definition of the excitation energy and determine the reaction thresholds, and the detailed gamma decay branching information needed to accurately model the gamma ray cascade.

Fortunately, a large number of the relevant properties have been measured, even for unstable nuclei. The wealth of data available at the present day exceeds that available to previous studies. However, in some cases the relevant quantities have not been measured, particularly with respect to ground state masses and gamma ray branching ratios. When this is the case, we use extrapolations and estimates.

This section details the sources of nuclear structure data used in our modeling effort, and provides comparisons with those used previously.

3.1 Ground State Spins and Parities

Our adopted ground state spins and parities come primarily from the Evaluated Nuclear Structure Data File (ENSDF). [3]. A full listing can be found in Appendix A. In Table 1 we highlight the differences between our values and those used by Woosley, et al. [6] and Rauscher and Thielemann [5]. Missing entries in Table 1 indicate that the nucleus was not included in the input decks. These missing entries account for half of the differences between the sets listed in Table 1. Parity assignments are consistent among the sets, with the exception on ^{63}Fe. When the spins of the sets differ, it is generally only by one unit. The exceptions are the spins of ^{54}V and ^{62}Co used by Woosley, et al. Of all the nuclei listed in this table, the

Table 1: Select ground state spins and parities in various modeling efforts. Nuclei involved in the reactions included in this work not appearing in this table have consistent J^π assignments in all three efforts.

Nucleus	Our Values	Woosley, et al.	Rauscher & Thielemann
^{54}Ti	0.0^+	–	0.0^+
^{54}V	3.0^+	5.0^+	3.0^+
^{56}V	2.0^+	–	–
^{57}V	1.5^+	–	–
^{59}Cr	1.5^+	–	–
^{60}Cr	0.0^+	–	–
^{48}Mn	4.0^+	–	4.0^+
^{59}Mn	1.5^-	2.5^-	1.5^-
^{61}Mn	2.5^-	1.5^-	2.5^-
^{51}Fe	2.5^-	3.5^-	2.5^-
^{63}Fe	2.5^-	1.5^-	2.5^+
^{52}Co	1.0^+	1.0^+	–
^{62}Co	2.0^+	5.0^+	2.0^+
^{56}Cu	3.0^+	2.0^+	–

only one that would affect the ^{59,60}Fe neutron capture cross sections is ^{59}Mn, which is the residual nucleus for the proton exit channel of the ^{60}Fe compound nucleus and the deuteron exit channel of the ^{61}Fe compound nucleus. However, the thresholds for ^{59}Fe(n,p)^{59}Mn and ^{60}Fe(n,d)^{59}Mn are 4.5 and 10.7 MeV, respectively. At these energies, the relevant capture cross sections have dropped to $\sim$1 millibarn, and the opening of the charged particle exit channels will only have negligible effects on the neutron capture cross sections. Thus, at least with regard to the ^{59}Fe(n,γ)^{60}Fe and ^{60}Fe(n,γ)^{61}Fe cross sections, the ground state spin and parity assignments of all three groups are essentially identical.

3.2 Masses and Separation Energies

The total mass of a system, and thus its binding energy, almost always changes in a nuclear reaction. A corresponding loss (increase) is mass is accompanied by an increase (decrease) in binding energy. Hence, a decrease in the total mass of a

nuclear system results in an excess amount of energy, which is often expressed in terms of a Q-value:

$$Q = (\sum_{initial} m - \sum_{final} m)c^2 \tag{54}$$

where the masses are in atomic units and $c^2 = 931.5$ MeV/amu. The Q-value should be raised by the appropriate energy if the target nucleus is in an isomeric state, and lowered when the residual is an isomer. When the Q-value is negative, the reaction will have a threshold. In the laboratory frame this threshold energy is

$$E_{th} = -\frac{m_X + m_a}{m_X} Q \tag{55}$$

where m_X and m_a are the masses of the target and projectile, respectively.

Once a compound nuclear state has been formed, certain exit channels may be kinematically forbidden at low excitation energies. The minimum excitation energy required for a particle k to exit the compound nucleus is called the separation energy, and is defined as

$$S_k = (m_Y - m_{X'} + m_k)c^2 \tag{56}$$

where $m_{X'}$ is the mass of the compound system, m_Y is the mass of the residual, and m_k is the mass of the exiting particle.

Each of the above equations may alternately be expressed in terms of binding energies. The binding energy for a particular nucleus may be derived from its mass, via the relation

$$B_X = (Z_X m_{^1H} + N_X m_n - m_X)c^2 \tag{57}$$

where Z_X, N_X and m_X are the proton number, neutron number, and mass of a nucleus X. The other masses appearing in this expression are those of the neutron and ^{1}H atom, the latter accounting for atomic binding energies.

Separation energies and Q-values serve indirectly as inputs to the Hauser-Feshbach

model in that they are used to determine the reaction thresholds and excitation energies of the various compound nuclei. In Appendix A we provide our adopted masses, binding energies, and separation energies. The masses are taken from [1], with extrapolations made for nuclei off stability without measured values. The binding and separation energies are then calculated from these masses. Table 2 highlights the differences between our binding energies (columns labeled "Adopted") and those used by Woosley, et al. (WFHZ) [6] and Rauscher and Thielemann (RT) [5]. This table includes only binding energies that differ by more than 10 keV. We have also only included nuclei from $24 \leq Z \leq 26$ in this table, representing possible residuals from the decay of iron compound nuclei. The differences in binding energies for other nuclei considered in this study are similar.

In most cases, the binding energies are within 100 keV of each other. The largest deviation is that of ^{60}Cr, which is 1.4 MeV. For the nuclei most important to neutron capture onto ^{59,60}Fe (^{56,57}Cr, $^{58-60}$Mn, and $^{59-61}$Fe), the largest deviation is that of ^{59}Mn. However, this residual represents the proton exit channel of the ^{60}Fe compound system and the deuteron exit channel of the ^{61}Fe system. As discussed in the previous section, the neutron capture cross section is quite small at the energies where these exit channels open, and changes in this separation energy will have negligible effects on the ^{59}Fe(n,γ)^{60}Fe and ^{60}Fe(n,γ)^{61}Fe cross sections.

3.3 Discrete Levels

Ideally one would have a complete set of discrete levels up to the necessary excitation energies for each of the compound nuclei involved in the modeled reaction. In such a scenario, one would not need to resort to empirical level density formulae. However, discrete level schemes are often only known up to a few MeV, and many of the measured levels do not have well established spins and parities. Additionally, one needs to know the gamma decay branching ratios for each of the discrete levels in

Table 2: Select binding energies (in MeV) adopted in various modeling efforts. Only nuclei for which the adopted energies differ by more than 10 keV are included in this table.

Nucleus	Adopted	WFHZ	RT	Nucleus	Adopted	WFHZ	RT
^{47}Cr	395.13	395.22	395.13	^{55}Mn	482.07	482.09	482.07
^{48}Cr	411.47	411.48	411.47	^{56}Mn	489.34	489.36	489.35
^{49}Cr	422.05	422.12	422.05	^{57}Mn	497.99	498.14	498.00
^{50}Cr	435.05	435.06	435.05	^{58}Mn	504.48	504.66	504.41
^{51}Cr	444.31	444.32	444.31	^{59}Mn	512.13	512.42	512.12
^{52}Cr	456.35	456.36	456.34	^{60}Mn	517.90	517.71	517.89
^{53}Cr	464.29	464.30	464.28	^{61}Mn	524.35	525.14	524.94
^{54}Cr	474.01	474.02	474.00	^{51}Fe	431.52	431.54	431.52
^{55}Cr	480.25	480.28	480.25	^{52}Fe	447.70	447.72	447.70
^{57}Cr	493.81	493.82	493.93	^{53}Fe	458.38	458.40	458.38
^{58}Cr	501.19	501.48	501.84	^{54}Fe	471.76	471.78	471.76
^{59}Cr	505.32	–	506.11	^{55}Fe	481.06	481.08	481.05
^{60}Cr	512.01	–	513.41	^{56}Fe	492.26	492.28	492.25
^{48}Mn	397.19	–	397.07	^{57}Fe	499.90	499.93	499.90
^{49}Mn	413.55	413.67	413.55	^{58}Fe	509.95	509.97	509.94
^{50}Mn	426.63	426.65	426.63	^{59}Fe	516.53	516.56	516.53
^{51}Mn	440.32	440.33	440.32	^{60}Fe	525.35	525.39	525.35
^{52}Mn	450.86	450.87	450.85	^{61}Fe	530.93	531.06	530.93
^{53}Mn	462.91	462.92	462.91	^{62}Fe	538.98	539.51	538.97
^{54}Mn	471.85	471.87	471.84	^{63}Fe	543.70	544.29	544.13

order to include detailed gamma ray cascades in the de-excitation of the compound nuclei.

The majority of our adopted level schemes are drawn from the RIPL database [4] and ENSDF [3]. Additional evaluations for select nuclei were performed by R. Bauer [2]. Complete information on our adopted discrete level schemes is presented in Appendix B.

In Tables 3 and 4, we compare our level schemes for ^{60,61}Fe (the most significant level schemes for neutron capture onto ^{59,60}Fe) with those of Woosley, et al. (WFHZ) [6] and Rauscher and Thielemann (RT) [5]. These tables include only the levels actually used in the calculations (note in particular that we begin with seven levels

Table 3: Discrete level schemes for ^{60}Fe. The first two columns list the energy, spin, and parity assignments adopted in this work. The third column indicates (with a black dot) the levels included in the modeling effort of Woosley *et al.*. The third column indicated the levels included in the modeling effort of Rauscher and Thielemann, with any differences between their adopted levels and ours listed in parenthesis. The final column indicates the modifications we made from the level schemes in the Reference Input Parameter Library. A "BR" indicates that we have modified the branching ratios, and "Added" indicates that the level was not included in RIPL.

Energy (MeV)	J^π	WFHZ	RT	Modified from RIPL
0.0000	0^+	•	•	
0.8236	2^+		•	
1.9738	0^+		(1.9750)	
2.1145	4^+		•	
2.2994	2^+		•	
2.3580	0^+			BR
2.6730	2^+		•	
2.7560	2^+		•	
2.7924	3^+		(2^+)	
3.0390	2^+		•	
3.0724	4^+		(3.0720, 2^+)	
3.2930	3^-			BR
3.3080	3^+			
3.5020	4^+			BR
3.5161	5^-		(2^+)	
3.5200	4^+			BR
3.5620	3^-			BR
3.6350	2^+			BR
3.6480	4^+			
3.6980	0^+			BR
3.7140	3^+			
3.8670	3^-			BR
3.8750	4^-			BR
3.9290	2^+			BR
3.9544	6^+			

for ^{61}Fe in Appendix B, but only include five of these levels in our calculation, due to difficulties encountered fitting the level density to this set of levels). The first two columns give the energy, spin, and parities of our adopted set of levels. The next two columns indicate (with a black dot) which of these levels are present in

Table 4: Discrete level schemes for ^{61}Fe. The first two columns list the energy, spin, and parity assignments adopted in this work. The third column indicates (with a black dot) the levels included in the modeling effort of Woosley *et al.*. The third column indicated the levels included in the modeling effort of Rauscher and Thielemann. The final column indicates the modifications we made from the level schemes in the Reference Input Parameter Library. A "BR" indicates that we have modified the branching ratios, and "Added" indicates that the level was not included in RIPL.

Energy (MeV)	J^π	WFHZ	RT	Modified from RIPL
0.0000	1.5^-	•	•	
0.2068	2.5^-			
0.3910	0.5^-			
0.6287	1.5^-			
0.8610	4.5^+			Added

the other two sets. If the level is present but the properties differ from our set, the values for the other set are given in parenthesis. The last column indicates which properties in our adopted level set were modified from what appears in [4] ('BR' indicates a modification to the branching ratios, 'Added' indicates the level was not included in [4]).

The most distinct difference between the various schemes is the number of levels included. Only the ground states for both nuclei are included in the WFHZ set. The RT set includes excited states for ^{60}Fe, but only a ground state for ^{61}Fe. There are some minor differences in a few of the energies in ^{60}Fe between our set and RT, and some more significant differences in a few spin and parity assignments. Our modifications to the data found in [4] include estimates of branching ratios in ^{60}Fe and the addition of a level (found in [3] but not in [4]) to ^{61}Fe. We further note that the modeled cross sections of [6] and [5] do not include detailed gamma ray cascades. These differences in the discrete level schemes, in conjunction with the appropriate level densities, may have a significant impact on the modeled cross sections. An investigation into this issue will be presented in Section 7.2.1.

References

[1] Audi, G., Wapstra, A.H., & Thibault C. 2003, Nuc. Phys. **A729**, 337

[2] Bauer, R. 2003, private communication.

[3] Evaluated Nuclear Structure Data File, Brookhaven National Laboratory, US Dept. of Energy, http://www.nndc.bnl.gov/nndc/ensdf/

[4] *Handbook for calculations of nuclear reaction data*, Reference input parameter library. 1998, IAEA-TECDOC-1034

[5] Rauscher, T. & Thielemann, F.-K. 2001, At. Data Nucl. Data Tables **79**, 47

[6] Woosley, S. E., Fowler, W. A., Holmes, J. A. & Zimmerman, B. A. 1978, Atomic Data & Nuclear Data Tables, **22**, 371

4 Nuclear Level Densities

In this section, we summarize the theoretical considerations with regard to the nuclear level density and describe our level density systematics. We also compare our systematics with those used in previous reaction rate libraries [27, 21]. We conclude by discussing the performance of the various level density prescriptions relative to neutron resonance data.

4.1 Theoretical Foundations of the Nuclear Level Density

Our level density prescription is similar to that of [21], in that we assume a back-shifted Fermi gas at high excitation energies and a constant temperature state density at lower energies.

4.1.1 The Fermi Gas State Density

Hans Bethe attempted to describe the density of states in a nucleus as a Fermi gas [1]. Others have derived similar expressions for a Fermi gas state density, including Lang and LeCouteur [18] and Newton [20]. The standard formulation used in the calculation of astrophysical reaction rates is that of Gilbert and Cameron [7], and it is this form that we adopt.

Consider N neutrons occupying single particle levels s of energy a_s, occupation number n_s, and magnetic quantum number m_s. Additionally there are Z protons occupying single particle states t of energy b_t, occupation number z_t, and magnetic quantum number m_t. The macroscopic state of this system is defined by four constants of motion: the total neutron and proton numbers (N and Z), the total energy E, and the net magnetic quantum number M of the system. These quantities

are defined by

$$\begin{aligned} N &= \sum_s n_s \\ Z &= \sum_t z_t \\ E &= \sum_s n_s a_s + \sum_t z_t b_t \\ M &= \sum_s n_s m_s + \sum_t z_t m_t \ . \end{aligned} \tag{58}$$

Using these one can define the grand partition function

$$\exp(\Omega) = \sum_{N',Z',E',M'} \exp[\beta(\mu_1 N' + \mu_2 Z' + \mu_3 M' - E')] \tag{59}$$

where the sum is over all possible macroscopic states. One can replace the energy with an integration over the density of states $P(E, N, Z, M)$

$$\exp(\Omega) = \sum_{N',Z',M'} \int dE' P(E', N', Z', M') \exp[\beta(\mu_1 N' + \mu_2 Z' + \mu_3 M' - E')] \ . \tag{60}$$

Then by a series of successive inverse Laplace transformations one obtains an expression for the density of states:

$$\begin{aligned} P(E, N, Z, M) = \left(\frac{1}{2\pi i}\right)^4 \int_{\gamma - i\infty}^{\gamma + i\infty} d\beta \int_{\gamma_3 - i\infty}^{\gamma_3 + i\infty} d\alpha_3 \int_{\gamma_2 - i\infty}^{\gamma_2 + i\infty} d\alpha_2 \int_{\gamma_1 - i\infty}^{\gamma_1 + i\infty} d\alpha_1 \\ \times \exp(\Omega - \alpha_1 N - \alpha_2 Z - \alpha_3 M + \beta E) \ . \end{aligned} \tag{61}$$

The total nuclear level $w(E)$ density is the sum of this quantity over all possible M, i.e.

$$w(E) = \sum_M P(E, N, Z, M) \ . \tag{62}$$

This is the basic procedure for determining the total nuclear state density for a gas of particles obeying Fermi-Dirac statistics. The earlier works of [18] and [20] use

this same method, but do not include M as a constant of the motion.

While making the inverse Laplace transformations, it is useful to describe the energy in terms of $U \equiv E - U_0$ where U_0 is the energy of the first fully degenerate state. The level densities may then be expressed as functions of U rather than E.

The process of evaluating Equation 61 is rather involved, and a full treatment is given in Appendix C of [7]. For our purposes, we need only consider the final result for the total state density, which is

$$w(U) = \frac{\sqrt{\pi}}{12} \frac{\exp(2\sqrt{aU})}{a^{1/4} U^{5/4}} \ . \tag{63}$$

In this expression, a is known as the level density parameter and is related to the sum of the neutron and proton single particle level spacings.

In statistical model calculations, we consider the absorption (emission) of the various particles into (from) a single particle state with a given spin. For this reason, we need to know the density of levels of a particular spin, referred to as the spin-dependent level density. The distribution of levels with total magnetic quantum number M is given by [7]

$$\begin{aligned} \rho(U, M) &= w(U) P(M) \\ &= w(U) \frac{\exp(-M^2/2\sigma^2)}{\sigma\sqrt{2\pi}} \end{aligned} \tag{64}$$

where $\sigma^2 = g \langle m^2 \rangle t$ is referred to as the spin cutoff parameter. Here, g is the sum of neutron and proton single particle level spacings, t is the thermodynamic temperature, and $\langle m^2 \rangle$ is the mean square magnetic quantum number for the single particle states. This level density includes all states of total magnetic quantum number M, all of which must have $J \geq M$. In the absence of external fields, single particle states that differ only in their magnetic quantum numbers are degenerate,

and $\rho(U, M = J) - \rho(U, M = J + 1)$ will count the total number of states with spin J. Hence, in the absence of external fields, we find

$$\begin{aligned} \rho(U, J) &= \rho(U, M = J) - \rho(U, M = J + 1) \\ &= \frac{w(U)}{\sigma\sqrt{2\pi}} \left[\frac{\exp(-J^2/2\sigma^2)}{\sigma\sqrt{2\pi}} - \frac{\exp(-(J+1)^2/2\sigma^2)}{\sigma\sqrt{2\pi}} \right] \\ &= \frac{w(U)}{\sigma\sqrt{2\pi}} f(J) \ . \end{aligned} \tag{65}$$

The quantity $f(J)$ is often replaced with an approximation involving only a single exponential. In this work we adopt

$$f(J) \approx \frac{2J+1}{2\sigma^2} \exp\left[-(J + \frac{1}{2})^2/2\sigma^2 \right] \ . \tag{66}$$

Hence we write the spin-dependent level density as

$$\rho(U, J) = \frac{1}{\sigma\sqrt{2\pi}} \frac{2J+1}{2\sigma^2} \exp\left[-(J + \frac{1}{2})^2/2\sigma^2 \right] \frac{\sqrt{\pi}}{12} \frac{\exp(2\sqrt{aU})}{a^{1/4}U^{5/4}} \ . \tag{67}$$

Previous level density descriptions have used other approximations for $f(J)$. These will be presented in Section 4.2.

Equation 67 is a function of energy and three other parameters: the level density parameter a, the spin cutoff parameter σ^2, and the energy of the first fully degenerate state U_0. In principle, these parameters can be determined from measured nuclear properties, as will be discussed later. Comparing these parameters with measured values often involves the total level density observable in the absence of external fields, i.e. ignoring the magnetic quantum number degeneracy. We can obtain an expression for this "observable level density" by summing over the angular

momenta

$$\begin{aligned}\rho(U) &= \sum_J \rho(U,J) \\ &\approx \frac{1}{\sigma\sqrt{2\pi}}\frac{\sqrt{\pi}}{12}\frac{\exp(2\sqrt{aU})}{a^{1/4}U^{5/4}} \ . \end{aligned} \tag{68}$$

We now consider the parity distribution of states represented by these expressions for the nuclear level density. The total parity of the nuclear state is given by the product of the parities of the constituent nucleons, so that if there are an odd number of odd parity nucleons, the macroscopic nuclear state will itself be of odd parity. In a system of n nucleons where the probability of each nucleon having odd parity is p, the probability P that a nuclear state will have odd parity given by [7]

$$P = \frac{1-(1-2p)^n}{2} \ . \tag{69}$$

It is generally assumed that p is on the order of $1/2$, so that $(1-2p) \ll 1$ and thus $P \approx 1/2$. This means that the distribution of parity states in roughly equal, so that

$$\rho(U,J,\Pi) = \frac{1}{2}\rho(U,J) \ . \tag{70}$$

Having discussed the origins of the Fermi gas level density formula, we now provide a more in depth discussion regarding the individual parameters of Equation 67.

4.1.2 The Backshift

As mentioned previously, the Fermi gas level density is expressed as a function of $U = E - U_0$, where U_0 is the energy of the first fully degenerate state. Hence, U is the excitation energy of the nucleus in question. The cumulative number of discrete

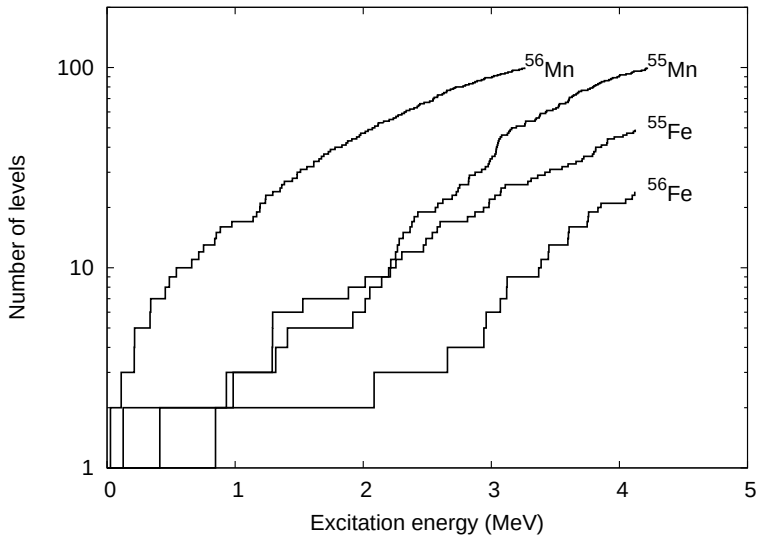

Figure 7: Cumulative number of levels in $^{55-56}$Mn and $^{55-56}$Fe as a function of excitation energy. The effect of pairing energies on the level density is clearly illustrated, with nuclei containing paired nucleons having considerably fewer levels at a given energy.

levels of neighboring nuclei, when plotted as a function of excitation energy, show a marked sensitivity to the pairing of the constituent nucleons. This sensitivity is illustrated in Figure 7. The level density for nuclei with unpaired nucleons tends to be higher. This sensitivity can be understood in terms of the pairing energies associated with paired nucleons. In order to excite a paired nucleon, one must first overcome the pairing energy, i.e. additional energy is required to separate paired nucleons. This type of odd-even effect can also be seen at higher energies, for example in measured resonance spacings.

Odd-even effects can be removed from the level density by substituting an effective excitation energy in place of the true excitation energy,

$$U_{eff} = U - \Delta \ . \tag{71}$$

The quantity Δ is referred to as the backshift.

As a first approximation, one would expect Δ to be the sum of the neutron and

proton pairing energies, Δ_n and Δ_p, which are either found in tables such as in [7] or determined by differences in nuclear binding energies:

$$\begin{aligned}
\Delta_n(Z,N) &= BE(Z,N) - \frac{1}{2}[BE(Z,N-1) + BE(Z,N+1)] \\
\Delta_p(Z,N) &= BE(Z,N) - \frac{1}{2}[BE(Z-1,N) + BE(Z+1,N)] \\
\Delta(Z,N) &= \Delta_n(Z,N) + \Delta_p(Z,N) \ . \qquad (72)
\end{aligned}$$

These latter expressions for Δ_p and Δ_n apply only for paired nucleons. There is not a pairing energy associated with unpaired nucleons. This simple parameterization of the backshift leads to a systematic disagreement between the a parameters inferred from resonance spacings and those obtained through an analysis of correlation widths of fluctuating cross sections [5]. It has been shown that this systematic disagreement can be eliminated by using a backshift of the form

$$\Delta = \Delta_n + \Delta_p - \frac{\eta}{A} \qquad (73)$$

where $\eta \approx 70$. Effectively, this formulation assigns a negative pairing energy to unpaired nucleons.

There is a second way to eliminate the disparity between level density parameters obtained through the evaluation of level spacings and correlation widths. This second method does not involve the introduction of a new parameter. One may determine the pairing energies Δ_n and Δ_p using Equation 72, but do so for all nuclei (including those that have unpaired nucleons). The unpaired nucleons are then assigned negative pairing energies, similar to Equation 73. The backshift is then taken to be the average of Δ_n and Δ_p, i.e.

$$\Delta(Z,N) = \frac{1}{2}\left(\Delta_n + \Delta_p\right) \ . \qquad (74)$$

This is the method employed by [22].

Hereafter, the variable U will always refer to the backshifted excitation energy U_{eff}.

4.1.3 Spin Cut-off Parameter

The spin cutoff parameter is defined in [7] as $\sigma^2 = g\,\langle m^2\rangle\, t$ where g is the sum of neutron and proton single particle level spacings, t is the thermodynamic temperature (not to be confused with the nuclear temperature), and $\langle m^2\rangle$ is the mean square magnetic quantum number for the single particle states. The single particle level spacing is related to the level density parameter via $a = \pi^2 g/6$. The thermodynamic temperature is given by

$$t = \frac{1}{\beta} \quad = \quad \sqrt{\frac{1}{a}}\sqrt{U - \frac{M^2}{4\,\langle m^2\rangle\, gU}}\ . \tag{75}$$

In the process of determining the state density, one may assume U is much larger than the single particle level spacing g^{-1}, and replace several sums with integrals. This allows one to approximate the thermodynamic temperature by $t \approx \sqrt{U/a}$. It has also been shown that $\langle m^2\rangle \approx 0.146A^{2/3}$ [15], so that the spin cutoff parameter may be written as a simple function of the level density parameter, the energy, and the nuclear mass:

$$\sigma^2 = 0.0888\sqrt{aU}A^{2/3}\ . \tag{76}$$

With these approximations, the level density (Equation 67) is a function of U and a only.

Other treatments have been suggested for the spin cutoff parameter. For instance, Rauscher and Thielemann [22] use

$$\sigma^2 = \frac{\Theta_{rigid}}{\hbar^2}t \tag{77}$$

with Θ_{rigid} being the moment of inertia for a sphere of mass 1 amu and nuclear radius R. If one makes the usual approximation $R = R_0 A^{1/3}$ with $R_0 = 1.25$ fm, this expression reduces to

$$\sigma^2 = 0.01496\sqrt{\frac{U}{a}}A^{5/3} \ . \tag{78}$$

Note that for $a = A/6$ (a value not far removed from the canonical $A/8$) Equations 76 and 78 are approximately equal.

4.1.4 The Level Density Parameter

There are several ways in which the level density parameter a can be extracted from experiment [4]:

1. At relatively low excitation energies (usually below 5 MeV), discrete levels can be counted directly.

2. The level density at the neutron binding energy (B_n, generally around 7-8 MeV of excitation energy) can be determined from measurements of the average S-wave resonance spacing (D_0).

3. An analysis of the spectra of particles emitted in statistical reactions can reveal information about the level density for excitation energies around 10 MeV.

4. Correlation widths of fluctuating cross sections can yield information for excitation energies from 10-20 MeV.

In this work we focus only on the first two methods. At excitation energies below 5 MeV the level density is better represented by a constant temperature formula which will be discussed later. Information about the a parameter is therefore most readily extracted from the resonance spacings.

The average S-wave resonance spacing at the neutron binding energy is related to the level density by

$$D_0 = \frac{2}{\rho(B_n - \Delta, J = 1/2)} \tag{79}$$

for a spin zero target and

$$D_0 = \frac{2}{\rho(B_n - \Delta, J = s + \frac{1}{2}) + \rho(B_n - \Delta, J = s - \frac{1}{2})} \tag{80}$$

for a target with non-zero spin s. Provided the backshift and spin cutoff parameter formulation have already been chosen, these expressions may be used to infer the value of a at the neutron binding energy (B_n). This is most easily accomplished with a bisectional root finding method.

Since the a parameter is proportional to the sum of the neutron and proton single particle level spacings, one would expect a systematic description of a to depend on mass number. This expectation has been borne out in several studies [6, 3, 13, 27, 25, 22]. Generally, the a parameter scales with the mass number, i.e. $a = A/X$ where X falls in the range of 6.0-9.0.

4.1.5 Shell Effects and the Level Density Parameter

Nuclei residing on or near closed neutron and proton shells tend to have level spacings much higher than their immediate neighbors that sit further from the closed shell. More simply put, closed shell nuclei have lower level densities. These so-called "shell effects" can be accounted for in terms of a shell correction applied to the level density parameter. In [7], the shell correction is of the form

$$a = (\alpha + \beta S)A \ . \tag{81}$$

In this expression, a is the level density parameter, and the constants α and β have values of approximately 1/8 and 1/100, respectively. The shell correction S receives contributions from both neutrons and protons, and their values are tabulated in [7]. This treatment applies the shell correction independent of excitation energy.

It has been shown that shell effects diminish with increasing excitation energy, becoming negligible around 30 MeV [4]. Such a vanishing shell correction may be described by an energy dependent a parameter. Ignatyuk, Smirenkin and, Tishin proposed using

$$a(U, Z, N) = \tilde{a}\left[1 + \delta W(Z, N)\frac{1 - \exp(-\gamma U)}{U}\right] \tag{82}$$

where δW is the ground state shell correction and γ is a thermal damping coefficient [13]. Generally, γ is assumed to have a value of approximately 0.02-0.08 MeV^{-1}, which ensures that the shell effects become negligible at energies greater than 20 MeV. At higher energies, the level density approaches $\tilde{a}$, referred to as the asymptotic a parameter. When an energy dependent a parameter is used, one extracts the value of $\tilde{a}$ (rather than a) from neutron resonance spacings. As with the a parameter, $\tilde{a}$ exhibits a systematic dependence on mass number.

The ground state shell correction is defined as the difference between the experimental mass and the mass predicted by nuclear models, such as the liquid drop model. It has also been suggested that the shell correction should be identified with a "microscopic correction" that describes the deviation of a nucleus from a spherical macroscopic shape [22].

4.1.6 Level Densities below the Neutron Binding Energy

The Fermi gas level density diverges at $U = 0$. If the backshift is positive, this divergence occurs when the true excitation energy is finite. In these cases one must

use some other description of the level density at and below $E = \Delta$. The simplest of parameterizations assume that the level density is constant below a certain energy [26], although one would hope for a better treatment.

Gilbert and Cameron showed that the cumulative number of levels at low energies can be fit with a constant temperature level density of the form

$$w(E) = \frac{1}{T} \exp\left[\frac{E - E_0}{T}\right] \ . \tag{83}$$

In this expression, T represents the temperature (assumed constant). Equation 83 does not provide a reasonable description of the level density above the neutron binding energy. Generally the constant temperature formulation is used up to an energy E_x (where $\Delta < E_x < B_n$), and the Fermi gas level density is used above E_x. The two level densities are required to match tangentially at E_x.

Similar to the Fermi gas, the observable level density is related in a simple way to the total level density,

$$\rho(E) = \frac{1}{\sqrt{2\pi}\sigma} w(E) = \frac{1}{T} \exp\left[\frac{E - E_0}{T}\right] \frac{1}{\sqrt{2\pi}\sigma} \ . \tag{84}$$

The spin cutoff parameter σ cannot have the same form as it does for the Fermi gas. Equations 76 and 78 are proportional to $\sqrt{U}$, and at $U = 0$ ($E = \Delta$) they become imaginary. This is, of course, unacceptable.

Several treatments have been proposed for the spin cutoff parameter in the constant temperature regime. The simplest method is to evaluate σ using Equation 76 or 78 at E_x and assume that the value remains constant at $\sigma(E_x)$ for lower energies. A second method, proposed by [23], evaluates σ at the energy of the

highest known discrete level for which the spin and parity are known (E_{cut}) as

$$\sigma^2(E_{cut}) = \frac{1}{2N}\sum_i \left(J_i + \frac{1}{2}\right)^2 \ . \tag{85}$$

The sum runs over all discrete states up to and including that at E_{cut}. Below E_{cut}, σ^2 is held constant at $\sigma^2(E_{cut})$. Between E_{cut} and E_x, σ^2 varies linearly with energy, i.e.

$$\sigma^2(E) = \sigma^2(E_x) - \frac{\sigma^2(E_x) - \sigma^2(E_{cut})}{E_x - E_{cut}}(E_x - E) \ . \tag{86}$$

Above E_x, the Fermi gas value of σ^2 is used.

A third treatment of σ^2 below E_x is given by [2]. At E_{cut} σ^2 is evaluated in the Fermi gas way. Then, for energies between $\frac{1}{2}E_{cut}$ and E_x, the spin cutoff parameter is given by

$$\sigma^2(E) = \sigma^2(E_{cut}) + \frac{\sigma^2(E_x) - \sigma^2(E_{cut})}{E_x - \frac{1}{2}E_{cut}}\left(E - \frac{1}{2}E_{cut}\right) \ . \tag{87}$$

Below $\frac{1}{2}E_{cut}$, σ^2 is held constant.

4.1.7 Fitting the Level Density Formulae to Spectroscopic States

As mentioned, the Fermi gas and constant temperature level densities, which we will refer to as ρ_1 and ρ_2, respectively, are required to match tangentially at the matching energy E_x. Specifically, we require

$$\begin{aligned} \rho_1(E-\Delta)\Big|_{E=E_x} &= \rho_2(E)\Big|_{E=E_x} \\ \frac{d\ \log\rho_1(E-\Delta)}{dE}\Bigg|_{E=E_x} &= \frac{d\ \log\rho_2(E)}{dE}\Bigg|_{E=E_x} \ . \end{aligned} \tag{88}$$

Assuming that the Fermi gas parameters are already fixed, these requirements place two constraints on the three degrees of freedom associated with the constant tem-

perature parameters E_0, T, and E_x. One may use the matching conditions to fix the values of E_0 and T, and then vary E_x to provide the best fit to the low lying levels. Given a particular E_x, the matching conditions yield

$$\begin{aligned} T &= \left\{ \sqrt{\frac{a}{U_x}} - \frac{3}{2U_x} + \frac{[\tilde{a} - a(U_x)](1+\gamma U_x) + \tilde{a}\gamma\delta W}{\sqrt{a(U_x)U_x}} \right\}^{-1} \\ E_0 &= E_x - T\log\left[T\rho_1(U_x)\right] \end{aligned} \tag{89}$$

with $U_x = E_x - \Delta$.

The Hauser-Feshbach formula makes explicit use of the discrete levels up to what we have defined as E_{cut}, and one must take care that the integrated level density matches the cumulative number of levels at E_{cut}. If not, the effective number of discrete levels used in the Hauser-Feshbach formula (see Equation 35) will have a discontinuity at E_{cut}, which may manifest itself as a kink in the resulting cross sections. To avoid this situation, one should ensure $\int_0^{E_{cut}} \rho(E)dE = N(E_{cut})$ whenever possible. In other words, one should try to match the level density as closely as possible to the level at E_{cut}.

It was mentioned previously that E_x should lie between Δ and the neutron binding energy (B_n). If E_x is greater than B_n, the level density at B_n (and consequently the calculated value of D_0, which we have fixed to measured or systematic values) will change. If $E_x \leq \Delta$, the discontinuity in the Fermi gas formula will reappear. Thus it is critical that we have $E_x > \Delta$, and desirable that $E_x < B_n$. Additional lower limits may be placed on E_x if we require $T > 0$. The ability to place the matching energy in this range is greatly affected by the level density parameter $\tilde{a}$. If $\tilde{a}$ is too large, one will need $E_x > B_n$ to match the discrete levels. Additionally, the validity of the constant temperature formula is questionable at best in this higher energy region. If $\tilde{a}$ is too small, we will need $E_x \leq \Delta$ to match the discrete level spectra. Also for small $\tilde{a}$ and in the case $\Delta < 0$, the integrated Fermi gas

level density may still be much greater than the cumulative number of levels at E_{cut} ($N(E_{cut})$), in which case matching the spectroscopic data is impossible. A consistent occurrence of these issues signals that the $\tilde{a}$ parameters are inappropriately high or low. The value of $\tilde{a}$ is inferred from measured resonance spacings after parameterization of Δ and σ^2 has been chosen. Thus, the inability to properly match the level density to discrete level spectra is most likely due to the chosen form of Δ or σ^2.

This concludes our discussion of the theoretical considerations relative to nuclear level densities. We will now provide an overview of the level density parameters used in previous reaction rate libraries and outline our methods for fixing the Fermi gas level density parameters using local systematics.

4.2 Past Approaches to the Level Density

In this section we provide an overview of the level densities used in previous cross section modeling. The first set of parameters comes from [27], which was used in the 1995 stellar evolution survey [28]. The second set of parameters comes from [22], used in the more recent 2001 stellar evolution calculations [21]. The third set of level densities presented in this section has not yet been used to develop a reaction library, but represents a recent attempt to calculate level densities in the microscopic Hartree-Fock BCS theory.

4.2.1 Woosley et al. (1978)

The reaction library used in [24] was developed in 1978 by Woosley et al. [27] (hereafter WFHZ) using the code CRSEC [26]. The level density parameters used in these rates are similar to those of Gilbert and Cameron [7], though there are some noteworthy modifications.

WFHZ use the spin cutoff parameter of Equation 78, while Gilbert and Cameron

use Equation 76. The parameterization of the backshift employed by WFHZ is that of Equation 73 with $\eta = 80$. Gilbert and Cameron use Equation 72. Both use the pairing energies tabulated in [7]. Both level density formulations also use the same shell corrections, though the dependence of the a parameter on the shell correction is slightly different for WFHZ. For nuclei with $Z < 30$ they use

$$\begin{aligned} \text{odd A}: \quad & a = (0.05260 + 0.002209\ S)A^{1.2} \\ \text{odd Z, odd N}: \quad & a = (0.05264 + 0.001592\ S)A^{1.2} \\ \text{even Z, even N}: \quad & a = (0.05267 + 0.001901\ S)A^{1.2}\ . \end{aligned} \tag{90}$$

Here, $S = S_n + S_p$ is the shell correction. For self-conjugate nuclei, a is reduced by a factor of 1.10 to account for isospin effects. These level density systematics were derived from neutron resonance spacings. For compound nuclei with measured resonance spacings, "experimental" values of the a parameter are provided. We note that while the choice of spin cutoff parameter and backshift are consistent with modern treatments, WFHZ use an energy independent a parameter, which maintains shell effects at all excitation energies.

The spin dependence of the level density employed by WHFZ according to [27] is slightly different than that of Equation 66:

$$f(J) = \frac{2J+1}{2\sigma^2} \exp\left[\frac{-J(J+1)}{2\sigma^2}\right]\ . \tag{91}$$

However, further investigation into the CRSEC code [26] utilized in the GCE survey [24] reveals a far more complex spin dependence:

$$\begin{aligned} f(J=0) &= \frac{3}{4\sigma^2} \exp\left(-\frac{1}{\sigma^2}\right) \\ f(J \neq 0) &= \frac{2J-1}{4\sigma^2} \exp\left[\frac{-J(J-1)}{2\sigma^2}\right] + \end{aligned}$$

$$\frac{2J+1}{4\sigma^2}\exp\left[\frac{-J(J+1)}{2\sigma^2}\right]+$$
$$\frac{2J+3}{4\sigma^2}\exp\left[\frac{-(J+1)(J+2)}{2\sigma^2}\right] \quad . \tag{92}$$

The last remaining issue to discuss regarding the WFHZ level densities is the treatment of the level density at low excitation energies. The CRSEC code indicates that the level density is held constant below the point at which the slope of the level density changes sign down to 0.5 MeV. Below 0.5 MeV, the level density is assumed to be zero. In cases where a sufficient amount of data on the discrete levels is available, the form of the level densities at such low excitation energies has no effect, since the Hauser-Feshbach model calls for the use of the explicitly known levels (see Equation 35). However, in nuclei with only a very few known levels, such as ^{61} Fe, this may not be the case, and the low energy behavior of the level density could affect the calculated cross sections.

To evaluate the performance of the WFHZ level densities (and other formulations that follow), we consider two quantities. First, we consider the ratio of the average resonance spacings predicted by the systematics to measured values. In this type of evaluation we use only the systematic values of level density parameters, and not those derived explicitly from measured data. In Figure 8 we present this ratio for nuclei used in this study ($20 \leq Z \leq 29$, select isotopes). Errorbars reflect the ratio obtained using the upper and lower limits of the measured values (i.e. the errors in the measured values). We find that the systematic level densities of WFHZ tend to overestimate the average resonance spacings, some by more than a factor of two (indicated by dotted lines). We shall see later that modern level density parameterizations more accurately replicate the measured D_0.

The second ratio we consider is the integrated level density at to the known cumulative number of discrete levels at E_{cut}. Ideally, this ratio should be close to

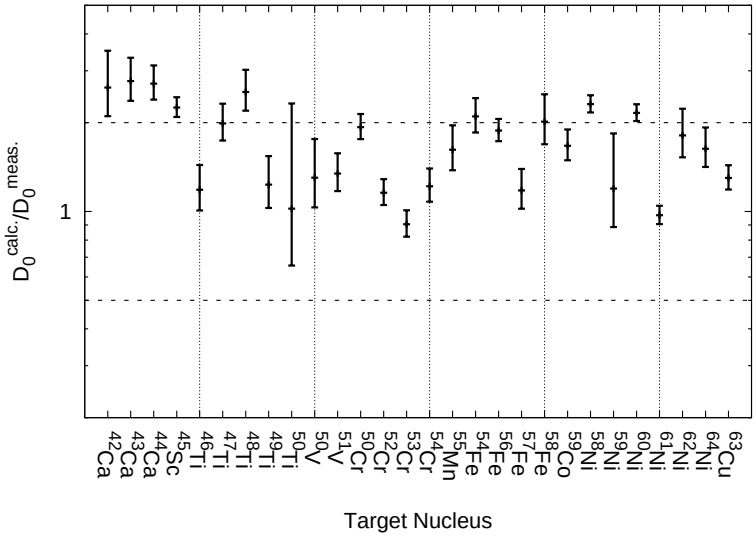

Figure 8: Ratio of calculated to measured resonance spacings using WFHZ level densities for various nuclei in the region of interest. The dotted lines denote a factor of two from unity.

unity, as such a value indicates a good fit to the highest known level. When making this sort of comparison, we always use the discrete levels associated with the level density in question, i.e. when considering WFHZ level densities we also use the discrete levels employed by WFHZ. Since WFHZ do not include a constant temperature formulation, there is no matching energy that can be adjusted to provide the best possible fit to the discrete levels. Thus we should not necessarily expect this ratio to be consistently close to unity. This is verified in Figure 9. Although the integrated level density is always within a factor of ten, only about half fall within a factor of two (denoted by the dotted lines).

4.2.2 Rauscher, Thielemann, and Kratz (1997)

We now consider the level densities of Rauscher, Thielemann, and Kratz [22] (hereafter RTK), used in the more recent stellar evolution [21].

The spin cutoff parameter is treated the same as in WFHZ. The backshift is taken to be the average of the neutron and proton pairing energies as determined as

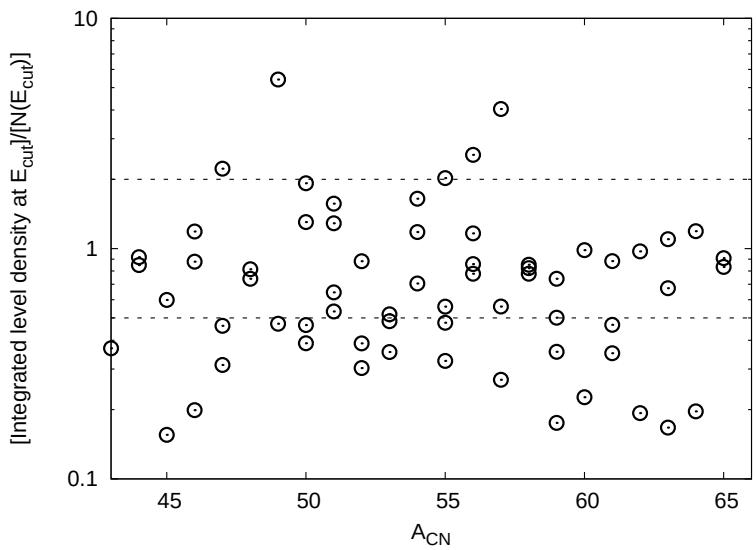

Figure 9: Ratio of the integrated level density to the measured cumulative number of discrete levels at E_{cut}, using the level densities and discrete levels of WFHZ. The dotted lines denote a factor of two from unity.

in Equation 74. Binding energies are calculated from the FRDM nuclear masses of [19]. The microscopic ground state energies of [19] are adopted as shell corrections (δW), and the level density parameter is given an energy dependence as in Equation 82. Systematic values of $\tilde{a}$ were developed by assuming a form

$$\tilde{a} = \alpha A + \beta A^{2/3} \tag{93}$$

and making a three parameter fit (for α, β, and the thermal damping coefficient γ) to a global set of measured average resonance spacings. This fit yields values of $\alpha = 0.1337$, $\beta = -0.06571$, and $\gamma = 0.04884$. The function $f(J)$ which describes the spin dependence of the level density is that of Equation 91.

The use of an energy dependent level density parameter is a marked improvement over WFHZ. Another major improvement comes from the use of a constant temperature formula at low excitation energies. The matching energies for the constant temperature fits are determined on a case by case basis, as outlined in Section

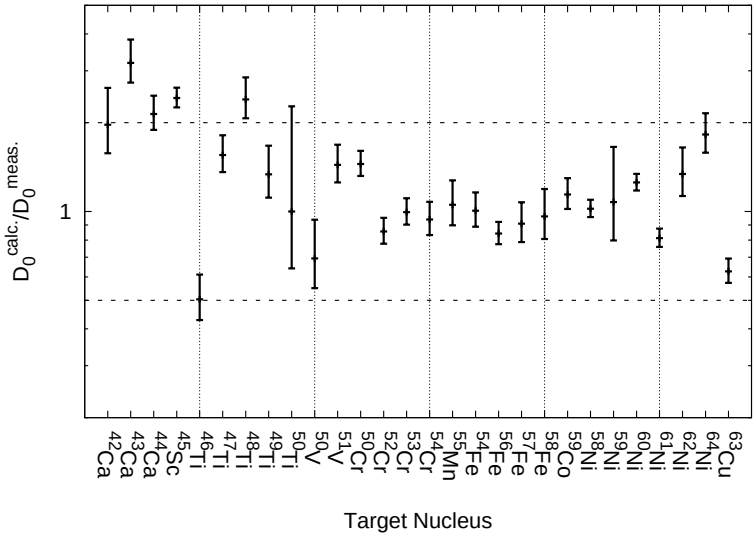

Figure 10: Ratio of calculated to measured resonance spacings using RTK level densities for various nuclei in the region of interest. The dotted lines denote a factor of two from unity.

4.1.7.

We must keep in mind that the systematic used for the level density parameter is a *global* systematic. The overall performance relative to the reproduction of measured resonance spacings is generally good for global systematics, in that a proper choice of backshift and shell correction remove many of the local effects caused by pairing gaps and closed shells. However, there may still be local regions where the performance is not as good. In Figure 10, we see that this global systematic does particularly good in reproducing resonance spacings for nuclei from chromium to cobalt, but not so good for nickel and elements below vanadium. In any event, most of the calculated D_0 are within a factor of two of the measured values, so the overall performance is fairly good. This prescription for the level density shows an improvement over WFHZ in this respect, as indicated by a comparison of Figures 8 and 10.

Since the RTK level density prescription includes a constant temperature fit, we also expect considerable improvement over WFHZ with regards to the ratio of

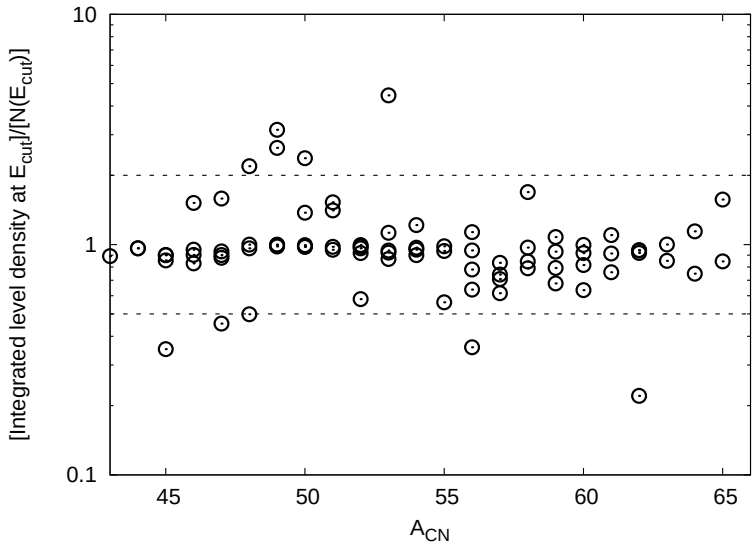

Figure 11: Ratio of the integrated level density to the measured cumulative number of discrete levels at E_{cut}, using the level densities from RTK and discrete levels adopted by RT. The dotted lines denote a factor of two from unity.

the integrated level density to the cumulative number of discrete levels, presented in Figure 11. RTK do not provide a tabulation of matching energies, and we were required to make our own constant temperature fits, matching the level density as closely as possible to the last discrete level. The discrete levels in this analysis are those used in [21], so that the treatment is consistent. As expected, introducing a constant temperature fit greatly improves the correlation of the integrated level density with the cumulative number of levels (compare Figures 9 and 11, most cases being within a factor of two.

4.2.3 Hartree-Fock BCS

In our investigation of the neutron capture rates on ^{59,60}Fe, we have also considered a completely different formulation of the level density derived from the Hartree-Fock BCS model [8]. The procedure for calculating these level densities does not resort to many of the approximations used in the backshifted Fermi gas densities. Microscopic nuclear structure properties, such as the density of single particle states

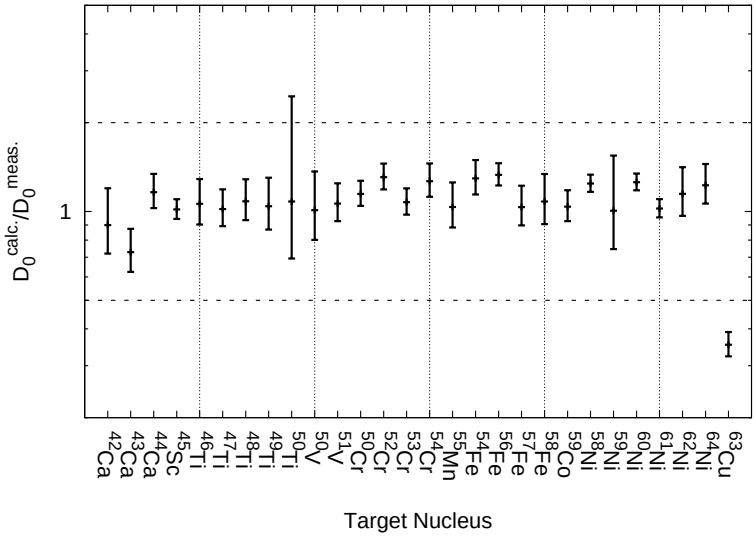

Figure 12: Ratio of calculated to measured resonance spacings using the Hartree-Fock BCS level densities for various nuclei in the region of interest. The dotted lines denote a factor of two from unity.

at the Fermi energy, are calculated within the context of the Hartree-Fock BCS model, using a Skyrme-type effective nucleon interaction. These level densities are available in tabular form online at the URL referenced in [8]. They suggest that globally the asymptotic level density parameter is best approximated by $\tilde{a} \approx A/11$. This value is markedly different from the canonical $\tilde{a} = A/8$.

Two of the Hartree-Fock BCS level density parameters, the excitation energy and entropy, can be adjusted in such a way to normalize the level densities to measured discrete level spectra and S-wave resonance spacings. In the cases where both quantities are available, both parameters can be normalized on a case-by-case basis, and generally do quite well in replicating experimental data. In cases where only a discrete level scheme is available (10 or more levels), only the excitation energy is adjusted. No attempt has been made to systematically normalize the level densities in [8] when data is not available.

We now consider how well experimental data is reproduced relative to our particular region of interest and our set of adopted discrete levels. First, we consider

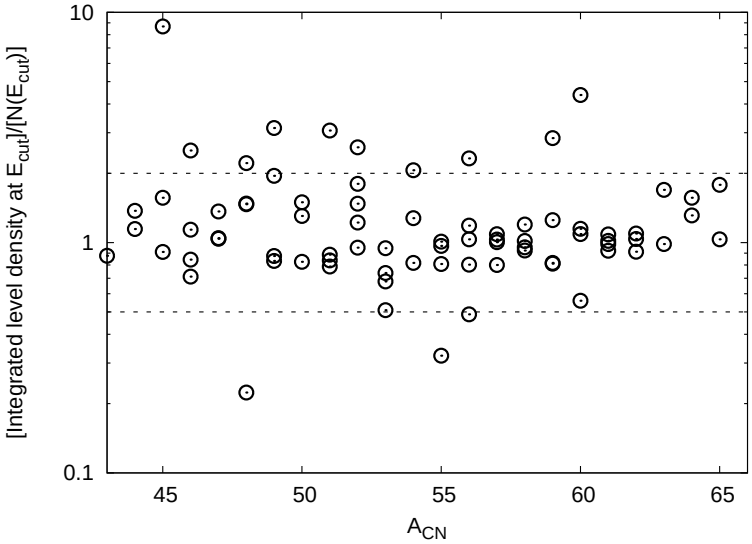

Figure 13: Ratio of the integrated level density to the measured cumulative number of discrete levels at E_{cut}, using the Hartree-Fock BCS level densities and our set of adopted discrete levels. The dotted lines denote a factor of two from unity.

the S-wave resonance spacings. Figure 12 seems to indicate that the Hartree-Fock BCS is superior in reproducing these values. However, one must temper any enthusiasm with the fact that the tabulated level densities provided by [8] have been individually normalized only when possible, and no systematic normalization has been applied to nuclei without measured resonance spacings. We can get a rough idea of the typical error in the calculated D_0 for nuclei without measured values by considering a similar analysis on unnormalized Hartree-Fock BCS level densities. The unnormalized densities are not provided in electronic format by the authors of [8], but they do present a plot similar to Figure 12 for the unnormalized densities (Figure 1 in their paper). In the range of $45 \leq A \leq 65$, the unnormalized calculated D_0 are generally within a factor of 3 of the measured values. There is no consistent tendency toward unity, as in Figure 10. The Fermi gas results depicted in Figures 8 and 10 are based on systematic level density parameters (as opposed to "experimental" parameters), and typical errors for nuclei without measured resonance spacings will be similar to those in the figures.

Now we turn our attention toward the reproduction of discrete level spectra. The authors of [8] demonstrate a remarkable agreement in their paper. However, the set of discrete levels we are using has received additional evaluation, and in some cases we include many more levels than used in the normalization process in [8]. Figure 13 provides us with an idea of how well the integrated Hartree-Fock BCS level densities replicate our preferred set of cumulative levels. The result is of a quality intermediate between WFHZ and RTK (Figures 9 and 11).

With regard to the reproduction of measured resonance spacings and discrete level spectra, we consider RTK to be superior thus far.

4.3 Local Systematics for Level Density Parameters

Global systematics for level density parameters, such as those developed by WFHZ and RTK ([27] and [22]) do remarkably well reproducing large sets of experimentally measured quantities. Local deviations due to pairing energies and shell effects can generally be removed with a proper parameterization of the backshift and shell correction. However, local deviations from the global systematic are inevitable, and hence in certain local regions of the isotopic plain global systematics may not be ideal (see Figure 10 for calcium and titanium nuclei). In this section, we discuss the development of a *local* systematic for $\tilde{a}$ which, due to its local nature, is superior in reproducing measured resonance spacings and discrete level spectra in the region of interest.

Global systematics are made by varying a set of parameters such that one can obtain the lowest reduced χ^2 fit to a large set of experimental data ranging over the entire isotopic plane. The development of local systematics is done in the same way, except that only a subset of the experimental data local to the region of interest is used. In this study, we define the local region to be $20 \leq Z \leq 29$. We include data for all mass numbers, although the data is mostly limited to nuclei on the

line of stability. Such local systematics have proven effective in past radiochemical studies [10, 11, 12, 16]. This particular local region does present a few difficulties, due primarily to the proximity of the $Z, N = 20, 28$ closed shells.

Local systematics can provide an improvement over global systematics, in that they can account for any local deviations as explained above. However, they also have limitations. In particular, a local systematic is of questionable value near the boundaries of the local region, and is certainly of no practical use outside of those boundaries.

In many respects, our systematic for the level density parameter is similar to that of RTK. We assume the usual Fermi gas at high excitation energies and a constant temperature form at lower energies. We also use the energy dependent a parameter of Equation 82.

In developing our systematic, we have considered several combinations of prescriptions for the backshift and spin cutoff parameter. For the backshift we initially consider both Equation 72 and Equation 74. In both cases, the pairing energies are determined from the adopted set of binding energies discussed in Section 3.2 and listed in Appendix A (Recall RTK derive their binding energies from mass excesses listed in [19]). For the spin cutoff parameter, we initially consider both Equation 76 and 78. For the shell corrections, we use the microscopic ground state energies from [19].

For each of the four combinations of Δ and σ described above, we assume that the asymptotic level density parameter is of the form of Equation 93. We then acquire a least squares fit for the parameters α, β, and γ. This fit is based only on measured S-wave resonance spacings for nuclei in the local region of interest ($20 \leq Z \leq 29$), taken from [9]. In addition to these four combinations, we have also considered a two parameter fit for α and β, assuming Equations 74 and 78 for the backshift and spin cutoff parameter and $\gamma = 0.04884$ (the value from RTK). For

Table 5: Local level density systematics trials. For each systematic named in the first column, the parameterization of the backshift and spin cutoff parameter is given in the second and third columns. The resulting best fit parameters are given in the next three columns. The χ^2 values for the fit is given in the final column.

Systematic	Δ	σ	γ	α	β	χ^2
1	Eqn. 74	Eqn. 78	0.07036	0.038139	0.301954	9.71
2	Eqn. 72	Eqn. 78	0.11227	0.091519	0.169690	19.54
3	Eqn. 74	Eqn. 76	0.10462	0.001056	0.411101	10.57
4	Eqn. 72	Eqn. 76	0.15585	0.061823	0.258793	19.07
5a	Eqn. 74	Eqn. 78	0.04884	-0.004942	0.468456	2.06
5b	Eqn. 74	Eqn. 78	0.04884	0.111903	0.024660	8.68
5c	Eqn. 74	Eqn. 78	0.04884	-0.030033	0.568457	4.05

this two parameter fit, we developed separate systematics for even-Z even-N nuclei, even-Z odd-N nuclei, and odd-Z nuclei.

The χ^2 values for each of these local systematics are given in Table 5. A small χ^2 indicates a good fit to measured resonance spacings. The three parameter fit using the backshift of Equation 74 and spin cutoff parameter of Equation 78 (Figure 14) provides the smallest χ^2, and is thus initially favored. Note that for the two parameter fit, one should compare the sum of the three χ^2 values for sets 5a (Even-Z Even-N nuclei), 5b (Even-Z Odd-N nuclei), and 5c (Odd-Z nuclei) to the χ^2 of the other systematics. We also note that the value of γ from this systematic is in closer agreement to the γ of previous level density prescriptions [14, 22] than the other three parameter fits.

The two systematics based on the backshift parameterization in 72 result in larger level density parameters. When the level density parameter is too large, issues may arise in making fits to the discrete levels, as discussed in Section 4.1.7. Since this backshift parameterization also often results in level density parameters inconsistent with those derived from coherence widths of fluctuating cross sections [5], it is further disfavored.

Being hesitant to rely solely on the value of χ^2 for determining which local sys-

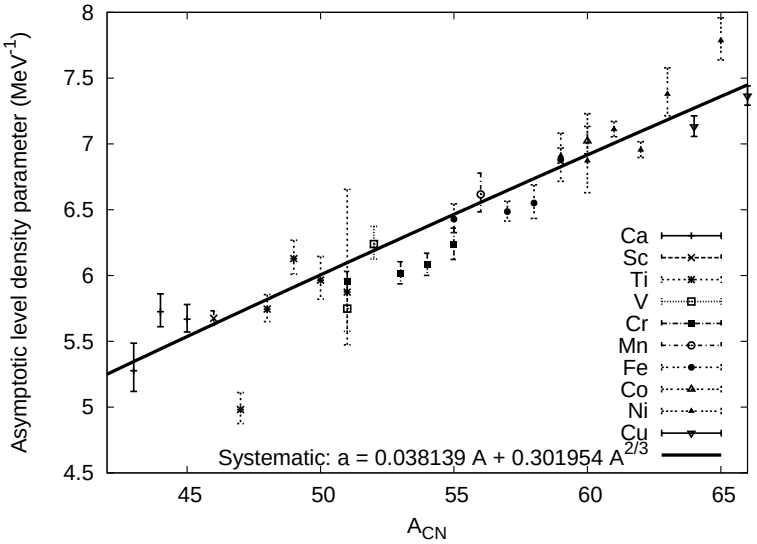

Figure 14: The local level density systematic, determined using a three parameter fit and Equations 74 and 78 for the backshift and spin cutoff parameter. The systematic values of $\tilde{A}$ are given as a function of mass number. The data points represent $\tilde{A}$ parameters derived from measured resonance spacings, and the error bars reflect the respective errors of the measured resonance spacings.

tematic is best, we have also compared cross sections calculated using the various local level density systematics (with all other Hauser-Feshbach inputs fixed to our preferred values). The level densities resulting from each of these systematics result in similar cross sections (see Section 7.2.1). Since this analysis lends no preference, we default to the systematic with the smallest χ^2. This prescription uses the backshift calculated as the average of the neutron and proton pairing energies (Equation 74), the spin cutoff parameter of Equation 78, the microscopic ground state energies of [19] as shell corrections, and the energy dependent level density parameter of Equation 82 with $\gamma = 0.070036$ and an asymptotic level density parameter given by

$$\tilde{a} = 0.038139\ A + 0.301954\ A^{2/3}\ . \tag{94}$$

Naturally, we use the experimentally derived $\tilde{a}$ in our cross section calculations when they are available.

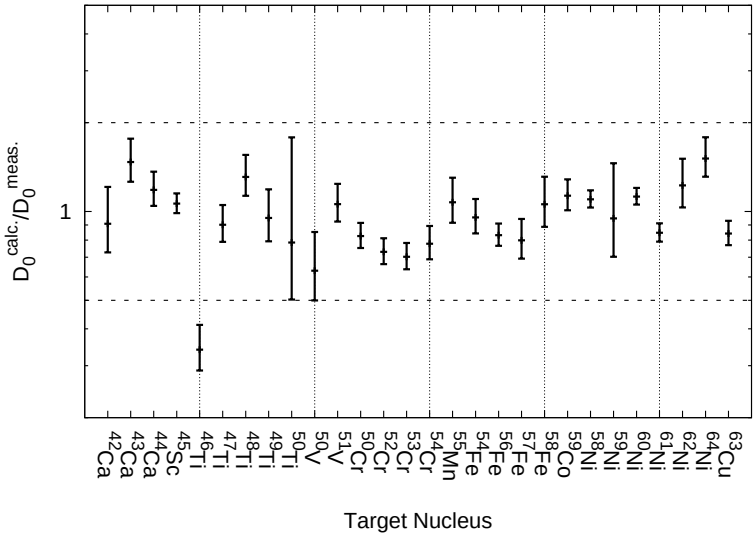

Figure 15: Ratio of calculated to measured resonance spacings using our local level density systematic for various nuclei in the region of interest. The dotted lines denote a factor of two from unity.

We now investigate how well this systematic reproduces the measured neutron resonance spacings, similar to the analysis in Figures 8, 10, and 12. Figure 15 shows the ratio of the calculated D_0 to measured values. Although the global systematic of RTK (Figure 10) does slightly better for the iron species, our local systematic is superior overall in this local region of interest. With the exception of ^{46}Ti, all the ratios are within a factor of two of unity. Many of the calculated D_0 are within the errors of the measured values.

We now proceed to fit the constant temperature portion of the level density to our adopted discrete levels. The fit is made individually for each nucleus, as opposed to a global prescription for the matching energy as is found in [7]. As explained earlier, the goal is to match the level density to the highest known discrete level with assigned spin and parity. This is done so that when one switches between the discrete levels and the level density in the Hauser-Feshbach formula, the effective level density at the transition will be smooth and continuous. If such a match is not made, the result will be the appearance of "kinks" in the modeled cross sections.

In previous sections we discussed some of the difficulties that may arise in making the constant temperature fits. In particular, if the level density parameter is too small, fitting to the highest known level may require a matching energy smaller than the backshift. Using such a matching energy would result in an unphysically divergent level density. Also, if the level density parameter is too high, one might have to choose a matching energy that is well above the neutron separation energy–a region where the constant temperature form is not valid.

However, when one cannot match the last discrete level, the cause may not necessarily be the level density parameter. In some cases, our initial set of adopted levels for a given nucleus appears to have regions where levels are missing, indicated by relatively large energy gaps between neighboring levels. When faced with a situation where we need a matching energy that is too small, the issue can generally be resolved by reducing the number of discrete levels used in the calculation. This solution is usually justifiable in the sense that the levels discarded are levels that were added in our evaluation of the discrete level schemes. In cases where discarding levels cannot be justified, we fit the level density as closely as possible we could to the discrete levels, keeping the matching energy between Δ and B_n. The resulting gap between the highest level and integrated level density was generally quite small.

In cases where there were no discrete levels to fit, we assumed the default matching energy from [7], given by

$$E_{GC} = \frac{5}{2} + \frac{150}{A} + \Delta \ . \tag{95}$$

If E_{GC} was greater than the neutron binding energy, we set $E_x = B_n$.

This matching procedure was carried out for each of the five local systematics developed for $\tilde{a}$ (listed in Table 5). Our preferred systematic for $\tilde{a}$ resulted in the fewest number of problematic fits. This increases our confidence in this choice of

local systematic.

Figure 16 illustrates typical constant temperature fits. In these plots, the horizontal axis is the excitation energy and the vertical axis in the number of discrete levels. The staircase represents the measured discrete level spectra, and the curved solid lines represent the integrated level density. In the larger plots, only the levels up to E_{cut} are included in the staircase. In the smaller plots, all levels available in [9] are shown, as well as dotted lines representing E_{cut} and B_n and a dashed line representing E_x. The fit for ^{48}Cr shows a gap in discrete levels (above E_{cut}), interpreted as missing levels. The fit for ^{49}V represents a typical case where the last level could not be matched exactly. The remaining fits in Figure 16 are the level densities most critical to this study, each of which represent what would be considered a good fit.

We may now perform the same analysis as in Figures 9, 11, and 13 for our local systematic. The ratio of our integrated level density to the cumulative number of levels at E_{cut} is presented in Figure 17. Comparing this figure with Figures 9, 11, and 13, we find that our level density performs better than the other prescriptions in this respect. Most of the ratios are quite close to unity. Most of the lowest ratios involve matching a very small number of levels.

This concludes the development of the level densities used in our modeling effort. Based on the relative abilities of the various prescriptions in reproducing measured discrete level spectra and S-wave resonance spacing, we find that our preferred local systematic, in conjunction with our adopted discrete levels and constant temperature fits, is superior to previous global systematics and microscopic level densities. In a later section we will investigate the sensitivity of the neutron capture rates to the level densities. This investigation includes both a consideration of possible errors related to our systematic as well as complete changes in level density prescription.

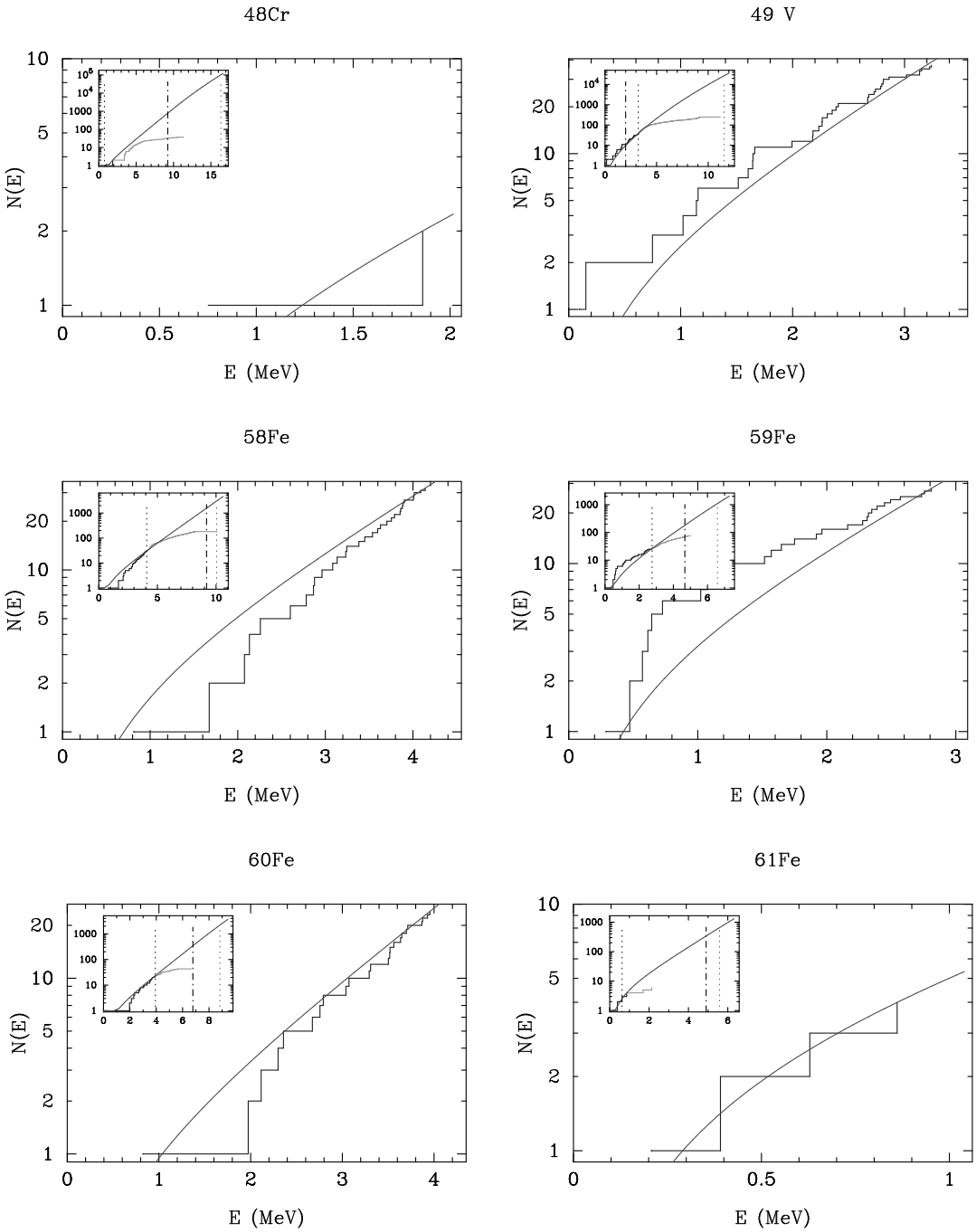

Figure 16: Select constant temperature fits to discrete level spectra. The measured cumulative number of levels as a function of excitation energy is denoted by the staircase, and the integrated level density is denoted by the smooth line. The larger viewport in each plot shows only the levels up to where the level scheme is known to be complete. The smaller viewport shows all levels included in the Reference Input Parameter Library. The dashed and dotted lines in the smaller viewport indicate E_{cut}, E_x, and the neutron binding energy.

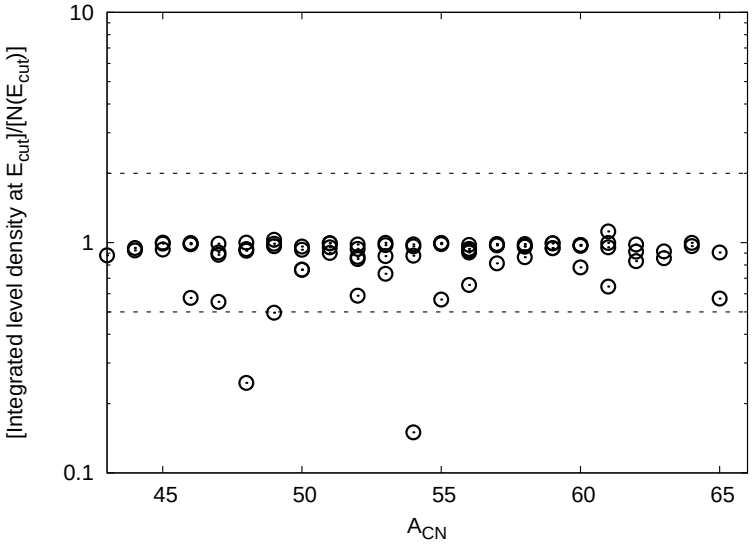

Figure 17: Ratio of the integrated level density to the measured cumulative number of discrete levels at E_{cut}, using the our local level density systematic and adopted set of discrete levels. The dotted lines denote a factor of two from unity.

References

[1] Bethe, H.A., 1936, Phys. Rev **50**, 332

[2] Chadwick, M. 1998, the GNASH statistical model code, http://www.nea.fr/abs/html/psr-0125.html

[3] Dilg, W., Schantl, W., Vonach, H. & Uhl, M., 1973, Nucl. Phys. **A217**, 269

[4] Gadioli, E. & Hodgson, P.E., 1992, Pre-Equilibrium Nuclear Reactions (Oxford: Clarendon Press)

[5] Gadioli, E. & Iori, I., 1967, Nuovo Cim. **51B**, 100

[6] Gadioli, E. & Zetta, L., 1968, Phys. Rev. **167**, 1016

[7] Gilbert, A., & Cameron, A.G.W. 1965, Can. J. Phys., **43**, 1446

[8] Demetriou, P., & Goriely, S. 2001, Nucl. Phys. **A695**, 95

[9] *Handbook for calculations of nuclear reaction data*, Reference input parameter library. 1998, IAEA-TECDOC-1034

[10] Hoffman, R.D., Dietrich, F.S., Bauer, R., Kelley, K., and Mustafa, M., "Neutron and Charged-Particle Induced Cross Sections for Radiochemistry in the Region of Bromine and Krypton", UCRL-TR-205563, LLNL, 2004 (available from http://www.osti.gov/bridge)

[11] Hoffman, R.D., Dietrich, F.S., Bauer, R., Kelley, K., and Mustafa, M., "Neutron and Charged-Particle Induced Cross Sections for Radiochemistry in the Region of Iodine and Xenon", UCRL-TR-206721, LLNL, 2004 (available from http://www.osti.gov/bridge)

[12] Hoffman, R.D., Dietrich, F.S., Bauer, R., Kelley, K., and Mustafa, M., "Neutron and Charged-Particle Induced Cross Sections for Radiochemistry in the Region of Samarium, Europium, and Gadolinium", UCRL-TR-211588, LLNL, 2005 (soon to be available at http://www.osti.gov/bridge)

[13] Ignatyuk, A.V., Smirenkin, G.N., & Tishin, A.S., 1975, Sov. J. Nucl. Phys. **21**, 255

[14] Iljinov, A.S., Mebel, M.V., Bianchi, N., De Sanctis, E., Guaraldo, C., Lucherini, V., Muccifora, V., Polli, E., Reolon, A.R., & Rossi, P. 1992, Nucl. Phys. **A543**, 517

[15] Jensen, J.H.D., & Luttinger, J.M., 1952, Phys. Rev. **86**, 907

[16] Kelley, K., Hoffman, R.D., Dietrich, F.S., Bauer, R., and Mustafa, M., "Neutron and Charged-Particle Induced Cross Sections for Radiochemistry for Isotopes of Scandium, Titanium, Vanadium, Chromium, Manganese, and Iron", UCRL-TR-211668, LLNL, 2005 (available from http://www.osti.gov/bridge)

[17] Kelley, K., Hoffman, R.D., Dietrich, F.S., Bauer, R., and Mustafa, M., "Neutron and Charged-Particle Induced Cross Sections for Radiochemistry for Isotopes of Yttrium, Zirconium, Niobium, Molybdenum, Technetium, and Ruthenium", 2005, in preparation

[18] Lang, J.M.B., & LeCouteur, K.J., 1954, Proc. Phys. Soc. **A67**, 586

[19] Möller, P., Nix, J.R., Myers, W.D., & Swiatecki, W.J. 1995, Atomic Data & Nuclear Data Tables, **59**, 185

[20] Newton, T.D., 1956, Can. J. Phys., **34**, 804

[21] Rauscher, T. & Thielemann, F.-K. 2001, At. Data Nucl. Data Tables **79**, 47

[22] Rauscher, T., Thielemann, F.-K. & Kratz, K.-L. 1997, Phys. Rev. C **56**, 1613.

[23] Reffo, G. 1978, ICTP Lecture Series, 17 Jan. - 10 Mar., Trieste

[24] Timmes, F.X., Woosley, S.E., Hartmann, D.H., Hoffman, R.D., Weaver, T.A., & Matteucci, F. 1995, ApJ **449**, 204

[25] Vonach, H., Uhl, M., Strohmaier, B., Smith, B.W., Bilpuch, E.G. & Mitchell, G.E., 1988, Phys. Rev. **C38**, 2541

[26] Woosley, S.E. & Fowler, W. A., UCID-17600, LLNL, 1977

[27] Woosley, S. E., Fowler, W. A., Holmes, J. A. & Zimmerman, B. A. 1978, Atomic Data & Nuclear Data Tables, **22**, 371

[28] Woosley, S.E., & Weaver, T.A. 1995, ApJS **101**, 181

5 Transmission Coefficients

We now turn our attention to the final ingredient of the Hauser-Feshbach model: the transmission coefficients.

Transmission coefficients describe the probability that an incident particle with a given energy will be absorbed into a particular state in a compound nucleus. In the context of reciprocity, they also describe the probability that a given particle will be emitted from a compound nuclear state. We need to include, therefore, transmission coefficients for the incident and each possible exit channel considered, for each of the compound nuclei involved in the reaction. This section will describe the formulation we use for the various transmission coefficients, as well as a comparison to those used by Rauscher and Thielemann [22] and Woosley, et al. [27]. We begin with the particle transmission coefficients, and conclude with the photon transmission coefficients.

5.1 Particle Transmission Coefficients

Ideally one could calculate the probability that an incident particle would be absorbed into a given nucleus in terms of the elementary particles and interactions present. In reality, such a calculation is impossible. To begin with, the QCD models that describe the fundamental physics governing strong interactions are non-perturbative in the energy range of interest in nuclear reactions. One might be able to substitute an effective field theory model for the nucleon-nucleon interaction, but the sheer number of nucleons involved makes the calculation infeasible. Hence, we must resort to simpler empirical models, the most popular being the optical model.

The absorption of an incident particle into a nucleus can be described in terms

of a potential having the form

$$U(r) = V(r) - iW(r) \ . \tag{96}$$

The elastic scattering of the incident particle due to the nuclear and Coulomb forces is fully described by the real term $V(r)$. The imaginary function $W(r)$ translates into a decrease in the elastic scattering amplitudes, or in other words, absorption of the incident particle [15].

Generally optical potentials are of a Woods-Saxon shape. There are volume potentials of the form

$$V_{WS}(r) = \frac{-V_0}{1 + \exp[(r - R)/a]} \tag{97}$$

and surface potentials with a radial dependence that goes as dV_{WS}/dr. In this expression, V_0 is the nominal depth of the potential, R is the nuclear radius, and a is the diffusivity of the surface. Separate real and imaginary volume and/or surface terms may be included. Additional terms may describe spin-orbit and Coulomb interactions, the latter when the incident particle has an electric charge. The various Woods-Saxon parameters are chosen to best reproduce experimentally measured quantities that can be derived from an optical potential, such as elastic cross sections, total reaction cross sections, S- and P-wave strength functions, and so on.

Transmission coefficients are calculated by solving the Schrodinger equation using the optical potential. The incident wavefunction is assumed to be a plane wave or Coulomb-distorted plane wave, and is separated into its various angular momentum components (which scatter independently) via the partial wave expansion. Once the Schrodinger equation has been solved, the complex scattering amplitudes can be determined. The transmission coefficients are related to these scattering amplitudes [15] (see Section 2.1.1).

5.1.1 Neutron and Proton Transmission Coefficients

In our modeling effort, we adopt the optical potential of Koning and Delaroche [16] (hereafter KD) for incident neutrons and protons. This particular optical model was chosen because of its superior ability to reproduce measured nuclear properties. The comparisons made in [16] are quite extensive. We provide supporting comparisons in this work. The Woods-Saxon parameters of the KD optical potential are functions of the atomic and mass numbers of the target, and also of the energy of the incident particle. We use the ECIS code [23] to solve the Schrödinger equation. Although the ECIS code is capable of coupled-channel calculations for deformed nuclei, the deformation parameters in this local region of the isotopic plane are small enough to justify using the code in a spherical mode.

The previous modeling effort of [22] used the optical model of Jeukenne, Lejeune, and Mahaux [11] (hereafter JLM). This optical potential is in many respects similar the KD potential, in that a Woods-Saxon form is assumed and the various parameters related to the potentials are functions of incident particle energy and the atomic and mass numbers of the target. However, this particular optical model does not include spin-orbit components.

The optical potential adopted by Woosley, at al. [27] is considerably simpler the KD and JLM models. They use the equivalent square well potential of Michaud and Fowler [19] (hereafter MF). The calculation of the transmission coefficients in this model is far less time consuming since analytic expressions may be obtained for the transmission coefficients in terms of the Coulomb wavefunctions. Hence, solving the Schrodinger equation for each energy at which the transmission coefficients are to be evaluated is not necessary. Since the ECIS code will only handle Woods-Saxon potentials, we have not calculated total neutron cross sections or neutron resonance parameters for this potential. In any event, we consider the Woods-Saxon potentials

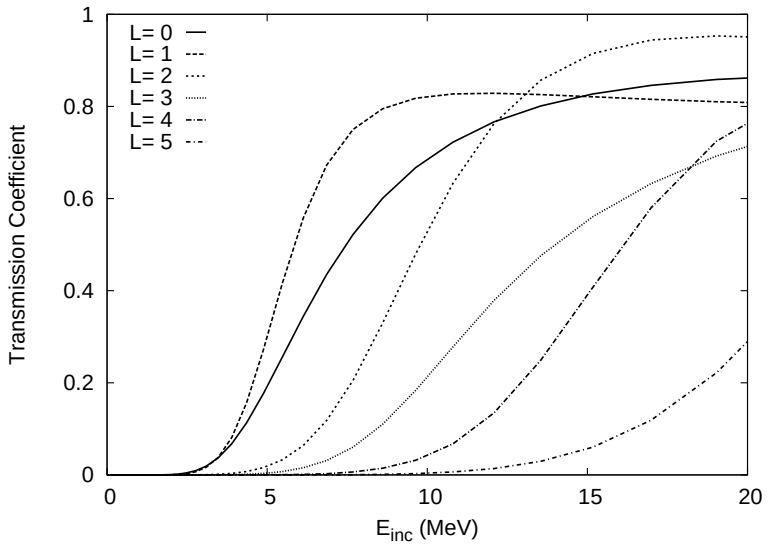

Figure 18: Transmission coefficients from the Koning and Delaroche optical potential for a proton incident on ^{58}Fe. The transmission coefficients for the first six partial waves are shown as a function of incident proton energy.

to be superior to MF, since they provide a more realistic description of the nuclear potential.

At the incident energies where the neutron capture cross section is most important (∼30 keV), the proton transmission coefficient is generally quite small, if not zero altogether (for example, see Figure 18 compared to 19). Consequently, the proton exit channel, if kinematically accessible at these energies, will be suppressed (more details regarding this suppression are given in Section 5.1.2). For this reason, the neutron capture cross sections will show very little sensitivity to the proton transmission coefficients, and we will focus primarily on the neutron transmission coefficients.

The optical potential can be used to calculate the total neutron cross section, and we use this particular quantity as one of our benchmark tests for optical model quality. In Figure 20 the predictions of the KD and JLM optical models are compared to measured total neutron cross section data in the region of interest. Since the ECIS code only evaluates Woods-Saxon potentials, we have not made a calcula-

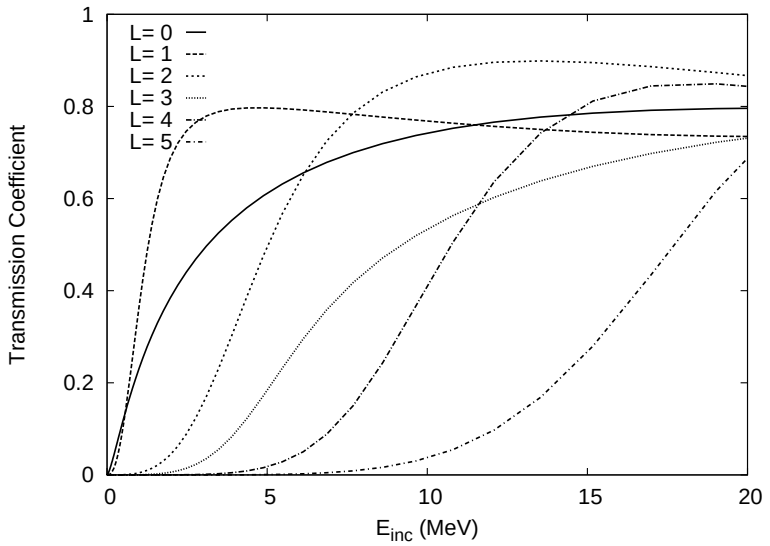

Figure 19: Transmission coefficients from the Koning and Delaroche optical potential for a neutron incident on ^{58}Fe. The transmission coefficients for the first six partial waves are shown as a function of incident neutron energy.

tion of the total neutron cross section using the MF equivalent square well potential. However, we fully expect the results of the two more modern Woods-Saxon potentials to give better agreement with the experimental data. The data on these figures is the aggregate of all total neutron cross section data available on EXFOR [4] at the time of the writing of this thesis. Individual data sets are not listed due to space constraints.

Both optical potentials do a good job replicating total neutron cross sections. There are some general features worth mentioning. First, the KD potential tends to yield a larger cross section than the JLM potential below ∼500 keV. At these energies, the resonance structure is very apparent in the measured data, and the error bars span a wide range. In general, both optical potentials result in cross sections within the error bars below 500 keV. The average central values of the experimental data may slightly favor the JLM potential.

Above 500 keV, both potentials still perform quite well, although the KD potential tends to lie closer to the central values of the measured data. In the cases

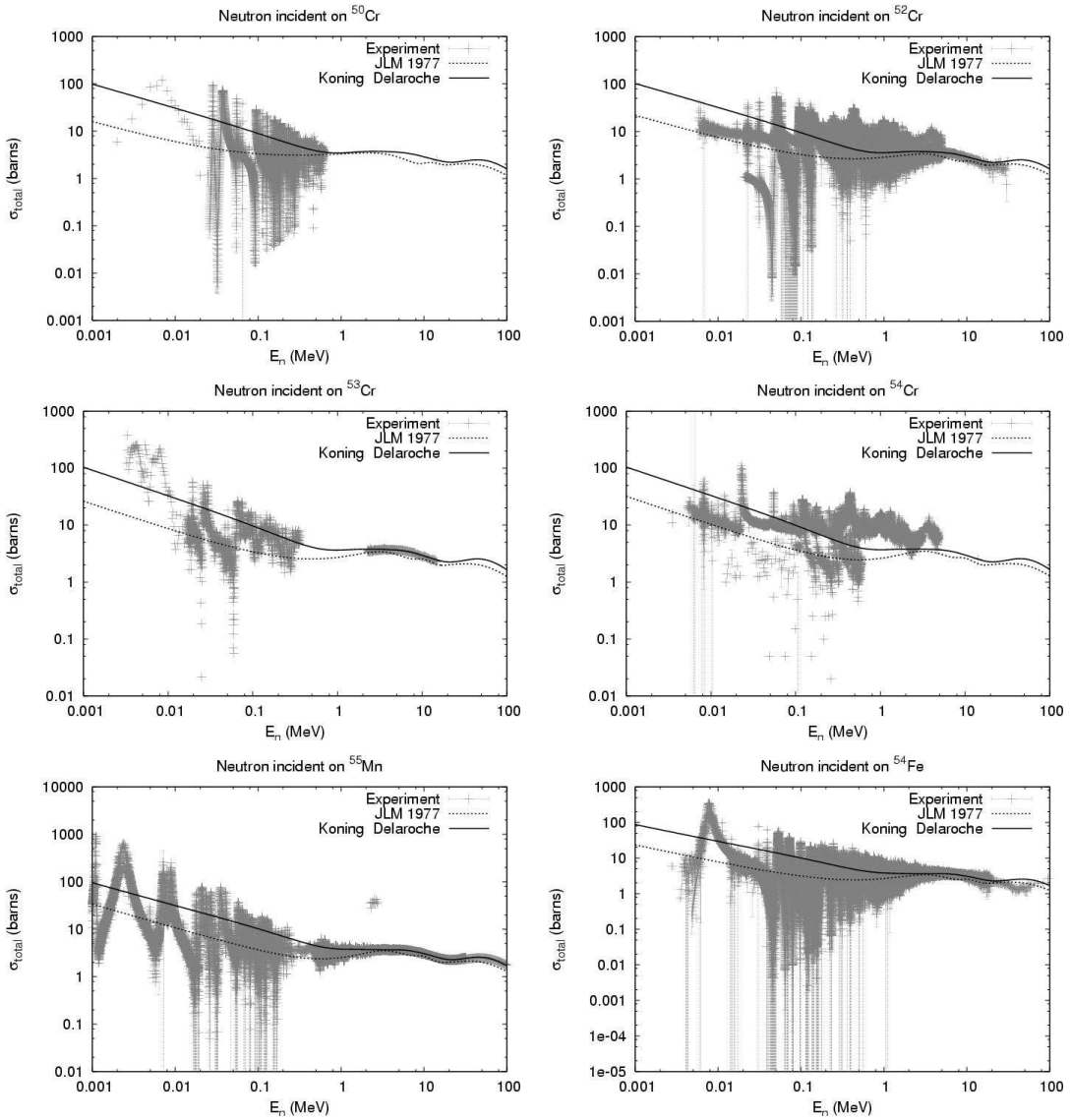

Figure 20: Modeled total neutron cross sections compared to measurements. Cross sections calculated with the Koning and Delaroche optical potential are shown by solid lines. Cross sections calculated with the JLM optical potential are indicated by dotted lines. The measured data represents all total neutron cross section data available from the EXFOR library as of 2004.

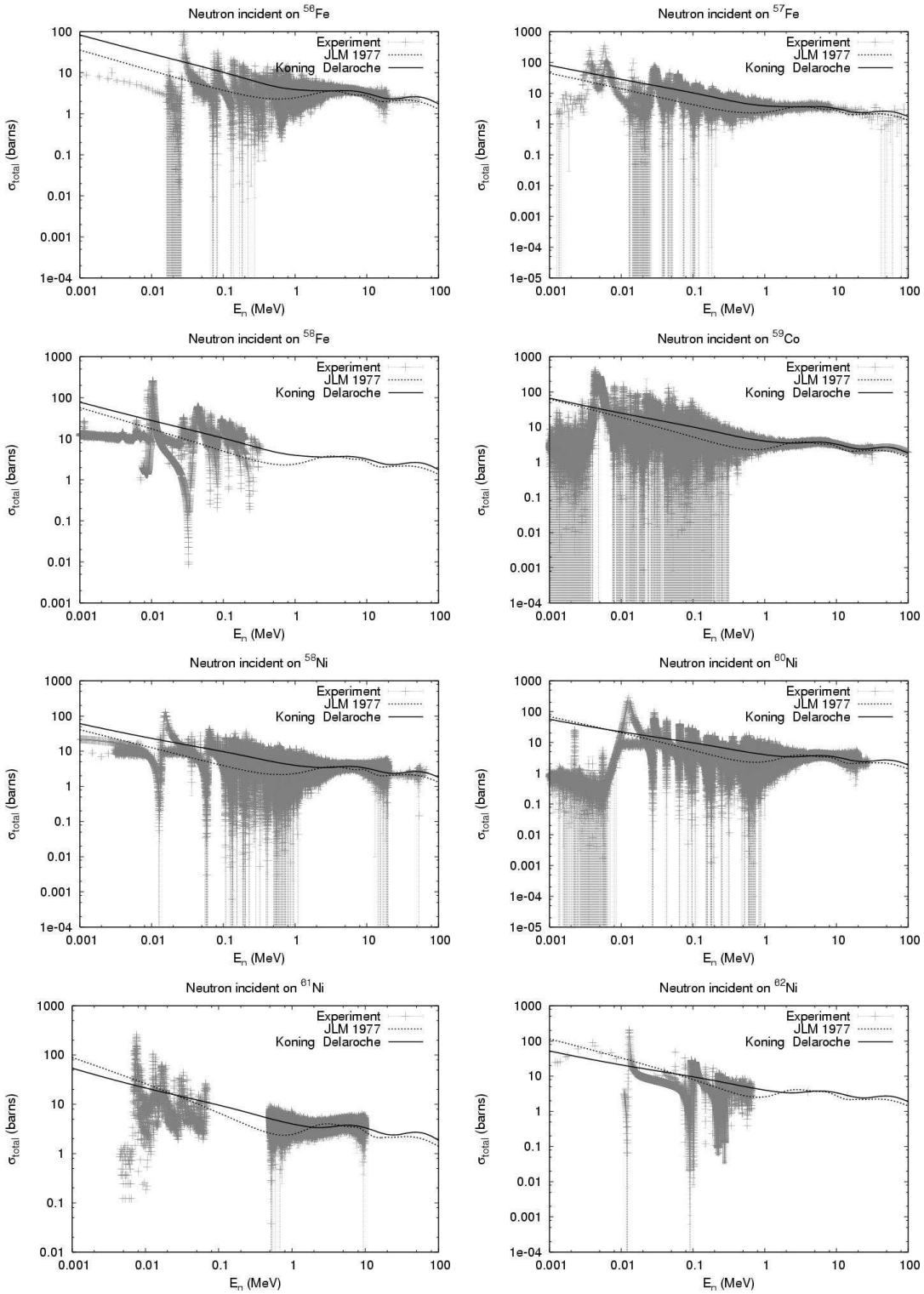

Figure 20: (continued)

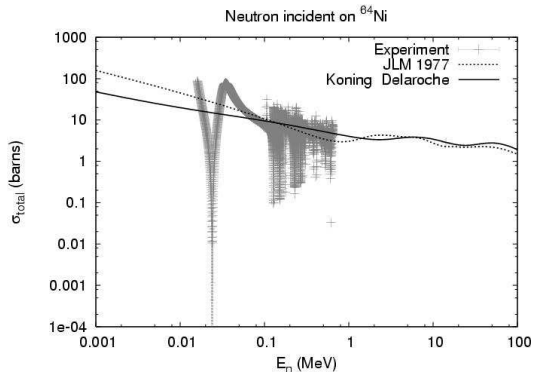

Figure 20: (continued)

of ^{50,54}Cr and ^{62,64}Ni, the Koning and Delaroche potential does considerably better at matching the measured cross section at 14 MeV. For ^{54}Cr, both potentials underestimate the total neutron cross section between 800 keV and 10 MeV. For the ^{54}Fe cross section, both potentials seem to overestimate the cross section above 20 MeV.

Overall, neither potential seems to be favorable over the other with respect the total neutron cross sections. We thus turn our attention toward other quantities in our effort to evaluate the neutron potentials.

The S- and P-wave strength functions (or S_0 and S_1, respectively) and potential scattering radius R' can also be calculated for an optical model. In Figures 21-23 we present the ratios of the calculated values of these quantities to experimental values. The experimental data for the S- and P-wave strength function plots is that provided in the obninsk file in the Reference Input Parameter Library [5]. The experimental data for the potential scattering radius is taken from [20].

The KD potential does better in reproducing the S-wave strength functions for $40 \leq A \leq 120$. Below $A = 115$, the calculated values are always within a factor of two of the experimental values. The situation is even better around the region of $A = 60$, which is of key interest to this study. In this region, the S-wave strength functions calculated from the KD optical potential are all within the errors of the

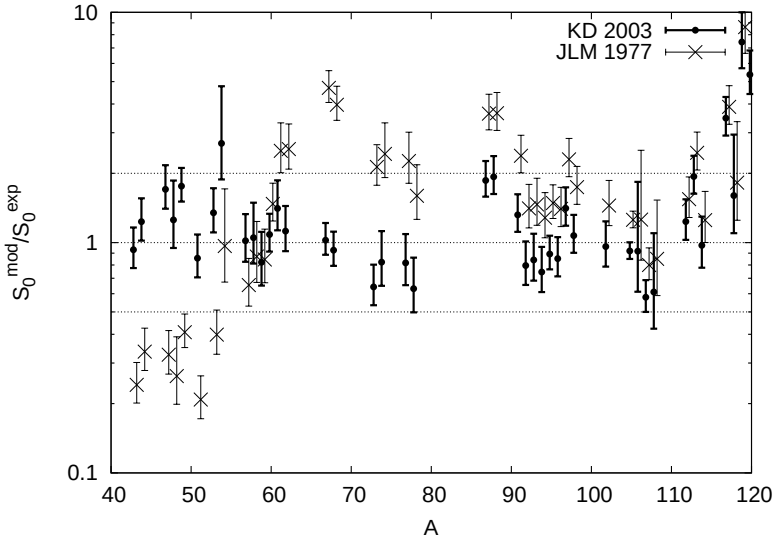

Figure 21: Ratio of S-wave strength functions modeled with the KD and JLM optical potentials to measured values taken from the Reference Input Parameter Library.

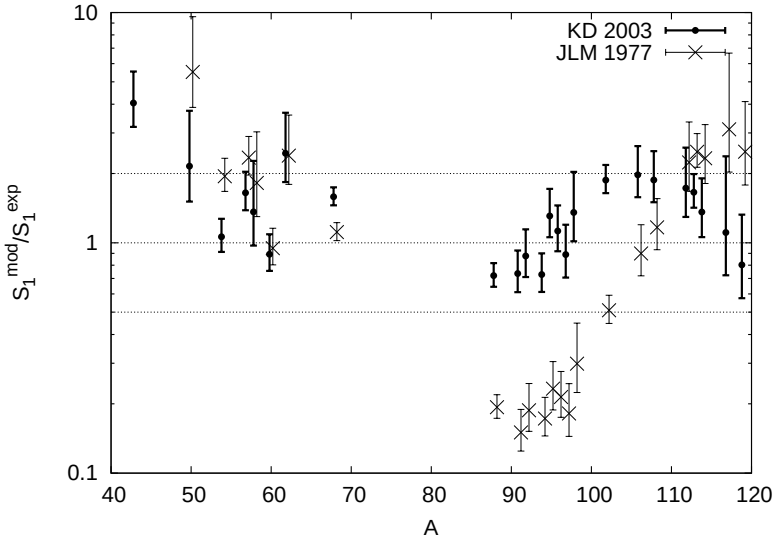

Figure 22: Ratio of P-wave strength functions modeled with the KD and JLM optical potentials to measured values taken from the Reference Input Parameter Library.

experimental values. On the other hand the JLM potential, while doing well at $A = 60$, tends to be quite low or high in the regions below and above mass 60.

With regard to the P-wave strength functions, the story is similar. Overall, the KD potential is superior, although the JLM potential does well around $A = 60$.

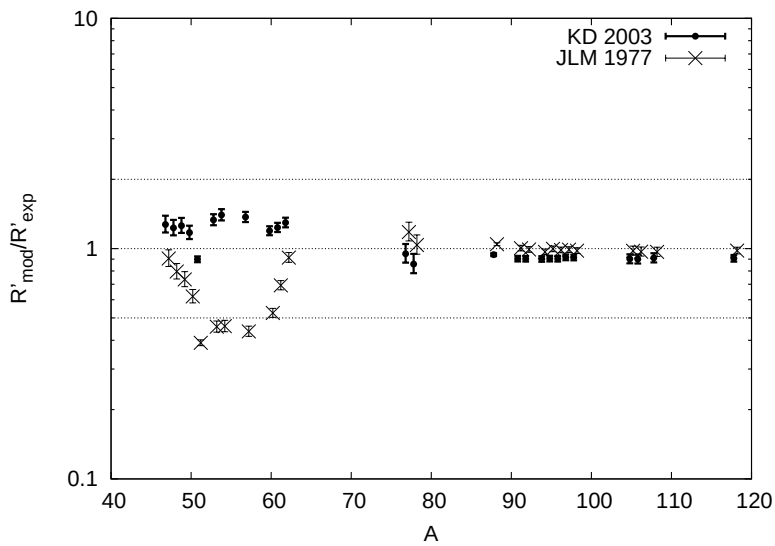

Figure 23: Ratio of potential scattering radii modeled with the KD and JLM optical potentials to measured values taken from [20].

Both potentials do well in reproducing the measured potential scattering radii, although KD does slightly better in the mass region of interest.

Overall, the S- and P-wave strength functions and potential scattering radii tend to favor KD potential over JLM. Additionally, this optical potential has proven quite effective in cross section modeling efforts in other mass regions between $A = 40$ and $A = 135$ [7, 8, 12, 13]. It is for these reasons that we have adopted the KD potential in our modeling effort.

We now make one last comparison of the neutron transmission coefficients from each of the three optical potentials considered. In Figures 24 and 25, we present the ratios of the neutron transmission coefficients from the JLM and MF potentials to those of the KD optical potential for the first six partial waves. These results are presented for the two most critical particle transmission coefficients to this study: neutrons incident on ^{59,60}Fe targets.

In both cases, the transmission coefficients for the first two partial waves (L=0 and L=1) for the JLM and KD potentials are quite similar. However, the coefficients for the third and subsequent partial waves are considerably lower for the JLM

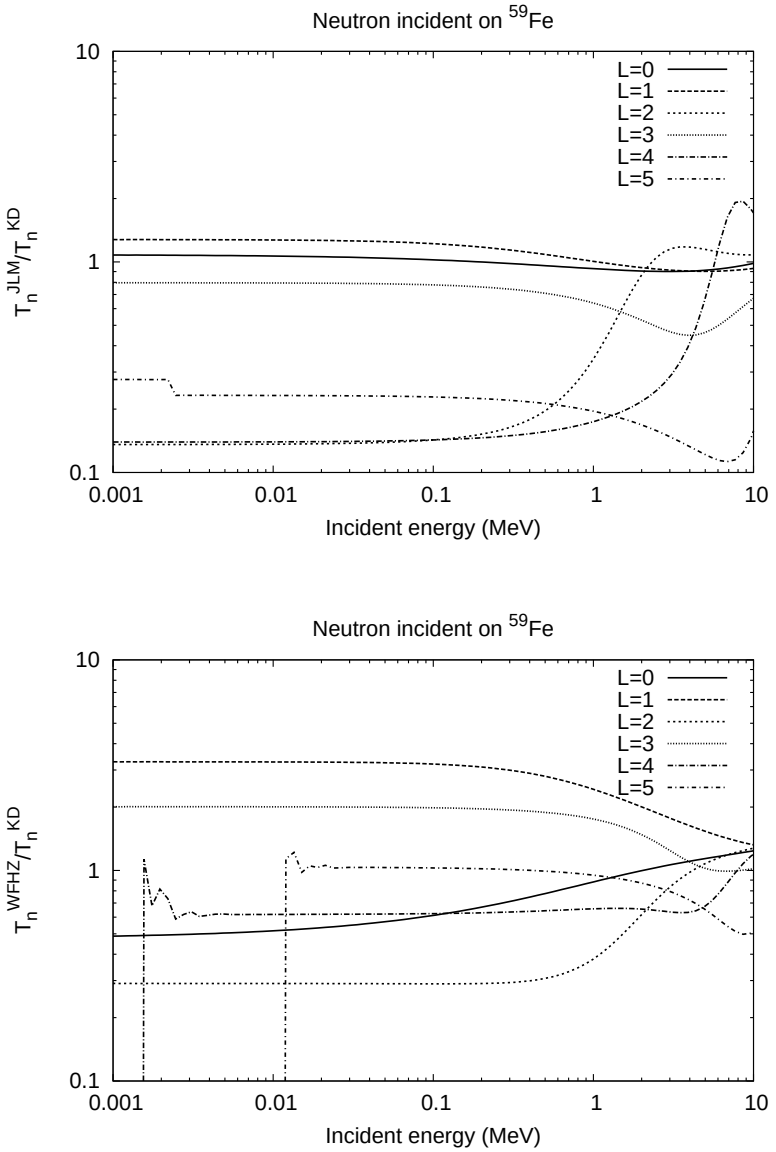

Figure 24: Ratio of transmission coefficients from the JLM and MF potentials to those of the KD potential for neutron incident on ^{59}Fe

potential below 1 MeV. This is consistent with the behavior of the calculated total neutron cross sections. When modeling reaction cross sections at low energies, it is these first few partial waves that account for most of the absorption of the incident particle into the compound nuclear state.

The comparison of the MF potential to KD yields a different result. The first

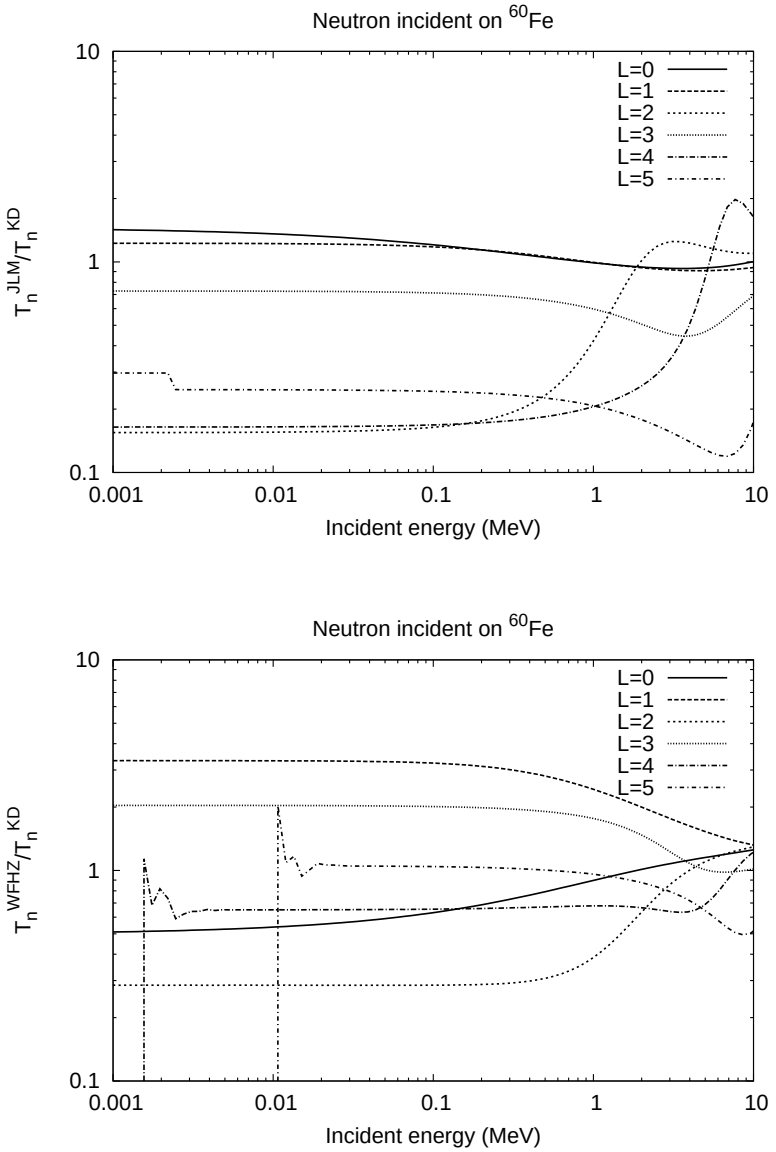

Figure 25: Ratio of transmission coefficients from the JLM and MF potentials to those of the KD potential for neutron incident on ^{60}Fe

partial wave transmission coefficient is only about half as large as its counterpart in the Koning and Delaroche potential. On the other hand, the coefficient for the second partial wave is roughly three times larger. Also, in the equivalent square well scheme, the coefficients for the L=4 and L=5 disappear completely below 2 and 10 keV, respectively. In both cases the ratios of the sums of the coefficients of

the first six partial waves exhibit an overall behavior quite similar to the ratios of the coefficients of the first partial waves.

This concludes our initial discussion regarding the neutron and proton transmission coefficients. An investigation of the sensitivity of the neutron capture cross sections to the neutron transmission coefficient will be provided in Section 7.2.2.

5.1.2 Alpha Particle Transmission Coefficients

For alpha particles we adopt the optical potential of McFadden and Satchler [17]. The transmission coefficients resulting from this optical potential are calculated using the SCAT2 subroutine built into the STAPRE code [25]. This optical potential was used by Rauscher and Thielemann in their cross sections [22]. The cross sections of Woosley, et al. [27] use the same equivalent square well potential of Michaud and Fowler [19] as was used for the neutrons and protons, except with the parameters $R_0 = 1.25\ A^{1/3}$ fm, $R_1 = R_0 + 2.3$ fm, $V_0 = 60$ MeV, and $f = 4.8$.

The inclusion of a possible alpha particle exit channel will have minimal effects on the neutron capture cross section, if any at all. The reasons for this are twofold. First, the thresholds for (n,α) reactions in this local region of the isotopic plane tend to be above the energies at which the neutron capture cross section becomes quite small. Second, in the event that a kinematic threshold does not exist, emission of alpha particles from the compound nucleus at low excitation energies is suppressed by the presence of a Coulomb barrier. In either case, alpha particle emission will only amount to a small fraction of the total reaction cross section at low excitation energies.

This can also be understood in terms of the transmission coefficients. With the Bohr independence hypothesis in mind, we recall that the transmission function for alpha particle emission is identical to the transmission function for alpha particle absorption in the incident channel. As can be seen in Figure 26, the transmission

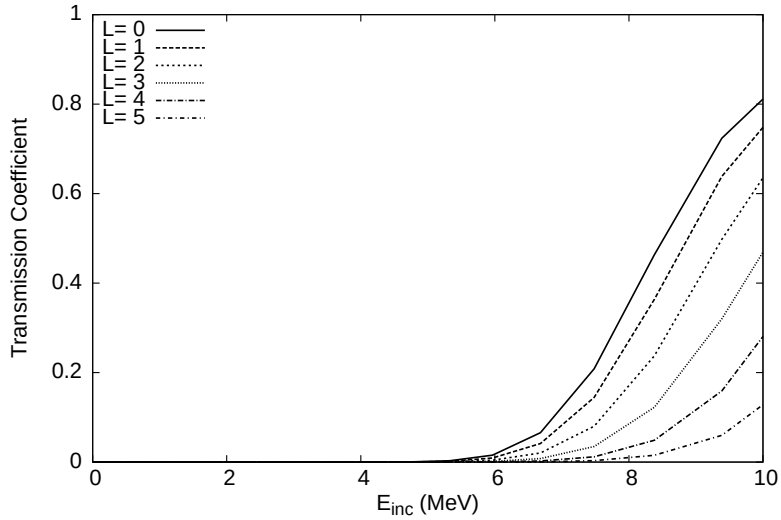

Figure 26: Transmission coefficients from the Equivalent Square Well potential for an alpha particle incident on ^{55}Cr. The transmission coefficients for the first six partial waves are shown as a function of incident energy.

coefficient for an alpha particle incident on ^{55}Cr (relevant to alpha particle emission from the ^{59}Fe compound nucleus) is negligible below 6.581 MeV (the neutron binding energy for ^{59}Fe, equal to the excitation energy of the compound nucleus formed by ^{58}Fe plus neutron at thermal incident energy). As a result, when the transmission function is calculated for energies below 6 MeV as in Equation 35, the resulting sum and integration will be quite small as well. Meanwhile, by 6 MeV of incident energy, the ^{58}Fe(n,γ)^{59}Fe cross section has dwindled to about 0.7 millibarns (it was roughly 3 millibarns at 1 MeV and 40 millibarns at 10 keV). This case is representative of the alpha particle transmission functions throughout this local region.

5.1.3 Deuteron Transmission Coefficients

In this modeling effort, we have included deuteron exit channels. As with the alpha particles, inclusion of this exit channel will make no difference in the neutron capture cross sections, since in many cases the (n,d) threshold ($\sim$ 10 MeV in this region) is at an incident energy where the neutron capture cross section is negligibly

small. Additionally, the presence of a Coulomb barrier for the exiting deuteron will suppress the cross section at low excitation energies. The deuteron exit channel is, thus, included only for the aesthetic reasons of completeness, and to a minor extent to allow some comparison with measured (n,d) cross sections in the local region of interest. A deuteron exit channel was not included in the modeling efforts of [22] and [27].

The optical potential we choose for the deuterons is that of Perey and Perey [21]. The transmission coefficients are calculated using the SCAT2 subroutine of the STAPRE code [25].

5.2 Photon Transmission Coefficients

Unlike massive particles, the photon absorption and decay widths cannot be described by an optical potential. Rather, photon decay widths are directly related to transition rates between states in the compound nucleus. These radiative transitions are described by the electromagnetic operator (in the radiation gauge), which can be written in terms of a complete set of spherical tensor operators. Breaking down the electromagnetic operator in this way is known as the "multipole expansion", and is useful when the transition energies do not exceed a few tens of MeV. The multipole operators have definite spin L_γ and parity π_γ. Operators with parity equal to $(-1)^{L_\gamma}$ are electric, and those with parity equal to $(-1)^{L_\gamma+1}$ are magnetic.

If the compound nucleus is in state μ prior to photon emission and state ν after, the transition rate is given by

$$R_\gamma^\mu(L_\gamma, m_\gamma, \pi_\gamma) = \frac{8\pi(L_\gamma+1)}{L_\gamma[(2L_\gamma+1)!!]^2}\frac{k_\gamma^{2L_\gamma+1}}{\hbar}\left|\left\langle\mu\middle|O(L_\gamma, m_\gamma, \pi_\gamma)\middle|\nu\right\rangle\right|^2 . \tag{98}$$

In this expression, m_γ is the projection of L_γ, k_γ is the photon wave number, and $O(L_\gamma, m_\gamma, \pi_\gamma)$ is the multipole operator. Such transitions are governed by selection

rules. In particular

1. $\left|J^\mu - J^\nu\right| \leq L_\gamma \leq J^\mu + J^\nu$, where J^μ and J^ν are the spins of the initial and final compound nuclear states. Transitions from $J^\mu = 0$ states to $J^\nu = 0$ states are not allowed.

2. $m^\mu = m_\gamma + m^\nu$, where m^μ and m^ν are the projections of J^μ and J^ν.

3. $\pi^\mu = \pi_\gamma \pi^\nu$, where π^μ and π^ν are the parities of the initial and final compound nuclear states.

Equation 98 needs to be averaged over initial nuclear orientations and summed over final orientations, since these orientations are random. The decay width may then be written in terms of the transition rate

$$\bar{\Gamma}^\mu_\gamma(L_\gamma, \pi_\gamma) = \hbar R^\mu_\gamma(L_\gamma, \pi_\gamma) \ , \tag{99}$$

and the photon transmission function can then be written in terms of this decay width:

$$T^\mu_\gamma(L_\gamma, \pi_\gamma) = 1 - \exp\left[-\frac{2\pi\bar{\Gamma}^\mu_\gamma(L_\gamma, \pi_\gamma)}{D(J^\nu, \pi^\nu)}\right] \tag{100}$$

where $D(J^\nu, \pi^\nu)$ is the spacing of levels with spin and parity J^ν and π^ν at the excitation energy. Generally, $T^\mu_\gamma(L_\gamma, \pi_\gamma) \ll 1$, and so

$$T^\mu_\gamma(L_\gamma, \pi_\gamma) \approx \frac{2\pi\bar{\Gamma}^\mu_\gamma(L_\gamma, \pi_\gamma)}{D(J^\nu, \pi^\nu)} \ . \tag{101}$$

Hereafter, we shall simplify the notation by using $T^\mu_\gamma(L_\gamma, \pi_\gamma) = T^\mu_{\gamma,XL}$ where X refers to the transition type (electric or magnetic) and L is the multipole order. Equation 98 can naturally be written in terms of the level density rather than level spacings.

The initial and final state wavefunctions that enter into Equation 98 are not well known. Practical constraints require that simple models be employed. In general, the resulting transition rates end up being essentially independent of the exact initial and final states, and depend primarily on the multipole type. As a result, the photon transmission coefficient may be written as

$$T^{\mu}_{\gamma,XL}(E_\gamma) = 2\pi E_\gamma^{2L+1} f_{XL}(E_\gamma) \tag{102}$$

where we are now writing the T_γ as a function of transition energy E_γ, as in Equation 34. The $f_{XL}(E_\gamma)$ appearing in Equation 102 is known as the strength function.

The first description of the strength function to emerge was that of Blatt and Weisskopf [2]. This model assumes that all transitions are single particle, and that the overlap of initial and final wavefunctions is maximal. The result is that the strength function is constant, i.e.

$$f_{XL}(E_\gamma) = \mathcal{N}_{XL} \frac{4}{3\pi} \frac{e^2}{\hbar c} \frac{1}{M_p c^2} \ . \tag{103}$$

Here, M_p is the proton mass, and $\mathcal{N}_{XL}$ is a normalization factor. Various modifications to the Blatt-Weisskopf model have been proposed [10].

Strength functions for multipole transitions can be studied via photoabsorption reactions. The statistical model photoabsorption cross section, ignoring for simplicity the sums and statistical factors, goes as $\sigma_{ph.abs.} \sim \lambda\!\!\!^{-} T_{\gamma,XL}(E_\gamma)$. We note that for incident photons $\lambda\!\!\!^{-} = \hbar c/E_\gamma$, so that the photoabsorption cross section will scale roughly as $E_\gamma^{2L-1} f_{XL}(E_\gamma)$. In the case of Blatt-Weisskopf, the photoabsorption cross section would increase with gamma ray energy, since the strength function is constant. Such an energy dependence is seen in experiments for incident gamma rays of energy less than a few MeV. However, at higher energies a giant resonance is

observed around ∼20 MeV. This indicates that the Blatt-Weisskopf model does not provide an adequate description of the photon transmission function for transition energies greater than a few MeV. This statement is further supported by the fact that this simple model violates electromagnetic sum rules [10].

The roots of the inadequacies of the Blatt-Weisskopf model may be traced back to the assumption that all transitions are single particle. In reality, nucleons tend to act, at least in part, in a collective manner. It is this semi-collective behavior that gives rise to the giant dipole resonance (GDR) seen in photoabsorption experiments. The GDR can be described using a strength function with a Lorentzian shape. The simplest such strength function (properly referred to as a simple Lorentzian or SLO [3]) may be written as

$$f_{XL,SLO}(E_\gamma) = \mathcal{N}_{XL}\frac{4}{3\pi}\frac{e^2}{\hbar c}\frac{1}{M_p c^2}\frac{\Gamma_{XL}E_\gamma}{(E_\gamma^2 - E_{XL}^2)^2 + (\Gamma_{XL}E_\gamma)^2} \ . \tag{104}$$

In this expression, M_p is the proton mass, E_{XL} is the GDR energy for multipole type XL, and Γ_{XL} is the width of the GDR. The factor $\mathcal{N}_{XL}$ is an overall normalization, which will be discussed in greater detail in the next few sections. The Lorentzian strength function is generally applied only to E1 transitions, although it has been suggested that an SLO model may also be used to describe M1 transitions [6].

The simple Lorentzian description is a definite improvement over the Blatt-Weisskopf strength function, but it also has its inadequacies. While it reproduces the giant dipole resonance behavior seen in photoabsorption cross sections, it has a tendency to overestimate these cross sections at low transition energies [14]. An improved model, known as the enhanced generalized Lorentzian or EGLO, provides a better description of the photon strength function at low E_γ. The EGLO differs from the SLO in its use of an energy dependent GDR width and an additional term

corresponding to zero transition energy. The EGLO strength function is given by

$$f_{XL,EGLO}(E_\gamma) = \mathcal{N}_{XL}\frac{4}{3\pi}\frac{e^2}{\hbar c}\frac{1}{M_p c^2} \times \left[\frac{E_\gamma \Gamma_{k,XL}(E_\gamma,T_f)}{(E_\gamma^2 - E_{XL}^2)^2 + (\Gamma_{k,XL}(E_\gamma,T_f)E_\gamma)^2} + 0.7\frac{\Gamma_{k,XL}(0,T_f)}{E_\gamma^3}\right] . \tag{105}$$

where the energy dependent width $\Gamma_{k,XL}(E_\gamma, T_f)$ is

$$\Gamma_{k,XL}(E_\gamma,T_f) = \left[\kappa + (1-\kappa)\frac{E_\gamma - \epsilon}{E_{XL} - \epsilon}\right]\frac{\Gamma_{XL}}{E_{XL}^2}\left[E_\gamma^2 + (2\pi T_f)^2\right] \tag{106}$$

with $\epsilon = 4.5$ MeV. For nuclei with $A < 148$, the factor κ is unity. For heavier nuclei, $\kappa = 1 + 0.009(A-148)^2\exp(-0.18(A-148))$.

The T_f that appears in Equations 105 and 106 is the temperature of the final state. This quantity is determined from the level density parameters. For a backshifted transition energy $\mathcal{U} = S_n - E_\gamma - \Delta$, one determines the energy dependent level density parameter (Equation 82) $a(\mathcal{U}, Z, N)$. Provided $\mathcal{U}$ is positive, the temperature is given by

$$T_f = \frac{a(\mathcal{U},Z,N)}{2}\left[1 + \sqrt{1 + 4a(\mathcal{U},Z,N)\mathcal{U}}\right] . \tag{107}$$

Otherwise, $T_f = 1/a(\mathcal{U}, Z, N)$.

Further refinements to the photon strength function have also been proposed [6]. These have not been considered in this study. The only additional modification we have considered is a possible low energy enhancement of the strength function. It has been suggested [26] that the total strength function (the sum of the strength functions for the individual multipoles) should be augmented with a term

$$f_{enh.}(E_\gamma) = \frac{A}{3\pi^2 c^2 \hbar^2}E_\gamma^{-B} \tag{108}$$

where A and B are parameters that can be measured by experiment. To date, these parameters have only been measured for ^{56,57}Fe.

At this point, we will review the photon transmission functions employed in previous cross section modeling efforts [27, 22]. Following this review, we will detail our own choice of strength functions. Finally, we will compare average radiation widths calculated with the various prescriptions (in conjunction with the appropriate level density formulation) with measured values. A detailed look at the sensitivity of the reaction rates to the photon strength function parameterization is given in Section 7.2.5.

5.2.1 Previous treatments

The cross sections of Woosley, et al. [27] employ an SLO strength function for E1 transitions and a Blatt-Weisskopf strength function for M1 transitions. Higher order transitions (E2, M2, E3, etc...) are not included. We therefore need to review their choice of E1 GDR parameters and the overall normalization for both the E1 and M1 strength functions.

Collective models predict that the energy of the peak of the GDR (E_{E1}, here) should go roughly as $A^{-1/3}$ or $A^{-1/6}$ [1]. Making a least squares fit to measured GDR energies using each power law, it was found that the GDR energy was more accurately described over a large range of nuclear masses by

$$E_{E1} = \frac{35}{A^{1/6}} \ . \tag{109}$$

The width of the GDR cannot be predicted by collective models, but is known to have some dependence on shell effects. The parameterization adopted by Woosley,

et al., again based on a least squares fit to measured widths, is

$$\Gamma_{E1} = \frac{33}{A^{1/3}} \ . \tag{110}$$

The width is reduced by a factor of 0.6 on closed shells and 0.8 for other nuclei within two nucleons of closed shells. The development of these systematics is explained in greater detail in [10]. Eventually we will see that the exact choice of GDR parameters makes very little difference in the modeled reaction rates.

The overall normalization for the E1 and M1 strength functions was determined by fitting two parameters globally to 30 keV neutron capture cross sections. At 30 keV, the neutron transmission coefficient is considerably larger than that of photons and other particles. In this case, the neutron transmission coefficient in the numerator of the Hauser-Feshbach formula will approximately cancel with the denominator. The result is that the capture cross section is mostly insensitive to the neutron transmission coefficient and highly sensitive to the photon transmission coefficient.

The development of the global normalizations is outlined in considerable detail in [10]. Ultimately it is found that

$$\mathcal{N}_{E1} = 0.25\frac{NZ}{A} \ , \tag{111}$$

$$\mathcal{N}_{M1} = \frac{9\pi}{32}\frac{1}{M_p c^2} \ . \tag{112}$$

These normalizations correspond to the strength functions in Equation 104 for E1 transitions and 103 for M1 transitions. The choice of parameterization for the E1 and M1 strength functions is somewhat significant, but the overall normalization of the strength functions is by far the most significant factor related to the photon transmission coefficient affecting the calculated neutron capture rates.

The photon transmission coefficients employed by Rauscher and Thielemann [22] are somewhat more complex than those of Woosley, et al.. They still use an SLO representation for the E1 strength function, but include an energy dependent width. The Blatt-Weisskopf model is used for the M1 transition. Again, higher order transitions are not taken into account. The omission of these transitions is justifiable, however, since the E2 strength function is generally about 50 times smaller than that of E1 transitions.

Rauscher and Thielemann use a more complex parameterization for the GDR. The peak of the GDR is located at

$$E_{E1} = \hbar c \sqrt{\frac{8J}{R^2 m^*} \left(1 + \mu - \epsilon \frac{1 + \epsilon + 3\mu}{1 + \epsilon + \mu}\right)^{-1}} \tag{113}$$

with $J = 36.8$ MeV, $R = r_0 A^{1/3}$, $m^* = 0.7 m_n$, $\epsilon = 0.0768$, $\mu = \frac{3Jr_0}{QR}$, $r_0 = 1.18$ fm, and $Q = 17.0$ MeV. This parameterization is based on a microscopic droplet model of the GDR [18]. The GDR width has an energy dependence, and is given by

$$\Gamma_{E1} = \left(\alpha E_{E1}^{\delta} + 2.35\sqrt{\frac{5}{8\pi}} E_{E1} \beta_2\right) \sqrt{\frac{E_\gamma}{E_{E1}}} \tag{114}$$

where $\alpha = 0.0205$, $\delta = 1.8$, and β_2 is the nuclear deformation parameter [24]. These parameterizations have been shown to be quite effective in replicating measured GDR energies and widths.

The overall normalizations are again determined globally, using an empirical fit to 30 keV Maxwellian averaged neutron capture cross sections. The M1 normalization is identical to that of Woosley, et al. (Equation 111). However, with a change of GDR parameters (particularly the inclusion of an energy dependent width), the

normalization for the E1 strength function now becomes

$$\mathcal{N}_{E1} = 1.2\frac{NZ}{A} \ . \tag{115}$$

5.2.2 Photon Strength Functions Based on Local Systematics

For our E1 strength function, we adopt the EGLO representation. As previously mentioned, this representation is an improvement over the SLO used in previous studies. We also include two resonances in the strength function. When available, we adopt the measured GDR parameters of [5]. Such measurements are sparse, though, and we are constrained to develop systematics.

As indicated in the previous section, the E1 GDR energy should have a dependence on the nuclear mass that goes roughly as $A^{-1/3}$ or $A^{-1/6}$. When one is considering a global systematic, such guidelines should be followed. However, we are only considering a narrow range of masses from $43 \leq A \leq 65$. In this narrow range, the mass dependence of the parameters is approximately linear, and we have developed our systematics using a least squares linear fit to the available data. For the GDR energies, we consider only the data in the mass range mentioned. For the GDR widths, the data in this mass range is scattered, and a fit to the data in a narrow mass range results in a systematic that varies far too rapidly. We have thus used all available data in determining our linear fit to the GDR widths. We have also developed systematics for the peak cross section associated with the GDR, although these values will be effectively negated by our process of normalizing the E1 strength function.

Our GDR systematics are presented in Figures 27-29. The systematics for the parameters are as follows:

$$E_{E1,1} \quad = \quad -0.1079\ A + 23.22\ ,$$

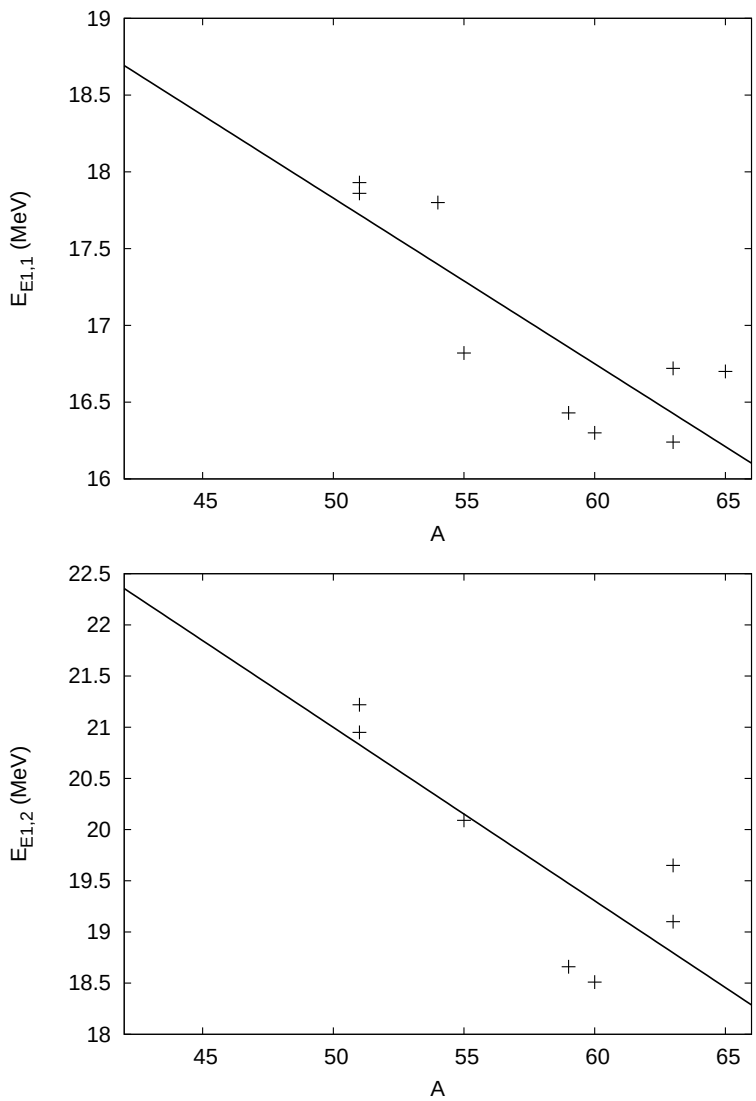

Figure 27: Systematics for E1 GDR energies. The systematics represent a linear fit to the measured GDR energies in the region of interest provided in the Reference Input Parameter Library.

$$
\begin{aligned}
E_{E1,2} &= -0.1695\ A + 29.47\ , \\
\Gamma_{E1,1} &= -0.0118\ A + 5.73\ , \\
\Gamma_{E1,2} &= -0.0134\ A + 7.39\ , \\
\sigma_{E1,1} &= 0.1050\ A + 51.25\ , \\
\sigma_{E1,2} &= -0.0365\ A + 42.84\ . \qquad (116)
\end{aligned}
$$

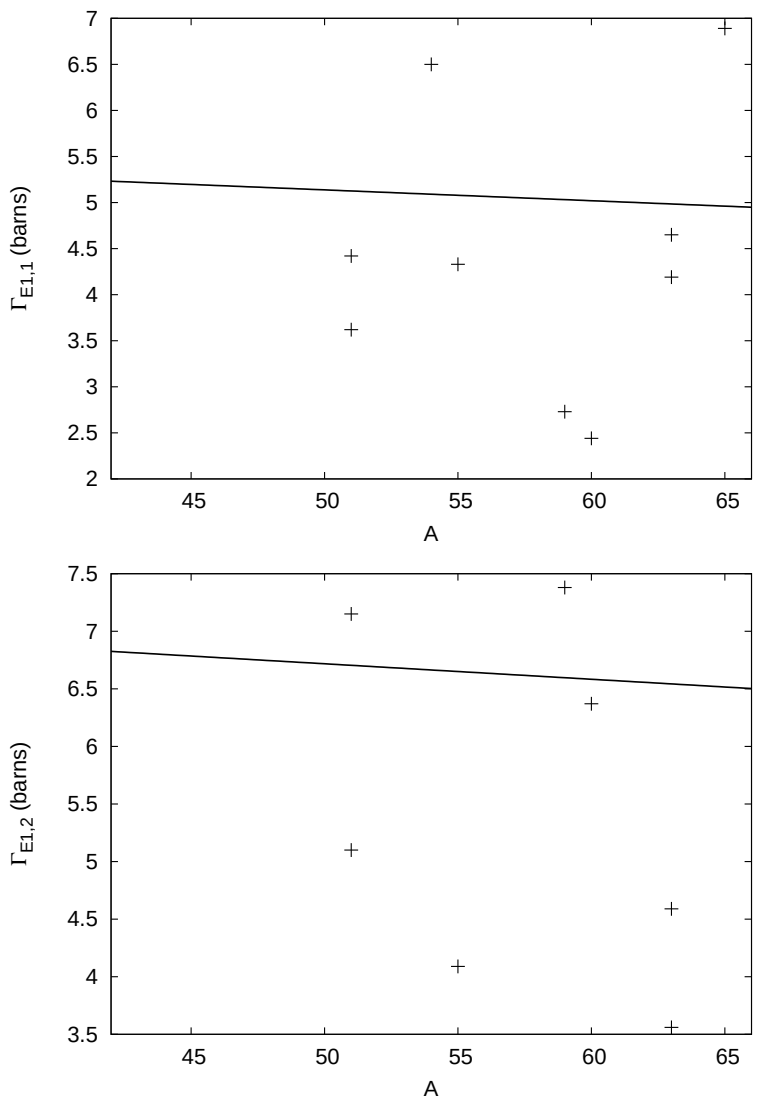

Figure 28: Systematics for E1 GDR widths. The systematics represent a linear fit to all measured GDR widths provided in the Reference Input Parameter Library.

These systematics are based on data in the local region only, and are of no value outside the range $43 \leq A \leq 65$. As mentioned, the GDR parameters only have a minor effect on the modeled cross sections, as will be detailed in Section 7.2.4.

Our process of normalizing the E1 transmission function is completely different from that of previous groups. Rather than normalizing to 30 keV Maxwellian averaged neutron capture cross sections, we consider the average S-wave radiation widths obtained from neutron resonance experiments. These radiation widths are

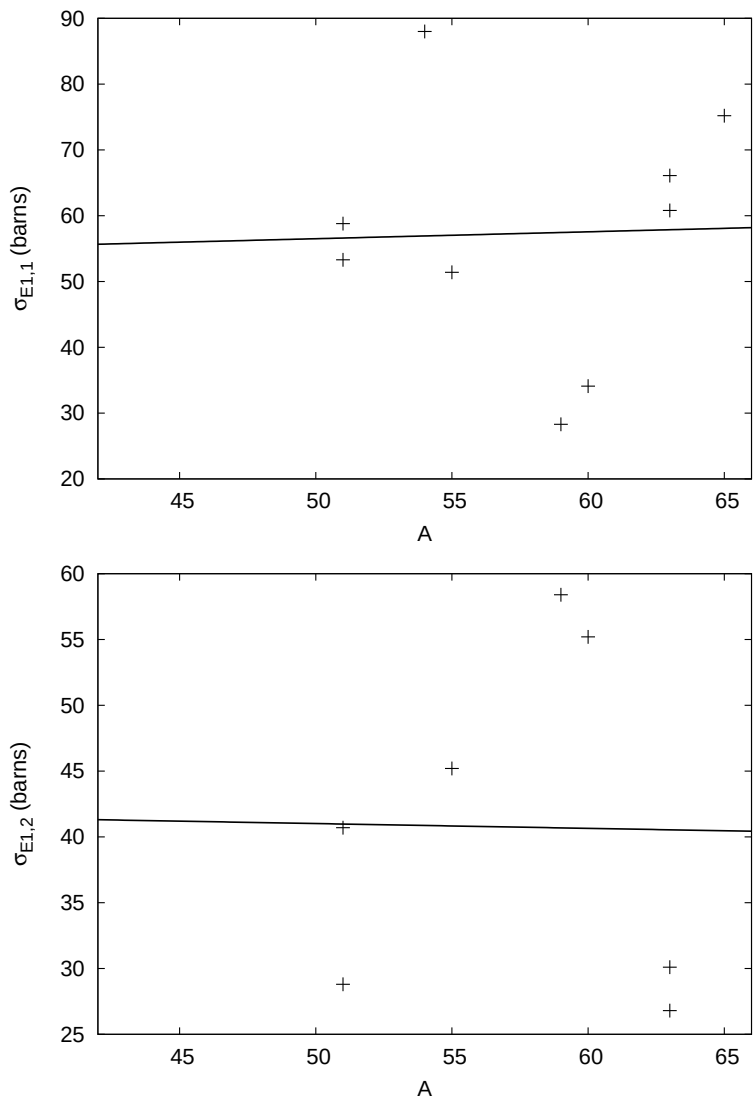

Figure 29: Systematics for E1 GDR peak cross sections. The systematics represent a linear fit to the measured GDR peak cross sections in the region of interest provided in the Reference Input Parameter Library.

related to the photon transmission coefficient, the discrete levels, and the level density. In particular,

$$\langle \Gamma\gamma \rangle_0 = \frac{J_t+1}{2J_t+1} \left\langle \Gamma\gamma \left(B_n, J_t + \frac{1}{2}, \Pi_t \right) \right\rangle + \frac{J_t}{2J_t+1} \left\langle \Gamma\gamma \left(B_n, J_t - \frac{1}{2}, \Pi_t \right) \right\rangle \ . \quad (117)$$

In this expression, J_t and Π_t are the spin and parity of the target nucleus, and B_n is the neutron binding energy (equivalent to the neutron separation energy). The

quantity $\langle \Gamma_\gamma(E, J, \Pi) \rangle$ is given by

$$\begin{aligned} \langle \Gamma\gamma(E, J, \Pi) \rangle &= \frac{1}{2\pi\rho(E, J, \Pi)} \times \\ & \sum_{XL} \sum_{J_f, \Pi_f} \Big[\sum_{\nu=1}^{\omega} T_{\gamma, XL}(E - E_\nu, J_\nu, \Pi_\nu) + \\ & \int_0^{E-E_\omega} d\epsilon \; T_{\gamma, XL}(\epsilon, J_f, \Pi_f) \rho(E - \epsilon, J_f, \Pi_f) \Big] \end{aligned} \tag{118}$$

where $\rho(E, J, \Pi)$ is the level density of the compound nucleus consisting of the target plus a neutron. Note that this quantity will change with variations to the level density prescription and discrete levels in addition to the photon transmission coefficient.

We define our E1 normalization to be

$$\mathcal{N}_{E1} = 0.26 \sigma_{E1} \Gamma_{E1} \xi \tag{119}$$

where ξ is defined as

$$\xi = \frac{\langle \Gamma\gamma \rangle_{0,\ meas.}}{\langle \Gamma\gamma \rangle_{0,\ calc.}} \ . \tag{120}$$

$\langle \Gamma\gamma \rangle_{0,\ meas.}$ is the measured average S-wave radiation width, and $\langle \Gamma\gamma \rangle_{0,\ calc.}$ is the value calculated using Equation 117 and $\mathcal{N}_{E1} = 0.26 \sigma_{E1} \Gamma_{E1}$ (Equation 119 with $\xi = 1$). Note that in this process of normalization, systematics for σ_{E1} become completely irrelevant: any change in σ_{E1} will be compensated for by a change in ξ.

Radiation widths have only been measured for a handful of nuclei, consisting primarily of stable targets plus neutron. As such, we are required to develop systematics for $\langle \Gamma\gamma \rangle_0$. Our systematics are based on data taken from [5]. In the local region of interest, even- and odd-Z nuclei appear to have a somewhat different systematic behavior, and we have consequently developed separate systematics for even-Z and odd-Z nuclei. These systematics are made by performing a least squares linear fit to

the appropriate measured values. The resulting systematics may be seen in Figure 30. The solid lines represent the systematics, which are as follows:

$$\begin{aligned} \langle \Gamma\gamma \rangle_0^{Even-Z} &= 0.8146\ A + 1707.22\ , \\ \langle \Gamma\gamma \rangle_0^{Odd-Z} &= -41.0663\ A + 3123.39\ . \end{aligned} \tag{121}$$

Higher order polynomials were also fit to the data. However, the values with small error bars drive higher order fits in such a way that the measured values around mass 60, which are important to this study, were not well replicated by the systematic. Hence we have adopted the linear fit. When they are available, we use measured values over systematic ones. This method of normalizing the E1 strength function to local systematic radiation widths has been proven successful in the past [7, 8, 9].

Capture reactions, particularly neutron capture reactions, are highly sensitive to this overall normalization. At this point we wish to emphasize that, although our method of normalizing the photon strength functions always reproduces measured $\langle \Gamma\gamma \rangle_0$, ultimately what we need to do is reproduce neutron capture cross sections, specifically Maxwellian-averaged cross sections (MACS). Both of the previous modeling efforts normalize the photon transmission coefficient by globally fitting to MACS. Eventually, we will also make a second empirical normalization to our photon strength functions to improve our performance in reproducing the recommended MACS. More will be said regarding this issue later.

For the M1 strength function, we adopt an SLO representation with GDR parameters and normalization relative to the E1 strength function as given in [6]. In particular the parameters of the M1 giant resonance are

$$\begin{aligned} E_{M1} &= \frac{41}{A^{1/3}}\ , \\ \Gamma_{M1} &= 4\ , \end{aligned} \tag{122}$$

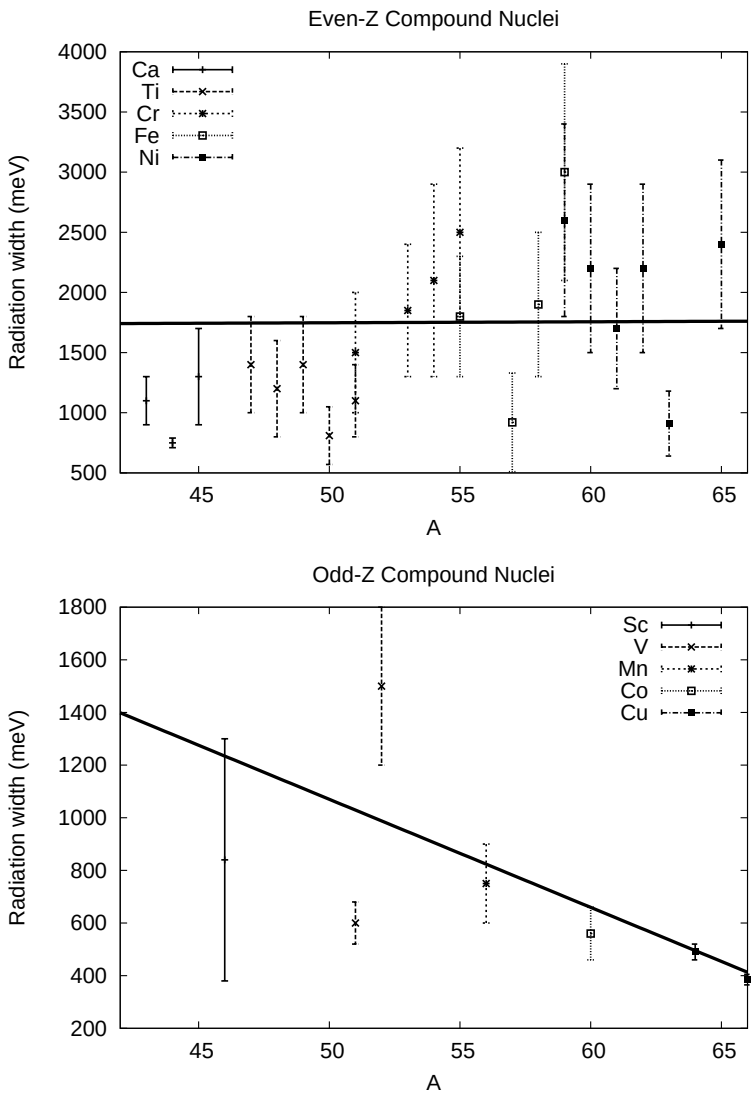

Figure 30: Systematics for average S-wave radiation widths as a function of mass number. The measured widths are from the Reference Input Parameter library. The upper and lower panels show the systematics for even- and odd-Z nuclei, respectively.

both with units of MeV. The normalization of the M1 strength function is chosen so as to satisfy

$$\frac{f_{\gamma,E1}(S_n)}{f_{\gamma,M1}(S_n)} = 0.0588\ A^{0.878}\ . \tag{123}$$

We also include higher order multipole transitions, including E2, M2, E3, and M3. For these we use Blatt-Weisskopf strength functions, normalized in such a way that

the following conditions are satisfied:

$$\begin{aligned}
\frac{f_{\gamma,E2}(S_n)}{f_{\gamma,E1}(S_n)} &= 7.2 \times 10^{-7}\ A^{2/3}\ , \\
\frac{f_{\gamma,M2}(S_n)}{f_{\gamma,E1}(S_n)} &= 2.2 \times 10^{-7}\ , \\
\frac{f_{\gamma,E3}(S_n)}{f_{\gamma,E1}(S_n)} &= 3.4 \times 10^{-13}\ A^{4/3}\ , \\
\frac{f_{\gamma,M3}(S_n)}{f_{\gamma,E1}(S_n)} &= 1.1 \times 10^{-13}\ A^{2/3}\ . \qquad (124)
\end{aligned}$$

These are the normalizations included as default in the version of the STAPRE Hauser-Feshbach code we use. The inclusion of these higher order transitions is, for the most part, purely academic. Their strength functions are several orders of magnitude smaller than the E1 strength at S_n, and remain small as the transition energy approaches zero. Hence, their contribution to the total photon transmission function is negligible.

We do not include the low energy enhancement suggested by [26] in our photon transmission coefficient. The parameters related to this enhancement have only been measured for the ^{57,58}Fe isotopes. Although one might reasonably extend these parameters to other nearby iron species, there is no reason to suspect that they would be valid for other nuclei. We consider the effect that such an enhancement may have on the ^{59,60}Fe capture rates in Section 7.2.5.

5.2.3 Average Radiation Widths

For the purposes of evaluating the overall quality of the photon transmission functions from all three cross section modeling efforts, we consider the corresponding calculated radiation widths compared to measured values. The formula for the radiation width (Equation 117) includes the photon transmission function, the level density, and a set of discrete levels. In this analysis, we maintain consistency in

Table 6: Modeled average S-wave radiation widths (in meV), listed by compound nucleus.

Nucleus	Measured Width	Woosley, et al.	Rauscher & Thielemann
^{56}Mn	750±150	381.91	722.51
^{55}Fe	1800±500	1060.90	1170.20
^{57}Fe	920±410	786.08	1088.30
^{58}Fe	1900±600	758.93	1300.10
^{59}Fe	3000±900	429.09	542.33
^{60}Co	560±100	358.42	510.03
^{59}Ni	2600±800	891.70	944.93
^{60}Ni	2200±700	516.14	971.08
^{61}Ni	1700±500	477.52	1050.60
^{62}Ni	2200±700	428.43	917.04
^{63}Ni	910±270	314.44	629.14
^{65}Ni	2400±700	217.29	430.80

our choice of input quantities, i.e., when we calculate a radiation width for a given transmission coefficient, we use the level densities and level schemes from the same modeling effort. Our process of normalizing the photon strength function ensures that our transmission coefficients will always exactly replicate the measured widths, regardless of our choice of level density and discrete levels. However, when we apply a secondary normalization to our photon strength functions in the next section, we will need to re-examine this issue.

Radiation widths calculated using the input quantities of Woosley, et al. and Rauscher and Thielemann are presented in Table 6. Values in this table are in meV. Both calculations tend to be low. Both groups are within the errors of the ^{57}Fe data, and Rauscher and Thielemann also are within the errors for ^{56}Mn, ^{58}Fe, and ^{60}Co. In some cases, particularly ^{59}Fe and the nickel isotopes, both groups underestimate the measured data considerably.

We have made a similar analysis in other isotopic regions around $A = 80$, $A = 125$, and $A = 150$. In each of these regions, the prescriptions of the two previous groups do better reproducing the measured widths than they do in this $A = 60$

region. We also note that the average radiation widths are much smaller in these other regions, as are the errors for the measurements.

In Section 7.1.3, we will investigate the sensitivity of reaction rates to variations in this normalization.

References

[1] Berman, B.L., & Fultz, S.C., 1975, Rev. Mod. Phys. **47**, 713

[2] Blatt, J.M., & Weisskopf, V.F., *Theoretical Nuclear Physics*, Wiley: New York, 1952

[3] Brink, D.M., 1955, Ph.D. Thesis, University of Oxford

[4] EXFOR: Experimental Nuclear Reaction Data, Brookhaven National Laboratory, U.S. Dept. of Energy, http://www.nndc.bnl.gov/exfor/

[5] *Handbook for calculations of nuclear reaction data*, Reference input parameter library. 1998, IAEA-TECDOC-1034

[6] *Handbook for calculations of nuclear reaction data*, Reference input parameter library-2. 2005, (http://www-nds.iaea.org/RIPL-2/)

[7] Hoffman, R.D., Dietrich, F.S., Bauer, R., Kelley, K., and Mustafa, M., "Neutron and Charged-Particle Induced Cross Sections for Radiochemistry in the Region of Bromine and Krypton", UCRL-TR-205563, LLNL, 2004 (available from http://www.osti.gov/bridge)

[8] Hoffman, R.D., Dietrich, F.S., Bauer, R., Kelley, K., and Mustafa, M., "Neutron and Charged-Particle Induced Cross Sections for Radiochemistry in the Region of Iodine and Xenon", UCRL-TR-206721, LLNL, 2004 (available from http://www.osti.gov/bridge)

[9] Hoffman, R.D., Dietrich, F.S., Bauer, R., Kelley, K., and Mustafa, M., "Neutron and Charged-Particle Induced Cross Sections for Radiochemistry in the Region of Samarium, Europium, and Gadolinium", UCRL-TR-211588, LLNL, 2005 (soon to be available at http://www.osti.gov/bridge)

[10] Holmes, J.A., 1976, Ph.D. Thesis, California Institute of Technology

[11] Jeukenne, J.-P., Lejeune, A., & Mahaux, C. 1977 Phys. Rev. **C16**, 80

[12] Kelley, K., Hoffman, R.D., Dietrich, F.S., Bauer, R., and Mustafa, M., "Neutron and Charged-Particle Induced Cross Sections for Radiochemistry for Isotopes of Scandium, Titanium, Vanadium, Chromium, Manganese, and Iron", UCRL-TR-211668, LLNL, 2005 (available from http://www.osti.gov/bridge)

[13] Kelley, K., Hoffman, R.D., Dietrich, F.S., Bauer, R., and Mustafa, M., "Neutron and Charged-Particle Induced Cross Sections for Radiochemistry for Isotopes of Yttrium, Zirconium, Niobium, Molybdenum, Technetium, and Ruthenium", 2005, in preparation

[14] Kopecky, J., & Uhl, M., 1990, Phys. Rev. **C41**, 1941

[15] Krane, K.S., *Introductory Nuclear Physics*, Wiley: New York, 1988

[16] Koning, A.J., & Delaroche, J.P. 2003, Nucl. Phys. **A713**, 231

[17] McFadden, L., and Satchler, G.R., 1966, Nuc. Phys. **84**, 177

[18] Meyers, W.D., Swiatecki, W.J., Kodama, T., El-Jaick, L.J., & Hilf, E.R., 1977, Phys. Rev. **C15**, 2032

[19] Michaud, G. & Fowler, W.A., 1970, Phys. Rev. **C2**, 2041

[20] Mughabghab, S.F., Divadeenam, M., & Holden, N.E., *Neutron Cross Sections*, Vol. 1, Academic Press, 1981

[21] Perey, C.M. and Perey, F.G., 1963, Phys. Rev. **132**, 755

[22] Rauscher, T. & Thielemann, F.-K. 2001, At. Data Nucl. Data Tables **79**, 47

[23] Raynal, J. "ECIS96", Proceedings of the Specialists' Meeting on the Nucleon Nucleus Optical Model up to 200 MeV, 13-15 November 1996, Bruyeres-le-Chatel, Franc (http://www.nea.fr/html/science/om200/raynal.pdf)

[24] Thielemann, F-K., & Arnould, M. *Proc. Int. Conf. on Nucl. Data for Sci. and Techn.* ed. K. Böckhoff (Reidel, Dordecht, 1983), 762

[25] Uhl, M., & Strohmaier, B. IRK-Vienna Report IRK-76/01 1976 (Upd. 1978)

[26] Voinov, A., et al., 2004, Phys. Rev. Lett. **93**, 142504

[27] Woosley, S.E., Fowler, W.A., Holmes, J.A. & Zimmerman, B.A. 1978, At. Data Nucl. Data Tables, **22**, 371

6 Cross Sections Modeled with Local Systematics

Having described the prescriptions used for our statistical model inputs, we now present our modeled cross sections. We begin with a short discussion on the normalization of modeled neutron capture cross sections to measured 30 keV Maxwellian averaged cross sections (MACS). Following this discussion, we present our modeled neutron capture cross sections in the region of interest compared to experimental data, followed by a comparison of our Maxwellian-averaged cross sections to a standard set of recommended values. The results for ^{59,60}Fe targets are then given. We also present results for other cross sections modeled using our preferred input parameters representing a variety of reaction channels. These calculations are compared to measured cross sections to assist in evaluating the Hauser-Feshbach input quantities. Last of all, we provide a brief discussion regarding direct reaction contributions.

6.1 Normalizing Capture Cross Sections

It is generally accepted that the statistical model can predict a neutron capture cross section to within a factor of two [6]. It is not uncommon for the modeled capture cross sections to be normalized to a standard set of Maxwellian-averaged cross sections (MACS). As its name suggests, the MACS is a cross section averaged over a Maxwellian distribution of incident particle (in this case, neutron) velocities. In general, the averaging of a cross section over a velocity distribution is given by

$$\langle \sigma \rangle_{kT} = \frac{\langle \sigma v \rangle}{\bar{v}} = \frac{\int_0^\infty \sigma v \ \Phi(v) dv}{\bar{v}} \ . \tag{125}$$

In this expression, $\bar{v}$ is the mean incident particle velocity and $\Phi(v)$ is the velocity distribution. The velocity of an incident particle is related to its energy, and one

can change the variable of integration to energy. This is convenient since the cross section is expressed as a function of incident energy.

In the simplest case, one well suited to stellar interiors, $\Phi(v)$ is assumed to be Maxwellian:

$$\Phi(v)dv = \frac{4}{\sqrt{\pi}} \left(\frac{v}{\bar{v}}\right)^2 \exp\left(-\frac{v}{\bar{v}}\right)^2 d\left(\frac{v}{\bar{v}}\right) \ . \tag{126}$$

The mean velocity of a Maxwellian distribution is a function of temperature

$$\bar{v} = \sqrt{\frac{2kT}{\mu}} \tag{127}$$

where μ is the reduced mass of the incident particle and k is the Boltzmann constant. Combining these two expressions with Equation 125, one can obtain an expression for the MACS:

$$\langle\sigma\rangle_{kT} = \frac{2}{\sqrt{\pi}(kT)^2} \int_0^\infty \sigma(E) E \exp(-E/kT) dE \tag{128}$$

where E is the center of mass energy.

The energy integral in Equation 128 is semi-infinite. One cannot accurately calculate a neutron capture cross section below a few keV. At such energies resonance structure is always apparent in the measured cross sections. This resonant behavior cannot be reproduced by a statistical model. However, the "average" behavior of capture cross sections at low energies tends to have an energy dependence going as $E^{-1/2}$ (or $1/v$). Thus, we assume that our modeled cross section has such a dependence below the last point in the energy grid. If E_{low} is the last point on the energy grid, and the cross section at E_{low} is σ_{low}, then below E_{low} the cross section is given by

$$\sigma(E < E_{low}) = \sigma_{low}\sqrt{\frac{E}{E_{low}}} \ . \tag{129}$$

In our modeling effort, we have considered incident neutron energies up to 20 MeV.

Table 7: Modeled 30 keV neutron capture MACS (in mb) compared to recommended values.

Target	Modeled MACS	Recommended MACS	Scale Factor
^{50}Cr	58.18	49±13	0.842
^{51}Cr	137.85	87±16	0.631
^{52}Cr	23.10	8.8±2.3	0.381
^{53}Cr	35.70	58±10	1.625
^{54}Cr	25.09	6.7±1.6	0.267
^{55}Mn	49.92	39.6±3.0	0.793
^{54}Fe	52.36	27.6±1.8	0.527
^{55}Fe	88.30	75±12	0.849
^{56}Fe	23.31	11.7±0.5	0.502
^{57}Fe	27.12	40±4	1.475
^{58}Fe	61.79	12.1±1.3	0.196
^{59}Co	59.84	38±4	0.635
^{58}Ni	78.59	41±2	0.522
^{59}Ni	130.90	87±14	0.665
^{60}Ni	55.43	30±3	0.541
^{61}Ni	104.14	82±8	0.787
^{62}Ni	37.13	12.5±4	0.337
^{63}Ni	70.93	31±6	0.437
^{64}Ni	63.72	8.7±0.9	0.136

The capture cross section at 20 MeV is on the order of hundreds of microbarns, whereas at energies of 30 keV it can be on the order of barns. It is thus safe to assume that above 20 MeV the capture cross section goes to zero. Using these prescriptions for incident energies outside our calculated range, we numerically evaluate Equation 128 for each of our modeled neutron capture cross sections. We interpolate between points on our energy grid using a cubic spline.

In Table 7, we present a list of MACS for our modeled cross sections at kT=30 keV compared to standard values compiled by Bao, et al. [1]. The last column of this table is a scaling factor, defined as the ratio of the standard 30 keV MACS to our modeled value. This scaling factor can be applied to the modeled cross sections (as a simple multiplicative factor) to normalize them to the recommended MACS.

While the majority of the MACS presented in Table 7 are within a factor of two

of the recommended values in [1], there are a few notable exceptions. In particular, the modeled MACS for targets ^{54}Cr, ^{58}Fe, and ^{62,64}Ni are more than a factor of two high. The most likely cause of this disagreement lies in the normalization of our photon strength functions. A quick glance at Figure 30 reveals that the measured average S-wave radiation widths for the compound nuclei ^{55}Cr, ^{59}Fe, and ^{63,65}Ni, which are the widths to which the key gamma ray transmission functions in the above cited reactions are normalized, are among the largest measured values. Additionally, the error bars on these measurements are generally in excess of 700 meV, bringing the accuracy of these quantities into question.

Furthermore, while the values in Table 7 allow us to normalize capture cross sections for which recommended MACS are available, they do not directly tell us how to normalize the cross sections on unstable targets, specifically ^{59,60}Fe. However, we can investigate systematic behavior in these quantities.

As mentioned, the source of the failure to replicate MACS lies primarily in the photon transmission coefficient. This is highly convenient, since other neutron induced reactions involving particles in the exit channels are mostly insensitive to variations in the radiative strength functions (the photon transmission coefficient is generally several orders of magnitude smaller than the particle transmission coefficients, and therefore makes a negligible contribution to the Hauser-Feshbach denominator). Hence, rather than simply applying these empirical factors to the cross sections themselves, we may apply them directly to the photon strength functions and get similar results.

Global systematics for $\langle\Gamma_\gamma\rangle_0$ [5] suggest that the quantity is not only a function of mass number but also of the resonance spacing at the neutron binding energy (D_0). When the the values in Table 7 are plotted as a function of A and D_0, they display a slight variation with mass number (decreasing with increasing A). The dependence on D_0 is more significant, and appears to be somewhat Lorentzian in shape, peaked

around $D_0 = 10$ keV. Based on this empirical behavior, we parameterize the MACS normalization as

$$\mathcal{N}(A, D_0) = \frac{\mathrm{MACS}_{\mathrm{meas.}}}{\mathrm{MACS}_{\mathrm{calc.}}} = (c_1 A + c_2)) \left[\frac{c_3 c_4^2 D_0}{\left(c_5^2 - D_0^2\right)^2 + \left(c_4 c_5\right)^2} + c_6 \right] \tag{130}$$

which has assumed a Lorentzian-like dependence on D_0 and a linear dependence on A. We determine the parameters c_i by making a weighted least squares fit to the scale factors in Table 7, using the measured error divided by our calculated value as weights. The resulting coefficients are

$$\begin{aligned} c_1 &= -0.028 \ , \\ c_2 &= 1.959 \ , \\ c_3 &= 1.747 \ , \\ c_4 &= 38.080 \ , \\ c_5 &= -1.649 \ , \\ c_6 &= 0.914 \ . \end{aligned} \tag{131}$$

The systematic, plotted against the scale factors with their associated errors, is shown in Figure 31.

Applying these secondary normalization factors to the photon strength function will destroy the perfect agreement with measured $\langle \Gamma_\gamma \rangle_0$. However, since our goal is to reproduce cross sections, not resonance parameters, this additional normalization is reasonable. We present the $\langle \Gamma_\gamma \rangle_0$ values calculated using our newly normalized radiative strength functions in Table 8. We include again the values calculated using the level densities and transmission functions of WFHZ [12] and RT [9] for comparison.

In some cases, our systematics reproduce the measured values better than the

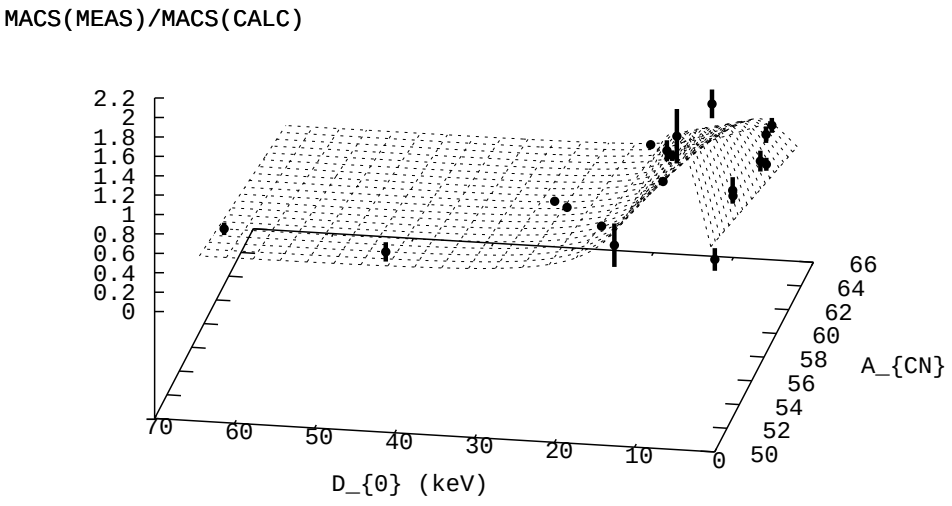

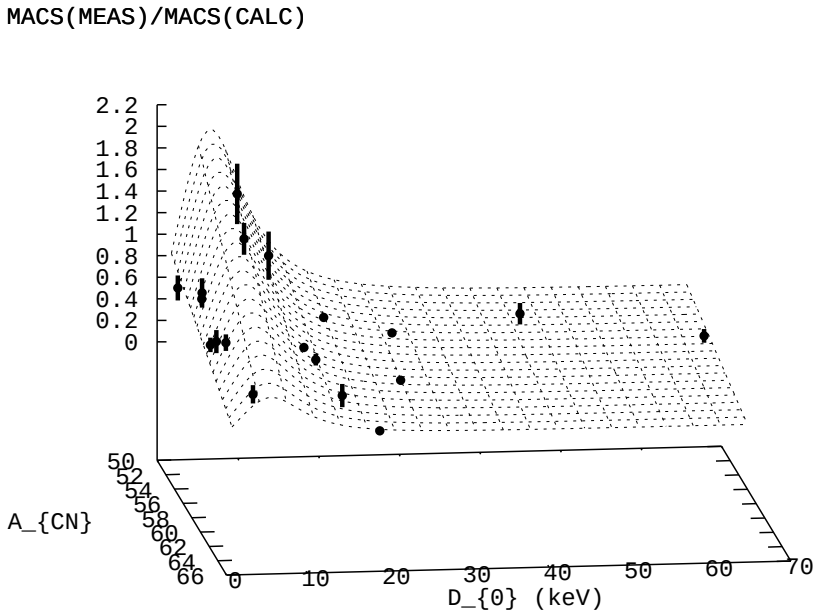

Figure 31: Secondary normalization factor applied to photon transmission coefficient to reproduce measured MACS. The data points represent the ratio of the recommended MACS to our modeled values found in Table 7.

Table 8: Calculated average S-wave radiation widths (in meV) after including the secondary normalization factors of Figure 31.

Compound Nucleus	Measured Width	WFHZ	RT	Our Calculation
^{56}Mn	750±150	381.91	722.51	676.33
^{55}Fe	1800±500	1060.90	1170.20	973.04
^{57}Fe	920±410	786.08	1088.30	340.74
^{58}Fe	1900±600	758.93	1300.10	2362.64
^{59}Fe	3000±900	429.09	542.33	929.81
^{60}Co	560±100	358.42	510.03	251.62
^{59}Ni	2600±800	891.70	944.93	1417.83
^{60}Ni	2200±700	516.14	971.08	1266.20
^{61}Ni	1700±500	477.52	1050.60	717.84
^{62}Ni	2200±700	428.43	917.04	1021.72
^{63}Ni	910±270	314.44	629.14	243.15
^{65}Ni	2400±700	217.29	430.80	360.42
g	–	2.263	1.630	1.950

other groups. In other cases they do not. To quantify the agreement with experimental values, we define a figure of merit

$$g^2 = \frac{1}{N}\sum_{i=1}^{N}\left(\frac{y_i - x_i}{\sigma_i}\right)^2 \tag{132}$$

where y_i are the measured data with errors σ_i, and x_i are the calculated values. The resulting figures of merit for the reproduction of the radiation widths listed in Table 8 are 2.263 for WFHZ, 1.630 for RT, and 1.950 for our latest effort. So RT does a slightly better job in reproducing these widths. However, as we have mentioned before, it is more important for our purposes to reproduce cross sections than it is to reproduce resonance parameters.

Having made this secondary normalization to the photon strength function, we recalculate our cross sections and MACS. The results, compared to WFHZ and RT, are presented in Table 9. Included in this table is the figure of merit for the MACS data, as defined in Equation 132. For reference, the figure of merit for our

Table 9: Calculated neutron capture MACS from various modeling efforts compared to recommended values, with the secondary photon transmission coefficient normalization applied to our calculation.

Target	Recommended MACS	WFHZ	RT	Our Calculation
^{50}Cr	49 ± 13	34	44.8	58.7
^{51}Cr	87 ± 16	63	86.0	131.1
^{52}Cr	8.8 ± 2.3	12	16.7	12.2
^{53}Cr	58 ± 10	24	26.0	54.5
^{54}Cr	6.7 ± 1.6	7.2	9.4	12.0
^{55}Mn	39.6 ± 3.0	28	35.5	46.3
^{54}Fe	27.6 ± 1.8	28	46.5	34.7
^{55}Fe	75 ± 12	46	83.9	85.9
^{56}Fe	11.7 ± 0.5	19	26.2	11.0
^{57}Fe	40 ± 4	21	30.3	33.9
^{58}Fe	12.1 ± 1.3	9.5	12.9	26.1
^{59}Co	38 ± 4	36	51.3	30.1
^{58}Ni	41 ± 2	29	50.5	54.3
^{59}Ni	87 ± 14	72	92.4	83.8
^{60}Ni	30 ± 3	20	33.2	30.6
^{61}Ni	82 ± 8	37	77.8	57.9
^{62}Ni	12.5 ± 4.0	12	19.2	13.3
^{63}Ni	31 ± 6	24	36.5	44.5
^{64}Ni	8.7 ± 0.9	6.1	10.1	15.2
g	–	4.399	7.349	3.823

MACS prior to the secondary normalization is 18.762. Renormalizing the radiative strengths to the measured MACS values improves our ability to reproduce capture cross sections as one would expect. We now do a better job replicating these values than either of the previous groups.

6.2 Neutron Capture Cross Sections

We now present our statistical model calculations of the neutron capture cross section on various stable targets in the local region of interest. These cross sections were modeled using our preferred Hauser-Feshbach inputs as described in the previous three sections. In each of the plots that follow, our cross section is represented with

a thick solid line. The dashed line represents the cross section as calculated using the NON-SMOKER code [8] used by RT [9]. The dotted line represents the cross section as calculated using the CRSEC code [11] used in [10]. Wherever isomeric states exist, they are treated as both a possible final state of the residual nucleus and as targets. Unless otherwise noted, the cross sections presented in this section are "activation" cross sections, i.e. the total cross section going to all possible final states in the product nucleus.

The measured data presented in these plots is a compilation of all data available from [3] at the time the calculations were carried out in February of 2005. For purposes of clarity, labels for the individual data sets have been left off these figures.

A common feature noticeable in the measured data is the dominance of resonance type behavior below ∼200 keV. This is to be expected in this region of the isotopic plane, since the level densities are relatively low for small excitation energies. The validity of a statistical model calculation in these resonance regions is questionable. However, when measured data is not available, modeled cross sections are all that we have.

Ultimately, we will only be making use of the reaction rates for neutron capture onto ^{59}Fe, and ^{60}Fe. Our purpose in presenting results for other reactions is to aid in the evaluation of our Hauser-Feshbach input quantities. If we are consistently successful at reproducing reactions with measured data, it gives us confidence in our calculations for reactions with unstable targets.

Figure 32 begins with our modeled cross sections on stable chromium targets. For these targets, all of the data is in the resonance regions, and it is difficult to gauge whether any single calculation does "better" than the others. Our cross sections tend to be higher than those of CRSEC and NONSMOKER. The results from all three modeling efforts for the chromium targets are similar, with the exception of ^{53}Cr(n,γ)^{54}Cr where our calculation is significantly larger. This is consistent with

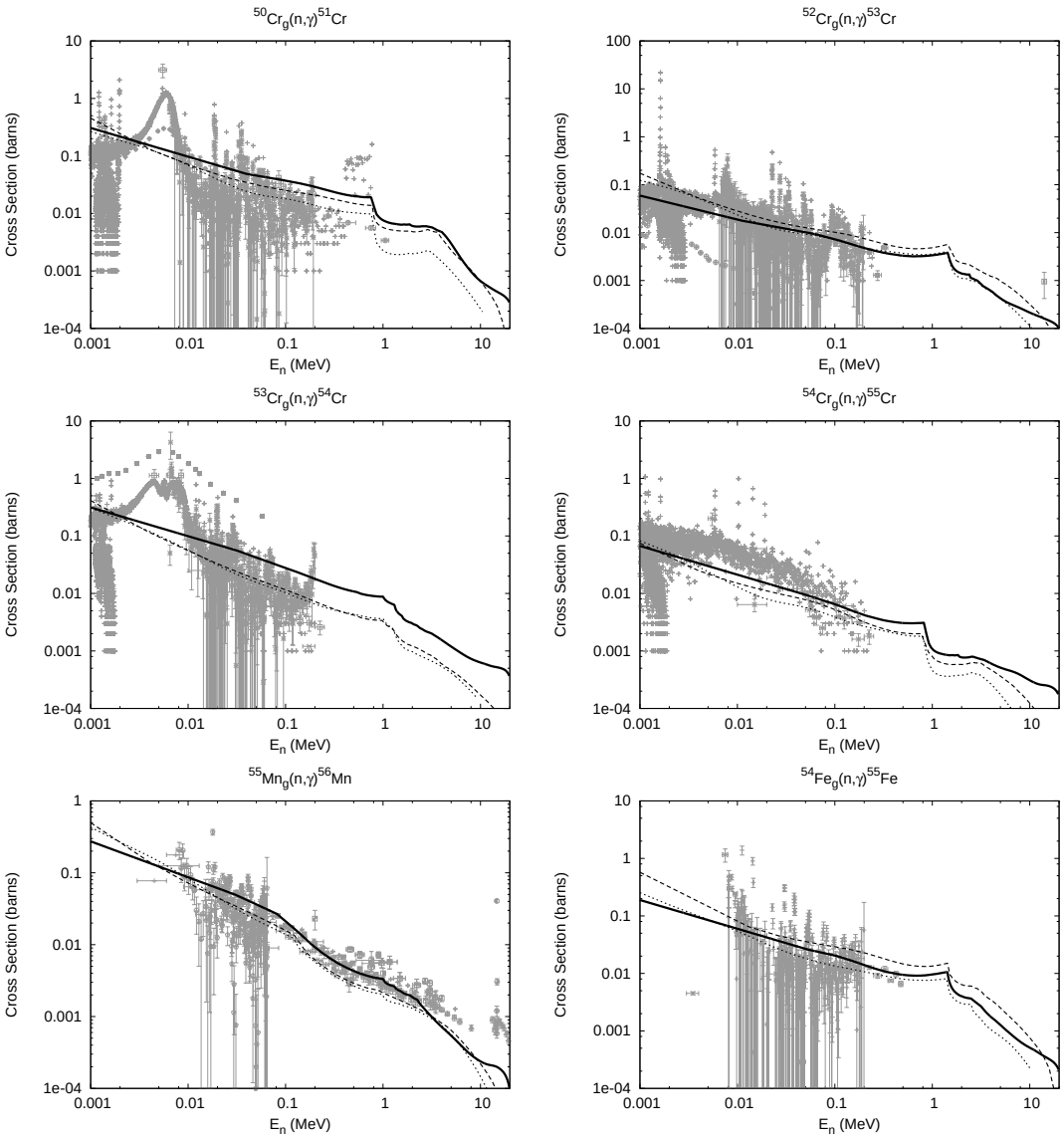

Figure 32: Modeled neutron capture cross sections compared to measurements. The solid lines represent modeled cross sections from the present work. Dotted lines represent cross sections calculated by the CRSEC code used by WFHZ. Dashed lines represent cross sections calculated with the NON-SMOKER code used by RT. Measured cross section data represents all cross section data available in the EXFOR libraray for the reaction as of 2004.

the MACS for this reaction in Table 9, where our result is within the errors of the recommended value. For ^{55}Mn(n,γ)^{56}Mn$_g$, all three calculations do reasonably well and are within a factor of two of each other.

The results for neutron capture by stable iron targets are similar to those for

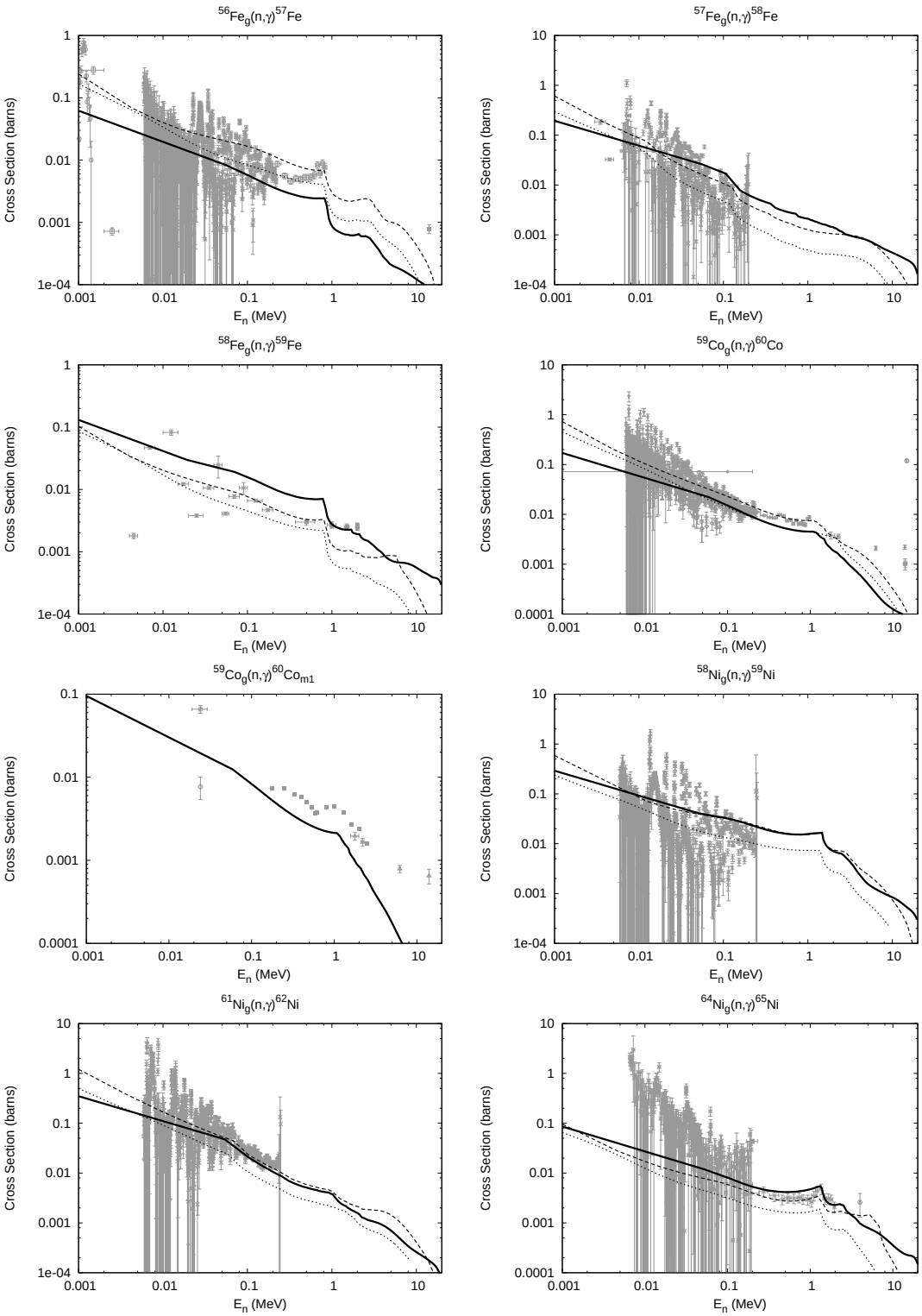

Figure 32: (continued)

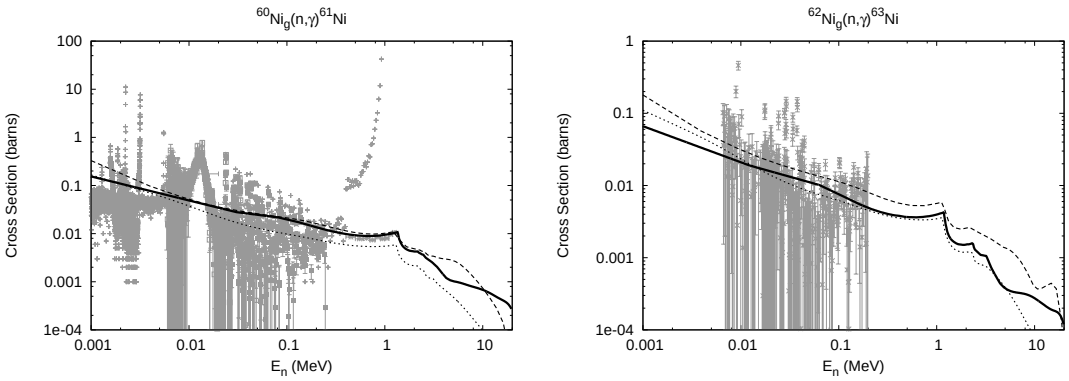

Figure 32: (continued)

chromium targets. Most of the measurements lie in the region where the effects of individual resonances are seen, making a qualitative statement regarding the reproduction of the cross section difficult. For ^{54}Fe$_g$(n,γ)^{55}Fe$_g$, the three calculations are quite similar. Our cross section for ^{56}Fe$_g$(n,γ)^{57}Fe$_g$ is lower than the other two, and considerably lower than the NON-SMOKER calculation. Our calculation is superior in reproducing the recommended MACS for this reaction (see Table 9). Our ^{57}Fe$_g$(n,γ)^{58}Fe$_g$ cross section is similar to that produced by the NON-SMOKER code, and significantly larger than that from CRSEC above 20 keV. Last of all, our ^{58}Fe$_g$(n,γ)^{59}Fe$_g$ is significantly larger than both previous calculations. We overpredict the MACS for this reaction. The source of this overprediction most likely lies in the photon transmission coefficient. Prior to the secondary normalization described in Section 6.1, the normalization for the ^{59}Fe radiative strength function was based on an experimentally measured radiation width of 3000$\pm$900 meV. This value is quite large compared to other measured widths, and the error bars are roughly 30% of the central value. Our initial calculation based on this value overpredicted the MACS by nearly a factor of six. The resulting ratio of measured to calculated MACS is considerably smaller than that of nearby nuclei, as may be seen in Figure 31, and lies below the systematic normalization represented by the dotted surface. Since we only use systematic values in the secondary normalization, an overpre-

diction of this particular cross section is expected. Since the ^{59,60}Fe capture cross sections are based initially on systematic values for the radiative strength function normalization (as opposed to a measured value such as that used for ^{58}Fe), it is not expected that this problem of gross overprediction will affect these two key cross sections.

The residual nucleus for the ^{59}Co(n,γ)^{60}Co reaction has an isomer, and a limited amount of experimental data for the cross section to the isomeric state is available. The CRSEC and NONSMOKER codes do not separate the excitation function into populations of the ground and metastable states. Similar to ^{55}Mn, all three calculations are fairly similar for this reaction. Our calculation appears to lie slightly below the data. This is true for both the activation cross section and the cross section to the isomer in ^{60}Co.

Figure 32 concludes with our modeled cross sections on stable nickel targets. While all three calculations are generally similar, our results tend to be in closer agreement with the NON-SMOKER cross sections.

Overall, our modeling reproduces measured (n,γ) cross sections reasonably well. Additionally, Table 9 indicates that our present effort is superior in modeling neutron capture cross sections around 30 keV.

6.3 Maxwellian-Averaged Capture Cross Sections

The MACS provided in [1] are accompanied by recommended values for the MACS at energies other than 30 keV. Specifically, these values are listed in their Table II. While estimated errors are given for the recommended values at $kT = 30$ keV, none are given for the other values of kT.

In Figure 33 we compare our calculated MACS to the recommended values in [1], represented by the gray circles. We also include MACS calculated from NONSMOKER and CRSEC cross sections, represented by the dashed and dotted

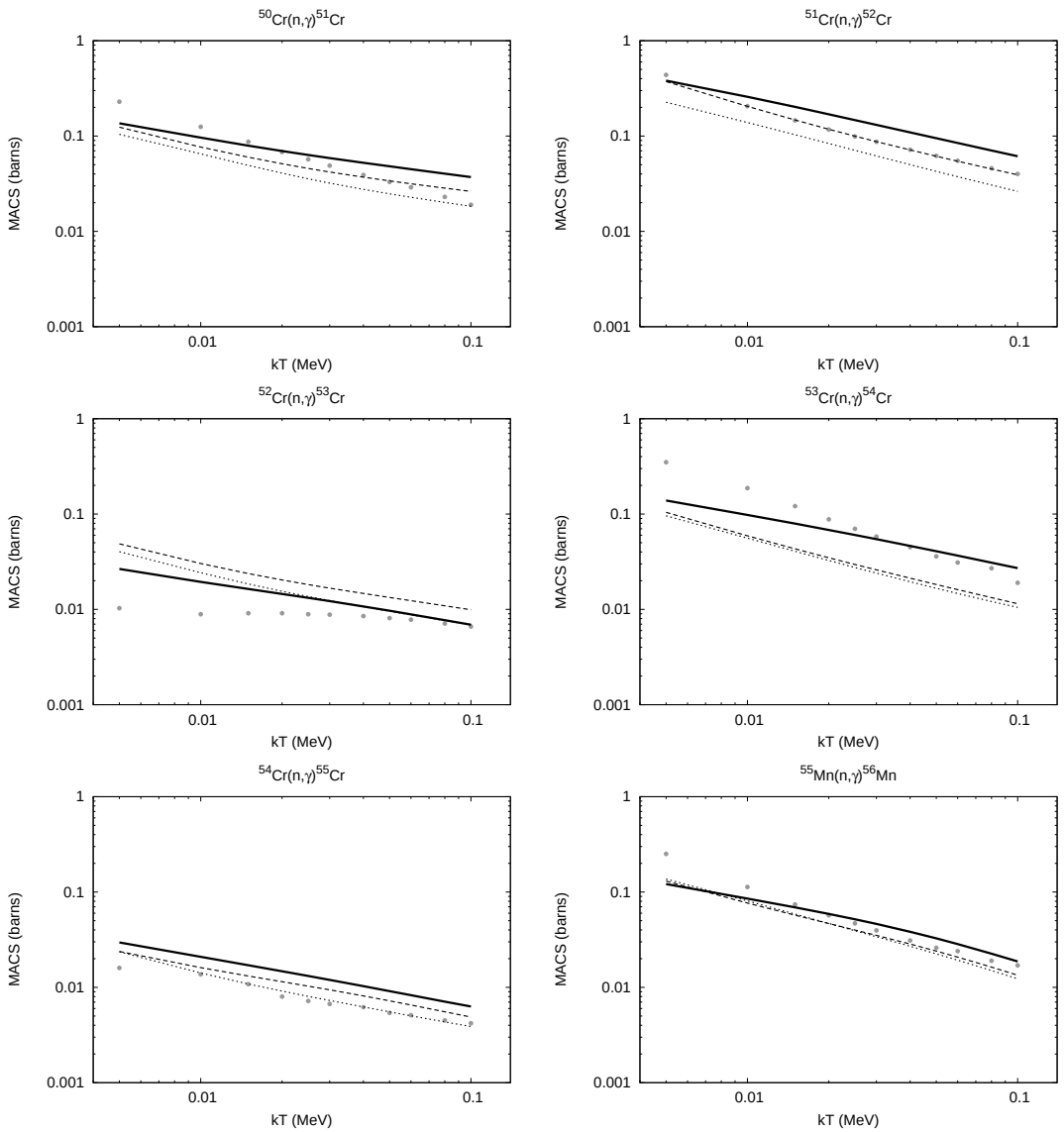

Figure 33: Modeled neutron capture MACS compared to recommended values from [1]. The solid lines represent MACS from the present work. Dotted lines represent MACS calculated from cross sections produced by the CRSEC code used by WFHZ. Dashed lines represent MACS calculated from cross sections produced by the NON-SMOKER code used by RT.

lines, respectively. Our calculation is represented by the heavy solid line. We have already seen how well our calculation compares against the 30 keV MACS in Table 9. Our purpose in making the present comparison is to see how the calculations compare to the recommended MACS at other values of kT.

The relative magnitudes of the various MACS are consistent with the cross

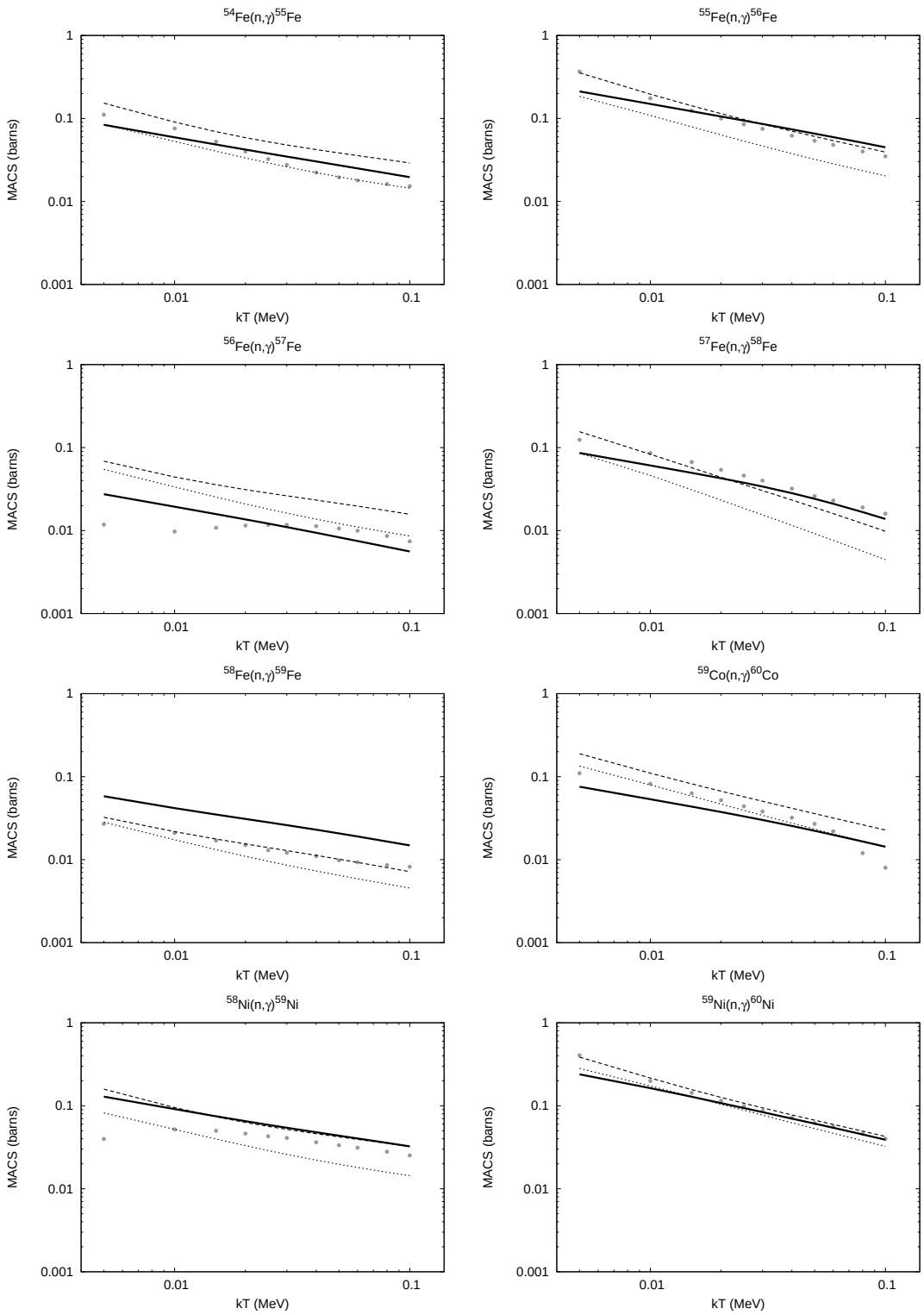

Figure 33: (continued)

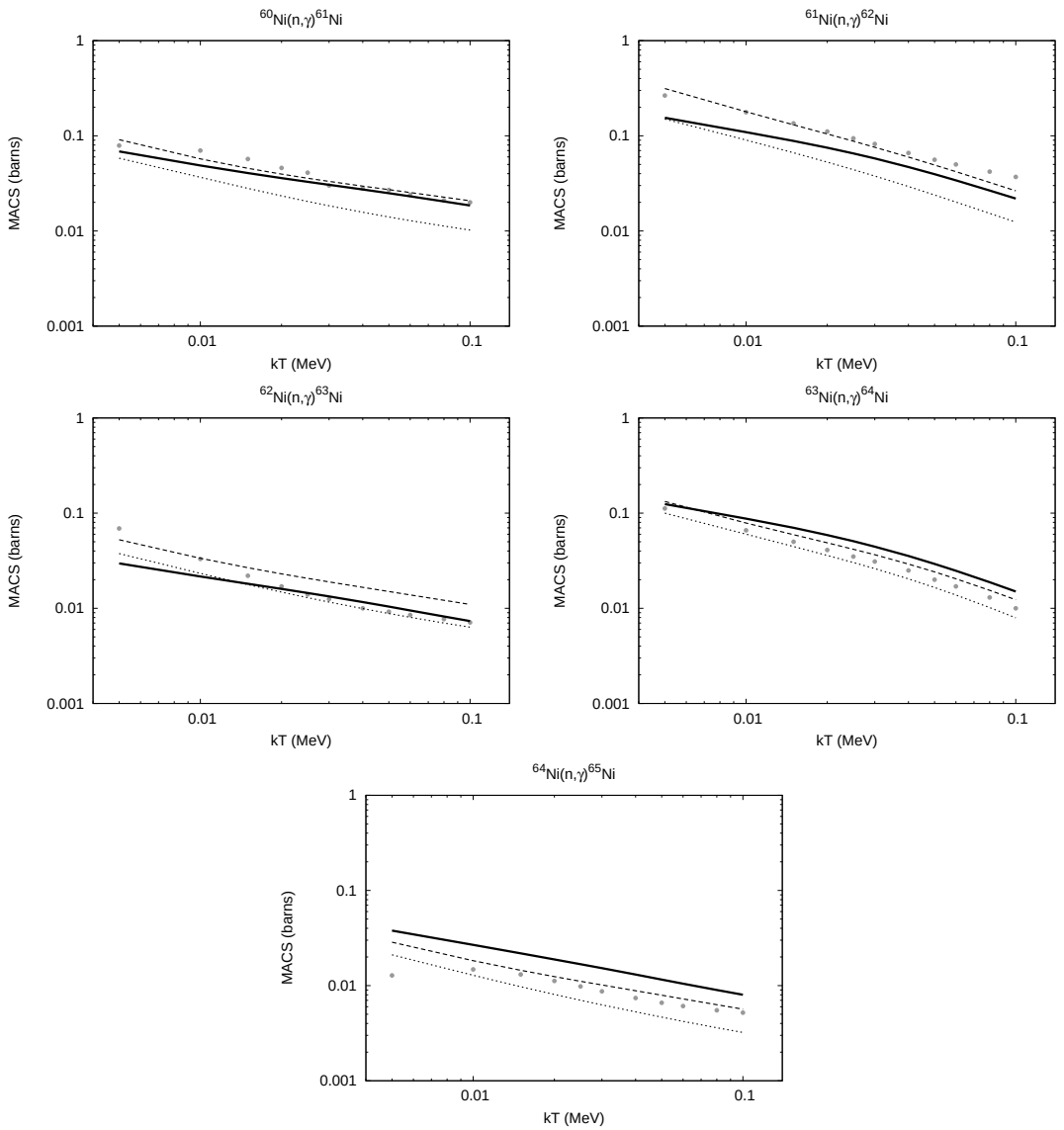

Figure 33: (continued)

sections in Figure 32. We note that the shape of the MACS is generally well reproduced by our calculation, particularly for $kT > 30$ keV. We further note that some of the recommended values in [1] are based on the NONSMOKER calculations. Specifically, these are the MACS for ^{51}Cr, ^{55}Fe, and ^{59}Ni.

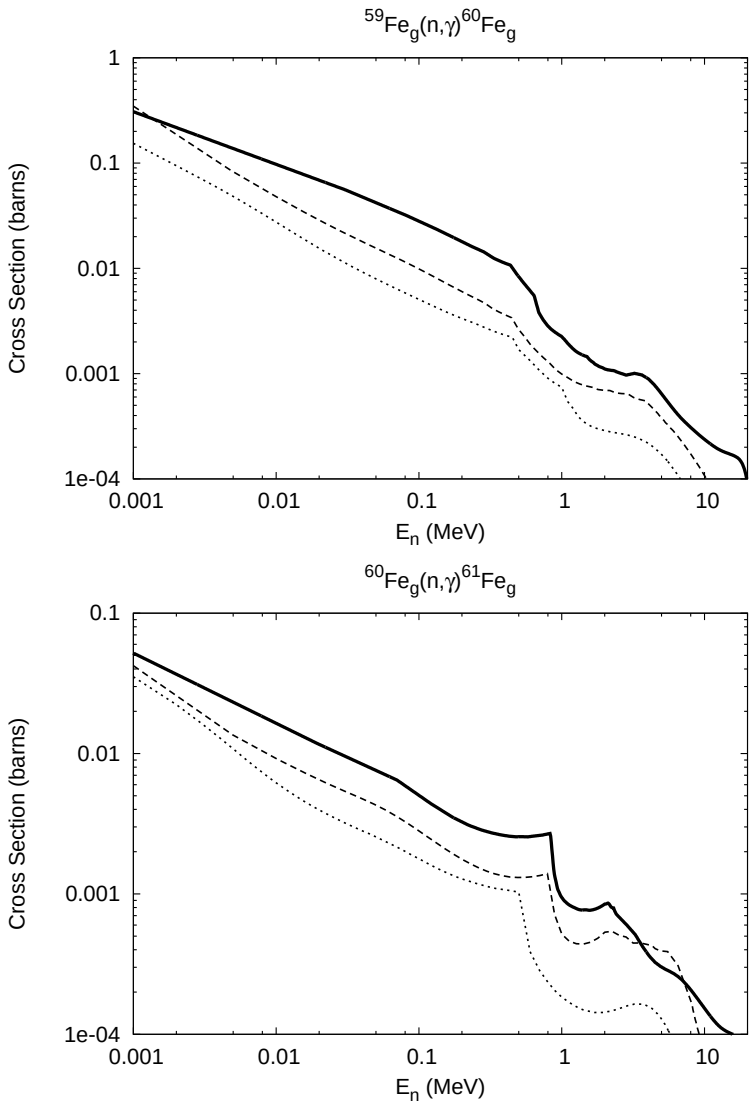

Figure 34: Modeled neutron capture cross sections for ^{59,60}Fe targets. The solid lines represent modeled cross sections from the present work. Dotted lines represent cross sections calculated by the CRSEC code used by WFHZ. Dashed lines represent cross sections calculated with the NON-SMOKER code used by RT.

6.4 Results for ^{59}Fe and ^{60}Fe Capture Cross Sections

We now present the results for the two key cross sections in this study, namely ^{59}Fe$_g$(n,γ)^{60}Fe and ^{60}Fe$_g$(n,γ)^{61}Fe. In Figure 34, our calculation is represented by a heavy solid line. The calculations from the NONSMOKER and CRSEC codes are represented by dashed and dotted lines, respectively.

For both cross sections our calculation is higher than the previous calculations. The larger cross section for $^{59}\mathrm{Fe}_g(\mathrm{n},\gamma)^{60}\mathrm{Fe}_g$ would supposedly result in a larger production of ^{60}Fe. Our cross section at 30 keV (the approximate energy of most importance to the *s* process) is roughly a factor of three larger than that of the NONSMOKER code. However, $^{60}\mathrm{Fe}_g(\mathrm{n},\gamma)^{61}\mathrm{Fe}_g$ is also larger than the previous calculations. This larger cross section out of ^{60}Fe would result in a higher rate of depletion.

Perhaps a more useful quantity to consider is the ratio of the $^{59}\mathrm{Fe}_g(\mathrm{n},\gamma)^{60}\mathrm{Fe}$ and $^{60}\mathrm{Fe}_g(\mathrm{n},\gamma)^{61}\mathrm{Fe}$ cross sections presented in Figure 35. One might expect ^{60}Fe production to scale roughly with this ratio. The line types correspond to the same calculations as in the previous figure, i.e. dashed lines represent the calculations from NONSMOKER and dotted lines represent those from CRSEC. We note that our calculation results in a larger ratio at 30 keV, suggesting that the production of ^{60}Fe may be higher when our calculated cross sections are used. However, there are many factors which go into the production of ^{60}Fe. A discussion on the effects these rates have in nucleosynthesis will be provided in Section 8.

6.5 Other Reactions with Stable Targets

We now present results for reactions other than neutron capture modeled in the local region of interest. Included on the following figures is our calculation, represented by a solid line, as well as the calculations from NONSMOKER and CRSEC, represented by dashed and dotted lines, respectively. The experimental data in these figures is a compilation of all data available from [3] as of February 2005. Labels for individual data sets have been omitted for clarity. Only data between 1 keV and 20 MeV is included.

In the previous modeling efforts of [12] and [9], all reactions involving a single neutron, proton, or alpha particle in the incident and exit channels were included,

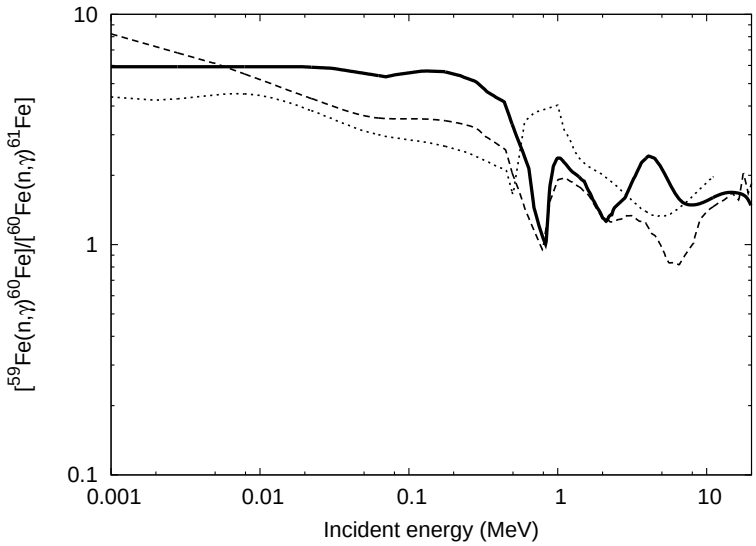

Figure 35: Ratio of ^{59,60}Fe neutron capture cross sections. The solid line represents the ratio from cross sections in the present work. Dotted lines represent the ratio from the CRSEC code used by WFHZ. Dashed lines represent the ratio from the NON-SMOKER code used by RT.

with the exception of elastic and inelastic scattering. Capture reactions were modeled for each of the three types of incident particles. In the present work, we consider primarily reactions with incident neutrons. However, we have included several additional exit channels. We also consider (p,n) reactions, which are highly sensitive to the level density and discrete level structure of the residual nucleus.

Many of the reactions presented in the following figures have thresholds well above the typical incident energies found in stellar environments. Our purpose in modeling these cross sections is to aid in the evaluation of our input quantities, particularly the particle transmission coefficients and level densities. We note that the photon transmission coefficient is much smaller than those for particles (particularly neutrons), so that the overall normalization of the radiative strength function, perhaps the most critical input parameter in neutron capture reactions, will have a negligible effect on reactions with particles in the exit channel.

The CRSEC code only calculates cross sections up to ∼10 MeV, while our calcu-

lations are carried up to 20 MeV. Also, the NONSMOKER and CRSEC calculations only include activation cross sections. In cases where there are isomers in the residual nucleus, our calculations also include the amount of cross section going to the ground state and isomers. We also have the option of treating isomers as targets, although no measured cross section data is available for such reactions. Activation cross sections are indicated on these figures by the absence of the final state identifiers g or $m1$ on the residual nucleus in the plot title.

Figure 36 presents the modeled (n,p) cross sections. Some general trends are notable. From threshold up to about 10 MeV, the three calculations tend to be quite similar. Between 10 and 15 MeV, the measured cross sections begin to taper off as additional exit channels open. In many of these (n,p) cross sections, the calculation from NONSMOKER continues to rise after the measured data has reached its peak. Overall, our calculation tends to be more consistent with the measured data than those from CRSEC and NONSMOKER.

The ^{58}Fe(n,p)^{58}Mn, ^{58}Ni(n,p)^{58}Co, ^{60}Ni(n,p)^{60}Co, and ^{62}Ni(n,p)^{62}Co cross sections have residual nuclei with isomers. In the case of ^{58}Fe(n,p)^{58}Mn, it appears that our distribution of the cross section to the ground state and first isomer of ^{58}Mn is somewhat inaccurate. However, only a single data point exists for the cross section to the isomer, and there is considerable disagreement in the data for the cross section to the ground state. It is possible that some of the ground state cross section data may actually be misidentified activation data, as the magnitude of these data points is similar to those for activation.

For the ^{58}Ni(n,p)^{58}Co reaction, it also appears that our distribution of cross sections to the ground state and isomers of the residual nucleus is questionable. The measured data seems to be far more consistent than in the case of ^{58}Fe(n,p)^{58}Mn. However, ^{58}Co has two isomeric states, and it is likely that the measured cross sections reportedly going to the first isomer are in fact the cross section going to

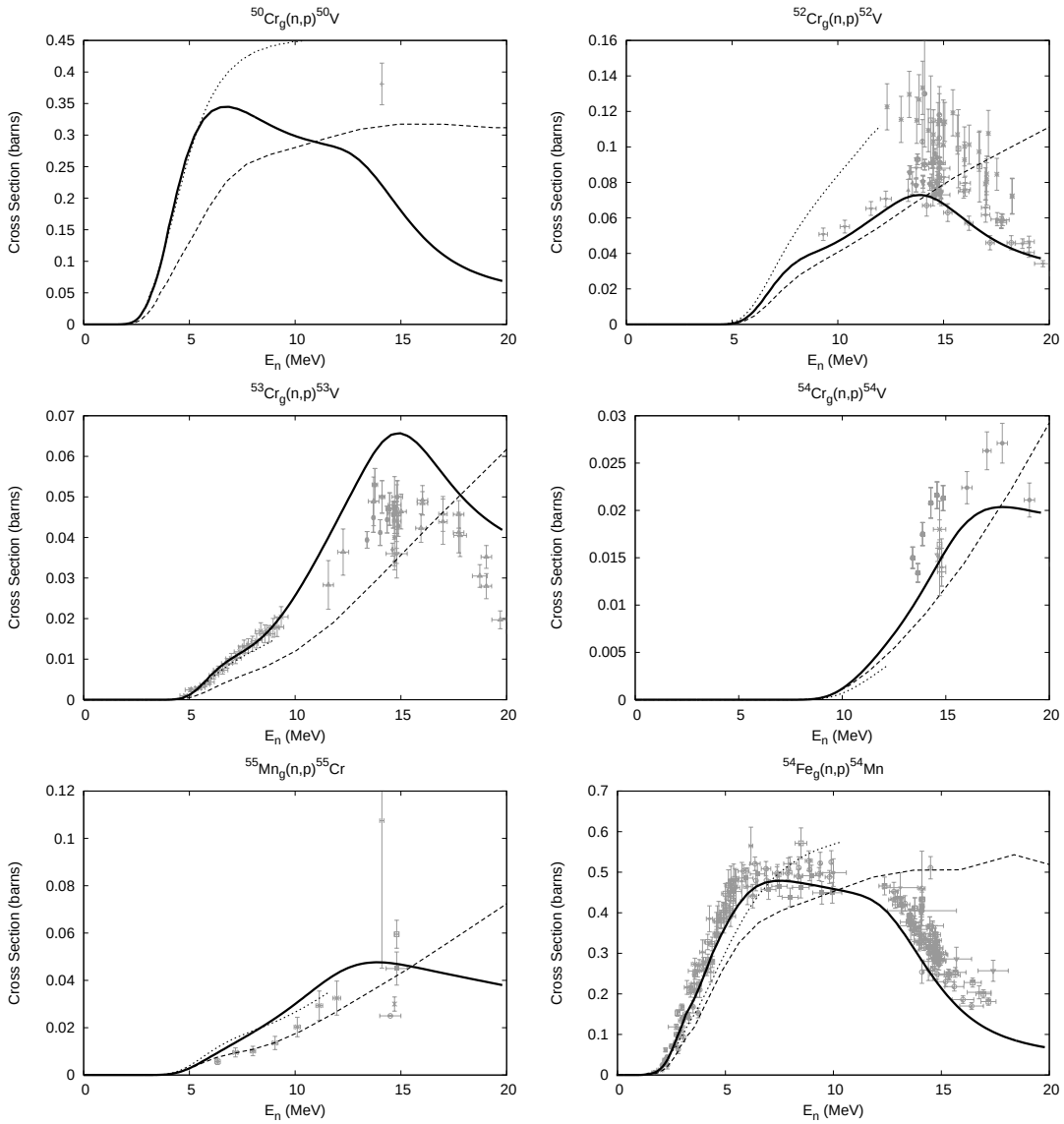

Figure 36: Modeled (n,p) cross sections compared to measurements. The solid lines represent modeled cross sections from the present work. Dotted lines represent cross sections calculated by the CRSEC code used by WFHZ. Dashed lines represent cross sections calculated with the NON-SMOKER code used by RT. Measured cross section data represents all cross section data available in the EXFOR libraray for the reaction as of 2004.

both isomers. Furthermore, the higher ground state cross section data is roughly equal to data reported as activation cross sections, and it is possible that the final state of these measurements was misidentified.

The various (n,α) calculations are presented in Figure 37. The results are similar

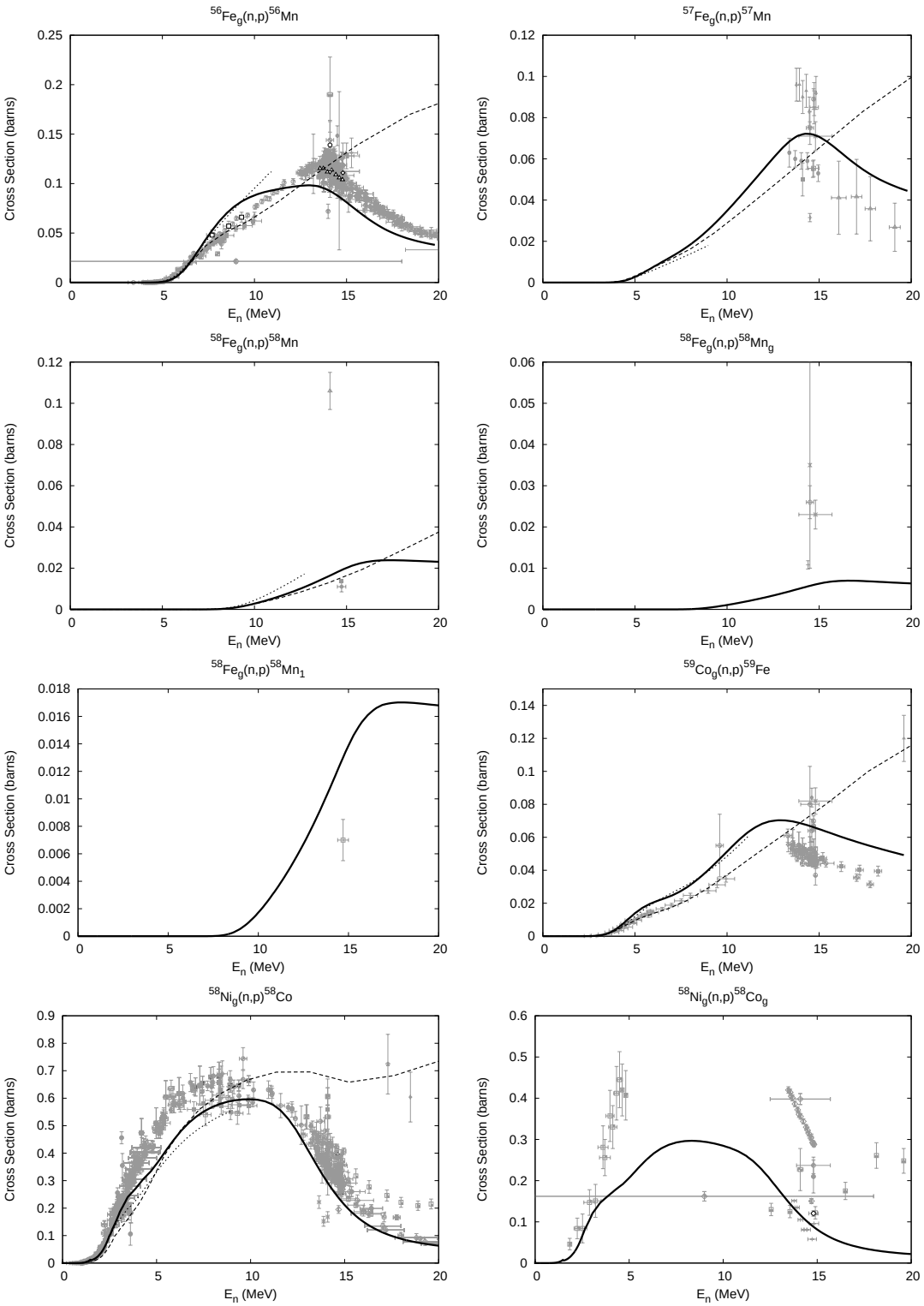

Figure 36: (continued)

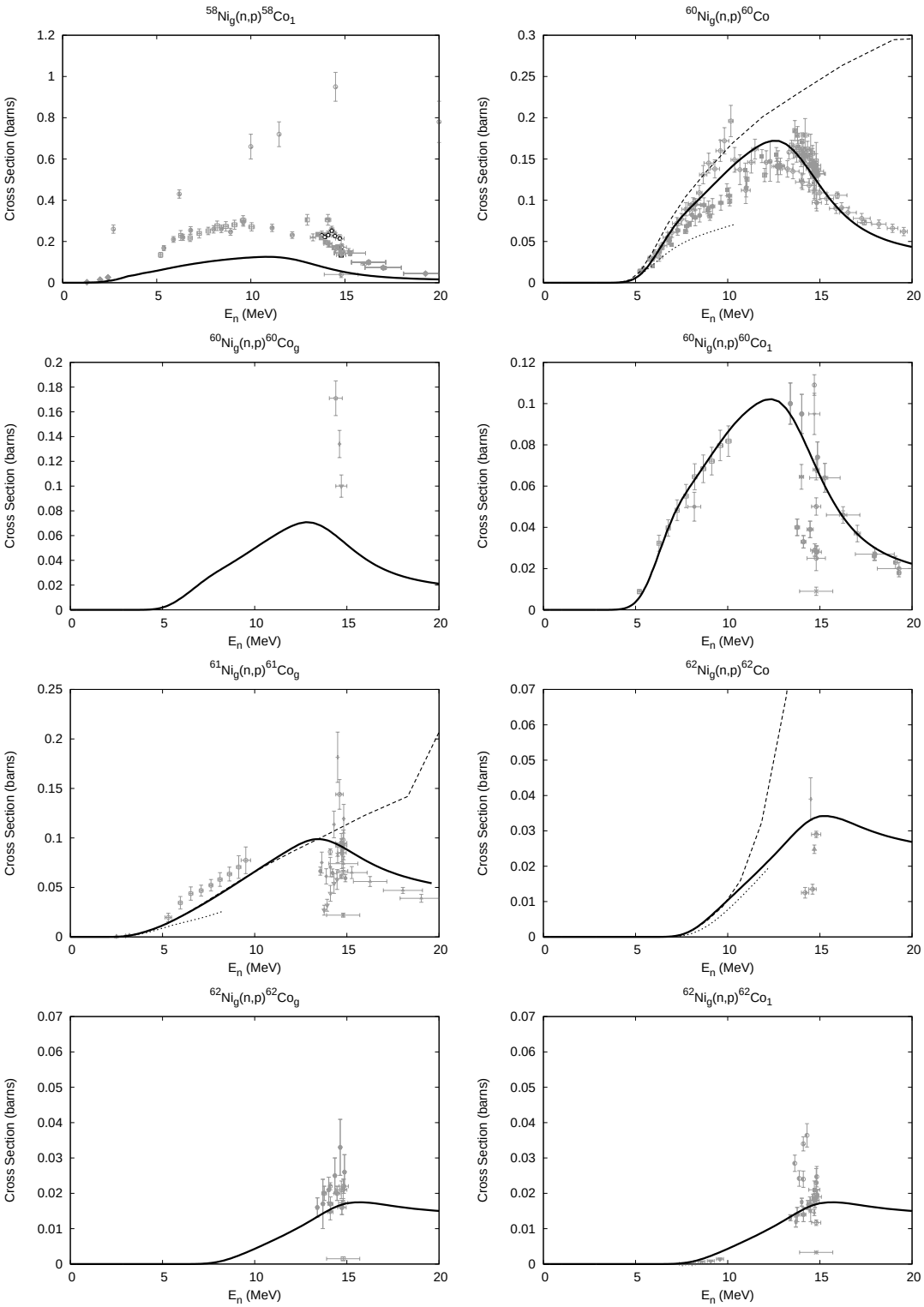

Figure 36: (continued)

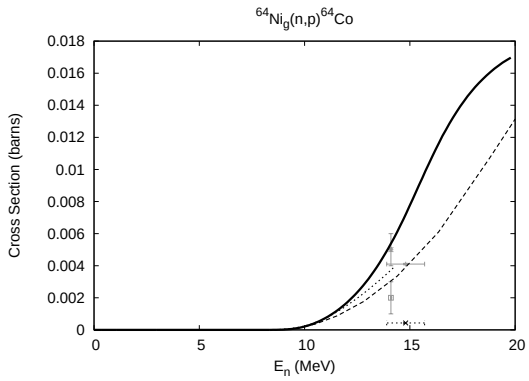

Figure 36: (continued)

to what we see in the (n,p) cross sections, with the three calculations having similar behavior up to 10 MeV. Beyond the peak of the cross section, both our calculation and that of NONSMOKER have a tendency to be high, though our calculation generally lies somewhat closer to the data. The likely cause of our overshooting the peak is our simplified treatment of pre-equilibrium. Pre-equilibrium processes for exiting alpha particles are somewhat more complex than those for single nucleons. The additional complexity arises from the tendency of nucleons to form alpha clusters [7]. The CRSEC calculations were not carried up to the peak of the cross section.

We have included deuterons as possible exit particles in our calculations, and the results of our (n,d) reaction modeling are found in Figure 38. Experimental data for these reactions is sparse. Usually there is only a single data point from a single measurement at 14 MeV. Our calculation tends to run below these data points, although we are usually within a factor of two of the error bars.

We have also modeled neutron induced cross sections with multiple particles in the exit channel. Figure 39 shows our combined results for (n,np) and (n,pn) reactions. The results for the two reactions are summed for comparison against the data, since experiments are not able to distinguish the order in which particles are emitted from the compound nucleus. Our ability to reproduce the measured values

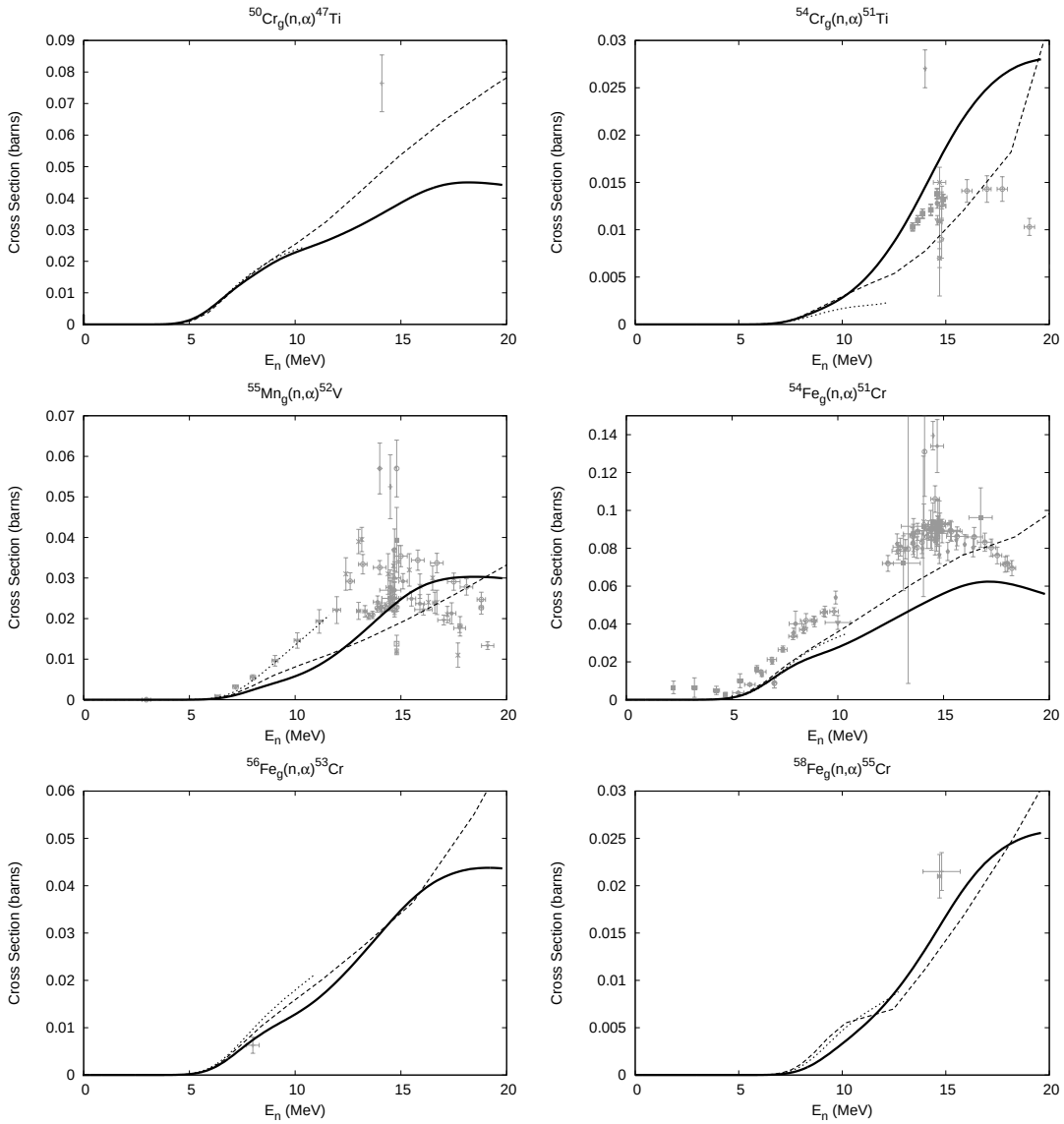

Figure 37: Modeled (n,α) cross sections compared to measurements. The solid lines represent modeled cross sections from the present work. Dotted lines represent cross sections calculated by the CRSEC code used by WFHZ. Dashed lines represent cross sections calculated with the NON-SMOKER code used by RT. Measured cross section data represents all cross section data available in the EXFOR libraray for the reaction as of 2004.

for these reactions is mixed. However, we tend to find better agreement with the larger data sets (^{57}Fe and ^{58}Ni targets, for example).

Figure 40 shows our results for (n,2n) reactions. For the most part, our agreement with the measured data is good. The most notable exception is ^{50}Cr(n,2n)^{49}Cr.

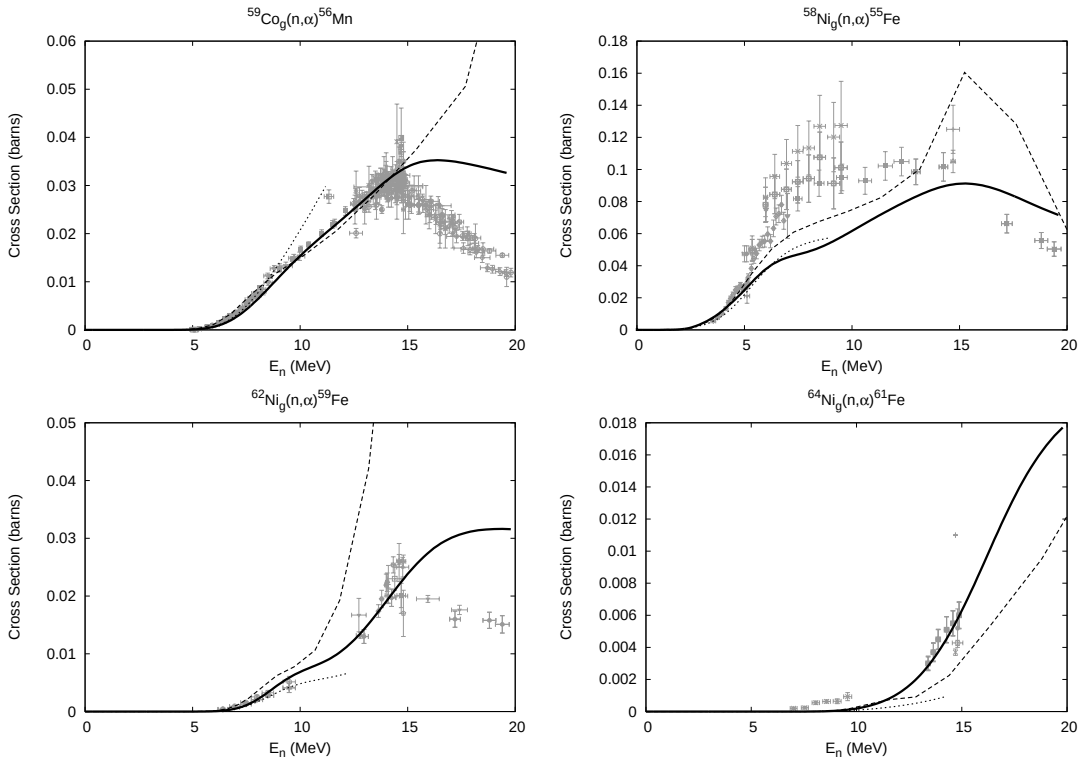

Figure 37: (continued)

Given the good agreement with the other (n,2n) reactions, we do not suspect that the issue here involves pre-equilibrium. Rather, an input quantity used only for this reaction, such as the neutron transmission coefficient leading to the ^{51}Cr compound nucleus or the level density for ^{49}Cr, is the most likely culprit. We see good agreement between our calculation and the measured activation cross section for ^{59}Co(n,2n)^{58}Co, as well as the portion going to the ground state. However, we appear to underpredict the amount going to the isomer. ^{58}Co in fact has two isomers, and the measured data is likely the sum of the cross section to both. No measurements were explicitly identified with the second isomer. This is consistent with the results seen for the ^{58}Ni(n,p)^{58}Co and ^{58}Fe(p,n)^{58}Co reactions. For ^{59}Ni(n,2n)^{58}Ni and ^{60}Ni(n,2n)^{59}Ni, the measured data consists of a single point at 14 MeV. The data points for both of these reactions seem to be unusually low, bringing their accuracy into question. Predicting (n,2n) cross sections is fairly straightforward,

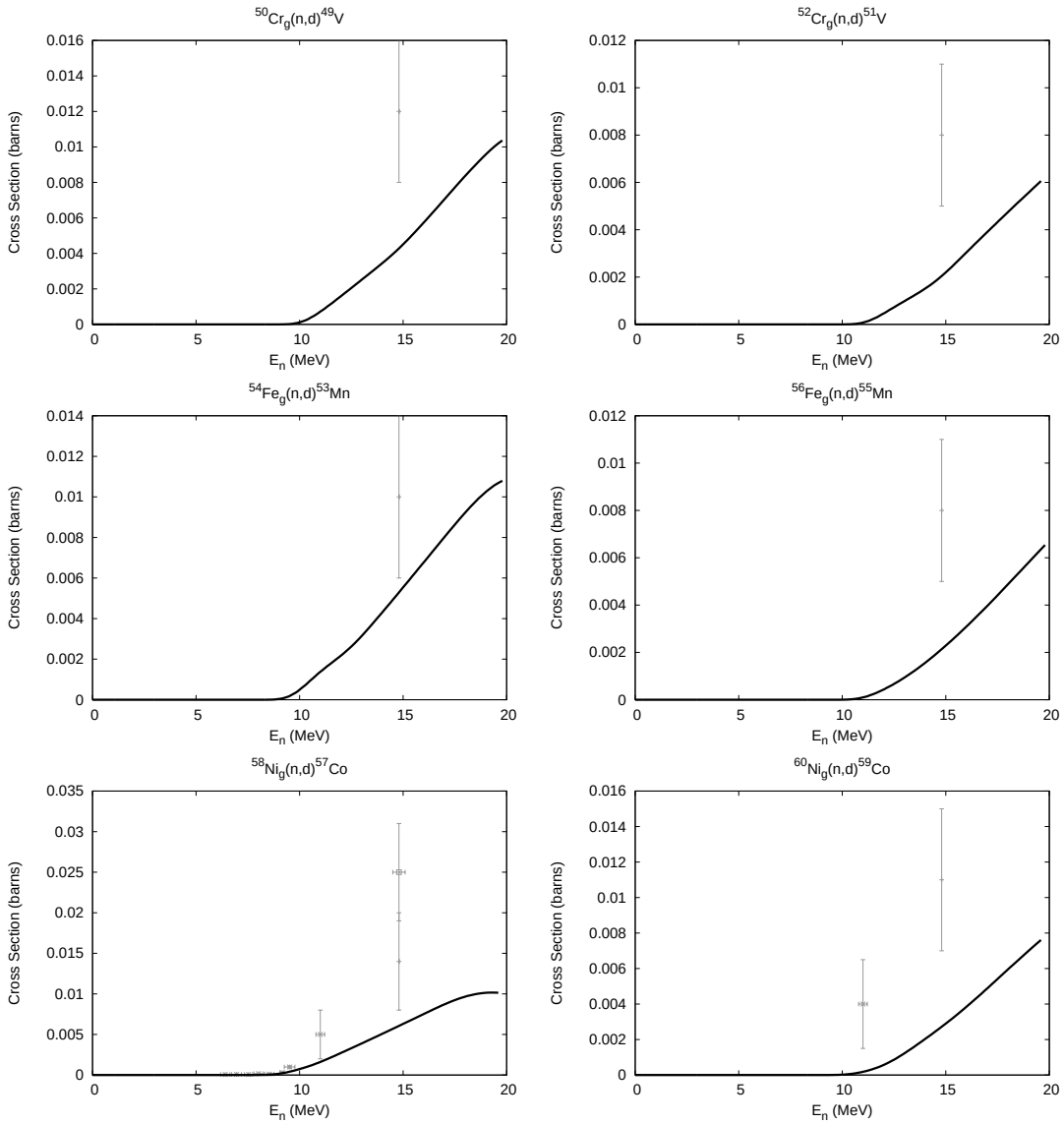

Figure 38: Modeled (n,d) cross sections compared to measurements. The solid lines represent modeled cross sections from the present work. Dotted lines represent cross sections calculated by the CRSEC code used by WFHZ. Dashed lines represent cross sections calculated with the NON-SMOKER code used by RT. Measured cross section data represents all cross section data available in the EXFOR libraray for the reaction as of 2004.

as they scale roughly with the size of the nucleus. The activation cross section is typically about a barn at 14 MeV regardless of atomic number.

Our success at modeling these cross sections gives us a good deal of confidence in our particle transmission coefficients, level densities, and treatment of

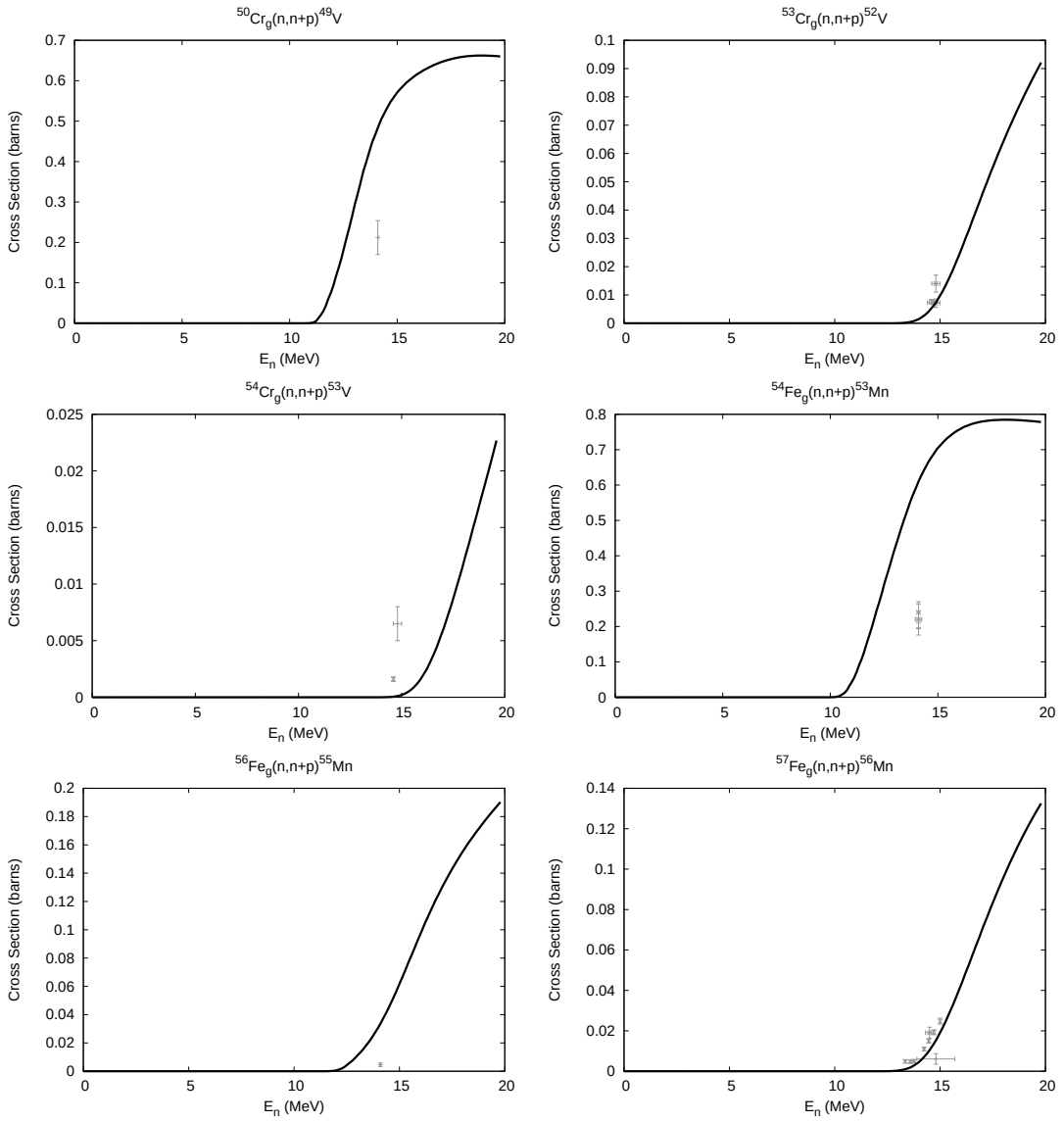

Figure 39: Modeled (n,np)+(n,pn) cross sections compared to measurements. The solid lines represent modeled cross sections from the present work. Dotted lines represent cross sections calculated by the CRSEC code used by WFHZ. Dashed lines represent cross sections calculated with the NON-SMOKER code used by RT. Measured cross section data represents all cross section data available in the EXFOR libraray for the reaction as of 2004.

pre-equilibrium. However, the photon transmission coefficient plays a negligible role in the calculation of these cross sections, while capture cross sections are extremely sensitive to it. Our most uncertain Hauser-Feshbach input quantity, relative to the calculation of neutron capture cross sections, is thus the photon strength function.

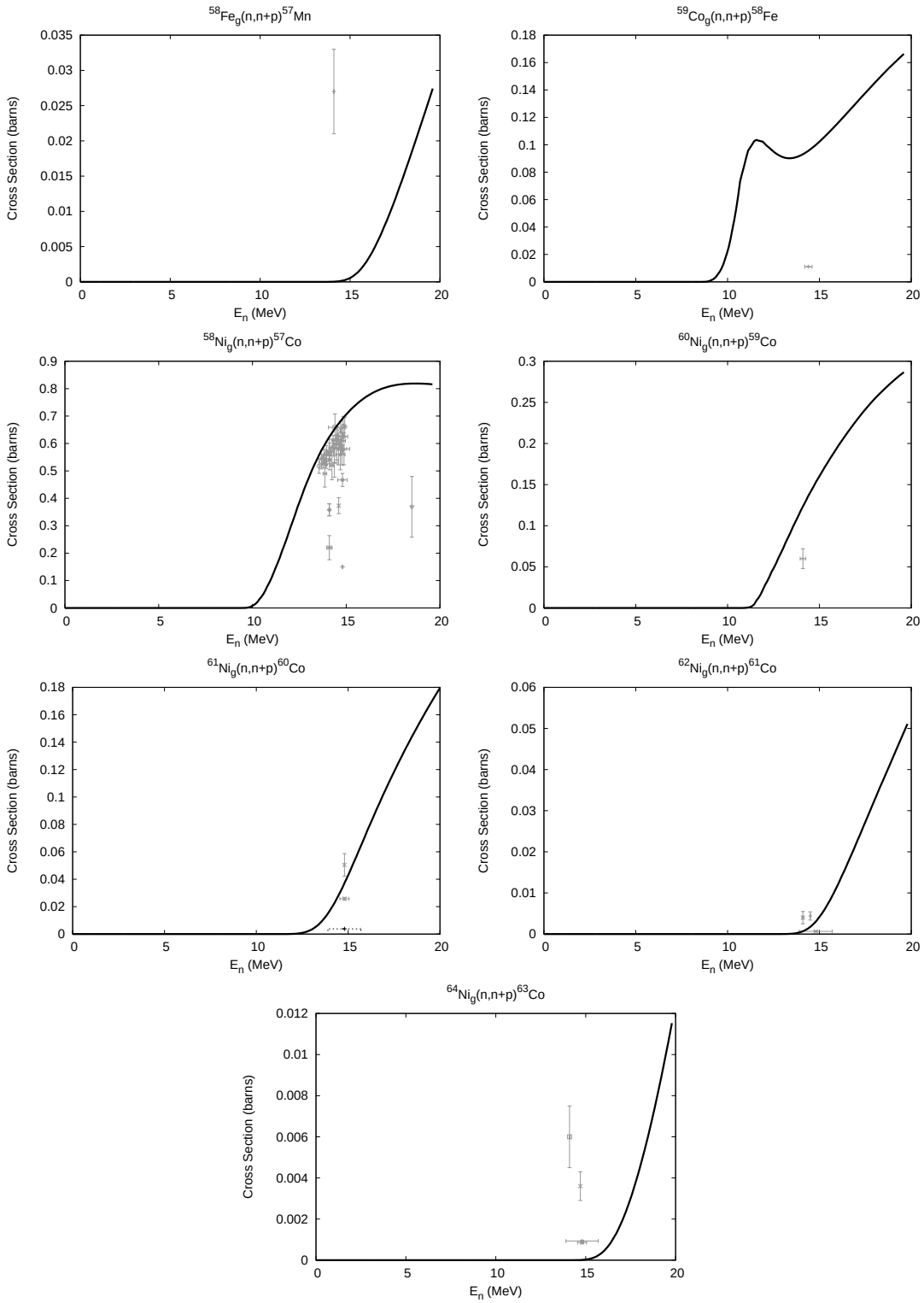

Figure 39: (continued)

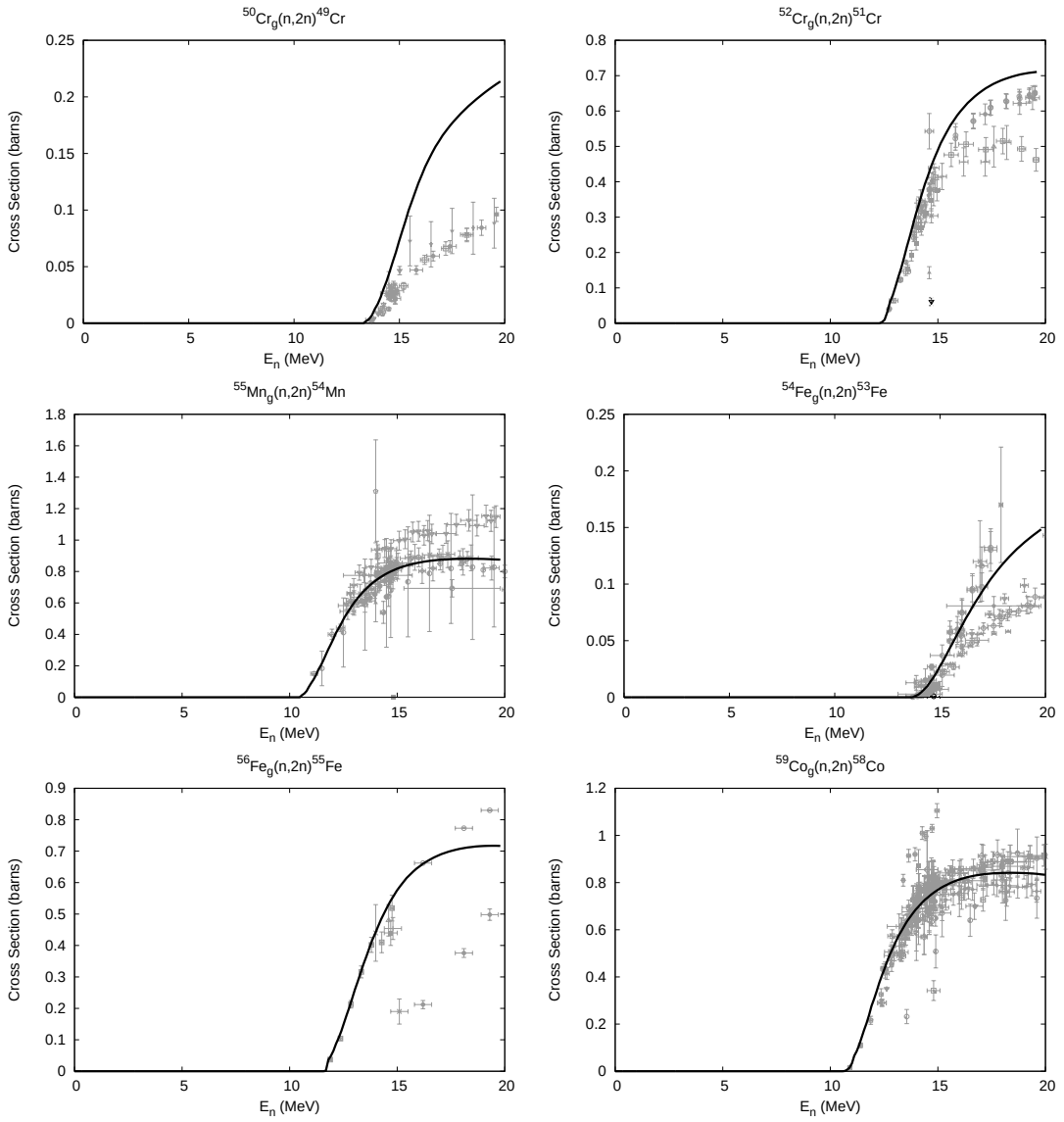

Figure 40: Modeled (n,2n) cross sections compared to measurements. The solid lines represent modeled cross sections from the present work. Dotted lines represent cross sections calculated by the CRSEC code used by WFHZ. Dashed lines represent cross sections calculated with the NON-SMOKER code used by RT. Measured cross section data represents all cross section data available in the EXFOR libraray for the reaction as of 2004.

Last of all, the calculations for (p,n) reactions may be found in Figure 41. The three calculations are similar up to 10 MeV, with our calculation tending to be more consistent in matching the data. Above 10 MeV, the NONSMOKER calculation again has a tendency to overshoot the peak. Only a limited amount of data close to

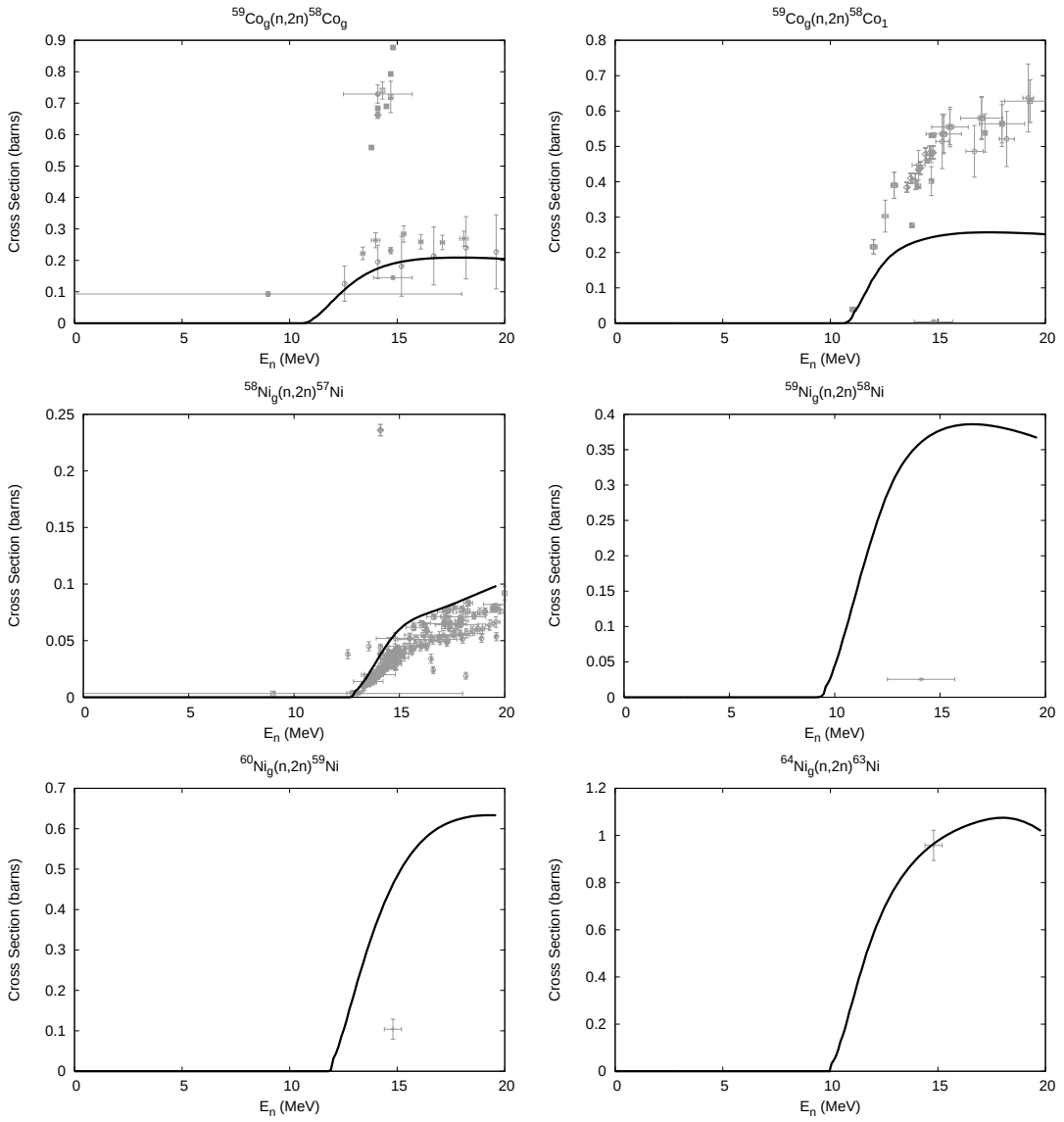

Figure 40: (continued)

threshold is available for ^{50}Cr(p,n)^{50}Mn. In fact, no activation data is available. The activation cross section has been included nonetheless for the purposes of comparing our calculation with previous ones. We note that identification of the isomeric final states in ^{58}Co is again the likely cause of the disagreement between our calculation and the measured ^{58}Fe(p,n)^{58}Co$_{m1}$ cross section.

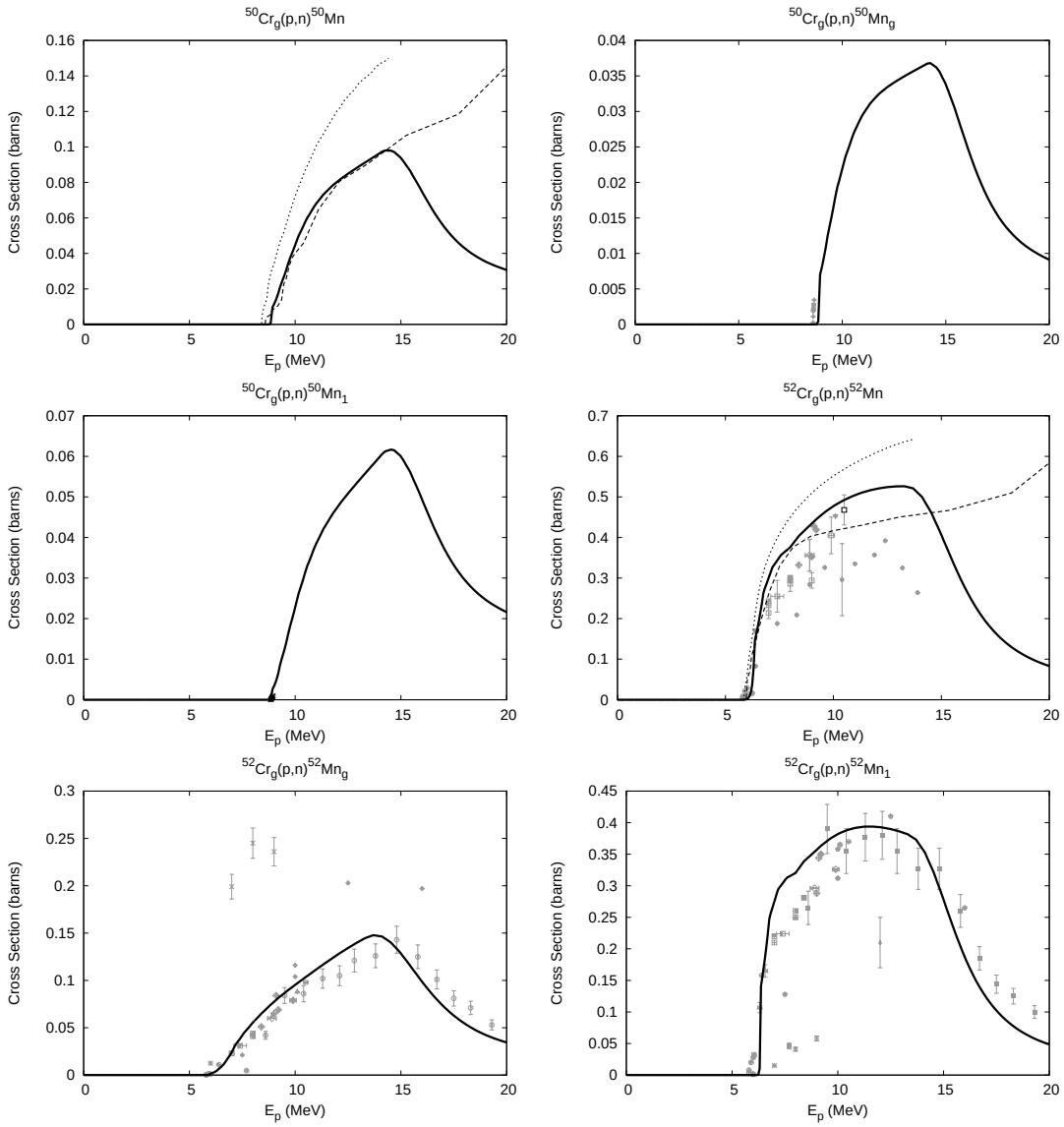

Figure 41: Modeled (p,n) cross sections compared to measurements. The solid lines represent modeled cross sections from the present work. Dotted lines represent cross sections calculated by the CRSEC code used by WFHZ. Dashed lines represent cross sections calculated with the NON-SMOKER code used by RT. Measured cross section data represents all cross section data available in the EXFOR libraray for the reaction as of 2004.

6.6 Direct Reaction Contributions

To this point we have only considered statistical model and pre-equilibrium contributions to the calculated cross sections. We now must justify neglecting direct reaction contributions to the capture cross sections.

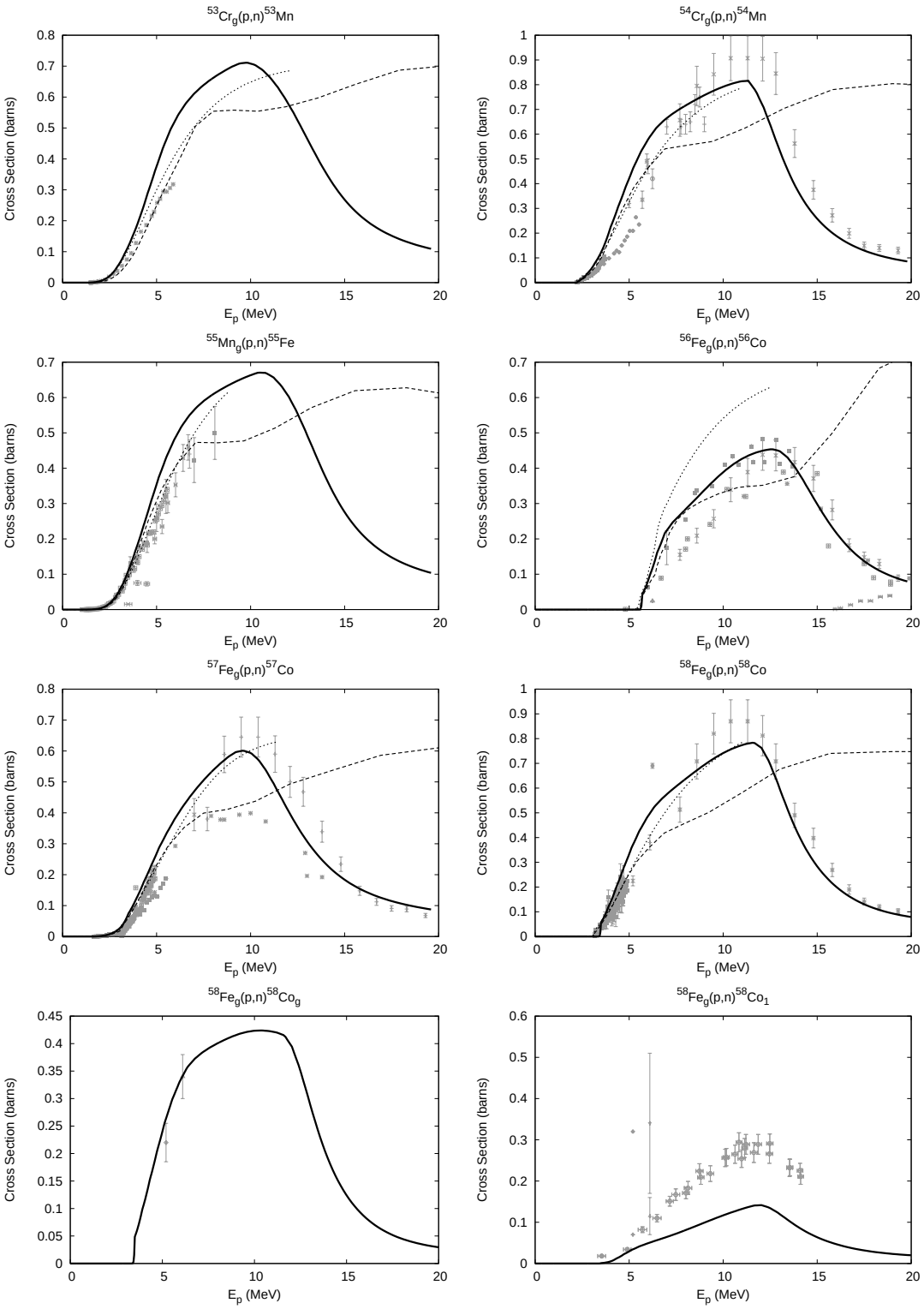

Figure 41: (continued)

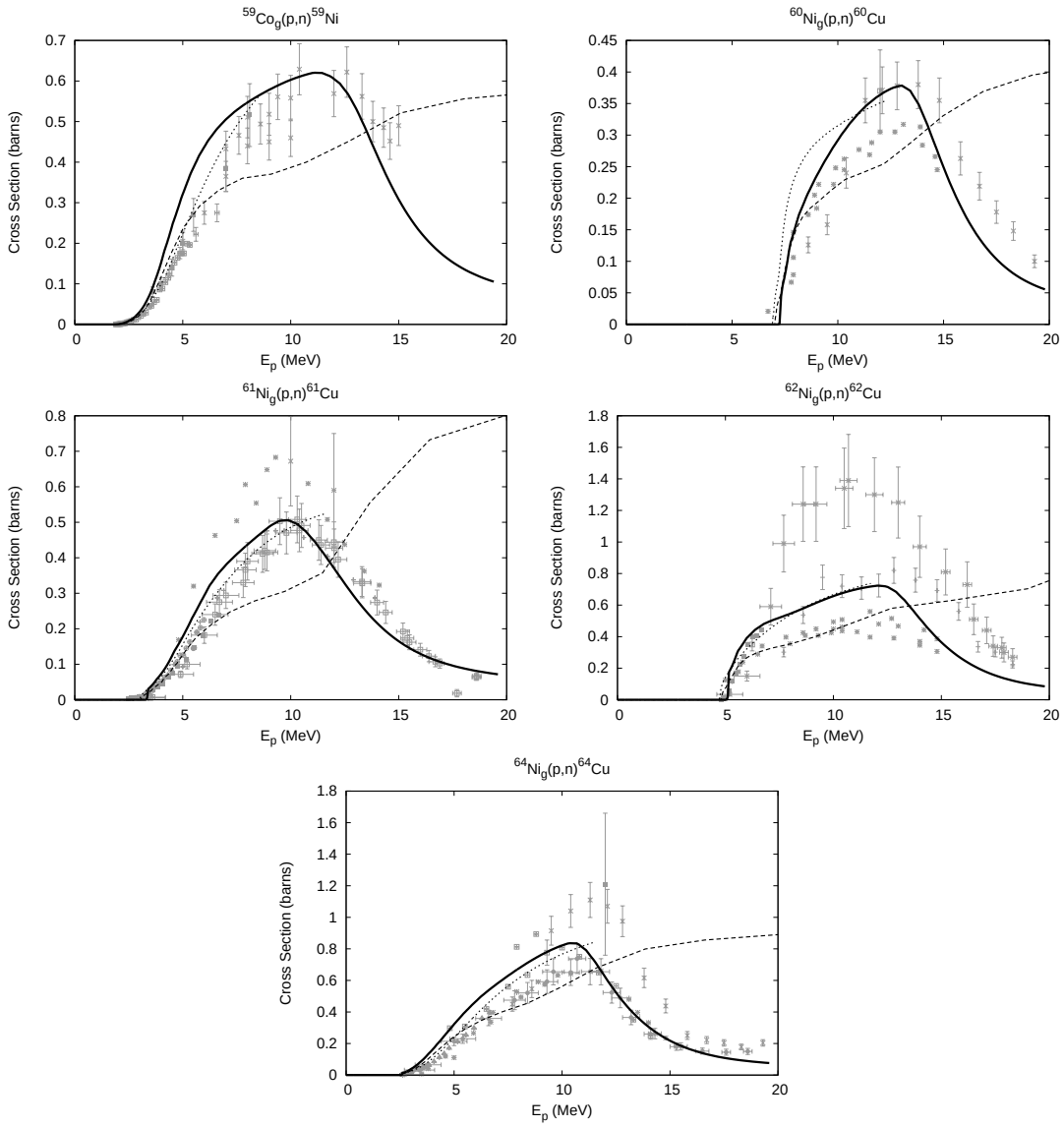

Figure 41: (continued)

Calculating the direct reaction contribution to neutron capture requires that one know the spectroscopic factors for the various resonances. These factors are generally measured in stripping reactions such as (d,p), and measured values are thus available only for stable targets. Ideally, we would calculate the direct reaction contribution for the ^{59}Fe(n,γ)^{60}Fe and ^{60}Fe(n,γ)^{61}Fe reactions. But in so doing we would rely on spectroscopic factors derived from models. For the present study we will restrict ourselves only to target nuclei for which the spectroscopic factors are

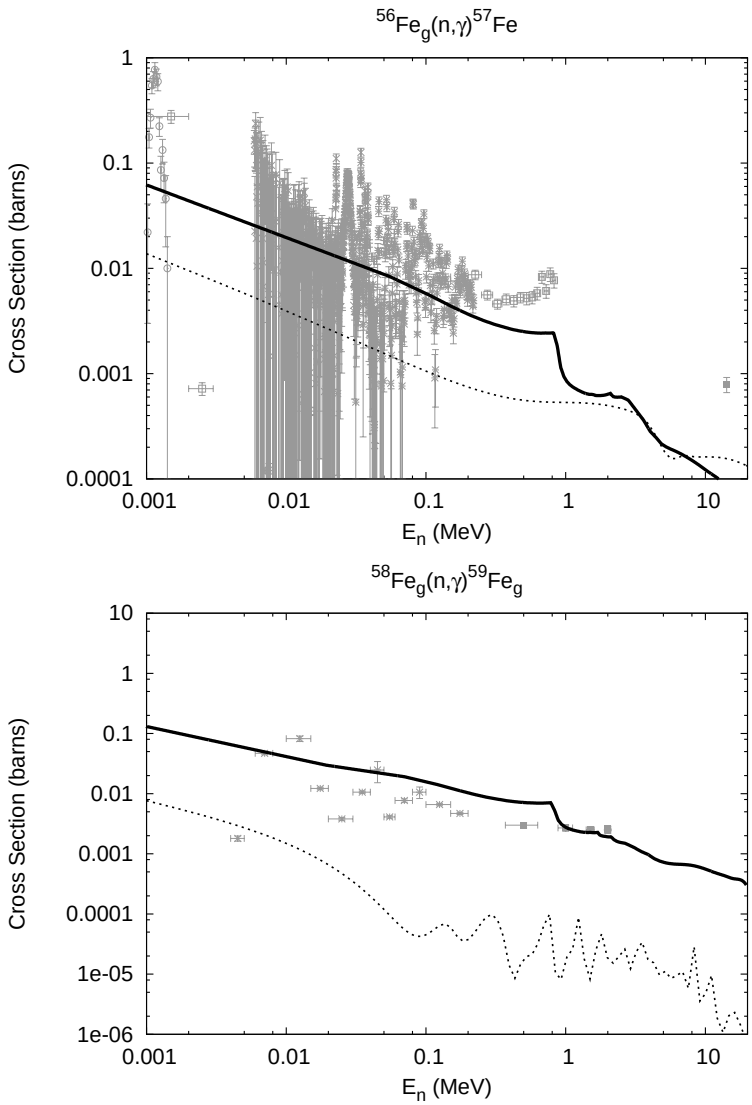

Figure 42: Direct reaction contributions to neutron capture by ^{56}Fe and ^{58}Fe. The solid line represents the compound nuclear contribution, and the dotted line represents the contribution from direct and semi-direct processes.

known, in particular ^{56,58}Fe.

The direct reaction contribution for ^{56}Fe(n,γ)^{57}Fe and ^{58}Fe(n,γ)^{59}Fe was calculated using the CUPIDO code [2]. This code includes both direct and semidirect contributions. The spectroscopic factors were taken from [4].

As can be seen in Figure 42, direct capture accounts for only about 20% of the ^{56}Fe(n,γ)^{57}Fe reaction up to about 1 MeV. In this plot, the compound nuclear

contribution is represented by a solid line and the direct contribution by a dotted line. For incident energies greater than 1 MeV it plays a more important role. However, for astrophysical purposes we are primarily interested in capture cross sections between 5 and 100 keV of incident energy. Direct capture plays an even less important role in ^{58}Fe(n,γ)^{59}Fe, as may be seen in Figure 42. Generally, this will be the case. Direct reactions are small compared to compound nuclear reactions at low incident energies. For these reasons, we can omit direct reactions from our analysis of the ^{59}Fe(n,γ)^{60}Fe and ^{60}Fe(n,γ)^{61}Fe cross sections and only introduce errors of (generally) less than $\sim$15%.

References

[1] Bao, Z.Y., Beer, H., Käppeler, F., Voss, F., & Wisshak, K. 2000, Atomic Data & Nuclear Data Tables, **76**, 70

[2] Dietrich, F.S. 2004, private communication

[3] Experimental Nuclear Reaction Data File, Brookhaven National Laboratory, US Dept. of Energy, http://www.nndc.bnl.gov/nndc/exfor/

[4] Evaluated Nuclear Structure Data File, Brookhaven National Laboratory, US Dept. of Energy, http://www.nndc.bnl.gov/nndc/ensdf/

[5] Gardner, D. G., "Model Calculations as one Means of Satisfying the Neutron Cross Section Requirements of the CTR Program", NBS Special Publication 425, Washington DC, March 3-7, 1975

[6] Hoffman, R. D., Rauscher, T., Woosley, S. E. & Thielemann, F.-K. 1999, ApJ, **521**, 735

[7] Milazzo-Colli, L., and Braga-Marcazzan, G.M., 1973, Nuc. Phys. **A210**, 297

[8] Rauscher, T., Thielemann, F.-K. 2000, Atomic Data & Nuclear Data Tables, **75**, 1 http://quasar.physik.unibas.ch/ tommy/reaclib.html#REACLIB

[9] Rauscher, T. & Thielemann, F.-K. 2001, At. Data Nucl. Data Tables **79**, 47

[10] Timmes, F.X., Woosley, S.E., Hartmann, D.H., Hoffman, R.D., Weaver, T.A., & Matteucci, F. 1995, ApJ **449**, 204

[11] Woosley, S.E. & Fowler, W. A., UCID-17600, LLNL, 1977

[12] Woosley, S.E., Fowler, W.A., Holmes, J.A. & Zimmerman, B.A. 1978, At. Data Nucl. Data Tables, **22**, 371

7 Reaction Rate Sensitivities

We now consider the approximate uncertainties in our ^{59}Fe(n,γ)^{60}Fe and ^{60}Fe(n,γ)^{61}Fe reaction rates with respect to the various input quantities. These uncertainties fall into one of two classifications: those associated with uncertainties in our local systematics, and those associated with differences in choices of prescriptions for the input parameters. Initially we vary only one input parameter at a time, and this analysis is followed by considering the collective effects of the uncertainties in all input parameters.

In these sensitivity studies, we focus our analysis on the reaction rates obtained from the cross sections rather than the cross sections themselves. We do this because it is the reaction rates that are used in nucleosynthesis calculations. Since measured cross sections do not exist for these reactions, we do not diminish the quality of our comparisons by making this choice. The reaction rate ($\langle\sigma v\rangle$) is related to the cross section by

$$\langle\sigma v\rangle = \int_0^\infty \sigma v \Phi(v) dv \ . \tag{133}$$

In this expression $\Phi(v)$ represents the velocity distribution, which we assume to be Maxwellian as we did for the MACS in Section 6.1. Making this assumption, Equation 133 simplifies to

$$\begin{aligned} \langle\sigma v\rangle &= \left(\frac{8}{\pi\mu}\right)^{1/2} \frac{1}{(kT)^{2/3}} \int_0^\infty \sigma(E) E \exp(-E/kT) dE \\ &= \frac{3.732 \times 10^{10}}{\hat{A}^{1/2} T_9^{3/2}} \int_0^\infty \sigma(E) E \exp(-11.605 \times E/T_9) dE \end{aligned} \tag{134}$$

where E is the center of mass energy, μ is the reduced mass of the incident particle plus target, $\hat{A}$ is the reduced mass in atomic units, k is the Boltzmann constant, and T_9 is the temperature in billions of degrees Kelvin.

We begin by considering the uncertainties introduced through our local system-

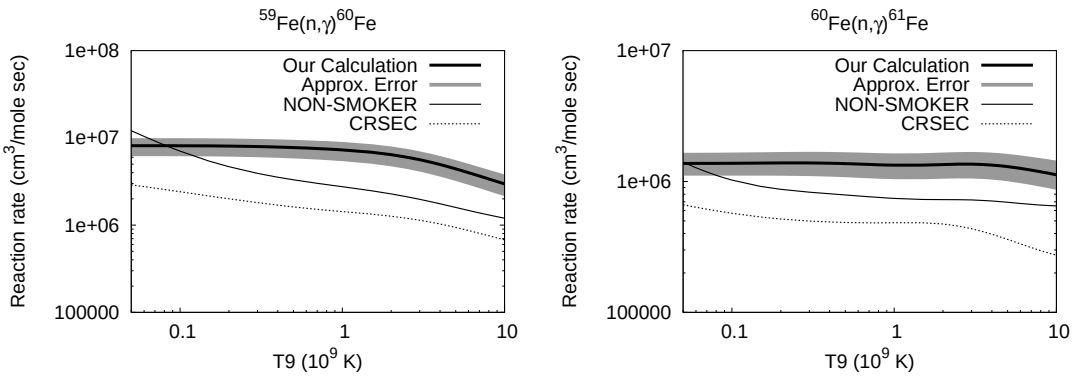

Figure 43: Uncertainties in the ^{59}Fe(n,γ)^{60}Fe and ^{60}Fe(n,γ)^{61}Fe reaction rates associated with uncertainties in the local level density systematic

atics.

7.1 Uncertainties in Systematic Input Parameters

The Hauser-Feshbach input quantities presented in Sections 3-5 represent our best estimates given available experimental data. As such, we consider our cross sections to be as accurate as may be reasonably expected. However, the key ^{59}Fe(n,γ)^{60}Fe and ^{60}Fe(n,γ)^{61}Fe cross sections are based on systematics, and any uncertainty associated with these systematics will translate into an uncertainty in the reaction rates.

7.1.1 Asymptotic Level Density Parameter

The standard deviation of "experimental" asymptotic level density parameters ($\tilde{a}$) from our systematic is 0.232 MeV^{-1} (see Figure 14), a value somewhat larger than the mean errorbar on the experimental values (0.135 MeV^{-1}). Assuming that the error in the level density parameters for ^{60,61}Fe are the same as the standard deviation of the experimental values, we determine an approximate error in the ^{59}Fe(n,γ)^{60}Fe and ^{60}Fe(n,γ)^{61}Fe neutron capture reaction rates stemming from these uncertainties by refitting the level densities to the discrete level spectra using the systematic

values plus or minus 0.232 MeV^{-1} (as in Section 4.1.7) and calculating the resulting cross sections and reaction rates. The results are shown in Figure 43. The uncertainties in the level density systematic amount to uncertainties in the reaction rates of 22-28% for ^{59}Fe(n,γ)^{60}Fe and 19-28% for ^{60}Fe(n,γ)^{61}Fe.

7.1.2 GDR Parameters

The standard deviation of measured GDR parameters from their respective systematic values are 0.482 MeV for the peak energy and 1.721 MeV for the width (see Figures 27 and 28). We examine the effects of these uncertainties by recalculating the cross sections and reaction rates using the systematic GDR parameters plus or minus their respective uncertainties. We do not consider uncertainties in the GDR peak cross section, since the effect of this value is eliminated by our process of normalizing the photon strength functions to measured/systematic radiation widths. Despite the rather large uncertainty in the GDR widths, the resulting uncertainties in the ^{59}Fe(n,γ)^{60}Fe and ^{60}Fe(n,γ)^{61}Fe reaction rates are negligibly small (less than 1.5% for ^{59}Fe, 0.5% for ^{60}Fe). We do not present figures illustrating these sensitivities here, but they are included in the collective uncertainties presented in Section 7.1.4.

7.1.3 Normalization of the γ-ray Transmission Coefficient

Measurements of the average total S-wave photon width ($\langle\Gamma_\gamma\rangle_0$) in the region of interest have an average error of ~600 meV for even-Z compound nuclei and ~160 meV for odd-Z compound nuclei. These average errors are similar to the standard deviations of the measured values from the primary systematic (Figure 30), which are 630.7 meV and 320.9 meV for even- and odd-Z compound nuclei, respectively. We assume the uncertainty in the systematic radiation widths of ^{60}Fe and ^{61}Fe are equal to the even-Z standard deviation. Upon recalculating the ^{59}Fe(n,γ)^{60}Fe

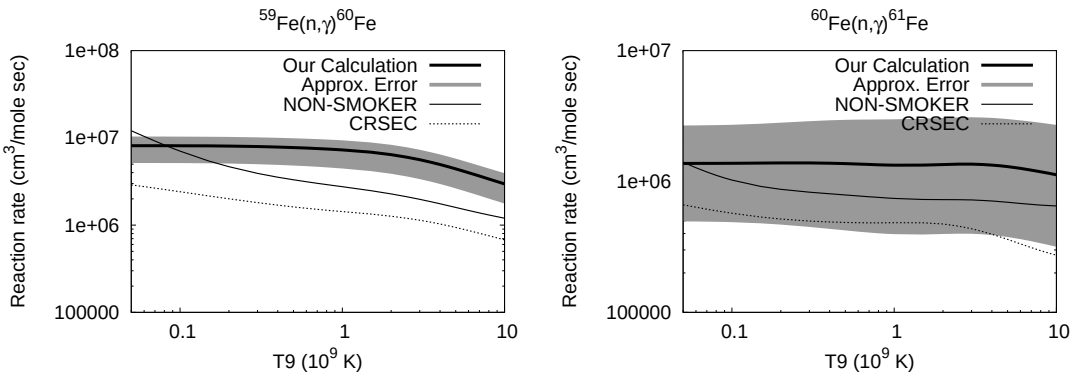

Figure 44: Uncertainties in the ^{59}Fe(n,γ)^{60}Fe and ^{60}Fe(n,γ)^{61}Fe reaction rates associated with uncertainties in the local radiation width systematic

and ^{60}Fe(n,γ)^{61}Fe reaction rates, we find the approximate uncertainties depicted in Figure 44. In this analysis, we enforce a lower limit on the radiation width of 100 meV. The approximate uncertainty in the reaction rates resulting this systematic are 27-41% for ^{59}Fe(n,γ)^{60}Fe and 63-140% for ^{60}Fe(n,γ)^{61}Fe. These are the largest uncertainties associated with these reactions.

7.1.4 Collective Uncertainties Arising from Local Systematics

We now provide an estimate of the collective range of uncertainty in our calculated capture reaction rates arising from our local systematics (level density parameter, GDR parameters, and radiation widths). This range is illustrated in Figure 45. Shown for reference are the reaction rates calculated from the CRSEC [5] and NON-SMOKER [2] codes. The range of uncertainty is +(60-75)% to -(49-55)% for ^{59}Fe(n,γ)^{60}Fe and +(135-210)% to -(71-78)% for ^{60}Fe(n,γ)^{61}Fe. The dominant contribution to these uncertainties comes from the radiation width systematic. We must stress that these cumulative uncertainties are approximate, and they do not represent an absolute error in our calculation. However, since this modeling effort is based on modern prescriptions and local systematics based on a relatively large set of experimental data, we have a reasonable degree of confidence in this result.

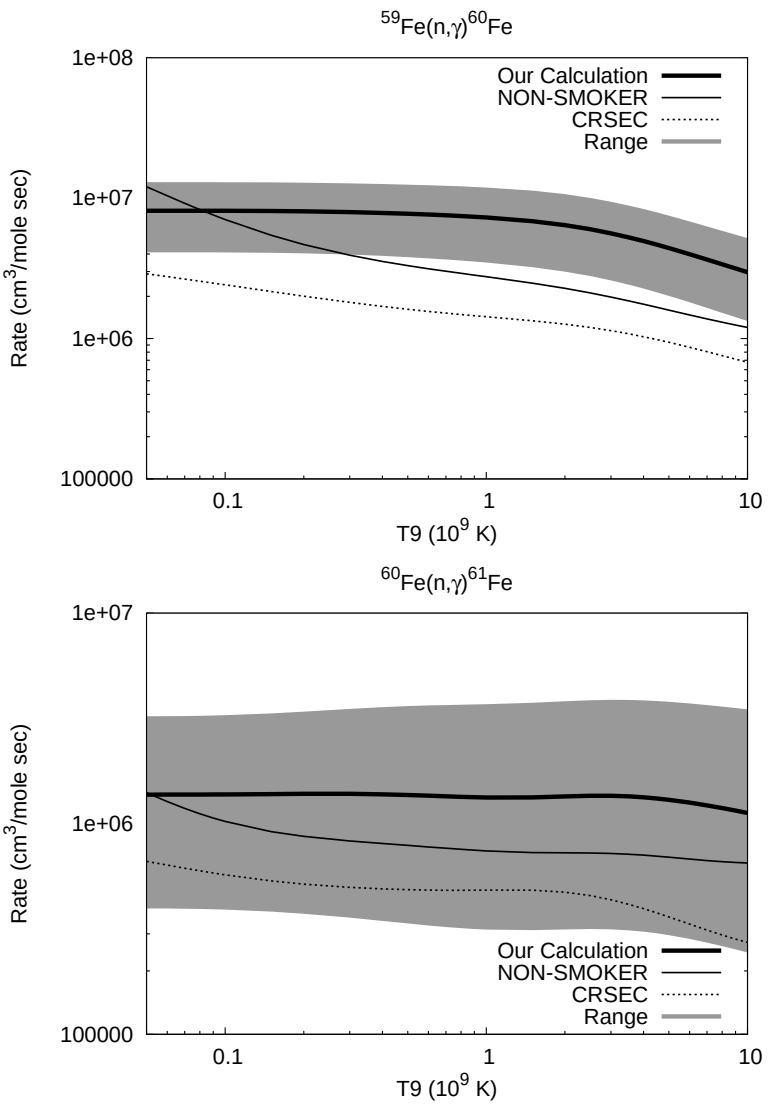

Figure 45: Collective uncertainties in the ^{59}Fe(n,γ)^{60}Fe and ^{60}Fe(n,γ)^{61}Fe reaction rates based on uncertainties in local systematics

7.2 Variations in Input Parameter Prescriptions

We consider the effect of choices for various prescriptions for the Hauser-Feshbach input quantities in addition to the uncertainties arising from our systematics. Again, we initially consider the effects of each quantity by varying one parameter at a time and conclude with an examination of the collective effect.

We have already considered the effect of variations on the level density parameter alone. We now present results where the overall treatment of the level density

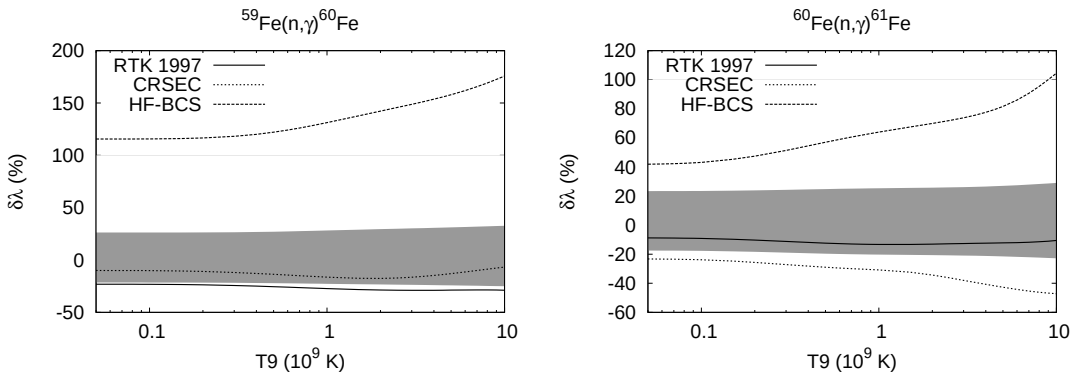

Figure 46: Variations in the ^{59}Fe(n,γ)^{60}Fe and ^{60}Fe(n,γ)^{61}Fe reaction rates arising from the choice of level density prescription (local systematic v. global systematics)

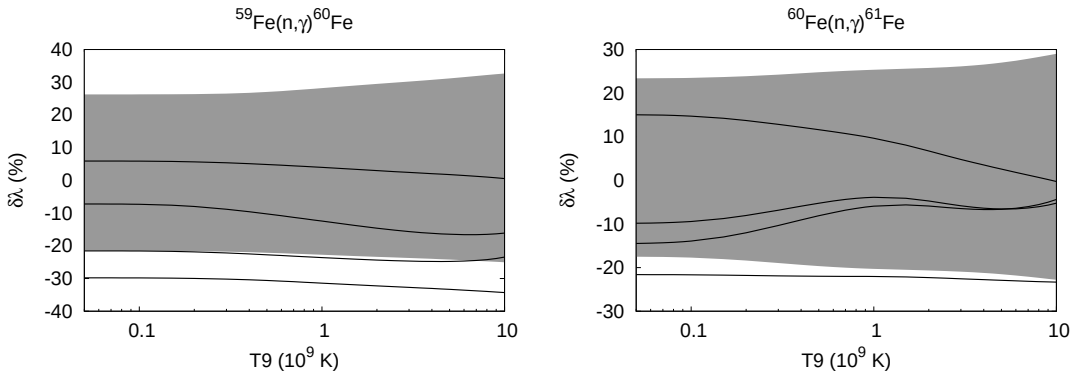

Figure 47: Variations in the ^{59}Fe(n,γ)^{60}Fe and ^{60}Fe(n,γ)^{61}Fe reaction rates arising from the choice of level density prescription (preferred systematic v. other local systematics)

prescription (in conjunction with the proper set of discrete levels) is varied, keeping all other parameter input fixed. Figures 46 and 47 illustrate this sensitivity.

7.2.1 Level Density Prescription and Discrete Levels

In these plots, the shaded region corresponds to the uncertainty in our level density systematic (see Section 7.1.1), shown for reference. These figures present the deviation from the reaction rate calculated using all of our preferred inputs (λ_{pref}), defined as

$$\delta\lambda = \frac{\lambda - \lambda_{pref}}{\lambda_{pref}} \times 100\% \tag{135}$$

rather than the rates themselves. In Figure 46, the solid and dotted lines correspond to the rates calculated using the level densities and discrete levels of Rauscher, Thielemann, and Kratz [3] (RTK) and Woosley, Fowler, Holmes, and Zimmerman [6] (WFHZ), respectively. The dashed line (the highest rates in both cases) correspond to level densities derived from the Hartree-Fock BCS model [1] and our full set of discrete levels. Because of the rather large deviations it introduces, and the lack of systematic normalization in this level density prescription, it is not included in our overall uncertainty provided in Section 7.2.6. The level densities of RT and WHFZ result in smaller rates for both reactions, with the greatest deviation for the WFHZ level densities used in ^{60}Fe(n,γ)^{61}Fe.

In Figure 47, the solid lines correspond to the other local systematics listed in Table 5. These systematics did not provide as good a fit to measured resonance spacings (as indicated by their larger χ^2) and generally led to conditions where either the parameter γ was unusually high (greater than 0.1 MeV^{-1}) or the matching energy frequently exceeded the the neutron binding energy. These systematics result in reaction rates similar to those produced using our preferred systematic. We include them in our overall uncertainty found in Section 7.2.6.

Note that the magnitude of the net uncertainties due to varying the level density prescription, excluding the Hartree-Fock BCS level densities, are similar to the uncertainties corresponding to the level density parameter systematic presented in Section 7.1.1. In general, the Fermi gas level density prescription can change the reaction rate by as much as 40-50%, but for most temperatures the variation is within 30%.

7.2.2 Neutron Transmission Coefficients

The sensitivity to the choice of neutron transmission coefficient is shown in Figure 48. The effects associated with this input prescription are smaller than those asso-

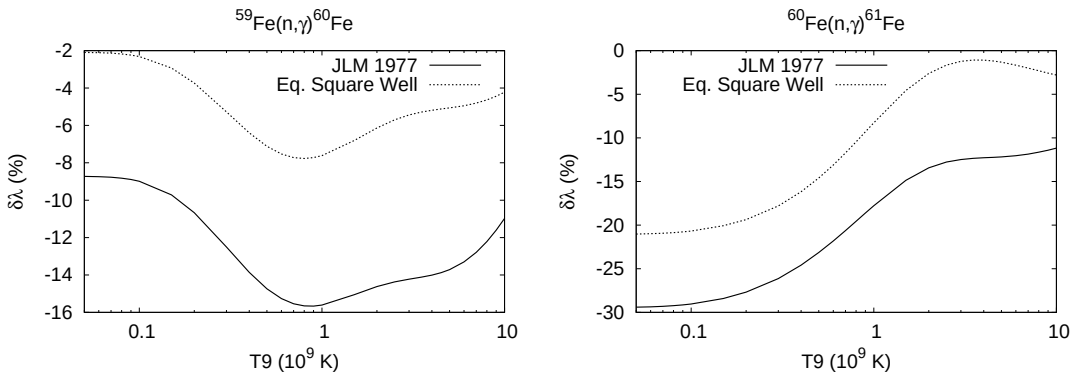

Figure 48: Variations in the ^{59}Fe(n,γ)^{60}Fe and ^{60}Fe(n,γ)^{61}Fe reaction rates arising from the choice of neutron transmission coefficient

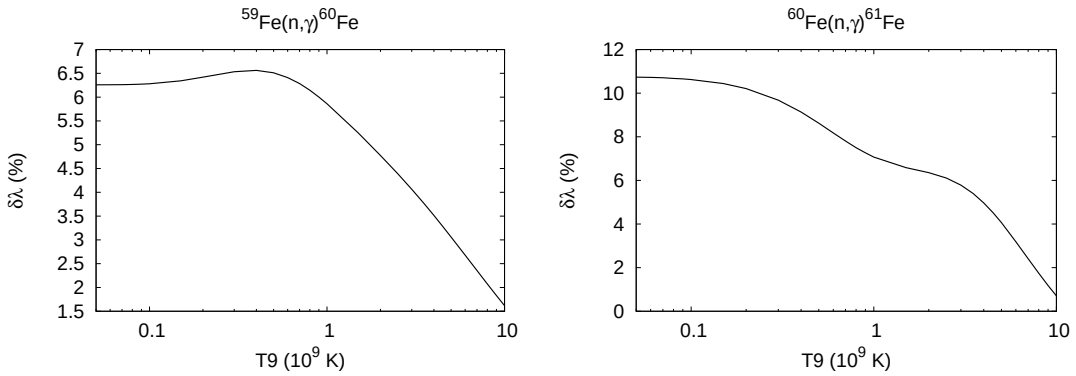

Figure 49: Variations in the ^{59}Fe(n,γ)^{60}Fe and ^{60}Fe(n,γ)^{61}Fe reaction rates with the inclusion of width fluctuation correlations.

ciated with the level density. Overall the Jeukenne, Lejeune, and Mahaux (JLM) and equivalent square well potentials both result in lower reaction rates, with the difference being more significant for the JLM potential (up to 30%). We do not consider uncertainties due to the charged particle transmission coefficients for the reasons given in Section 5.1.2.

7.2.3 Width Fluctuation Correlation

Figure 49 shows the effect of the Width Fluctuation Correlation on the ^{59}Fe(n,γ)^{60}Fe and ^{60}Fe(n,γ)^{61}Fe capture rates. These figures depict the effect when the WFC is turned off, and represent an enhancement of the capture cross section of 7-12%.

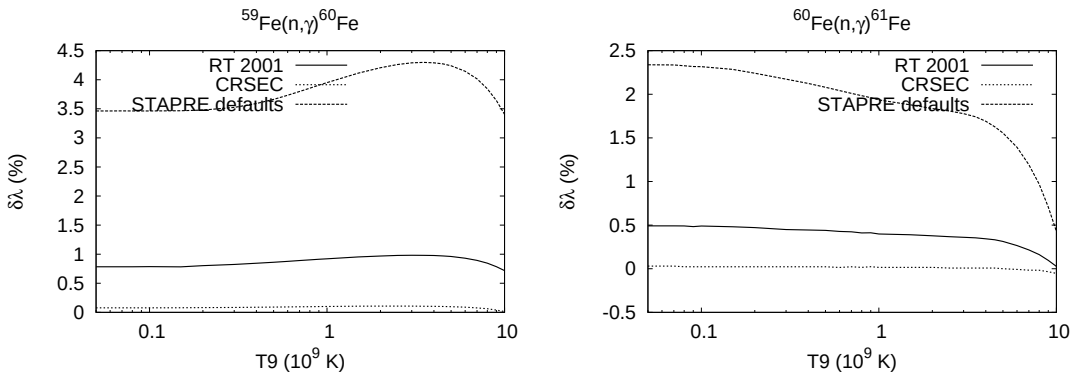

Figure 50: Variations in the ^{59}Fe(n,γ)^{60}Fe and ^{60}Fe(n,γ)^{61}Fe reaction rates arising from the choice of GDR parameters.

7.2.4 GDR parameters

In Section 7.1.2 we have shown that the ^{59}Fe(n,γ)^{60}Fe and ^{60}Fe(n,γ)^{61}Fe rates bear a minimal sensitivity to uncertainties in the GDR systematics. We now consider the effect of adopting an entirely different prescription for the GDR parameters. As can be seen in Figure 50, the reaction rates are minimally sensitive to the GDR parameters, even though the additional systematics in this figure include only a single resonance. The STAPRE default GDR parameters ($E_{GDR} = 80/A^{1/3}$ and $\Gamma_{GDR} = 5$ MeV) represent the largest departure from our systematic values (see Figures 27 and 28). Such a wide departure from our systematic still only results in a 2-4% change in the reaction rates, confirming that the choice of GDR parameters makes little difference in the calculation of these rates.

7.2.5 E1 and M1 Strength Functions

In our modeling effort we use the EGLO representation of the E1 giant dipole resonance and the SLO representation for the M1 strength function. We now investigate the sensitivity of the ^{59}Fe(n,γ)^{60}Fe and ^{60}Fe(n,γ)^{61}Fe reaction rates to these choices. Figure 51 shows the percent change in the reaction rates obtained when using SLO E1 and Blatt-Weisskopf M1 strength functions. In both cases this choice results in

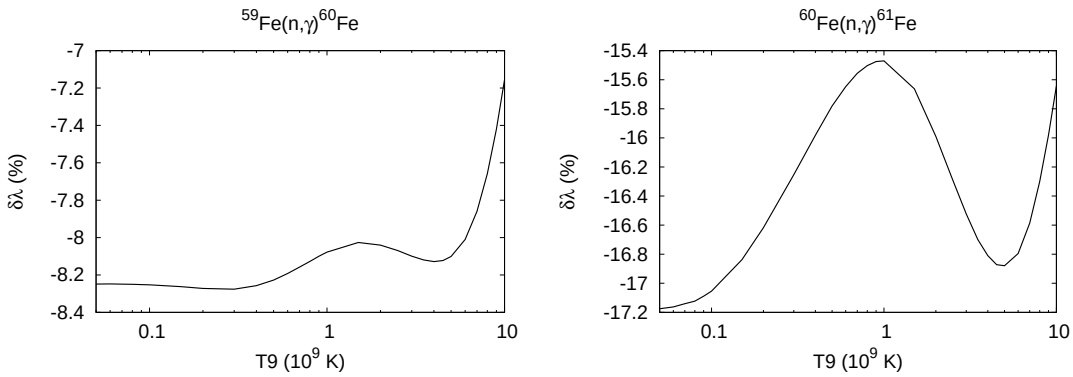

Figure 51: Variations in the ^{59}Fe(n,γ)^{60}Fe and ^{60}Fe(n,γ)^{61}Fe reaction rates arising from the choice of E1 and M1 strength function shapes.

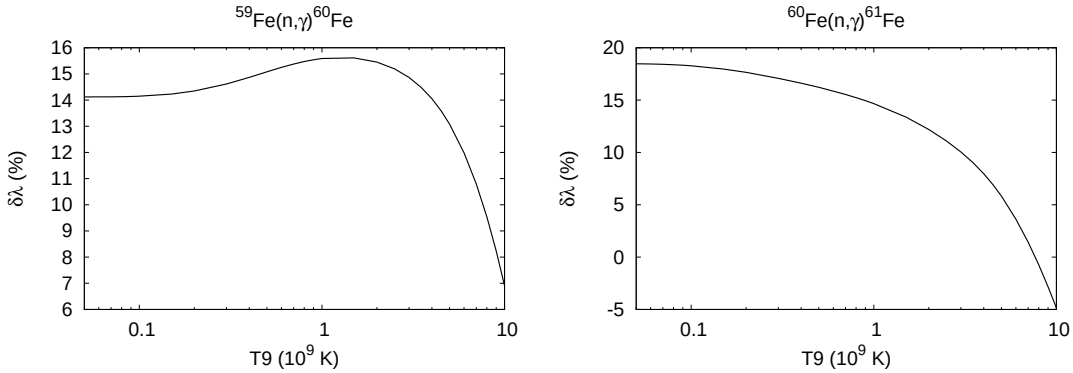

Figure 52: Variations in the ^{59}Fe(n,γ)^{60}Fe and ^{60}Fe(n,γ)^{61}Fe reaction rates with the inclusion of the low energy E1 strength function enhancement.

a lower cross section and reaction rate, by roughly 8% in the case of ^{59}Fe(n,γ)^{60}Fe and the order of 15-18% for ^{60}Fe(n,γ)^{61}Fe.

Recently an enhancement of the photon strength function for low energy gamma rays was measured in iron isotopes [7]. Our preferred photon transmission coefficient does not include this enhancement, though we desire to know roughly what the effect would be were such an enhancement to be included in our calculations. Assuming that the parameters for ^{57}Fe given in [7] would also apply to heavier iron isotopes, we obtain the result seen in Figure 52. Adding this enhancement to the photon strength function increases the reaction rates by roughly 15-20% at low temperatures, with the effect tapering for higher T_9.

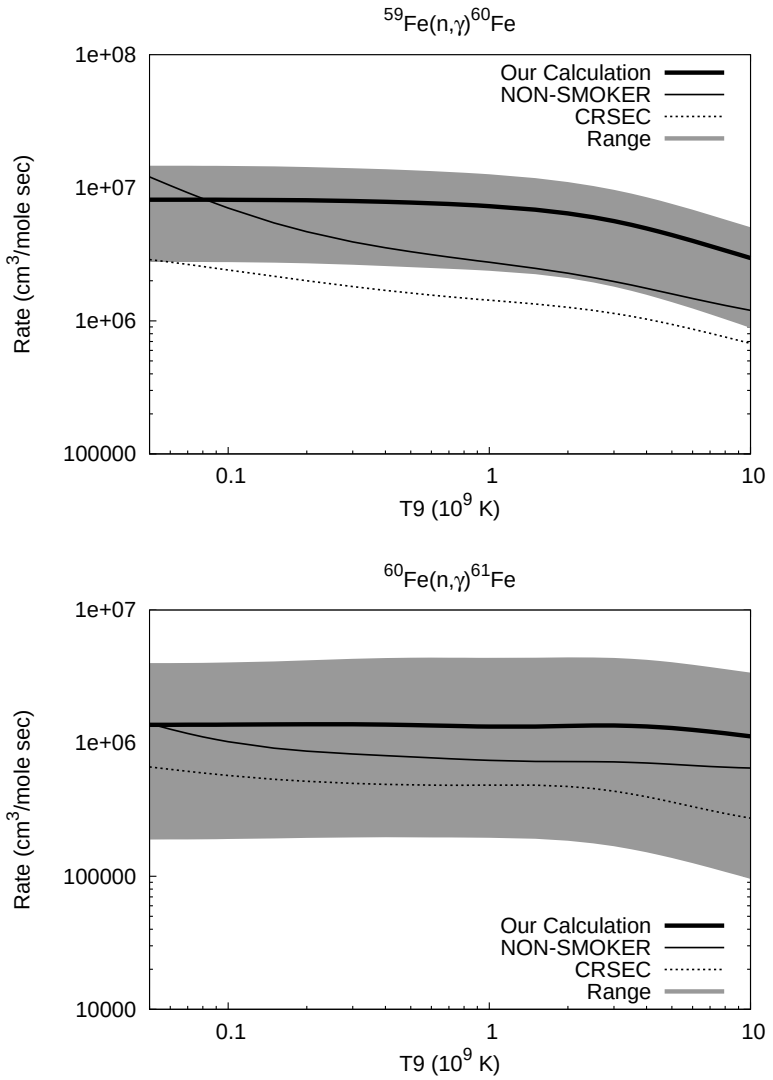

Figure 53: Range in the ^{59}Fe(n,γ)^{60}Fe and ^{60}Fe(n,γ)^{61}Fe reaction rates attainable by varying input parameter prescriptions

7.2.6 Collective Variations

Figure 53 presents the range of variations in the ^{59}Fe(n,γ)^{60}Fe and ^{60}Fe(n,γ)^{61}Fe reaction rates attainable by the collective substitution of input parameter prescriptions. Included in this range are the prescriptions for the level density and discrete levels, neutron optical potential, width fluctuation corrections, GDR parameters, and photon strength function prescription. Additionally, the approximate systematic uncertainties on the average S-wave photon width of Section 7.1.3 have been

included. The range of uncertainty is +(70-80)% to -(66-70)% for ^{59}Fe(n,γ)^{60}Fe and +(190-230)% to -(85-92)% for ^{60}Fe(n,γ)^{61}Fe.

Note that some of the prescriptions used in developing these ranges of uncertainty are based on more limited amounts of experimental data and in some cases represent simpler models. As such, this second uncertainty range should not be interpreted as an error in the calculated reaction rates, but rather a demonstration of the range attainable by varying input quantity prescriptions, of which some variations are not well motivated.

As suggested in Figures 45 and 53, our rates for both reactions are always higher than either CRSEC [5] or NONSMOKER [2], but tend to be closer to those from NONSMOKER. We are now ready to investigate the effect of these newly modeled reaction rates on the stellar synthesis of ^{60}Fe.

References

[1] Demetriou, P., & Goriely, S. 2001, Nucl. Phys. **A695**, 95

[2] Rauscher, T., Thielemann, F.-K. 2000, Atomic Data & Nuclear Data Tables, **75**, 1 http://quasar.physik.unibas.ch/ tommy/reaclib.html#REACLIB

[3] Rauscher, T., Thielemann, F.-K. & Kratz, K.-L. 1997, Phys. Rev. C **56**, 1613.

[4] Uhl, M., & Strohmaier, B. IRK-Vienna Report IRK-76/01 1976 (Upd. 1978)

[5] Woosley, S.E. & Fowler, W. A., UCID-17600, LLNL, 1977

[6] Woosley, S. E., Fowler, W. A., Holmes, J. A. & Zimmerman, B. A. 1978, Atomic Data & Nuclear Data Tables, **22**, 371

[7] Voinov, A., et al., 2004, Phys. Rev. Lett. **93**, 142504

8 Parameterized Single-Zone Nucleosynthesis

We now investigate the effect of our newly evaluated ^{59}Fe(n,γ)^{60}Fe and ^{60}Fe(n,γ)^{61}Fe rates will have on the production of ^{60}Fe. Included in this analysis is an evaluation of the significance of the uncertainties in our calculation. We simulate stellar environments using a single zone nucleosynthesis code with an appropriate choice of thermodynamic parameters. We choose this simple code over a more complex stellar evolution code involving multiple zones, so as to eliminate effects due to convection, mass loss, and other physics not directly related to the reaction rates.

The first part of this section outlines our reaction networks. The second part describes the approximate thermodynamic conditions of various stages of stellar evolution. In the third part, we detail our method of evaluating reaction rates in nucleosynthesis calculations. The fourth part presents the results of our modeling. We conclude with an analysis of the sensitivity of ^{60}Fe abundances relative to uncertainties in the neutron capture rates.

8.1 Nuclear Reaction Networks

The abundance of a given isotope i can be expressed in terms of the mass fraction X_i, defined as the decimal fraction of the total mass. A similar quantity is the mole number, defined as

$$Y_i = \frac{X_i}{A_i} \tag{136}$$

where A_i is the mass number of species i. This quantity has units of mol/g. The number density is then given by

$$n_i = \rho N_A Y_i \tag{137}$$

where N_A is Avogadro's number and ρ is the density of the stellar matter.

When considering how the abundance of a particular species changes over time, one must include all significant energetically accessible channels for the production and destruction of the isotope. One should also consider all reactions producing (or destroying) the isotopes that feed into the species of interest. As a result, the synthesis of a particular isotope is described by a large set of reactions, which can be represented as a set of coupled differential equations. For each isotope i included in the reaction network, the production rate is given by

$$\frac{dY_i}{dt} = -\sum_{j,k} \rho Y_i Y_j \lambda_{jk}(i) + \sum_{l,m} \rho Y_l Y_m \lambda_{mn}(l) \tag{138}$$

where again ρ is the density. The λ_{jk} are reaction rates as given in Equation 134. In this expression, the first sum accounts for all possible reactions leading to the destruction of species i. The rate at which i is destroyed depends not only on the reaction rate itself, but also the molar abundances of i and the incident particle j. The second sum accounts for all reactions producing i. In this sum, we require $l + m = i + n$ (i.e. we only include the target nuclei l for which the reaction rate λ_{mn} is leading to species i).

The size of the reaction network will vary depending upon the specific application. Omission of an important isotope (i.e. an isotope with large reaction rates leading to its production in addition to large abundances of the proper targets) should be avoided. As a general rule, the total mass should be conserved throughout the evolution. This condition is given by $\sum_i Y_i A_i = 1$. Any deviation from unity indicates that an important species has been omitted from the network.

For very small reaction networks, consisting of only a few species and a handful of reaction rates, the differential equations describing the nucleosynthesis may have an approximate closed form solution. However, such small networks are rare and of limited use. Generally, the nucleosynthesis must be modeled by numerically

integrating the set of differential equations, using a forward differencing method to avoid numerical instability [2].

Nuclear energy generation is also related to Equation 138. The energy released during thermonuclear processes is equal to the differences between the total initial and final binding energies, and thus

$$S = 9.647 \times 10^{17} \sum_i \Delta Y_i BE_i(\text{MeV}) \text{ erg g}^{-1} \ . \tag{139}$$

The rate of energy production is then

$$\frac{dS}{dt} = 9.647 \times 10^{17} \sum_i \frac{dY_i}{dt} BE_i(\text{MeV}) \text{ erg g}^{-1}\text{s}^{-1} \ . \tag{140}$$

This latter quantity will be important in discussing the typical thermodynamic conditions of various nuclear burning stages.

On a final note, one should in principle include all binary reactions in Equation 138, and also all reactions corresponding to important fusion processes, such as ^{3}He $+^3$ He $\rightarrow^6$ Be, $3\alpha \rightarrow^{12}$ C, ^{12}C $+^{12}$ C $\rightarrow^{24}$ Mg, ^{12}C $+^{16}$ O $\rightarrow^{28}$ Si, and ^{16}O $+^{16}$ O $\rightarrow^{32}$ S. Each of these reactions produces a residual in an excited state, which subsequently may shed excitation energy via the emission of particles or radiation. In our study, these rates are taken from either [15] or [8], as will be described later. Additionally, one must include rates to account for the radioactive decay of unstable isotopes.

8.2 Thermodynamic Conditions of Burning Stages

Once the reaction rates have been determined, the time evolution of the reaction network depends only on the initial compositions, the temperature, and the density (density appears explicitly in Equation 138, while the reaction rates are a function

of T_9). The initial compositions of each burning stage will be given in Section 8.4, as will be specific temperatures and densities. For the time being, we make a few general statements regarding how the thermodynamic conditions are determined.

Hydrostatic Burning

We first consider pre-explosive processes where the stellar shells exist in approximate hydrostatic equilibrium. The temperature and density can be determined by solving the stellar structure equations. However, an assumption that stellar environments are in equilibrium, combined with a mechanism for energy loss, makes it possible to estimate the thermodynamic conditions in a zone without resorting to the solution of stellar structure.

In the absence of convection and mass loss (which are not present in single zone calculations), the only processes affecting the thermodynamic state are nuclear energy generation and energy losses. Maintaining hydrostatic equilibrium requires that the additional energy generated through nuclear processing be dissipated through some mechanism, such as luminosity or neutrino loss. In the early burning stages (hydrogen and helium burning), neutrino losses are much too small to counter the energy generation. For carbon burning and other advanced burning stages, neutrino losses become the dominant mechanism for power loss, and one may use the "balanced power" approximation [12]

$$\frac{dS}{dt} \approx \frac{d\epsilon_\nu}{dt} \tag{141}$$

where ϵ_ν is the total neutrino energy. In cases where the abundance of nuclear fuel is too low to account for all of the energy losses (specifically during Carbon and Neon burning in very massive stars), additional energy may be provided by "gravitational

energy release", and Equation 141 is modified to read [2]

$$\frac{dS}{dt} \approx \epsilon_\nu \frac{RS}{GM} \ . \tag{142}$$

The neutrino loss rate (RHS of Equation 141) can be approximated by a simple expression depending only on the temperature [4, 2]. For low temperatures ($T_9 \leq 1$), the approximation is based on the assumption that the neutrino pair process is the dominant source of neutrino losses. In this case, the loss rate is roughly

$$\frac{d\epsilon_\nu}{dt} \approx 4.9 \times 10^{18} \exp(-11.86/T_9) \text{ erg cm}^{-3}\text{sec}^{-1} \ . \tag{143}$$

For temperatures greater than $T_9 = 3$, a relativistic approximation yields

$$\frac{d\epsilon_\nu}{dt} \approx 4.6 \times 10^{15} \ T_9^9 \text{ erg g}^{-1}\text{sec}^{-1} \ . \tag{144}$$

Between these temperature ranges, the relativistic form is generally used.

Nuclear binding energy may be released by hundreds or even thousands of the reactions in the network, but usually only a few account for the majority of the nuclear energy produced at each stage. Thus dS/dt (Equation 140) may be approximated by a function of a few reaction rates and the density.

Equating these approximations for the nuclear energy production and neutrino losses, one may solve for a temperature or a relationship between the temperature and density. In cases where the temperature is obtained, it is generally assumed that density scales as the cube of the temperature. In cases where only a relationship between ρ and T_9 is obtained, one may use densities predicted by more complete stellar models to obtain estimates of the temperature.

Explosive Burning

During the explosion of a type II supernova stellar matter is ejected by an overpressure resulting from a shock. After the initial explosion, the ejecta is slowed by gravitational acceleration. The explosion and subsequent cooling of the ejecta may be modeled as a reverse free-fall. Such a free-fall is characterized by a hydrodynamic time scale τ_{HD}, defined as the time during which the density decreases by a factor of e, i.e.

$$\rho(t) = \rho_0 \exp(-t/\tau_{HD}) \ . \tag{145}$$

The temperature has a similar time dependence. If one assumes t is small, this expression yields

$$\tau_{HD} \left(\frac{d}{dt} \log \rho \right)^{-1} \ . \tag{146}$$

The density of a sphere is given by

$$\rho = \frac{3M}{4\pi r^3} \tag{147}$$

and we find

$$\frac{d}{dt} \log \rho = -\frac{3}{r} \frac{dr}{dt} \ . \tag{148}$$

Now consider an object of mass m falling freely under the gravitational influence of mass M. As the mass falls inward, the reduction in potential energy translates to an increase in kinetic energy. Assuming m is initially at rest,

$$\frac{m}{2} \dot{r}^2 = GMm \left(\frac{1}{r} - \frac{1}{r_0} \right) \ . \tag{149}$$

This expression may be solved for $\dot{r}$ of a free falling mass (we are interested in the reverse process, so we include an additional sign change). Now we find

$$\begin{aligned} \frac{d}{dt}\log\rho &= \frac{3}{r}\left(\frac{2GM}{r}-\frac{2GM}{r_0}\right)^{1/2} \\ &= \sqrt{24\pi G\rho_0}\left[\frac{\rho}{\rho_0}\left(1-\frac{\rho_0}{\rho}^{1/3}\right)\right]^{1/2} . \end{aligned} \tag{150}$$

The term in square brackets varies slowly, and for $\rho/\rho_0 > 1/e$ is approximately unity. Hence,

$$\tau_{HD} \approx \frac{1}{\sqrt{24\pi G\rho_0}} = \frac{466}{\sqrt{\rho_0}} . \tag{151}$$

The shock is relatively weak, and the initial density ρ_0 will not be much higher than the pre-shock density. The peak temperature will depend on the supernova energy (assumed to originate from the center of the star) and radius [14]. For our investigation, we use the peak temperatures and densities given in [2].

8.3 Fitting Reaction Rates to Parameterized Forms

Before evolving the reaction network using the conditions in the previous section, we should review which reaction rates are being used (our cross section modeling will only provide the neutron capture rates most significant to the production of ^{60}Fe) and how those rates are supplied.

Before proceeding, we must say a few words regarding modifications to Hauser-Feshbach rates at high temperatures. In Equations 32 and 134, we have assumed a target nucleus existing in the ground state, since this is most convenient for comparisons to measured cross sections. However, the extreme conditions found in stellar environments can thermally populate the excited states of the target. Thus for stellar nucleosynthesis we should use rates derived from so-called "stellar cross sections", which account for the thermal population of excited states. If $\bar{\sigma}^{\mu}_{jk}$ is the

cross section for a target in state μ (summed over final states), the stellar cross section is

$$\bar{\sigma}^*_{jk} = \frac{\sum_\mu (2J^\mu + 1)\bar{\sigma}^\mu_{jk} \exp(-E^\mu/kT)}{\sum_\mu (2J^\mu + 1)\exp(-E^\mu/kT)} \ . \tag{152}$$

A related quantity is the "effective cross section", given by

$$\bar{\sigma}^{eff}_{jk} = \sum_{\mu,\nu} \frac{(2J^\mu + 1)E^\mu}{(2J^0 + 1)E^0} \sigma^{\mu\nu}_{jk} \ . \tag{153}$$

The stellar reaction rate may be expressed in terms of either of these quantities. For the reaction $\mathcal{I}(j,k)\mathcal{L}$

$$\begin{aligned} \lambda^*_{jk} &= \frac{3.732 \times 10^{10}}{\hat{A}_j^{1/2} T_9^{3/2}} \frac{1}{G_{\mathcal{I}}(T_9)} \\ &\quad \int_0^\infty \sum_\mu \frac{2J^\mu + 1}{2J^0 + 1} \bar{\sigma}^\mu_{jk} E_j \exp[-11.605\ (E_j + E^\mu)/T_9] dE_j \ \mathrm{cm^3 mol^{-1} sec^{-1}} \\ &= \frac{3.732 \times 10^{10}}{\hat{A}_j^{1/2} T_9^{3/2}} \frac{1}{G_{\mathcal{I}}(T_9)} \int_0^\infty \bar{\sigma}^{eff}_{jk} E_j \exp(-11.605\ E_j/T_9) dE_j \ \mathrm{cm^3 mol^{-1} sec^{-1}} \ . \end{aligned} \tag{154}$$

$G_{\mathcal{I}}(T_9)$ is the partition function defined as

$$\begin{aligned} G(T_9) = \frac{1}{2J^0 + 1} \Big[&\sum_{\mu=0}^{\omega} (2J^\mu + 1) \exp(-11.605\ E^\mu/T_9) + \\ &\sum_{J,\Pi} \int_{E^\omega}^\infty (2J + 1) \exp(-11.605\ E'/T_9) \rho(E', J, \Pi) dE' \Big] \end{aligned} \tag{155}$$

where the sum extends through levels of known spin and parity and $\rho(E', J, \Pi)$ is the usual level density. The exponential factor in the integrand dominates at high E', and the integral can be cut off at a finite temperature for a given T_9. The sum over spins may also be cut off at $J \approx J^0 + 20$, since the spin dependence of the level density is suppressed by an exponential factor (see Equation 66).

The ratio of the stellar rate to the lab rate is referred to as the stellar enhance-

ment factor (SEF). This quantity indicates the significance of including thermally populated states in a given reaction. The STAPRE code does not calculate an effective cross section, and we have not calculated stellar rates for either of the ^{59}Fe(n,γ)^{60}Fe or ^{60}Fe(n,γ)^{61}Fe reactions. However, for $T_9 < 4$ the SEF for these reactions from both the CRSEC and NON-SMOKER codes do not vary significantly from unity, as seen in Table 10. As will be seen shortly, ^{60}Fe production is significant primarily around $T_9 \sim 2$, and should therefore exhibit minimal sensitivity to the inclusion of the SEF. We have verified this explicitly, with our results provided in Table 11. In this table, the calculated mass fractions were generated using the Rauscher and Thielemann rates [8] for all reactions except neutron capture onto ^{59,60}Fe, for which our rates were used (this combination of rates is designated set 2c in the next section). The first two columns indicate which burning stage is being evaluated. The third and fourth columns give the thermodynamic conditions of the zone (peak temperature and density in the case of explosive burning). The last two columns give the resulting ^{60}Fe abundances when the SEF are omitted and included. The differences in ^{60}Fe production when omitting the SEF are generally less than 30%, and most deviations greater than 30% only occur when the production is insignificant (mass fraction below 10^{-6}). We conclude that we may use our lab rates in lieu of stellar rates and only introduce errors on the order of 30%. This error is small relative to errors introduced by the uncertainties in the cross sections and stellar structure.

Once one has obtained a stellar rate for a given reaction, one may also determine a reverse rate through detailed balance [2]. The relationship between the forward and reverse rates (with the forward rate λ_{jk} including a particle in the exit channel) is

$$\lambda^*_{kj} = \frac{g_{\mathcal{I}} g_j}{g_{\mathcal{L}} g_k} \frac{G_{\mathcal{I}}}{G_{\mathcal{L}}} \left(\frac{A_{\mathcal{I}} A_j}{A_{\mathcal{L}} A_k} \right)^{3/2} \lambda^*_{jk} \exp\left(-\frac{11.605\ Q_{jk}}{T_9} \right) \ . \tag{156}$$

Table 10: Stellar enhancement factors for ^{59}Fe(n,γ)^{60}Fe and ^{60}Fe(n,γ)^{61}Fe

	CRSEC		NON-SMOKER	
T_9	^{59}Fe(n,γ)^{60}Fe	^{60}Fe(n,γ)^{61}Fe	^{59}Fe(n,γ)^{60}Fe	^{60}Fe(n,γ)^{61}Fe
0.1	1.000	1.000	1.000	1.000
0.2	1.000	1.000	1.000	1.000
0.5	0.999	1.000	1.000	1.000
1.0	0.983	1.006	0.985	1.000
2.0	0.879	1.050	0.880	0.996
3.0	0.784	1.016	0.796	0.986
4.0	0.738	0.965	0.754	0.992

In this expression, $G_{\mathcal{I}}$ and $G_{\mathcal{L}}$ are temperature dependent partition functions, $A_{\mathcal{I}}$, A_j, $A_{\mathcal{L}}$, and A_k are mass numbers, and $g_{\mathcal{I}}$, g_j, $g_{\mathcal{L}}$, and g_k are statistical factors given by $g_i = 2J_i + 1$. If the forward rate corresponds to a capture reaction, the expression is somewhat modified. These photodisintegration rates are given by

$$\lambda^*_{\gamma j} = 9.8677 \times 10^9 T_9^{3/2} \frac{g_{\mathcal{I}} g_j}{g_{\mathcal{L}}} \frac{G_{\mathcal{I}}}{G_{\mathcal{L}}} \left(\frac{A_{\mathcal{I}} A_j}{A_{\mathcal{L}}} \right)^{3/2} \lambda^*_{j\gamma} \exp\left(-\frac{11.605\ Q_{j\gamma}}{T_9} \right) \ . \qquad (157)$$

Detailed balance assumes that the cross sections obey reciprocity, which is true for the effective cross section. Cross sections for targets in their ground states do not obey reciprocity, and detailed balance should only be employed using stellar rates. Given this relationship between forward and reverse rates, it is only necessary to tabulate forward rates in nucleosynthesis codes. Hereafter we define forward rates as those rates which increase charge or mass.

Ideally, one would provide rates to a reaction network code by evaluating Equation 134 over many representative temperatures, storing the results in tabular form, and interpolating as needed. The large number of rates required (at least six per isotope for potentially thousands of isotopes) make such a method impractical. The preferred method for providing rates to a nucleosynthesis code is to fit the tabulated rates to a parameterized form. Many such parameterizations exist. The ones used

Table 11: Sensitivity of ^{60}Fe production to inclusion of stellar enhancement factors

Primary Fuel	Hydrostatic/ Explosive	T_9	ρ (g/cm^3)	^{60}Fe Mass Fraction without SEF	with SEF
H	Hydrostatic	0.03	5.00×10^{0}	1.009×10^{-44}	8.914×10^{-45}
He	Hydrostatic	0.20	1.00×10^{3}	3.627×10^{-10}	6.523×10^{-10}
He	Explosive	1.00	1.00×10^{4}	1.169×10^{-09}	3.072×10^{-09}
He	Explosive	1.50	1.00×10^{4}	1.621×10^{-05}	6.446×10^{-06}
He	Explosive	2.00	1.00×10^{4}	1.214×10^{-18}	2.211×10^{-18}
He	Explosive	2.50	1.00×10^{4}	1.945×10^{-24}	1.907×10^{-24}
C	Hydrostatic	0.80	1.00×10^{5}	7.617×10^{-07}	1.522×10^{-06}
C	Hydrostatic	1.00	1.00×10^{5}	1.620×10^{-04}	2.067×10^{-04}
C	Hydrostatic	1.20	1.00×10^{5}	3.499×10^{-04}	3.515×10^{-04}
C	Hydrostatic	1.40	1.00×10^{5}	4.805×10^{-04}	3.746×10^{-04}
C	Hydrostatic	1.60	1.00×10^{5}	7.183×10^{-04}	6.287×10^{-04}
C	Hydrostatic	1.80	1.00×10^{5}	6.521×10^{-04}	5.817×10^{-04}
C	Hydrostatic	2.00	1.00×10^{5}	3.892×10^{-04}	3.688×10^{-04}
C	Hydrostatic	2.20	1.00×10^{5}	8.116×10^{-05}	6.198×10^{-05}
C	Explosive	1.60	1.00×10^{5}	1.137×10^{-07}	3.177×10^{-07}
C	Explosive	1.80	1.00×10^{5}	5.630×10^{-05}	1.038×10^{-04}
C	Explosive	2.00	1.00×10^{5}	7.547×10^{-04}	7.267×10^{-04}
C	Explosive	2.20	1.00×10^{5}	8.106×10^{-04}	8.030×10^{-04}
Ne	Hydrostatic	1.00	3.00×10^{5}	7.428×10^{-24}	1.549×10^{-23}
Ne	Hydrostatic	1.30	3.00×10^{5}	6.892×10^{-04}	5.826×10^{-04}
Ne	Hydrostatic	1.50	3.00×10^{5}	6.869×10^{-04}	5.920×10^{-04}
Ne	Hydrostatic	1.70	3.00×10^{5}	6.780×10^{-04}	5.932×10^{-04}
Ne	Hydrostatic	2.00	3.00×10^{5}	4.876×10^{-04}	4.236×10^{-04}
Ne	Hydrostatic	2.30	3.00×10^{5}	1.764×10^{-04}	1.447×10^{-04}
Ne	Hydrostatic	2.50	3.00×10^{5}	4.399×10^{-05}	3.192×10^{-05}
Ne	Explosive	1.80	2.33×10^{5}	7.183×10^{-04}	6.287×10^{-04}
Ne	Explosive	2.00	3.20×10^{5}	7.178×10^{-04}	6.283×10^{-04}
Ne	Explosive	2.20	4.26×10^{5}	6.880×10^{-04}	6.020×10^{-04}
Ne	Explosive	2.30	4.87×10^{5}	5.560×10^{-04}	4.865×10^{-04}
Ne	Explosive	2.40	5.53×10^{5}	2.589×10^{-04}	2.234×10^{-04}
Ne	Explosive	2.50	6.25×10^{5}	6.721×10^{-05}	5.423×10^{-05}
Ne	Explosive	2.70	7.78×10^{5}	2.097×10^{-06}	3.309×10^{-07}
Ne	Explosive	2.90	9.76×10^{5}	1.629×10^{-11}	7.186×10^{-12}
Ne	Explosive	3.20	1.31×10^{6}	4.484×10^{-13}	2.654×10^{-13}
O	Hydrostatic	2.00	5.00×10^{5}	3.378×10^{-21}	3.385×10^{-21}
O	Hydrostatic	2.20	5.00×10^{5}	5.314×10^{-21}	5.741×10^{-21}
O	Explosive	2.50	1.00×10^{6}	6.520×10^{-04}	5.176×10^{-04}
O	Explosive	3.00	1.00×10^{6}	2.185×10^{-10}	1.162×10^{-10}

Table 12: Fitting constants for parameterized neutron capture rates

Reaction	c_0	c_1	c_2	c_3
^{59}Fe(n,γ)^{60}Fe	7.898×10^{6}	-1.515×10^{-1}	4.782×10^{-3}	1.005×10^{-2}
^{60}Fe(n,γ)^{61}Fe	1.383×10^{6}	-7.129×10^{-3}	-1.523×10^{-3}	-6.087×10^{-4}
^{59}Fe(n,γ)^{60}Fe (high)	1.268×10^{7}	-1.349×10^{-1}	3.881×10^{-3}	1.169×10^{-2}
^{60}Fe(n,γ)^{61}Fe (high)	3.546×10^{6}	-1.420×10^{-2}	-8.479×10^{-4}	5.732×10^{-2}
^{59}Fe(n,γ)^{60}Fe (low)	3.920×10^{6}	-1.711×10^{-1}	6.279×10^{-3}	-2.084×10^{-3}
^{60}Fe(n,γ)^{61}Fe (low)	3.516×10^{5}	2.921×10^{-2}	-4.055×10^{-3}	-8.411×10^{-2}
Reaction	c_6	c_7	c_9	
^{59}Fe(n,γ)^{60}Fe	5.309×10^{-3}	7.698×10^{10}	1.024×10^{2}	
^{60}Fe(n,γ)^{61}Fe	1.424×10^{-2}	4.813×10^{9}	6.477×10^{1}	
^{59}Fe(n,γ)^{60}Fe (high)	9.403×10^{-3}	7.698×10^{10}	1.024×10^{2}	
^{60}Fe(n,γ)^{61}Fe (high)	7.860×10^{-3}	4.813×10^{9}	6.477×10^{1}	
^{59}Fe(n,γ)^{60}Fe (low)	4.933×10^{-3}	7.698×10^{10}	1.024×10^{2}	
^{60}Fe(n,γ)^{61}Fe (low)	2.240×10^{-2}	4.813×10^{9}	6.477×10^{1}	

in the current study are given in [13] and [8]. We make particular mention of the form used for neutron capture reactions:

$$\begin{aligned} \lambda^*_{n\gamma} &= c_0\rho\left(\frac{T_9}{0.348}\right)^{c_3}\exp\left[c_1*(T_9-0.348)+c_2*(T_9-0.348)^2\right] \\ \lambda^*_{\gamma n} &= \lambda^*_{n\gamma}c_7\frac{T_9^{3/2}}{\rho}\exp\left[-\frac{c_9}{T_9}\right]\frac{G_{\mathcal{I}}}{G_{\mathcal{L}}}\ . \end{aligned} \tag{158}$$

Equation 157 indicates that c_7 is proportional to a product of statistical factors and masses and c_9 is proportional to the reaction Q-value. The remaining constants (c_0 - c_3) are determined by making a least squares fit to calculated reaction rates. The differences between the calculated rates and the parameterized fits are generally small. Our fits to our recommended ^{59}Fe(n,γ)^{60}Fe and ^{60}Fe(n,γ)^{61}Fe rates, presented in Table 12, do not vary from the calculated rates by more than 4% for any given T_9. The constants c_4, c_5, and c_8 of Equation 158 are zero for each of these fits.

8.4 Nuclear Burning Stages

We now present the results of our nucleosynthesis calculations using ten sets of reaction rates. All calculations were carried out using the single zone nucleosynthesis code BURN [6]. This code embodies the single zone stellar physics discussed in the previous sections. To investigate the sensitivity of ^{60}Fe production to the two capture rates, we consider the following rate sets

- Set 1a: The rates on which the 1995 GCE survey was based [15, 10, 9]. These rates come primarily from [13] and [3]. An additional factor of 1.7 has been applied to the ^{12}C(α,n)^{15}O rate as described in Section 1.4. We will refer to this rate set as the WFHZ set. Sets 1b-1e are based on this set.

- Set 1b: The same as set 1a, except with our recommended rates for ^{59}Fe(n,γ)^{60}Fe and ^{60}Fe(n,γ)^{61}Fe. The initial compositions used in this set are identical to those used in set 1a (initial compositions are determined cumulatively for the other WFHZ rate sets).

- Set 1c: The same as set 1a except with our recommended rates for ^{59}Fe(n,γ)^{60}Fe and ^{60}Fe(n,γ)^{61}Fe. Initial compositions for this set and sets 1d and 1e are determined cumulatively.

- Set 1d: Set 1a except using the upper uncertainty of our recommended rates as shown in Figure 45.

- Set 1e: Set 1a except using the lower uncertainty of our recommended rates as shown in Figure 45.

- Set 2a: The rates used in the more recent stellar evolution survey [7]. These rates come primarily from [8]. An additional factor of 1.2 has been applied to the ^{12}C(α,n)^{15}O rate as described in Section 1.4. We will refer to this rate set as the RT set. Sets 2b-2e are based on this set.

Table 13: Isotopes included in reaction networks

Element	Masses	Element	Masses	Element	Masses	Element	Masses
H	1-3	Na	20-25	Sc	40-51	Ga	67-75
He	3-4	Mg	22-28	Ti	42-52	Ge	68-76
Li	6-7	Al	24-29	V	44-53	As	71-79
Be	7-9	Si	26-34	Cr	46-56	Se	72-82
B	9-11	P	28-35	Mn	48-57	Br	75-85
C	11-14	S	30-38	Fe	50-62	Kr	76-88
N	13-17	Cl	33-39	Co	53-65	Rb	81-89
O	14-20	Ar	34-42	Ni	56-68	Sr	82-90
F	17-21	K	36-43	Cu	61-71	Y	87-91
Ne	18-24	Ca	38-50	Zn	64-74	Zr	90-98

- Set 2b: The same as set 2a, except with our recommended rates for ^{59}Fe(n,γ)^{60}Fe and ^{60}Fe(n,γ)^{61}Fe. The initial compositions used in this set are identical to those used in set 2a. (initial compositions are determined cumulatively for the other RT rate sets).

- Set 2c: The same as set 2a except with our recommended rates for ^{59}Fe(n,γ)^{60}Fe and ^{60}Fe(n,γ)^{61}Fe. The initial compositions for this set and the two sets following are determined cumulatively.

- Set 2d: Set 2a except using the upper uncertainty of our recommended rates as shown in Figure 45.

- Set 2e: Set 2a except using the lower uncertainty of our recommended rates as shown in Figure 45.

Each of these calculations include the network of 336 isotopes presented in Table 13.

For advanced burning stages, we investigate nucleosynthesis over a range of typical temperatures. In the 1995 survey [15], most of the ^{60}Fe was produced in neon burning shells, both pre- and post-explosively. Hence, we focus our attention on these stages in particular, as well as carbon and oxygen burning.

Table 14: ^{26}Al and ^{60}Fe from hydrostatic hydrogen burning

Set	Evolution Time (sec)	^{26}Al Mass Fraction	^{60}Fe Mass Fraction
1a	2.717×10^{15}	5.296×10^{-11}	3.715×10^{-45}
1b	2.717×10^{15}	5.296×10^{-11}	1.004×10^{-44}
1c	2.717×10^{15}	5.296×10^{-11}	1.004×10^{-44}
1d	2.717×10^{15}	5.296×10^{-11}	1.597×10^{-44}
1e	2.717×10^{15}	5.296×10^{-11}	5.167×10^{-45}
2a	2.715×10^{15}	5.108×10^{-11}	1.009×10^{-44}
2b	2.715×10^{15}	5.108×10^{-11}	8.839×10^{-45}
2c	2.715×10^{15}	5.108×10^{-11}	8.839×10^{-45}
2d	2.715×10^{15}	5.108×10^{-11}	1.406×10^{-44}
2e	2.715×10^{15}	5.108×10^{-11}	4.549×10^{-45}

Hydrostatic Hydrogen Burning

We begin our single zone nucleosynthesis with thermodynamic conditions typical of a hydrogen envelope. The nuclear fuel is processed hydrostatically at a temperature of 0.03×10^9 K and a density of 5 g/cm^3. The initial composition of the star is 70.6% ^{1}H and 27.5% ^{4}He, plus solar seeds from [1] (listed in Appendix F).

The primary nuclear processes that occur in hydrogen burning involve the fusion of protons to other very light isotopes (deuterons, ^{3}He, ^{4}He, etc...). Hence the largest nuclear flows result in the production of ^{4}He from ^{1}H. However, there are also significant flows among the carbon and oxygen species producing ^{14}N in the classic CNO cycle. For our purposes, the burn is allowed to continue until the hydrogen fuel is used up, i.e. the mass fraction of hydrogen ($X_{^1H}$) drops below 10^{-5}. The evolution time and resulting mass fractions of ^{26}Al and ^{60}Fe are listed in Table 14.

As expected, the ^{59}Fe(n,γ)^{60}Fe and ^{60}Fe(n,γ)^{61}Fe rates have no detectable effect on the ^{26}Al abundances at this stage. Production of ^{60}Fe is completely insignificant. As explained earlier, ^{60}Fe production will not be appreciable until we reach the advanced nuclear burning stages.

Hydrostatic Helium Burning

Following the depletion of hydrogen, we simulate a helium burning shell. We first explore hydrostatic burning. Typical thermodynamic conditions for this nuclear burning stage, as outlined in [2], consist of a temperature of 0.2×10^9 K and a density of 10^3 g/cm^3. For the initial composition of the helium shell, we take the ashes of the previous respective hydrogen burning (except for rate sets 1b and 2b, which use the hydrogen burning ashes from sets 1a and 2a).

The primary nuclear flow during helium burning is the 3α reaction making ^{12}C, which contributes heavily to the depletion of the helium fuel. Also significant is the production of ^{16}O by ^{12}C(α,γ). ^{22}Ne is also produced in smaller but significant abundances.

The hydrostatic evolution is allowed to proceed until the helium is depleted to a mass fraction less than 10^{-5}. The resulting mass fractions of the two isotopes of interest in the present study are listed in Table 15. Again, the mass fractions for ^{60}Fe are comparatively small (less than $\sim 10^{-7}$), and varying the ^{59}Fe(n,γ)^{60}Fe and ^{60}Fe(n,γ)^{61}Fe rates has a negligible effect on the production of ^{26}Al.

It is interesting to note that the ^{60}Fe mass fractions are considerably, larger than those for ^{26}Al. Intuitively, one would suppose that the lighter isotopes would be produced in greater abundances in the early burning stages. However, ^{26}Al lies on the proton rich side of stability, and cannot be made by the s-process. In stellar environments ^{26}Al is formed by charged particle induced reactions (primarily ^{25}Mg(p,γ)^{26}Al), and the low energy cross sections of such reactions are suppressed by the Coulomb barrier. ^{60}Fe, on the other hand, lies on the neutron rich side of stability and is readily formed via neutron capture, which tends to have large cross sections at low energies.

Table 15: ^{26}Al and ^{60}Fe from hydrostatic helium burning

Set	Evolution Time (sec)	^{26}Al Mass Fraction	^{60}Fe Mass Fraction
1a	4.231×10^{13}	6.240×10^{-19}	2.415×10^{-10}
1b	4.231×10^{13}	6.240×10^{-19}	7.124×10^{-10}
1c	4.231×10^{13}	6.240×10^{-19}	7.124×10^{-10}
1d	4.231×10^{13}	6.240×10^{-19}	5.711×10^{-10}
1e	4.231×10^{13}	6.240×10^{-19}	5.112×10^{-10}
2a	4.166×10^{13}	5.137×10^{-19}	3.627×10^{-10}
2b	4.166×10^{13}	5.137×10^{-19}	6.490×10^{-10}
2c	4.166×10^{13}	5.137×10^{-19}	6.490×10^{-10}
2d	4.166×10^{13}	5.137×10^{-19}	5.244×10^{-10}
2e	4.166×10^{13}	5.137×10^{-19}	4.637×10^{-10}

Explosive Helium Burning

Although ^{60}Fe is not abundantly produced during hydrostatic helium burning, it can be made explosively. As explained previously, we simulate explosive conditions in our single zone calculations via the time dependence of the temperature and density, which are assumed to have initial peak values as the shock enters the shell and subsequently reduce exponentially. We investigate a range of peak temperatures from $T_9 = 1$ to $T_9 = 2.5$, as suggested in [2]. We assume a peak density of 10^4 g/cm^3. The initial composition consists of the ashes of hydrogen burning. The evolution is allowed to continue until the temperature drops below $T_9 = 0.1$

The resulting abundances of ^{26}Al and ^{60}Fe are shown in Table 16. We note that ^{26}Al is produced in great amounts at $T_9 = 1.0$, with the rate sets based on RT (sets 2a-2e) producing roughly four times more than the WFHZ sets. ^{60}Fe is produced in greater abundance at $T_9 = 1.5$. The rate sets based on RT produce nearly 20 times less ^{60}Fe. The production of ^{26}Al is negligibly affected by the ^{59}Fe(n,γ)^{60}Fe and ^{60}Fe(n,γ)^{61}Fe rates at this time. However, the sets that include our recommended rates for these two reactions (1b, 1c, 2b, and 2c) result in ^{60}Fe abundances that are roughly a factor of two smaller that those from the WFHZ

Table 16: ^{26}Al and ^{60}Fe from explosive helium burning

	^{26}Al Mass Fraction			
Set	$T_9 = 1.0$	$T_9 = 1.5$	$T_9 = 2.0$	$T_9 = 2.5$
1a	7.122×10^{-4}	8.224×10^{-11}	4.606×10^{-11}	1.522×10^{-11}
1b	7.122×10^{-4}	8.276×10^{-11}	4.766×10^{-11}	1.541×10^{-11}
1c	7.122×10^{-4}	8.276×10^{-11}	4.766×10^{-11}	1.541×10^{-11}
1d	7.122×10^{-4}	8.270×10^{-11}	4.840×10^{-11}	1.543×10^{-11}
1e	7.122×10^{-4}	8.255×10^{-11}	4.537×10^{-11}	1.528×10^{-11}
2a	2.546×10^{-3}	8.898×10^{-10}	1.168×10^{-10}	7.780×10^{-10}
2b	2.546×10^{-3}	9.153×10^{-10}	1.179×10^{-10}	7.793×10^{-10}
2c	2.546×10^{-3}	9.153×10^{-10}	1.179×10^{-10}	7.793×10^{-10}
2d	2.546×10^{-3}	9.314×10^{-10}	1.180×10^{-10}	7.780×10^{-10}
2e	2.546×10^{-3}	8.702×10^{-10}	1.130×10^{-10}	7.682×10^{-10}
	^{60}Fe Mass Fraction			
Set	$T_9 = 1.0$	$T_9 = 1.5$	$T_9 = 2.0$	$T_9 = 2.5$
1a	1.717×10^{-9}	2.119×10^{-4}	1.422×10^{-19}	8.084×10^{-25}
1b	8.887×10^{-9}	1.154×10^{-4}	1.027×10^{-19}	7.180×10^{-25}
1c	8.887×10^{-9}	1.154×10^{-4}	1.027×10^{-19}	7.180×10^{-25}
1d	1.390×10^{-8}	3.698×10^{-5}	1.206×10^{-19}	7.155×10^{-25}
1e	4.421×10^{-9}	2.845×10^{-4}	1.766×10^{-19}	8.391×10^{-25}
2a	1.169×10^{-9}	1.621×10^{-5}	1.214×10^{-18}	1.945×10^{-24}
2b	3.183×10^{-9}	6.585×10^{-6}	2.332×10^{-18}	1.905×10^{-24}
2c	3.183×10^{-9}	6.585×10^{-6}	2.332×10^{-18}	1.905×10^{-24}
2d	5.050×10^{-9}	1.458×10^{-6}	3.408×10^{-18}	1.895×10^{-24}
2e	1.567×10^{-9}	2.916×10^{-5}	1.881×10^{-18}	2.071×10^{-24}

and RT sets (1a and 2a). Using the upper and lower values of our rates results in lower and higher abundances, respectively. This possibly suggests that at this stage of nuclear burning the destruction reaction out of ^{60}Fe is more significant (i.e. When both rates are higher there is a greater production of ^{60}Fe, but also a greater depletion of ^{60}Fe via ^{60}Fe(n,γ)^{61}Fe).

Hydrostatic Carbon Burning

In the carbon burning phase, the reaction of primary importance is the fusion of ^{12}C forming ^{24}Mg in an excited state, which subsequently decays by particle emission to ^{23}Mg, ^{20}Ne, or ^{23}Na. The decay to ^{23}Mg is endothermic, but could possibly be

a significant source of neutrons. Other reactions of secondary importance occur at this stage as well. The ^{23}Na(p,α)^{20}Ne converts most of the sodium produced by carbon fusion into neon. The neon may then subsequently capture alpha particles and produce ^{24}Mg. These latter two nuclides, ^{20}Ne and ^{24}Mg, are the chief products of carbon burning.

In our analysis, we consider a range of temperatures for hydrostatic carbon burning from $T_9 = 1.2$ to $T_9 = 2.2$. The evolution continues until the mass fraction of ^{12}C drops below 10^{-3}. The evolution time varies according to temperature. For $T_9 = 1.2$, carbon burning continues for a period of $\sim 2.9 \times 10^7$ seconds. At $T_9 = 1.6$, the time has reduced to $\sim 3.2 \times 10^4$ seconds. For every increase of 2×10^8 K in temperature thereafter, the evolution time drops by roughly an order of magnitude, so that at $T_9 = 2.2$ the whole process occurs in ~ 37 seconds. Variations in evolution time between the rate sets is always within 10% and usually within 5%. Temperatures below $T_9 = 1.2$ were also considered. These low temperatures resulted in ^{60}Fe abundances several orders of magnitude smaller than those at $T_9 = 1.2$, and are not included in the results presented here. We assume a density of 10^5 g/cm^3 in all cases. Initial compositions are the ashes of the respective hydrostatic helium burning, with the appropriate exceptions made for sets 1b and 2b. The results are summarized in Table 17.

The ^{26}Al abundances are similar for all rate sets, even between those based on RT and WFHZ. Our recommended rates generally result in a slightly reduced abundance of ^{60}Fe at $T_9 = 1.5$, where the production of ^{60}Fe is most significant. Again we note that the rate sets using the upper limits of uncertainty in our calculated ^{59}Fe(n,γ)^{60}Fe and ^{60}Fe(n,γ)^{61}Fe rates (sets 1d and 2d) result in smaller abundances of ^{60}Fe, while the lower rates (sets 1e and 2e) result in larger abundances. Interestingly enough, at $T_9 = 2.0$, the production of ^{60}Fe shows little sensitivity to the ^{59}Fe(n,γ)^{60}Fe and ^{60}Fe(n,γ)^{61}Fe rates.

Table 17: ^{26}Al and ^{60}Fe from hydrostatic carbon burning

	^{26}Al Mass Fraction					
Set	$T_9 = 1.2$	$T_9 = 1.4$	$T_9 = 1.6$	$T_9 = 1.8$	$T_9 = 2.0$	$T_9 = 2.2$
1a	3.94×10^{-10}	3.10×10^{-8}	9.11×10^{-6}	6.52×10^{-5}	1.71×10^{-5}	6.15×10^{-7}
1b	4.14×10^{-10}	3.09×10^{-8}	9.08×10^{-6}	6.75×10^{-5}	1.84×10^{-5}	7.17×10^{-7}
1c	4.14×10^{-10}	3.09×10^{-8}	9.08×10^{-6}	6.75×10^{-5}	1.84×10^{-5}	7.17×10^{-7}
1d	3.55×10^{-10}	3.14×10^{-8}	9.10×10^{-6}	7.03×10^{-5}	1.90×10^{-5}	6.86×10^{-7}
1e	3.77×10^{-10}	3.12×10^{-8}	9.17×10^{-6}	6.51×10^{-5}	1.88×10^{-5}	7.06×10^{-7}
2a	5.08×10^{-10}	4.03×10^{-8}	9.80×10^{-6}	4.58×10^{-5}	1.29×10^{-5}	7.08×10^{-7}
2b	4.97×10^{-10}	3.85×10^{-8}	9.74×10^{-6}	4.78×10^{-5}	1.22×10^{-5}	6.71×10^{-7}
2c	4.97×10^{-10}	3.85×10^{-8}	9.74×10^{-6}	4.78×10^{-5}	1.22×10^{-5}	6.71×10^{-7}
2d	4.92×10^{-10}	4.12×10^{-8}	9.69×10^{-6}	4.79×10^{-5}	1.23×10^{-5}	7.39×10^{-7}
2e	5.22×10^{-10}	4.12×10^{-8}	9.80×10^{-6}	5.00×10^{-5}	1.29×10^{-5}	7.32×10^{-7}
	^{60}Fe Mass Fraction					
Set	$T_9 = 1.2$	$T_9 = 1.4$	$T_9 = 1.6$	$T_9 = 1.8$	$T_9 = 2.0$	$T_9 = 2.2$
1a	2.64×10^{-6}	2.35×10^{-4}	4.70×10^{-4}	5.81×10^{-4}	4.12×10^{-4}	1.49×10^{-4}
1b	2.12×10^{-6}	1.02×10^{-4}	3.16×10^{-4}	4.51×10^{-4}	3.77×10^{-4}	1.11×10^{-4}
1c	2.12×10^{-6}	1.02×10^{-4}	3.16×10^{-4}	4.51×10^{-4}	3.77×10^{-4}	1.11×10^{-4}
1d	4.84×10^{-7}	2.80×10^{-5}	2.37×10^{-4}	3.85×10^{-4}	3.52×10^{-4}	8.49×10^{-5}
1e	3.65×10^{-6}	3.11×10^{-4}	5.84×10^{-4}	6.51×10^{-4}	4.46×10^{-4}	1.40×10^{-4}
2a	3.50×10^{-4}	4.81×10^{-4}	7.18×10^{-4}	6.52×10^{-4}	3.89×10^{-4}	8.12×10^{-5}
2b	3.56×10^{-4}	3.80×10^{-4}	6.31×10^{-4}	5.82×10^{-4}	3.68×10^{-4}	5.89×10^{-5}
2c	3.56×10^{-4}	3.80×10^{-4}	6.31×10^{-4}	5.82×10^{-4}	3.68×10^{-4}	5.89×10^{-5}
2d	1.79×10^{-4}	1.67×10^{-4}	5.17×10^{-4}	5.26×10^{-4}	3.53×10^{-4}	4.51×10^{-5}
2e	4.63×10^{-4}	6.60×10^{-4}	8.44×10^{-4}	7.28×10^{-4}	4.02×10^{-4}	7.63×10^{-5}

Explosive Carbon Burning

Any significant amount of ^{60}Fe produced in hydrostatic carbon burning was made within the first second. We should thus expect that the production of ^{60}Fe in explosive carbon burning will be similar to the maximum abundances produced in the hydrostatic case. For these explosive calculations, we use the ashes of helium burning as our initial composition. We consider peak temperatures ranging from $T_9 = 1.6$ to $T_9 = 2.2$, with the peak density being 10^5 g/cm^3 in all cases. The evolution continues until the temperature drops to $T_9 = 0.1$. Results are given in Table 18.

Table 18: ^{26}Al and ^{60}Fe from explosive carbon burning

	^{26}Al Mass Fraction			
Set	$T_9 = 1.6$	$T_9 = 1.8$	$T_9 = 2.0$	$T_9 = 2.2$
1a	2.450×10^{-6}	2.823×10^{-6}	6.205×10^{-5}	2.070×10^{-4}
1b	2.464×10^{-6}	3.090×10^{-6}	6.253×10^{-5}	2.073×10^{-4}
1c	2.464×10^{-6}	3.090×10^{-6}	6.253×10^{-5}	2.073×10^{-4}
1d	2.490×10^{-6}	3.215×10^{-6}	6.297×10^{-5}	2.074×10^{-4}
1e	2.457×10^{-6}	2.904×10^{-6}	6.179×10^{-5}	2.071×10^{-4}
2a	2.881×10^{-6}	2.534×10^{-6}	1.190×10^{-5}	6.658×10^{-5}
2b	2.882×10^{-6}	2.566×10^{-6}	1.223×10^{-5}	6.665×10^{-5}
2c	2.882×10^{-6}	2.566×10^{-6}	1.223×10^{-5}	6.665×10^{-5}
2d	2.883×10^{-6}	2.591×10^{-6}	1.248×10^{-5}	6.667×10^{-5}
2e	2.881×10^{-6}	2.543×10^{-6}	1.179×10^{-5}	6.659×10^{-5}
	^{60}Fe Mass Fraction			
Set	$T_9 = 1.6$	$T_9 = 1.8$	$T_9 = 2.0$	$T_9 = 2.2$
1a	1.276×10^{-6}	1.806×10^{-4}	6.987×10^{-4}	7.397×10^{-4}
1b	6.239×10^{-6}	2.907×10^{-4}	6.926×10^{-4}	7.527×10^{-4}
1c	6.239×10^{-6}	2.907×10^{-4}	6.926×10^{-4}	7.527×10^{-4}
1d	8.823×10^{-6}	1.870×10^{-4}	6.447×10^{-4}	7.406×10^{-4}
1e	3.338×10^{-6}	3.249×10^{-4}	8.292×10^{-4}	7.925×10^{-4}
2a	1.137×10^{-7}	5.630×10^{-5}	7.547×10^{-4}	8.106×10^{-4}
2b	3.396×10^{-7}	1.082×10^{-4}	7.280×10^{-4}	8.025×10^{-4}
2c	3.399×10^{-7}	1.083×10^{-4}	7.280×10^{-4}	8.025×10^{-4}
2d	5.391×10^{-7}	1.048×10^{-4}	6.793×10^{-4}	7.963×10^{-4}
2e	1.660×10^{-7}	7.936×10^{-5}	8.544×10^{-4}	8.217×10^{-4}

Again, we see no significant change in ^{26}Al abundances when the ^{59}Fe(n,γ)^{60}Fe and ^{60}Fe(n,γ)^{61}Fe rates are modified. More significant (though still relatively minor) differences arise between the sets based on WFHZ and those based on RT, with RT producing less ^{26}Al at higher temperatures. The production of ^{60}Fe is mostly independent of the rate set for the two higher temperatures. For $T_9 = 1.6$ and $T_9 = 1.8$, the RT sets produce less ^{60}Fe than the WFHZ sets by factors of ~ 10 and ~ 2, respectively. In the previous burning stages, our recommended rates generally led to smaller ^{60}Fe abundances. In explosive carbon burning, this is no longer the case. For the two higher temperatures, the production is roughly the same when our rates are substituted. Using our rates at the lower temperatures results in more

^{60}Fe by a factor of 2-3.

Another interesting occurrence at these lower temperatures has to do with the upper and lower limits of our recommended cross sections. In the previous stages, the lower cross sections resulted in greater abundances of ^{60}Fe and vice versa. The $T_9 = 1.6$ results show an opposite effect: the higher cross sections result in greater abundances. Here it is more likely that the destruction of ^{60}Fe by neutron capture does not play as large a role.

We now should emphasize a key result. Although our recommended ^{59}Fe(n,γ)^{60}Fe and ^{60}Fe(n,γ)^{61}Fe rates tend to result in somewhat smaller ^{60}Fe abundances, the differences arising from the base set of rates used (WFHZ v. RT) appear to be more significant. In the hydrostatic stages where ^{60}Fe production is significant (i.e. carbon burning), RT based rates produce more ^{60}Fe than WFHZ based rates. In explosive nucleosynthesis the RT sets produce somewhat less ^{60}Fe. This perhaps implies that the ^{59}Fe(n,γ)^{60}Fe and ^{60}Fe(n,γ)^{61}Fe rates are not the primary underlying cause of the disparity between the flux ratio calculated in the most recent nucleosynthesis and observation. More will be said about this issue in Section 8.5 and the conclusions.

Additionally, in previous studies ^{60}Fe was produced primarily in the neon burning shell [9]. What we are seeing here is ^{60}Fe is being produced abundantly in thermodynamic conditions typical of carbon burning.

Hydrostatic Neon Burning

The issue of initial compositions becomes somewhat more complex once we reach neon burning. Since our primary goal is to study the uncertainties in ^{60}Fe production based on the two capture rates, and since the production of ^{26}Al will show only a minimal sensitivity to these rates, we would like to use the ashes of the hydrostatic carbon burning that produced the greatest abundance of ^{60}Fe. For all of the WFHZ

based sets, these are the ashes from $T_9 = 1.8$. However, for the RT set (2a), more ^{60}Fe is produced at $T_9 = 1.6$. We desire to maintain consistency between sets based on RT and sets based on WFHZ, and thus use the ashes of $T_9 = 1.8$ hydrostatic carbon burning as initial compositions for the WFHZ based sets (1a-1e), and the ashes of $T_9 = 1.6$ for the RT based sets (2a-2e). This means a direct comparison between all sets to gauge the effect of using WFHZ v. RT will no longer be possible. However, we will still be able to investigate the sensitivity to our ^{59}Fe(n,γ)^{60}Fe and ^{60}Fe(n,γ)^{61}Fe rates.

The primary reactions in neon burning ultimately produce oxygen from neon. At temperatures where oxygen fusion is not accessible, the ^{20}Ne(γ,α)^{16}O rate can be significant, and this photodissociation augments the abundance of oxygen fuel. The alpha particles produced may subsequently capture onto ^{16}O or ^{20}Ne, so that ^{24}Mg will also be produced in abundance. Alpha particle capture onto magnesium results in the synthesis of silicon.

For hydrostatic neon burning, we consider temperatures ranging from $T_9 = 1.3$ to $T_9 = 2.5$, and a density of 3×10^5 g/cm^3. The composition evolves at these temperatures and densities until the mass fraction of ^{20}Ne drops below 10^{-3}. Typical timescales for this evolution range from 10^{10} seconds to 10^{-2} seconds, with the longer times associated with the lower temperatures. Since the initial compositions of the RT and WFHZ sets are different, the evolution times differ, though never by more than 50%. Varying only the the ^{59}Fe(n,γ)^{60}Fe and ^{60}Fe(n,γ)^{61}Fe rates changes the evolution time by only $\sim$5%.

The abundances of ^{26}Al and ^{60}Fe following hydrostatic neon burning are shown in Table 19. At low temperatures the abundances of ^{26}Al are small. This is also true for ^{60}Fe in the WFHZ based sets, with ^{60}Fe abundances not being significant until $T_9 = 1.7$. For $T_9 > 1.5$ in the WFHZ sets and for all T_9 in the RT sets, the ^{60}Fe abundances are similar to those used in the initial compositions (see Table

Table 19: ^{26}Al and ^{60}Fe from hydrostatic neon burning

			^{26}Al Mass Fraction			
Set	$T_9 = 1.3$	$T_9 = 1.5$	$T_9 = 1.7$	$T_9 = 2.0$	$T_9 = 2.3$	$T_9 = 2.5$
1a	5.00×10^{-13}	7.24×10^{-10}	3.39×10^{-7}	7.51×10^{-5}	5.99×10^{-5}	4.35×10^{-5}
1b	5.00×10^{-13}	7.24×10^{-10}	3.39×10^{-7}	7.51×10^{-5}	5.99×10^{-5}	4.37×10^{-5}
1c	4.80×10^{-13}	7.48×10^{-10}	3.37×10^{-7}	7.69×10^{-5}	6.34×10^{-5}	4.47×10^{-5}
1d	5.09×10^{-13}	7.32×10^{-10}	3.30×10^{-7}	7.36×10^{-5}	6.01×10^{-5}	4.62×10^{-5}
1e	4.90×10^{-13}	7.62×10^{-10}	3.36×10^{-7}	7.51×10^{-5}	6.23×10^{-5}	4.41×10^{-5}
2a	1.91×10^{-12}	2.47×10^{-9}	7.13×10^{-7}	4.21×10^{-5}	2.48×10^{-5}	1.60×10^{-5}
2b	1.91×10^{-12}	2.47×10^{-9}	7.23×10^{-7}	4.21×10^{-5}	2.46×10^{-5}	1.59×10^{-5}
2c	1.77×10^{-12}	2.40×10^{-9}	6.68×10^{-7}	4.26×10^{-5}	2.38×10^{-5}	1.65×10^{-5}
2d	1.80×10^{-12}	2.70×10^{-9}	7.66×10^{-7}	4.42×10^{-5}	2.43×10^{-5}	1.67×10^{-5}
2e	1.89×10^{-12}	2.47×10^{-9}	6.84×10^{-7}	4.21×10^{-5}	2.41×10^{-5}	1.65×10^{-5}
			^{60}Fe Mass Fraction			
Set	$T_9 = 1.3$	$T_9 = 1.5$	$T_9 = 1.7$	$T_9 = 2.0$	$T_9 = 2.3$	$T_9 = 2.5$
1a	1.52×10^{-16}	1.27×10^{-13}	3.07×10^{-4}	5.48×10^{-4}	4.99×10^{-4}	4.38×10^{-4}
1b	1.52×10^{-16}	1.62×10^{-13}	3.07×10^{-4}	5.44×10^{-4}	4.76×10^{-4}	3.78×10^{-4}
1c	7.20×10^{-17}	7.19×10^{-14}	2.37×10^{-4}	4.22×10^{-4}	3.68×10^{-4}	2.91×10^{-4}
1d	6.42×10^{-17}	6.66×10^{-14}	2.00×10^{-4}	3.57×10^{-4}	2.99×10^{-4}	2.19×10^{-4}
1e	1.08×10^{-16}	9.83×10^{-14}	3.43×10^{-4}	6.13×10^{-4}	5.50×10^{-4}	4.65×10^{-4}
2a	6.89×10^{-4}	6.87×10^{-4}	6.78×10^{-4}	4.88×10^{-4}	1.76×10^{-4}	4.40×10^{-5}
2b	6.66×10^{-4}	6.81×10^{-4}	6.82×10^{-4}	4.86×10^{-4}	1.65×10^{-4}	3.52×10^{-5}
2c	5.85×10^{-4}	5.94×10^{-4}	5.95×10^{-4}	4.25×10^{-4}	1.44×10^{-4}	3.09×10^{-5}
2d	4.25×10^{-4}	4.77×10^{-4}	4.88×10^{-4}	3.47×10^{-4}	1.11×10^{-4}	2.09×10^{-5}
2e	8.27×10^{-4}	8.19×10^{-4}	7.96×10^{-4}	5.72×10^{-4}	2.04×10^{-4}	4.97×10^{-5}

17). The general trend appears to be that the abundance of ^{60}Fe does not change much during the course of neon burning. The nuclide exists essentially in statistical equilibrium, being produced and destroyed at roughly the same rate. In no case has the abundance of ^{60}Fe increased significantly. This again suggests that most of the ^{60}Fe is made in conditions typical of hydrostatic carbon burning.

Explosive Neon Burning

For explosive neon burning, we consider peak temperatures ranging from $T_9 = 1.8$ to $T_9 = 3.2$. In massive stars, the entropy in the convective neon burning shell is roughly constant prior to and after the shock. This condition results in a relationship

Table 20: ^{26}Al and ^{60}Fe from explosive neon burning

	^{26}Al Mass Fraction				
Set	$T_9 = 1.8$	$T_9 = 2.0$	$T_9 = 2.2$	$T_9 = 2.3$	$T_9 = 2.4$
1a	6.503×10^{-5}	6.540×10^{-5}	7.604×10^{-5}	1.040×10^{-4}	1.251×10^{-4}
1b	6.503×10^{-5}	6.540×10^{-5}	7.604×10^{-5}	1.040×10^{-4}	1.251×10^{-4}
1c	6.734×10^{-5}	6.772×10^{-5}	7.868×10^{-5}	1.073×10^{-4}	1.285×10^{-4}
1d	7.014×10^{-5}	7.054×10^{-5}	8.188×10^{-5}	1.114×10^{-4}	1.323×10^{-4}
1e	6.489×10^{-5}	6.526×10^{-5}	7.588×10^{-5}	1.038×10^{-4}	1.252×10^{-4}
2a	9.957×10^{-6}	2.282×10^{-5}	1.419×10^{-4}	1.894×10^{-4}	1.255×10^{-4}
2b	9.957×10^{-6}	2.282×10^{-5}	1.420×10^{-4}	1.893×10^{-4}	1.255×10^{-4}
2c	9.890×10^{-6}	2.272×10^{-5}	1.435×10^{-4}	1.905×10^{-4}	1.262×10^{-4}
2d	9.844×10^{-6}	2.265×10^{-5}	1.445×10^{-4}	1.917×10^{-4}	1.268×10^{-4}
2e	9.953×10^{-6}	2.281×10^{-5}	1.419×10^{-4}	1.886×10^{-4}	1.253×10^{-4}
	^{60}Fe Mass Fraction				
Set	$T_9 = 1.8$	$T_9 = 2.0$	$T_9 = 2.2$	$T_9 = 2.3$	$T_9 = 2.4$
1a	5.807×10^{-4}	5.807×10^{-4}	5.784×10^{-4}	5.673×10^{-4}	5.264×10^{-4}
1b	5.807×10^{-4}	5.807×10^{-4}	5.783×10^{-4}	5.660×10^{-4}	5.175×10^{-4}
1c	4.510×10^{-4}	4.509×10^{-4}	4.490×10^{-4}	4.391×10^{-4}	4.002×10^{-4}
1d	3.849×10^{-4}	3.849×10^{-4}	3.831×10^{-4}	3.738×10^{-4}	3.357×10^{-4}
1e	6.509×10^{-4}	6.508×10^{-4}	6.482×10^{-4}	6.353×10^{-4}	5.858×10^{-4}
2a	7.183×10^{-4}	7.178×10^{-4}	6.880×10^{-4}	5.560×10^{-4}	2.589×10^{-4}
2b	7.183×10^{-4}	7.180×10^{-4}	6.904×10^{-4}	5.581×10^{-4}	2.564×10^{-4}
2c	6.307×10^{-4}	6.303×10^{-4}	6.039×10^{-4}	4.880×10^{-4}	2.239×10^{-4}
2d	5.169×10^{-4}	5.166×10^{-4}	4.951×10^{-4}	3.999×10^{-4}	1.816×10^{-4}
2e	8.437×10^{-4}	8.432×10^{-4}	8.079×10^{-4}	6.538×10^{-4}	3.041×10^{-4}

between the peak temperature and density, where $\rho_p = 4 \times 10^4$ g/cm^{3}K^{27} T_{9p}^3 [14]. Initial compositions are the same as those for hydrostatic neon burning. The mass fractions of ^{26}Al and ^{60}Fe resulting from these explosive runs are summarized in Table 20. Note that there are two parts to this table for temperatures of $T_9 < 2.45$ and $T_9 > 2.45$.

While ^{26}Al is being produced at lower temperatures (compare to the initial compositions in Table 17, ^{60}Fe abundances remain essentially unmodified up to temperature of $T_9 = 2.4$. Above $T_9 = 2.4$, the ^{60}Fe begins to be depleted.

Table 20: (continued)

	^{26}Al Mass Fraction			
Set	$T_9 = 2.5$	$T_9 = 2.7$	$T_9 = 2.9$	$T_9 = 3.2$
1a	5.161×10^{-5}	5.645×10^{-7}	6.762×10^{-8}	2.317×10^{-8}
1b	5.181×10^{-5}	5.643×10^{-7}	6.817×10^{-8}	2.274×10^{-8}
1c	5.284×10^{-5}	5.672×10^{-7}	6.842×10^{-8}	2.316×10^{-8}
1d	5.432×10^{-5}	5.677×10^{-7}	6.819×10^{-8}	2.325×10^{-8}
1e	5.164×10^{-5}	5.927×10^{-7}	6.795×10^{-8}	2.306×10^{-8}
2a	4.582×10^{-5}	2.907×10^{-7}	3.452×10^{-8}	1.487×10^{-8}
2b	4.583×10^{-5}	2.905×10^{-7}	3.438×10^{-8}	1.483×10^{-8}
2c	4.599×10^{-5}	2.865×10^{-7}	3.457×10^{-8}	1.513×10^{-8}
2d	4.607×10^{-5}	2.829×10^{-7}	3.490×10^{-8}	1.520×10^{-8}
2e	4.592×10^{-5}	2.912×10^{-7}	3.444×10^{-8}	1.479×10^{-8}
	^{60}Fe Mass Fraction			
Set	$T_9 = 2.5$	$T_9 = 2.7$	$T_9 = 2.9$	$T_9 = 3.2$
1a	4.489×10^{-4}	2.252×10^{-4}	5.174×10^{-7}	2.203×10^{-12}
1b	4.036×10^{-4}	2.248×10^{-5}	2.813×10^{-10}	1.019×10^{-12}
1c	3.107×10^{-4}	1.726×10^{-5}	1.988×10^{-10}	1.169×10^{-12}
1d	2.418×10^{-4}	2.689×10^{-6}	1.471×10^{-10}	8.159×10^{-13}
1e	4.836×10^{-4}	1.093×10^{-4}	4.092×10^{-10}	1.494×10^{-12}
2a	6.721×10^{-5}	2.097×10^{-6}	1.629×10^{-11}	4.484×10^{-13}
2b	6.167×10^{-5}	2.658×10^{-7}	9.228×10^{-12}	2.355×10^{-13}
2c	5.375×10^{-5}	2.282×10^{-7}	6.927×10^{-12}	2.420×10^{-13}
2d	4.074×10^{-5}	2.938×10^{-8}	5.195×10^{-12}	1.389×10^{-13}
2e	7.801×10^{-5}	1.479×10^{-6}	1.133×10^{-11}	3.663×10^{-13}

Hydrostatic and Explosive Oxygen Burning

Little ^{60}Fe has been produced beyond carbon burning in our investigation. Nuclear stages beyond neon burning, such as oxygen and silicon burning, generally occur at higher temperatures. As we have just seen in the neon burning analysis, ^{60}Fe tends to be destroyed at higher temperatures. Thus we can expect no ^{60}Fe to be produced in oxygen burning, and more than likely any existing abundances will be depleted.

The key nuclear process in oxygen burning is the fusion of two ^{16}O to form ^{32}S in an excited state, which subsequently decays via particle emission to ^{31}S, ^{31}P, ^{30}P, and ^{28}Si. In explosive conditions the fusion of ^{16}O and ^{12}C may be of significance, as well as the photodissociation of oxygen via ^{16}O(γ,α)^{12}C. Photodissociation also tends to

destroy elements heavier than iron, and the chief remnants of both hydrostatic and explosive oxygen burning will lie between silicon (Z=14) and chromium (Z=24).

Hydrostatic oxygen burning is considered for temperatures of $T_9 = 2.0$ and $T_9 = 2.2$, using a density of 5×10^5 g/cm^3. The explosive runs are taken at $T_9 = 2.5$ and $T_9 = 3.0$, using a density of 1×10^6 g/cm^3. Initial compositions for the WFHZ based sets are the ashes of hydrostatic neon burning at $T_9 = 2.0$, and the ashes from the $T_9 = 1.3$ hydrostatic neon run for the RT based sets. These compositions were chosen because they are the most rich in ^{60}Fe. Results are given in Table 21. The only case with a significant remnant of ^{60}Fe is explosive oxygen burning at $T_9 = 2.5$. In this case, the zone cools rapidly, reaching a temperature of $T_9 = 0.1$ in ~ 4 seconds. Essentially, there isn't enough time to destroy the ^{60}Fe. However, at higher temperatures the destruction reactions exhaust any ^{60}Fe abundance.

8.5 Analysis of Resulting ^{26}Al and ^{60}Fe Abundances

We now summarize the results of the various single zone nucleosynthesis calculations and make some general statements regarding the abundances of ^{26}Al and ^{60}Fe.

We begin with the sensitivity of the production of ^{26}Al to variations in the ^{59}Fe(n,γ)^{60}Fe and ^{60}Fe(n,γ)^{61}Fe capture rates. We have already seen that this sensitivity is low. The abundances of ^{26}Al are presented graphically in Figures 54 and 55. Figure 54 includes all rate sets based on the WFHZ rates (sets 1a-1e), and Figure 55 includes the RT based sets (sets 2a-2e). The nuclear burning stages considered are listed on the horizontal axis. The stages are named by the primary fuel, whether they are hydrostatic (h) or explosive (x), and the temperature in T_9 (this is the peak temperature for explosive calculations). The lower panel in these figures shows the mass fraction of ^{26}Al resulting from the burning stage listed on the ordinate axis. The upper panel shows the ratio of the ^{26}Al mass fraction for a given rate set compared to the mass fraction in the unmodified base set, i.e. the ratio of

Table 21: ^{26}Al and ^{60}Fe from hydrostatic and explosive oxygen burning

	^{26}Al Mass Fraction			
	Hydrostatic		Explosive	
Set	$T_9 = 2.0$	$T_9 = 2.2$	$T_9 = 2.5$	$T_9 = 3.0$
1a	1.756×10^{-14}	5.015×10^{-13}	1.556×10^{-5}	4.057×10^{-8}
1b	1.879×10^{-14}	4.775×10^{-13}	1.555×10^{-5}	3.997×10^{-8}
1c	1.823×10^{-14}	5.023×10^{-13}	1.588×10^{-5}	3.992×10^{-8}
1d	1.793×10^{-14}	4.708×10^{-13}	1.504×10^{-5}	4.037×10^{-8}
1e	1.795×10^{-14}	4.940×10^{-13}	1.555×10^{-5}	4.027×10^{-8}
2a	6.699×10^{-15}	5.281×10^{-13}	1.065×10^{-5}	5.419×10^{-8}
2b	7.295×10^{-15}	5.172×10^{-13}	1.050×10^{-5}	5.424×10^{-8}
2c	6.896×10^{-15}	5.663×10^{-13}	9.752×10^{-6}	5.415×10^{-8}
2d	7.025×10^{-15}	5.623×10^{-13}	1.003×10^{-5}	5.409×10^{-8}
2e	6.680×10^{-15}	5.500×10^{-13}	1.039×10^{-5}	5.431×10^{-8}
	^{60}Fe Mass Fraction			
	Hydrostatic		Explosive	
Set	$T_9 = 2.0$	$T_9 = 2.2$	$T_9 = 2.5$	$T_9 = 3.0$
1a	2.905×10^{-16}	1.539×10^{-18}	5.272×10^{-4}	2.097×10^{-10}
1b	1.703×10^{-16}	4.296×10^{-19}	4.856×10^{-4}	9.935×10^{-11}
1c	1.736×10^{-16}	4.691×10^{-19}	3.739×10^{-4}	7.963×10^{-11}
1d	1.335×10^{-16}	3.036×10^{-19}	2.974×10^{-4}	5.471×10^{-11}
1e	2.312×10^{-16}	7.884×10^{-19}	5.718×10^{-4}	1.362×10^{-10}
2a	3.378×10^{-21}	5.314×10^{-21}	6.520×10^{-4}	2.185×10^{-10}
2b	3.434×10^{-21}	5.094×10^{-21}	6.030×10^{-4}	1.413×10^{-10}
2c	3.431×10^{-21}	5.762×10^{-21}	5.132×10^{-4}	1.096×10^{-10}
2d	3.509×10^{-21}	6.149×10^{-21}	3.462×10^{-4}	5.930×10^{-11}
2e	3.306×10^{-21}	5.039×10^{-21}	7.677×10^{-4}	2.130×10^{-10}

sets 1b-1e to 1a and sets 2b-2e to 2a. As expected, the production of ^{26}Al is mostly unmodified by variations in the ^{59}Fe(n,γ)^{60}Fe and ^{60}Fe(n,γ)^{61}Fe capture rates. The small variations that do occur can be attributed to changes in the neutron fluxes, e.g. if the ^{60}Fe neutron capture rate is large, there will be fewer neutrons available to destroy ^{26}Al via (n,p) reactions.

Worth noting is the difference in ^{26}Al production in the unmodified WFHZ and RT sets (1a and 2a). The mass fractions are presented in Figure 56, along with the ratio of the RT mass fraction to that from the WFHZ set. In analyzing these results

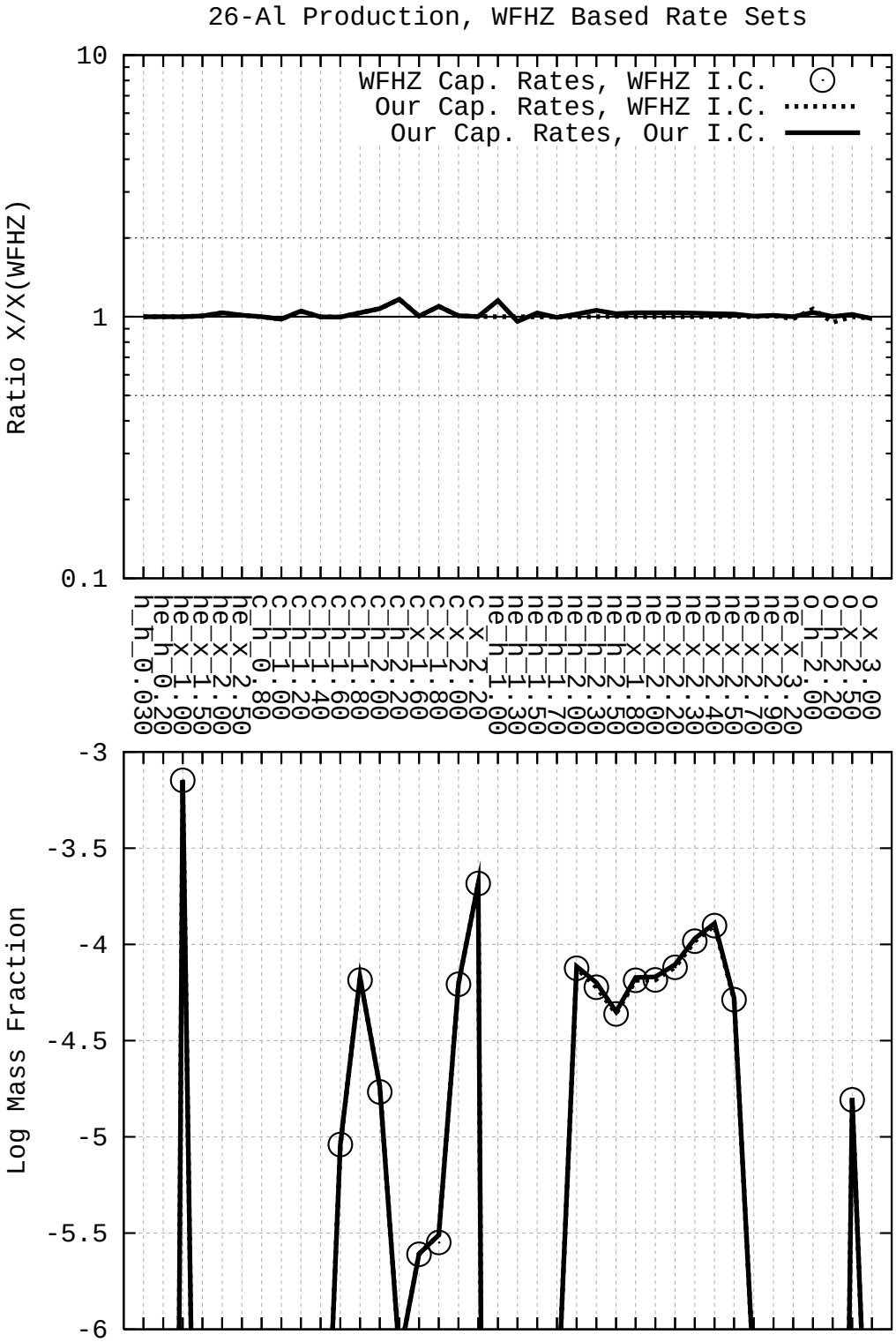

Figure 54: ^{26}Al production using WFHZ based rate sets

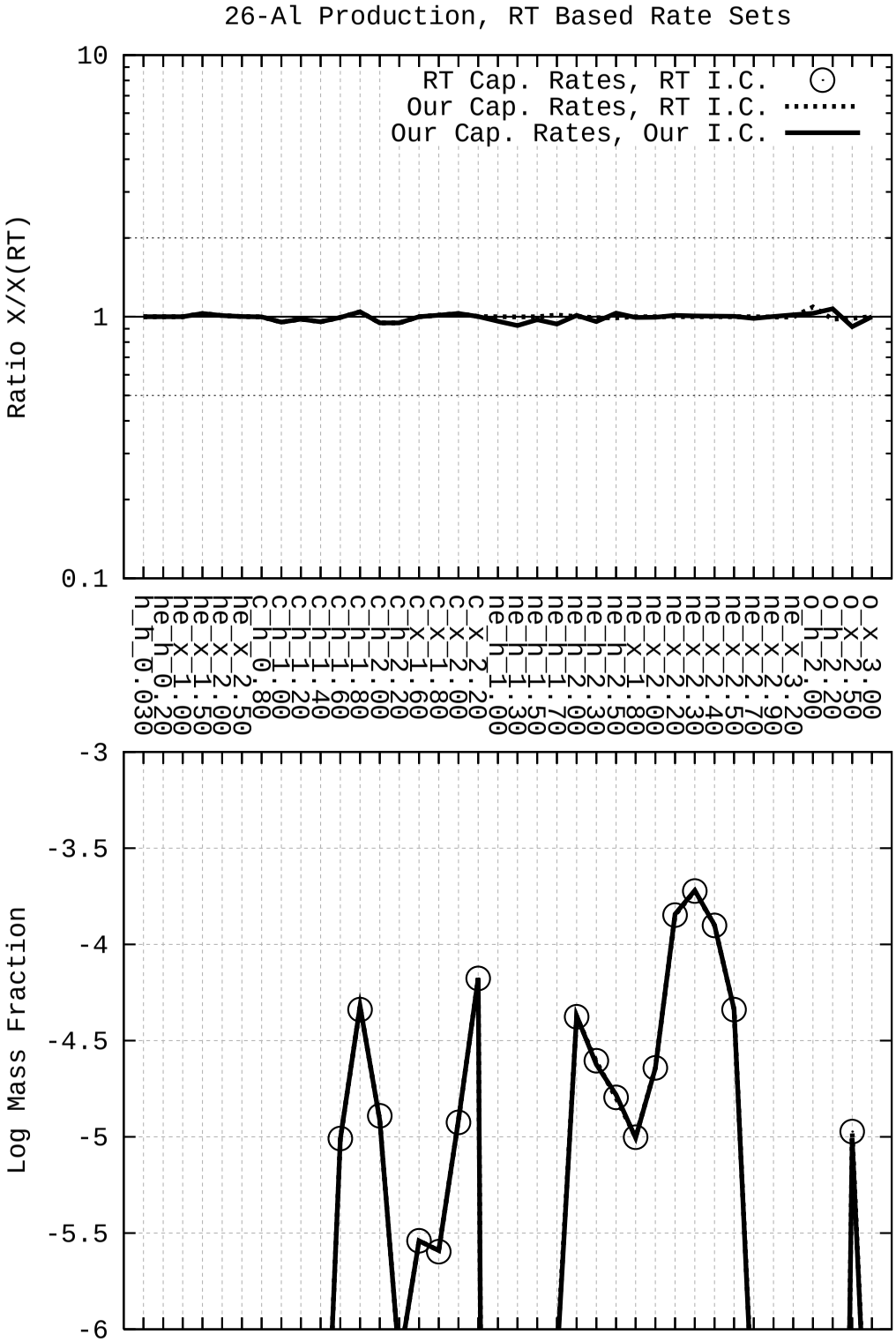

Figure 55: ^{26}Al production using RT based rate sets

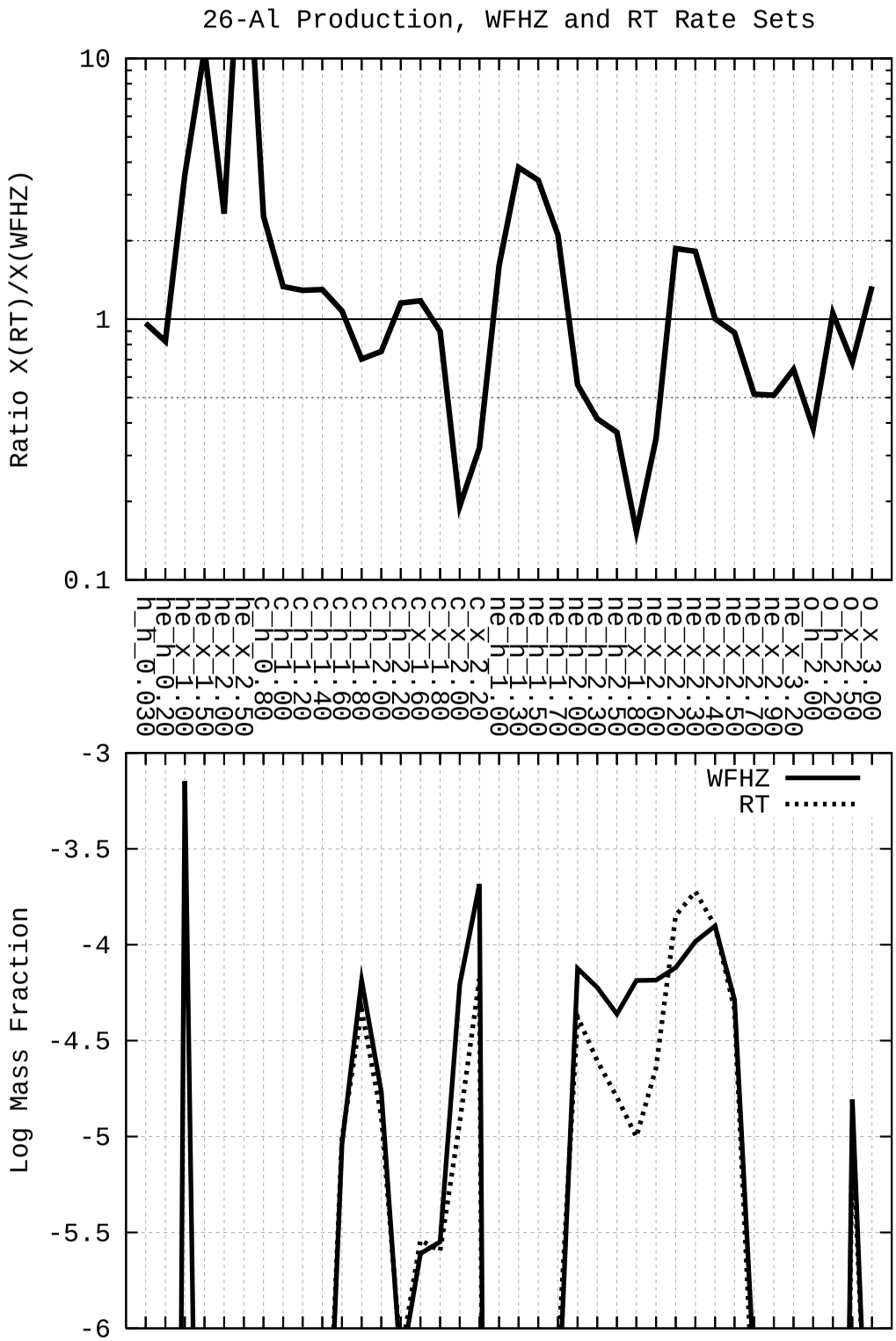

Figure 56: ^{26}Al production using WFHZ and RT rate sets

we must be careful to recall that the advanced burning stages (neon, oxygen) for the two rate sets are using different initial compositions (the WFHZ set uses the ashes of hydrostatic carbon burning at $T_9 = 1.8$ to seed the neon burning runs, while the RT set uses the ashes of hydrostatic carbon burning at $T_9 = 1.6$). A similar statement applies to the initial compositions for oxygen burning. Hence, a direct comparison between the sets can only be made up through the carbon burning stages. However, the abundance of ^{26}Al in the neon and oxygen burning stages is determined primarily by the initial abundance, so a few inferences can be made.

The primary result is that where ^{26}Al is produced most abundantly (such as in hydrostatic carbon burning around $T_9 = 1.8$ and explosive carbon burning around $T_9 = 2.0$), the RT rates yield smaller abundances. The only exception is for explosive neon burning around $T_9 = 2.3$. The decrease can be as large as a factor of 1.5 in the hydrostatic stages and a factor of 6 in the explosive stages. This is significant because it implies that the RT rates will produce less ^{26}Al, and that the resulting ^{60}Fe/^{26}Al flux ratio will be larger. More will be said regarding this issue in the conclusions and summary. In any event, these results indicate that the abundance of ^{26}Al is significantly affected by the base set of rates (WFHZ v. RT), and negligibly affected by the ^{59}Fe(n,γ)^{60}Fe and ^{60}Fe(n,γ)^{61}Fe capture rates as expected.

We now turn our attention to ^{60}Fe production. The results from the various burning stages are summarized in Figures 57 and 58. The information displayed on each of the panels is similar to that for Figures 54 and 55. A comparison of the abundances resulting from the unmodified WFHZ and RT rate sets appears in Figure 59.

Again we note that the initial compositions for neon and oxygen burning are not consistent between these two sets. However, the abundance of ^{60}Fe is generally unmodified during the neon burning stages except at the highest or lowest temperatures, where it is destroyed. When the mass fraction at the end of a neon burning

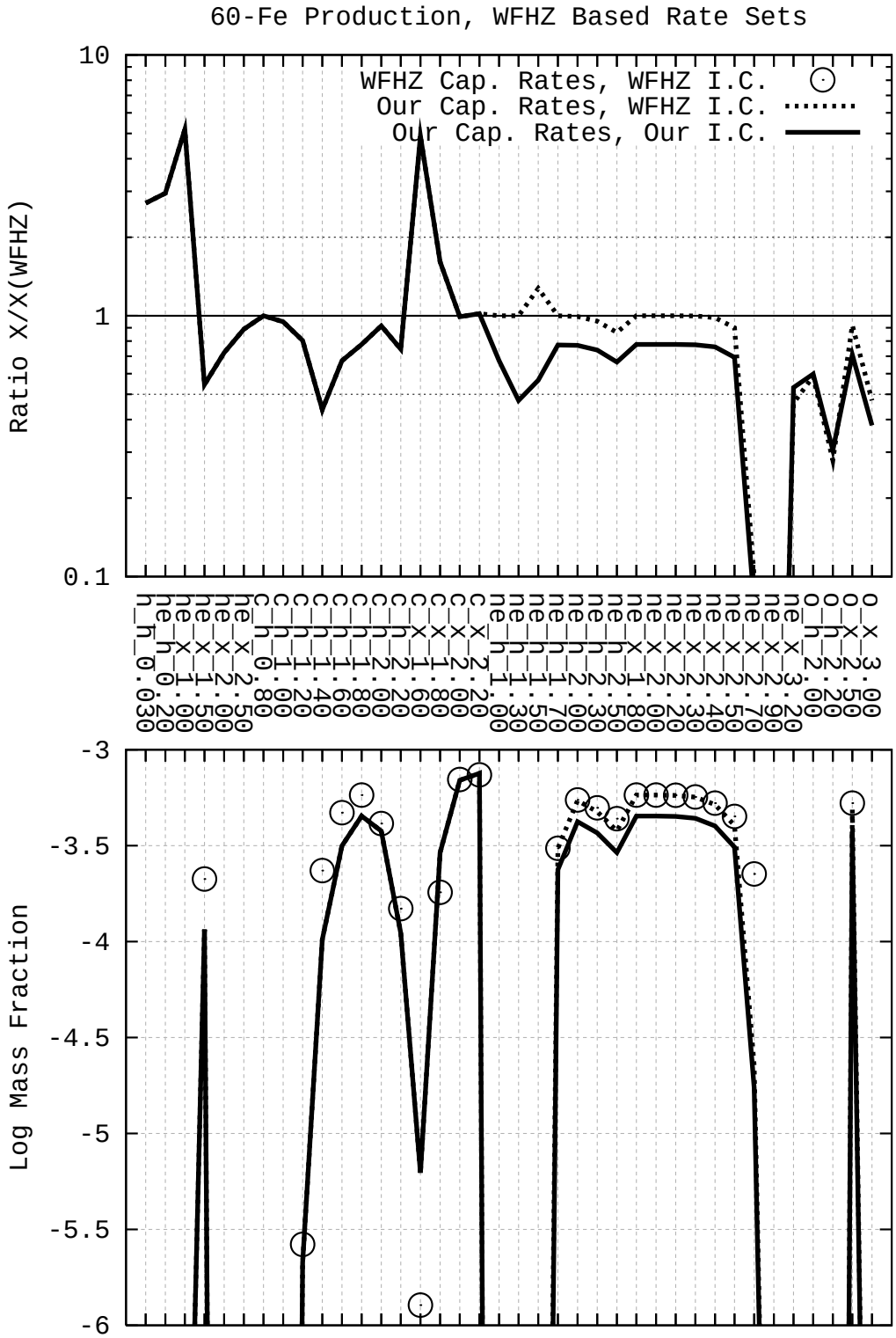

Figure 57: ^{60}Fe production using WFHZ based rate sets

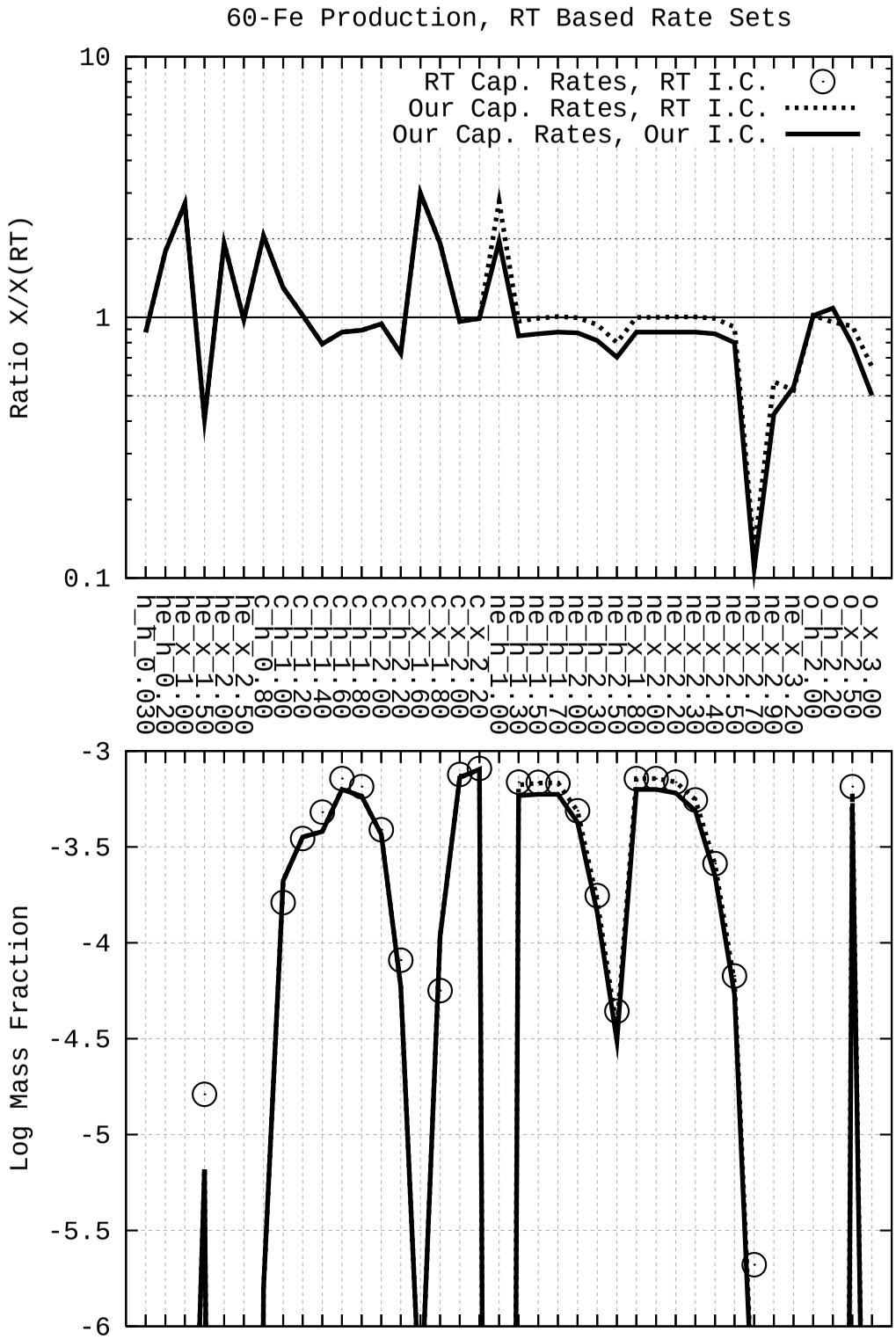

Figure 58: ^{60}Fe production using RT based rate sets

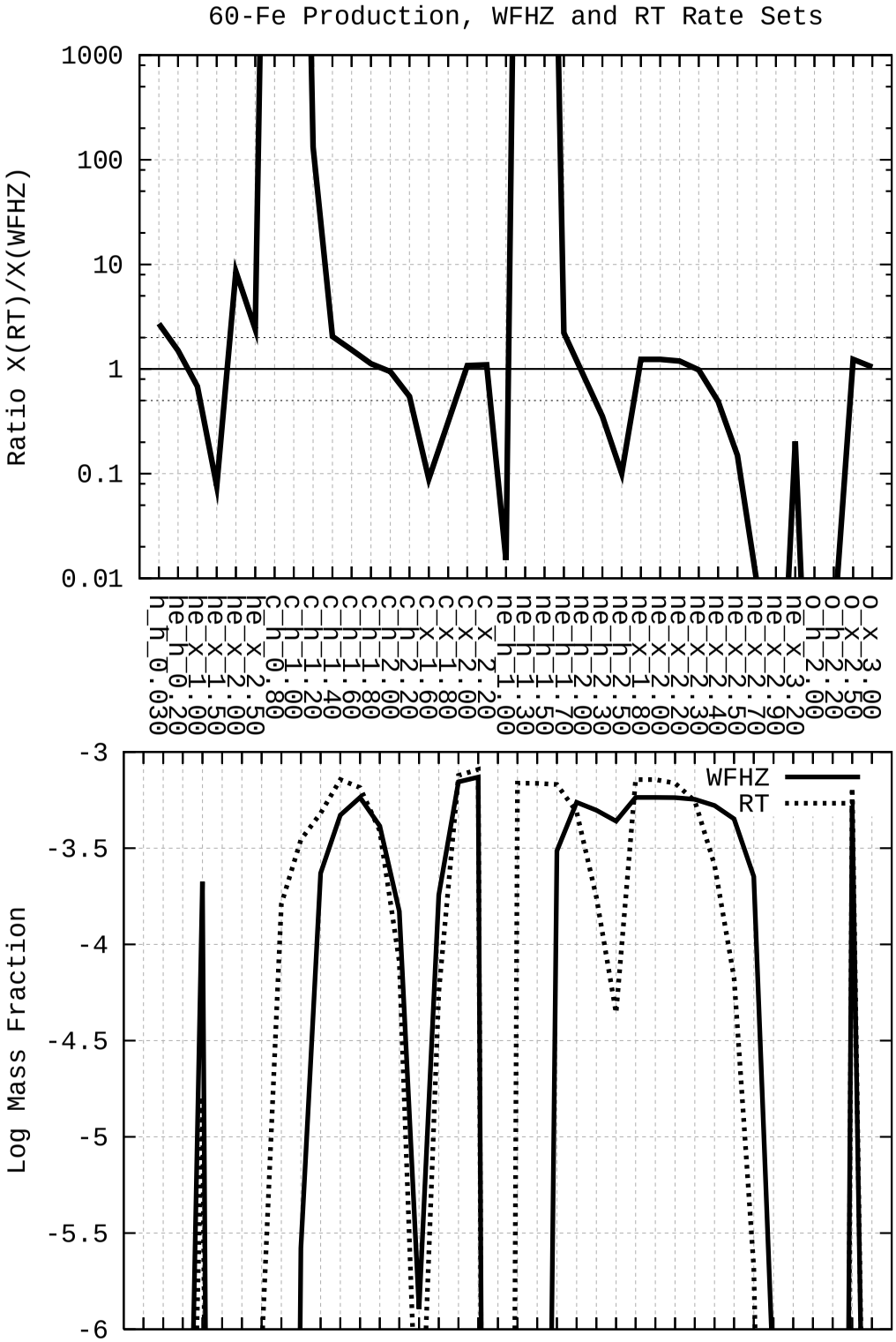

Figure 59: ^{60}Fe production using WFHZ and RT rate sets

stage is significant, it is only because the ^{60}Fe produced during hydrostatic carbon burning remained in nuclear statistical equilibrium. Thus in the neon burning stages the initial compositions have a greater effect on the ^{60}Fe abundances than the ^{59}Fe(n,γ)^{60}Fe and ^{60}Fe(n,γ)^{61}Fe rates.

In the carbon burning phases, where the initial compositions of the WFHZ and RT sets are similar, we note that RT tends to produce more ^{60}Fe, in some cases by several orders of magnitude (e.g. at $T_9 = 1.0$). This again would result in RT producing a larger ^{60}Fe abundance and consequently a larger ^{60}Fe/^{26}Al flux ratio than WFHZ.

When we insert our recommended ^{59}Fe(n,γ)^{60}Fe and ^{60}Fe(n,γ)^{61}Fe rates, the resulting ^{60}Fe abundance is smaller for both rate sets, as can be seen in Figures 57 and 58. Again, the ^{60}Fe mass fraction at the end of any neon burning stage is primarily determined by the initial abundance. This is most apparent in a comparison of the results from the sets using our rates but the initial compositions from WFHZ and RT (the dashed lines on Figures 57 and 58) and those using our rates and initial compositions (the solid lines). Our neutron capture rates result in smaller ^{60}Fe abundances by roughly the same factor for both base rate sets. This seems to indicate that, while the neutron capture rates have a direct effect on the ^{60}Fe abundance, there are likely other rates not considered in this study that significantly affect the overall production of ^{60}Fe. These other rates would most likely affect the production of ^{60}Fe by modifying the flux of neutrons available for capture onto the iron targets.

Last of all, we consider the ratio of ^{60}Fe and ^{26}Al mass fractions. Since the ^{26}Al mass fraction is essentially unaffected by the insertion of our capture rates, one would expect that differences in the ratio will correlate directly with differences in the ^{60}Fe abundances. This is what is seen in Figures 60 and 61. The lower panel shows the log of the ratio of ^{60}Fe and ^{26}Al mass fractions. The upper panel shows

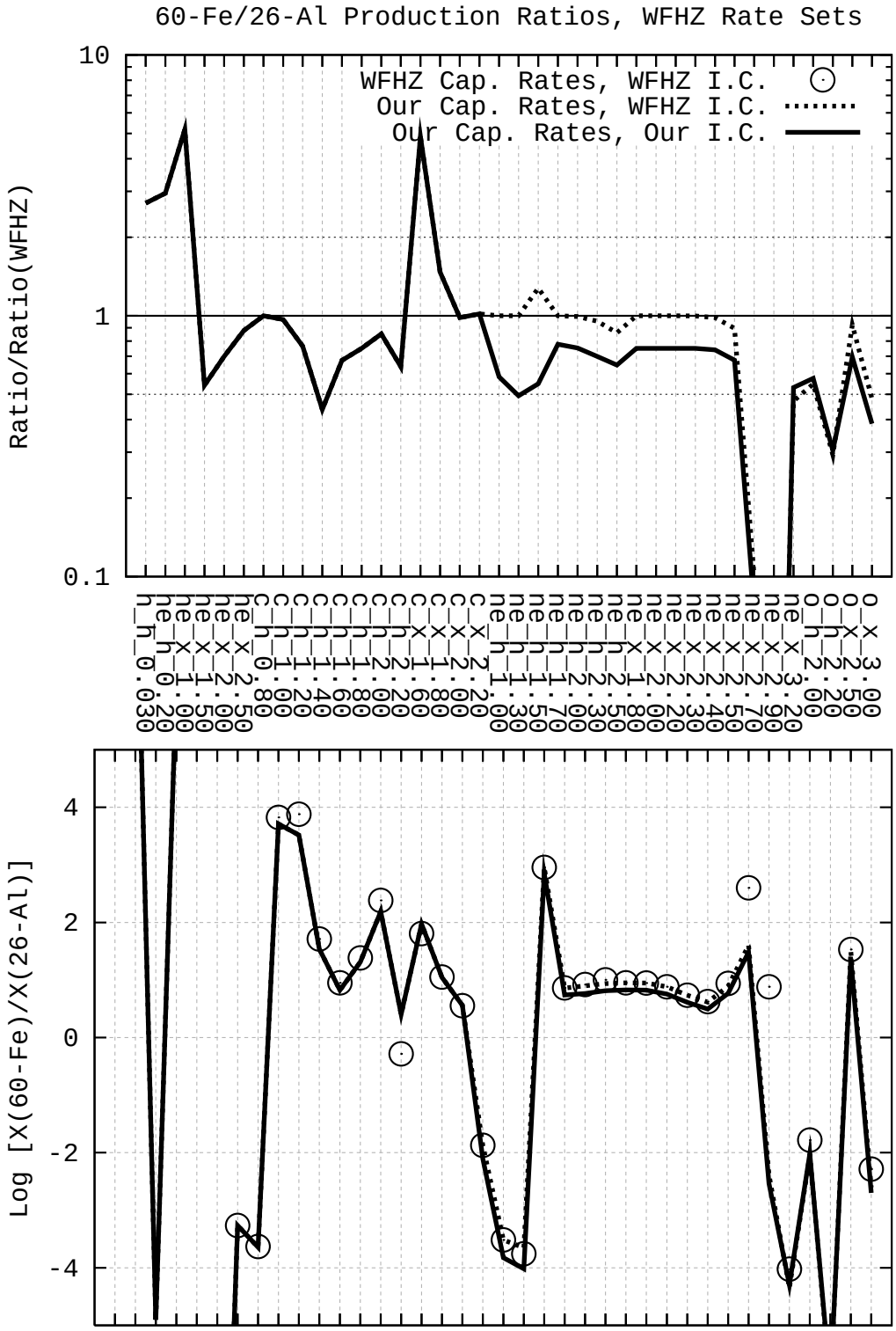

Figure 60: ^{60}Fe/^{26}Al production ratio using WFHZ based rate sets

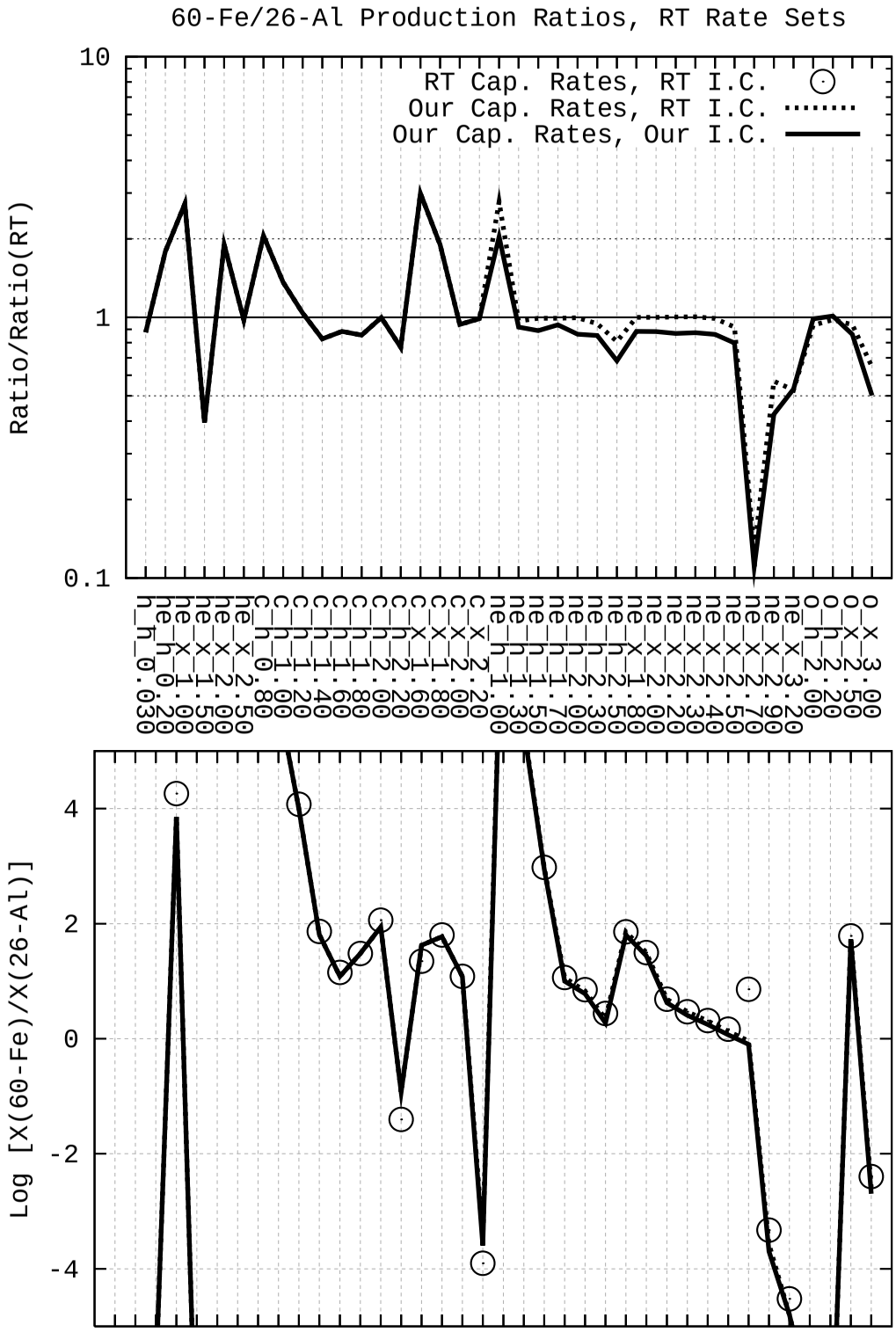

Figure 61: ^{60}Fe/^{26}Al production ratio using RT based rate sets

the ratio obtained using the indicated rate set divided by the ratio using the base set of rates.

Considering primarily the burning stages for which the ^{60}Fe/^{26}Al is the largest, we see that the use of our recommended rates (along with the initial compositions resulting from those rates) lowers the ^{60}Fe/^{26}Al ratio by roughly a factor 1.5 with respect to the WFHZ rates and by a factor of about 1.1 with respect to the RT rates (see the solid lines in Figures 60 and 61). Although this is a move in the right direction with regard to reconciling the RT nucleosynthesis with the observed flux ratio, it also will lower the WFHZ flux ratio (0.16), which is only slightly higher than the observation (0.11±0.03 from INTEGRAL [5]). Even so, the RT flux ratio (∼0.6) exceeds the observation by more than a factor of four, and the reduction in ^{60}Fe abundance suggested in this study likely cannot entirely account for the discrepancy. More will be said regarding these issues in the conclusions.

8.6 A Result From KEPLER

The process of parameterizing the thermodynamic conditions allows us to study the direct effects of the rates on nucleosynthesis. However, there are aspects of stellar environments that may affect the production of a given isotope which are not accounted for in a single zone calculation. For instance, we have seen that the initial composition can have a significant impact on the nucleosynthesis. In a true stellar model, convection may carry stellar matter from one zone to another, which could result in a continuous supply of, say perhaps, new ^{58}Fe nuclei to seed the production of ^{60}Fe.

Stan Woosley has used our recommended capture rates, along with their upper and lower uncertainties, and modeled the production of ^{60}Fe using the stellar evolution code KEPLER [11]. The case chosen was a 25 $M_\odot$ star, which in previous studies had produced large amounts of ^{60}Fe. Using the unmodified WFHZ

rate set, this particular star produced a total of 2.61×10^{-4} $M_\odot$ of ^{60}Fe. Using our recommended rates, the same star produces 1.86×10^{-4} $M_\odot$ of ^{60}Fe – a factor of 1.4 reduction. This is consistent with the single zone results shown in Figure 57. The upper and lower limits of our recommended rates produce 2.85×10^{-4} and 2.27×10^{-4} $M_\odot$, respectively. Such non-monotonic behavior is likely due to the fact that raising the rates will increase both the production and destruction of the isotope. This also is consistent with the results in Figure 57 for carbon burning around $T_9 = 1.4$.

The range in ^{60}Fe abundances resulting from modification of the ^{59}Fe(n,γ)^{60}Fe and ^{60}Fe(n,γ)^{61}Fe capture rates is again too small to account for the discrepancy between the predicted and observed flux ratios. It appears likely that other aspects of nucleosynthesis, be it other reaction rates or stellar structure, will have a greater impact on the ^{60}Fe abundance [11].

References

[1] Anders, E. & Grevesse, N. 1989, Geochim. Cosmochim. Acta, **53**, 197

[2] Audouze, J., Chiosi, C., & Woosley, S.E., 1986, Nucleosynthesis and Chemical Evolution (Switzerland:Geneva Observatory)

[3] Caughlan, G.R. & Fowler, W.A. 1988, At. Data Nucl. Data Tables, **40**, 283

[4] Clayton, D.D. 1968, Principles of Stellar Evolution and Nucleosynthesis (New York:McGraw Hill)

[5] Harris, M.J. 2005, A&A **433**, L49

[6] Hoffman, R.D. 2005, private communication

[7] Rauscher, T., Heger, A., Hoffman, R.D. & Woosley, S.E. 2002, ApJ **576**, 323

[8] Rauscher, T. & Thielemann, F.-K. 2000, At. Data Nucl. Data Tables **75**, 1

[9] Timmes, F.X., Woosley, S.E., Hartmann, D.H., Hoffman, R.D., Weaver, T.A., & Matteucci, F. 1995, ApJ **449**, 204

[10] Timmes, F. X., Woosley, S. E., & Weaver, T. A. 1995, ApJS **98** , 617

[11] Woosley, S.E. 2005, private communication

[12] Woosley, S.E., Arnett, W.D., & Clayton, D.D. 1973, ApJS **26**, 231

[13] Woosley, S.E., Fowler, W.A., Holmes, J.A. & Zimmerman, B.A. 1978, At. Data Nucl. Data Tables, **22**, 371

[14] Woosley, S.E., & Weaver, T.A. 1980, ApJ **238**, 1017

[15] Woosley, S.E., & Weaver, T.A. 1995, ApJS **101**, 181

9 Summary and Conclusions

Recent nucleosynthesis studies have predicted a ^{60}Fe/^{26}Al flux ratio that is several times greater than the observed fluxes [2, 4, 1]. An earlier study [5] had predicted the flux ratio roughly in agreement with the observations. Since the more recent calculations involved well-motivated changes to the stellar and nuclear physics, we desire to know the cause of this discrepancy. Likely candidates in the nuclear aspects of the problem are the ^{59}Fe(n,γ)^{60}Fe and ^{60}Fe(n,γ)^{61}Fe reaction rates, which are the primary production and destruction channels for ^{60}Fe.

We have modeled the ^{59}Fe(n,γ)^{60}Fe and ^{60}Fe(n,γ)^{61}Fe cross sections responsible for the production and destruction of ^{60}Fe in stellar environments. The modeling effort includes the development of local systematics for a number of important input quantities to the Hauser-Feshbach statistical model. These local systematics result in calculations that reproduce measured cross sections to a relatively high degree of accuracy (on average we reproduce recommended neutron capture Maxwellian averaged cross sections to within 31.6%, while within a factor of two is generally considered good). Additionally we have compared our results with calculations used in previous nucleosynthesis studies, and have found better overall agreement with measured data with our modeling effort. The accuracy with which we are able to model measured cross sections gives us confidence that our modeled cross sections for unstable nuclei are reasonable.

We have investigated the sensitivity of the ^{59}Fe(n,γ)^{60}Fe and ^{60}Fe(n,γ)^{61}Fe cross sections to errors and variations in the statistical model input quantities. The cross sections are most sensitive to the overall normalization of the photon transmission coefficient, although significant sensitivities also arise from the nuclear level density (with the associated discrete level scheme), the neutron transmission coefficient, and the overall form of the photon strength function. For the latter two quantities,

we have used modern prescriptions (Koning and Delaroche optical potential for neutron transmission coefficient, enhanced generalized Lorentzian for E1 strength function). Our level densities and photon transmission coefficient normalization are based on local rather than global systematics. The cumulative sensitivity to these input quantities leads us to a rough estimate of the uncertainty in our calculated ^{59}Fe(n,γ)^{60}Fe and ^{60}Fe(n,γ)^{61}Fe cross sections and reaction rates. We find that the more recent cross sections of Rauscher and Thielemann [3] are close to being within this range of uncertainty for both reactions, as is the ^{60}Fe(n,γ)^{61}Fe cross section of Woosley, et al [7]. In both cases our recommended rates are higher than the previous ones.

We have also performed single-zone nucleosynthesis calculations using our recommended ^{59}Fe(n,γ)^{60}Fe and ^{60}Fe(n,γ)^{61}Fe rates along with their upper and lower uncertainties. These calculations were carried out using the rates of two previous nucleosynthesis studies as base sets. The abundance of ^{26}Al is not significantly affected by the capture rates, but is considerably affected by the base set. In the conditions where ^{60}Fe is produced most abundantly, our neutron capture rates result in a smaller ^{60}Fe mass fraction, although the reduction is generally only on the order of 20%. When we use the upper and lower limits of our recommended rates, we see more variation in the ^{60}Fe abundance. However, the uncertainties in these rates can affect a change of no more than a factor of $\sim$1.5. Hence, the uncertainties in these rates cannot be fully responsible for the discrepancy between the observed ^{60}Fe/^{26}Al flux ratio and the value predicted in the latest nucleosynthesis study.

Between the completion of this study and the preparation of this document, other interesting results have come to light. The ^{26}Al(n,p)^{26}Mg rate (the primary destruction reaction for ^{26}Al) used in the latest nucleosynthesis is more than three times larger than that used in the 1995 survey. This could have a significant impact on the ^{26}Al abundance, which in turn would impact the predicted flux ratio, ac-

counting for as much as half of the discrepancy between the predicted and measured values [6]. An initial investigation into this issue using parameterized single zone calculations seems to indicate that this is not the case, and that increasing this rate by a factor of three only has a minimal effect of the ^{26}Al abundance. This particular issue is still under investigation.

Additionally, aspects of the stellar models now appear to be likely causes of the large ^{60}Fe abundances. In particular, the opacities adopted in the latest modeled nucleosynthesis [2] may be at fault. When used in complex stellar evolution codes, the new opacities cause the helium convection zone to recede near the end of helium burning, leaving behind a gradient of He/C. Eventually the helium ignites, producing a miniature convective helium shell that affects the structure of the core and produces large amounts of ^{60}Fe. This effect was not present in the 1995 calculation [6].

In conclusion, the implementation of our newly modeled neutron capture rates can lower the predicted flux ratio, but it now appears more likely that the apparent overproduction of ^{60}Fe in [2] is due primarily to issues pertaining to the stellar model rather than the nuclear physics.

This work was supported in part by the Deparment of Energy (DOE) Program for Scientific Discovery through Advanced Computing (SciDAC; DE-FC02-01ER41176). Portions of this work were performed under the auspices of the U.S. Department of Energy by the University of California Lawrence Livermore National Laboratory under contract W-7405-ENG-48.

References

[1] Harris, M.J. 2005, A&A **433**, L49

[2] Rauscher, T., Heger, A., Hoffman, R.D. & Woosley, S.E. 2002, ApJ **576**, 323

[3] Rauscher, T. & Thielemann, F.-K. 2000, At. Data Nucl. Data Tables **75**, 1

[4] Smith, D.M. 2004, in The INTEGRAL Universe, ed. V. Schönfelder, G.G. Licht & C. Winkler (Noordwljki:ESA), ESA Spec. Publ. 552, 45

[5] Timmes, F.X., Woosley, S.E., Hartmann, D.H., Hoffman, R.D., Weaver, T.A., & Matteucci, F. 1995, ApJ **449**, 204

[6] Woosley, S.E. 2005, private communication

[7] Woosley, S.E., Fowler, W.A., Holmes, J.A. & Zimmerman, B.A. 1978, At. Data Nucl. Data Tables, **22**, 371

A Ground State Nuclear Properties

In this table we present our adopted nuclear ground state spins and parities, as explained in Section 3.1. We also list our adopted nuclear masses, binding energies, and separation energies as explained in Section 3.2. The energies listed are in units of MeV. Masses are in amu.

Table 22: Adopted ground state nuclear properties

Nucleus	J^π	Mass	BE	S_n	S_p	S_α	S_d
^{43}Ca	3.5^-	42.958767	369.828	7.933	10.676	7.590	15.985
^{44}Ca	0^+	43.955482	380.960	11.131	12.164	8.852	19.583
^{45}Ca	3.5^-	44.956184	388.374	7.415	12.291	10.168	17.355
^{46}Ca	0^+	45.953693	398.769	10.394	13.816	11.136	20.461
^{47}Ca	3.5^-	46.954544	406.045	7.276	14.211	12.754	18.868
^{45}Sc	3.5^-	44.955910	387.848	11.323	6.888	7.932	15.795
^{46}Sc	4^+	45.955173	396.608	8.761	8.234	9.159	13.424
^{47}Sc	3.5^-	46.952408	407.255	10.646	8.486	10.162	16.656
^{48}Sc	6^+	47.952232	415.490	8.235	9.445	11.110	14.497
^{49}Sc	3.5^-	48.950024	425.618	10.128	9.627	12.368	17.348
^{50}Sc	5^+	49.952187	431.673	6.056	10.537	11.542	13.459
^{44}Ti	0^+	43.959690	375.475	16.299	8.650	5.126	18.563
^{45}Ti	3.5^-	44.958126	385.003	9.529	8.479	6.292	15.954
^{46}Ti	0^+	45.952633	398.192	13.189	10.345	8.000	19.443
^{47}Ti	2.5^-	46.951763	407.073	8.880	10.464	8.947	17.000
^{48}Ti	0^+	47.947945	418.699	11.627	11.445	9.443	19.866
^{49}Ti	3.5^-	48.947868	426.842	8.142	11.352	10.170	17.363
^{50}Ti	0^+	49.944790	437.781	10.939	12.163	10.715	20.066
^{51}Ti	1.5^-	50.946613	444.153	6.372	12.480	9.811	16.311
^{52}Ti	0^+	51.946896	451.962	7.808	13.536	7.674	18.064
^{53}Ti	1.5^-	52.949726	457.397	5.435	13.761	7.963	16.746
^{54}Ti	0^+	53.951054	464.234	6.837	15.260	8.447	18.374
^{45}V	3.5^-	44.965775	377.095	15.835	1.620	5.661	15.694
^{46}V	0^+	45.960201	390.360	13.265	5.356	7.375	12.660
^{47}V	1.5^-	46.954910	403.360	13.000	5.168	8.238	16.132
^{48}V	4^+	47.952255	413.905	10.545	6.832	9.083	13.488
^{49}V	3.5^-	48.948517	425.457	11.553	6.758	9.313	16.160
^{50}V	6^+	49.947159	434.793	9.336	7.952	9.888	13.870
^{51}V	3.5^-	50.943958	445.845	11.051	8.064	10.293	16.778
^{52}V	3^+	51.944775	453.156	7.311	9.002	9.369	13.150
^{53}V	3.5^-	52.944336	461.635	8.479	9.673	7.720	15.257

Table 22: (continued)

Nucleus	J^π	Mass	BE	S_n	S_p	S_α	S_d
^{54}V	3^+	53.946438	467.748	6.113	10.351	7.778	13.562
^{55}V	3.5^-	54.947235	475.080	7.332	10.846	8.357	15.458
^{56}V	2^+	55.950531	480.080	5.000	11.699	8.147	13.622
^{57}V	1.5^-	56.952560	486.260	6.180	12.541	8.989	15.654
^{47}Cr	1.5^-	46.962898	395.134	13.156	4.774	7.661	15.815
^{48}Cr	0^+	47.954033	411.466	16.332	8.106	7.694	18.882
^{49}Cr	2.5^-	48.951336	422.049	10.583	8.144	8.748	16.464
^{50}Cr	0^+	49.946045	435.049	13.000	9.592	8.560	18.920
^{51}Cr	3.5^-	50.944767	444.310	9.261	9.516	8.940	16.628
^{52}Cr	0^+	51.940506	456.349	12.039	10.504	9.353	19.331
^{53}Cr	1.5^-	52.940651	464.288	7.939	11.132	9.150	16.219
^{54}Cr	0^+	53.938881	474.007	9.719	12.373	7.929	18.627
^{55}Cr	1.5^-	54.940838	480.254	6.246	12.505	7.803	16.394
^{56}Cr	0^+	55.940651	488.499	8.245	13.419	8.240	18.526
^{57}Cr	1.5^-	56.943611	493.813	5.314	13.733	8.119	16.508
^{58}Cr	0^+	57.944351	501.195	7.382	14.935	8.664	18.890
^{59}Cr	1.5^-	58.948586	505.323	4.128	14.972	8.645	16.839
^{60}Cr	0^+	59.950077	512.007	6.684	16.726	9.991	19.431
^{48}Mn	4^+	47.968521	397.188	15.132	2.054	7.631	12.985
^{49}Mn	2.5^-	48.959618	413.552	16.364	2.085	8.160	16.193
^{50}Mn	0^+	49.954239	426.634	13.082	4.585	7.977	12.943
^{51}Mn	2.5^-	50.948212	440.320	13.686	5.271	8.663	16.047
^{52}Mn	6^+	51.945564	450.855	10.535	6.546	8.654	13.582
^{53}Mn	3.5^-	52.941288	462.909	12.054	6.560	9.155	16.375
^{54}Mn	3^+	53.940357	471.848	8.939	7.560	8.757	13.274
^{55}Mn	2.5^-	54.938046	482.074	10.227	8.067	7.933	15.562
^{56}Mn	3^+	55.938904	489.345	7.270	9.091	7.892	13.113
^{57}Mn	2.5^-	56.938286	497.993	8.648	9.495	8.061	15.515
^{58}Mn	3^+	57.939980	504.485	6.491	10.672	8.439	13.761
^{59}Mn	1.5^-	58.940441	512.129	7.644	10.934	8.752	16.091
^{60}Mn	3^+	59.942909	517.898	5.770	12.575	9.521	14.479
^{61}Mn	2.5^-	60.944653	524.347	6.449	12.341	9.791	16.800
^{51}Fe	2.5^-	50.956818	431.518	13.818	4.884	8.087	15.742
^{52}Fe	0^+	51.948112	447.699	16.181	7.379	7.936	18.841
^{53}Fe	3.5^-	52.945309	458.384	10.685	7.529	8.038	15.840
^{54}Fe	0^+	53.939610	471.763	13.379	8.854	8.417	18.683
^{55}Fe	1.5^-	54.938293	481.061	9.298	9.213	8.454	15.927
^{56}Fe	0^+	55.934937	492.258	11.197	10.184	7.612	18.186
^{57}Fe	0.5^-	56.935394	499.904	7.646	10.559	7.319	15.605
^{58}Fe	0^+	57.933273	509.949	10.045	11.956	7.644	18.380
^{59}Fe	1.5^-	58.934875	516.530	6.581	12.045	7.979	16.312

Table 22: (continued)

Nucleus	J^π	Mass	BE	S_n	S_p	S_α	S_d
^{60}Fe	0^+	59.934071	525.350	8.820	13.221	8.554	18.641
^{61}Fe	1.5^-	60.936745	530.931	5.581	13.033	8.821	16.578
^{62}Fe	0^+	61.936768	538.981	8.051	14.634	9.490	18.859
^{63}Fe	2.5^-	62.940369	543.698	4.716	14.796	10.078	17.126
^{52}Co	1^+	51.963589	432.501	14.713	0.983	7.016	12.576
^{53}Co	3.5^-	52.954220	449.301	16.800	1.602	7.453	15.558
^{54}Co	0^+	53.948460	462.737	13.436	4.353	7.806	12.814
^{55}Co	3.5^-	54.941998	476.827	14.089	5.064	8.210	16.218
^{56}Co	4^+	55.939838	486.910	10.083	5.849	7.758	12.923
^{57}Co	3.5^-	56.936291	498.286	11.376	6.028	7.080	15.001
^{58}Co	2^+	57.935753	506.859	8.573	6.955	6.714	12.376
^{59}Co	3.5^-	58.933193	517.313	10.454	7.364	6.941	15.184
^{60}Co	5^+	59.933815	524.805	7.492	8.275	7.163	12.631
^{61}Co	3.5^-	60.932476	534.125	9.321	8.776	7.835	15.371
^{62}Co	2^+	61.934052	540.730	6.604	9.799	7.948	13.156
^{63}Co	3.5^-	62.933613	549.210	8.480	10.229	8.784	16.055
^{64}Co	1^+	63.935810	555.234	6.024	11.536	9.038	14.028
^{55}Ni	3.5^-	54.951328	467.352	14.196	4.615	7.537	15.826
^{56}Ni	0^+	55.942131	483.992	16.639	7.165	7.996	19.030
^{57}Ni	1.5^-	56.939793	494.241	10.250	7.332	7.560	15.190
^{58}Ni	0^+	57.935341	506.458	12.217	8.173	6.399	17.324
^{59}Ni	1.5^-	58.934345	515.458	8.999	8.599	6.100	14.947
^{60}Ni	0^+	59.930786	526.845	11.388	9.533	6.290	17.762
^{61}Ni	1.5^-	60.931057	534.666	7.820	9.861	6.464	15.128
^{62}Ni	0^+	61.928345	545.262	10.597	11.137	7.016	18.233
^{63}Ni	0.5^-	62.929668	552.100	6.838	11.370	7.273	15.750
^{64}Ni	0^+	63.927967	561.758	9.658	12.548	8.111	18.804
^{65}Ni	2.5^-	64.930084	567.856	6.098	12.622	8.628	16.421
^{56}Cu	3^+	55.958561	467.907	15.048	0.554	7.109	12.526
^{57}Cu	1.5^-	56.949211	484.687	16.780	0.695	7.088	15.110
^{58}Cu	1^+	57.944538	497.110	12.424	2.869	6.076	10.894
^{59}Cu	1.5^-	58.939499	509.877	12.766	3.418	4.753	13.411
^{60}Cu	2^+	59.937366	519.935	10.058	4.477	4.728	11.252
^{61}Cu	1.5^-	60.933456	531.646	11.711	4.800	5.063	13.964
^{62}Cu	1^+	61.932583	540.531	8.885	5.866	5.375	11.461
^{63}Cu	1.5^-	62.929596	551.385	10.853	6.122	5.775	14.494
^{64}Cu	1^+	63.929764	559.300	7.916	7.201	6.199	11.814
^{65}Cu	1.5^-	64.927788	569.211	9.911	7.453	6.789	14.887

B Discrete Levels and Branching Ratios

The following table presents our adopted discrete levels (energies in MeV), along with their spins, parities, and branching ratios. Isomers are indicated in the fourth column (GS for ground state, M1 for first isomer, M2 for second isomer, etc...). The branching ratios are given by the number of the level decayed to, followed by the branching ratio in parenthesis. For example, a branching ratio of 1(56),3(23),4(21) would indicate that the given level decays to level 1 56% of the time, to level 3 23% of the time, and to level 4 21% of the time.

Table 23: Adopted discrete levels

^{A}Z		Energy	J^{π}	M	Branching Ratios
^{43}Ca	1	0.00000	3.5^-	GS	
	2	0.37276	2.5^-		1(100)
	3	0.59339	1.5^-		1(70), 2(30)
	4	0.99026	1.5^+		2(87), 3(13)
	5	1.39447	2.5^+		1(5), 2(75), 3(6), 4(14)
	6	1.67780	5.5^-		1(100)
	7	1.90180	3.5^+		1(70), 4(13), 5(17)
	8	1.93130	2.5^-		1(58), 2(35), 3(7)
	9	1.95740	0.5^+		3(78), 4(22)
	10	2.04625	1.5^-		1(63), 2(20), 3(8), 4(7), 5(2)
	11	2.06730	3.5^-		1(78), 2(22)
	12	2.09390	4.5^-		1(100)
	13	2.10270	1.5^-		1(25), 2(50), 3(25)
	14	2.22400	1.5^-		2(43), 3(57)
	15	2.24900	4.5^-		1(87), 2(11), 6(2)
	16	2.27270	2.5^+		4(84), 5(16)
	17	2.40980	4.5^+		1(45), 5(44), 7(11)
^{44}Ca	1	0.00000	0^+	GS	
	2	1.15705	2^+		1(100)
	3	1.88351	0^+		2(100)
	4	2.28314	4^+		2(100)
	5	2.65650	2^+		1(11), 2(89)
	6	3.04433	4^+		2(49), 4(51)
	7	3.28500	6^+		4(100)
	8	3.30130	2^+		1(31), 2(69)
	9	3.30786	3^-		2(71), 4(20), 5(9)
	10	3.35720	3^+		2(12), 4(88)
	11	3.58040	3^+		2(100)

Table 23: (continued)

^{A}Z		Energy	J^{π}	M	Branching Ratios
	12	3.66153	1^-		1(67), 2(8), 3(25)
	13	3.67607	2^-		2(76), 5(6), 8(1), 9(17)
	14	3.71180	4^-		6(30), 9(70)
	15	3.77620	2^+		2(93), 5(7)
^{45}Ca	1	0.00000	3.5^-	GS	
	2	0.17427	2.5^-		1(100)
	3	1.43471	1.5^-		1(33), 2(67)
	4	1.55437	5.5^-		1(100)
^{46}Ca	1	0.00000	0^+	GS	
	2	1.34600	2^+		1(100)
	3	2.42310	0^+		2(100)
	4	2.57470	4^+		2(100)
	5	2.97390	6^+		4(100)
	6	3.02260	2^+		1(39), 2(61)
	7	3.61400	3^-		2(100)
^{47}Ca	1	0.00000	3.5^-	GS	
	2	2.01354	1.5^-		1(100)
	3	2.57834	1.5^+		1(30), 2(70)
	4	2.59955	0.5^+		1(1), 2(99)
^{45}Sc	1	0.00000	3.5^-	GS	
	2	0.01240	1.5^+	M1	
	3	0.37650	1.5^-		1(8), 2(92)
	4	0.54306	2.5^+		1(37), 2(52), 3(11)
	5	0.72012	2.5^-		1(97), 2(3)
	6	0.93924	0.5^+		2(83), 3(17)
	7	0.97438	3.5^+		1(59), 2(31), 4(10)
	8	1.06760	1.5^-		1(3), 3(74), 5(23)
	9	1.23670	5.5^-		1(100)
	10	1.30318	1.5^+		2(34), 3(21), 4(45)
	11	1.40887	3.5^-		1(89), 3(4), 5(7)
	12	1.43348	4.5^+		1(11), 4(68), 7(18), 9(3)
	13	1.47250	3.5^+		1(60), 2(30), 4(10)
	14	1.55620	1.5^-		3(5), 6(8), 8(87)
	15	1.66200	4.5^-		1(68), 5(10), 9(13), 11(9)
	16	1.71600	2.5^-		1(100)
	17	1.80000	2.5^+		1(9), 2(40), 3(9), 4(24), 5(3), 8(3), 10(12)
	18	1.90070	1.5^-		8(100)
	19	1.93060	1.5^-		6(100)
	20	1.93550	1.5^+		1(100)
	21	1.93550	2.5^+		3(100)
	22	2.03120	5.5^+		7(47), 9(6), 12(47)
	23	2.09000	7.5^-		9(100)
	24	2.09300	2.5^-		1(83), 3(7), 8(10)
	25	2.10620	3.5^-		8(100)

Table 23: (continued)

^{A}Z		Energy	J^{π}	M	Branching Ratios
	26	2.10627	7.5^-		9(100)
	27	2.13840	1.5^-		1(71), 14(29)
	28	2.15100	1.5^+		2(90), 10(10)
	29	2.15200	0.5^-		4(39), 8(21), 14(40)
	30	2.22180	2.5^+		1(32), 2(68)
	31	2.22420	2.5^+		4(29), 5(39), 10(10), 12(22)
	32	2.28850	4.5^-		1(42), 7(24), 9(34)
	33	2.30380	2.5^-		2(25), 3(32), 8(34), 15(9)
	34	2.32150	1.5^-		1(31), 2(69)
	35	2.34100	3.5^-		1(41), 5(18), 11(41)
	36	2.35220	1.5^-		1(2), 2(25), 5(43), 8(9), 14(21)
^{46}Sc	1	0.00000	4^+	GS	
	2	0.05201	6^+		1(100)
	3	0.14253	1^-	M1	
	4	0.22777	3^+		1(100)
	5	0.28070	5^+		1(6), 2(94)
	6	0.28954	2^-		3(99), 4(1)
	7	0.44414	2^+		4(100)
	8	0.58478	3^-		1(32), 3(1), 6(67)
	9	0.62743	4^-		1(92), 4(8)
	10	0.77402	5^+		1(55), 2(45)
	11	0.83509	4^+		1(16), 5(84)
	12	0.97700	7^+		2(75), 5(25)
	13	0.99133	1^+		7(100)
	14	1.08859	4^+		1(2), 4(36), 5(57), 10(5)
	15	1.12423	4^-		5(15), 8(83), 9(2)
	16	1.14100	3^-		1(75), 4(25)
	17	1.27046	4^-		1(41), 8(21), 9(38)
	18	1.29800	2^+		3(40), 6(30), 8(30)
	19	1.32112	3^+		11(100)
	20	1.39418	2^+		4(79), 13(21)
	21	1.42790	2^+		3(100)
	22	1.52674	3^+		7(51), 9(49)
	23	1.64268	4^-		8(56), 9(44)
	24	1.67700	5^-		1(75), 2(25)
	25	1.69220	3^-		9(100)
	26	1.70783	2^-		1(21), 8(71), 17(8)
^{47}Sc	1	0.00000	3.5^-	GS	
	2	0.76683	1.5^+		1(100)
	3	0.80789	1.5^-		1(100)
	4	1.12300	2.5^-		1(50), 2(50)
	5	1.14500	0.5^-		2(80), 3(20)
	6	1.14699	5.5^-		1(100)
	7	1.29712	2.5^-		1(90), 3(10)

Table 23: (continued)

^{A}Z		Energy	J^{π}	M	Branching Ratios
	8	1.31600	0.5^-		2(75), 3(25)
	9	1.39130	0.5^+		2(13), 3(87)
	10	1.40440	2.5^+		1(72), 2(15), 3(13)
	11	1.63900	3.5^-		1(50), 2(50)
	12	1.71700	3.5^+		1(100)
	13	1.74500	2.5^-		2(100)
	14	1.79760	3.5^-		3(52), 7(48)
	15	1.79800	0.5^+		2(25), 3(75)
	16	1.85710	2.5^-		1(89), 2(9), 10(2)
	17	1.87820	4.5^-		1(69), 6(31)
	18	2.00230	1.5^+		3(58), 7(20), 10(22)
	19	2.14820	4.5^-		6(100)
	20	2.20750	3.5^-		1(40), 3(44), 7(9), 17(7)
	21	2.23200	3.5^-		1(50), 3(50)
	22	2.38130	2.5^+		1(38), 2(44), 3(18)
	23	2.40860	3.5^-		1(76), 6(24)
	24	2.41030	3.5^+		2(39), 3(61)
	25	2.49940	3.5^-		1(27), 7(52), 17(21)
	26	2.52940	0.5^+		2(31), 3(69)
	27	2.64190	7.5^-		19(100)
^{48}Sc	1	0.00000	6^+	GS	
	2	0.13094	5^+		1(100)
	3	0.25235	4^+		2(100)
	4	0.38800	4^-		2(100)
	5	0.62264	3^+		3(100)
	6	1.09600	7^+		1(75), 2(25)
	7	1.14258	2^+		5(100)
	8	1.40170	2^-		5(96), 7(4)
	9	1.43200	1^-		7(100)
	10	1.89107	3^-		3(50), 5(6), 7(7), 8(37)
	11	2.06410	5^+		1(76), 3(24)
	12	2.10360	4^-		2(26), 3(23), 5(51)
	13	2.16500	4^-		2(30), 3(30), 5(40)
	14	2.19046	3^+		3(78), 5(22)
	15	2.19600	5^+		1(75), 3(25)
	16	2.20200	3^+		3(75), 5(25)
	17	2.27549	2^+		5(30), 7(70)
	18	2.31000	3^-		3(100)
	19	2.39000	2^+		5(50), 7(50)
	20	2.39070	4^+		3(47), 5(53)
	21	2.51730	1^+		7(100)
	22	2.56020	3^-		3(42), 7(58)
	23	2.61960	5^+		2(56), 3(44)
	24	2.62600	2^+		5(50), 7(50)

Table 23: (continued)

^{A}Z		Energy	J^{π}	M	Branching Ratios
	25	2.64010	2^-		8(100)
	26	2.67030	1^-		8(100)
	27	2.72900	5^+		3(100)
^{49}Sc	1	0.00000	3.5^-	GS	
	2	2.22810	0.5^+		1(100)
	3	2.37130	1.5^+		1(93), 2(7)
	4	3.08450	1.5^-		1(100)
	5	3.30000	2.5^-		3(100)
	6	3.51620	1.5^-		2(40), 3(60)
	7	3.55000	1.5^+		1(75), 2(25)
	8	3.58100	3.5^-		1(75), 3(25)
	9	3.75500	2.5^+		1(100)
	10	3.80840	3.5^-		1(100)
	11	3.92100	4.5^-		1(100)
	12	3.95100	1.5^+		4(75), 5(25)
	13	3.99130	0.5^+		4(75), 6(25)
	14	4.04100	4.5^-		1(100)
	15	4.07207	2.5^-		1(99), 4(1)
^{50}Sc	1	0.00000	5^+	GS	
	2	0.25690	2^+	M1	
	3	0.32845	3^+		2(100)
^{44}Ti	1	0.00000	0^+	GS	
	2	1.08299	2^+		1(100)
	3	1.90430	0^+		2(100)
	4	2.45433	4^+		2(100)
	5	2.53060	2^+		1(25), 2(71), 3(4)
	6	2.88660	2^+		1(59), 2(38), 3(3)
	7	3.17580	3^-		1(1), 2(97), 4(2)
	8	3.36400	4^+		2(95), 5(5)
	9	3.41530	3^+		2(98), 6(2)
	10	3.64580	4^-		4(4), 7(96)
	11	3.75590	1^-		1(72), 2(28)
	12	3.94270	3^-		2(95), 4(5)
	13	3.98000	4^+		2(52), 4(15), 6(25), 7(4), 9(4)
	14	4.01530	6^+		4(100)
	15	4.06120	3^-		4(50), 7(50)
	16	4.11650	2^+		1(31), 2(47), 5(22)
	17	4.22700	2^-		2(6), 5(17), 6(29), 7(34), 9(5), 10(9)
^{45}Ti	1	0.00000	3.5^-	GS	
	2	0.03674	1.5^-		1(100)
	3	0.03971	2.5^-		1(100)
	4	0.32950	1.5^+		2(99), 3(1)
	5	0.74414	2.5^+		2(7), 3(3), 4(90)
	6	1.22703	3.5^+		1(7), 3(10), 4(39), 5(44)

Table 23: (continued)

^{A}Z		Energy	J^{π}	M	Branching Ratios
	7	1.35363	4.5^{-}		1(93), 3(7)
	8	1.46816	5.5^{-}		1(100)
	9	1.52100	2.5^{-}		1(26), 2(37), 3(37)
	10	1.56560	0.5^{+}		2(13), 4(87)
	11	1.79920	1.5^{-}		2(50), 3(50)
	12	1.88208	4.5^{+}		1(5), 5(70), 6(25)
	13	1.95840	1.5^{+}		3(15), 5(85)
	14	2.01600	4.5^{-}		1(31), 2(34), 3(35)
	15	2.25840	2.5^{+}		4(55), 5(40), 10(2), 13(3)
	16	2.43210	3.5^{+}		1(66), 3(17), 2(17)
	17	2.47480	5.5^{+}		6(69), 12(31)
	18	2.50000	2.5^{-}		1(40), 2(30), 3(30)
	19	2.53160	2.5^{+}		10(100)
	20	2.65649	6.5^{-}		8(100)
	21	2.84960	0.5^{+}		10(100)
	22	2.89000	1.5^{+}		3(60), 5(40)
	23	2.91190	3.5^{+}		5(46), 12(31), 13(23)
	24	3.00000	1.5^{+}		3(60), 5(40)
	25	3.01526	7.5^{-}		8(80), 20(20)
^{46}Ti	1	0.00000	0^{+}	GS	
	2	0.88929	2^{+}		1(100)
	3	2.00985	4^{+}		2(100)
	4	2.61100	0^{+}		2(100)
	5	2.96180	2^{+}		1(4), 2(96)
	6	3.05860	3^{-}		3(90), 5(10)
	7	3.16818	1^{-}		1(45), 2(55)
	8	3.21300	2^{+}		2(100)
	9	3.23570	2^{+}		1(16), 2(84)
	10	3.29900	6^{+}		3(100)
	11	3.33800	3^{+}		2(60), 3(40)
	12	3.44120	4^{-}		3(26), 6(74)
	13	3.56940	3^{-}		2(21), 3(79)
	14	3.57170	0^{+}		2(100)
	15	3.58200	2^{-}		3(100)
	16	3.60800	1^{+}		2(100)
	17	3.67700	2^{-}		3(100)
	18	3.69600	2^{+}		1(20), 2(80)
	19	3.72390	2^{+}		2(76), 3(24)
	20	3.73100	1^{+}		2(100)
	21	3.73790	1^{-}		1(100)
	22	3.78000	0^{+}		2(100)
	23	3.82690	5^{-}		6(50), 10(50)
	24	3.84500	2^{+}		2(100)
	25	3.84800	4^{+}		3(50), 6(100)

Table 23: (continued)

^{A}Z		Energy	J^{π}	M	Branching Ratios
	26	3.85240	5^-		3(84), 6(12), 12(4)
	27	3.85700	3^-		3(100)
^{47}Ti	1	0.00000	2.5^-	GS	
	2	0.15938	3.5^-		1(100)
	3	1.25060	1.5^-		1(75), 2(25)
	4	1.25210	4.5^-		1(6), 2(94)
	5	1.44425	5.5^-		2(94), 4(6)
	6	1.54980	1.5^-		1(46), 2(54)
	7	1.67000	2.5^+		1(50), 2(50)
	8	1.79390	0.5^-		1(67), 6(33)
	9	1.82500	1.5^+		1(100)
	10	2.16320	1.5^-		1(95), 2(5)
	11	2.16670	2.5^-		2(100)
	12	2.25950	2.5^+		1(82), 2(18)
	13	2.29710	2.5^-		1(78), 2(22)
	14	2.34400	4.5^+		1(60), 2(40)
	15	2.36490	0.5^+		9(100)
	16	2.40620	4.5^-		1(9), 2(63), 4(19), 5(9)
	17	2.41630	1.5^-		1(34), 6(23), 9(43)
	18	2.49940	2.5^+		1(100)
	19	2.52000	0.5^+		9(50), 15(50)
	20	2.52580	1.5^-		1(51), 2(49)
	21	2.54820	1.5^-		1(100)
	22	2.57290	0.5^+		6(73), 9(27)
	23	2.59960	1.5^-		1(48), 2(39), 9(13)
	24	2.61940	3.5^-		1(18), 2(73), 4(7), 11(2)
	25	2.66800	4.5^+		5(100)
	26	2.68231	5.5^-		4(69), 5(30), 16(1)
^{48}Ti	1	0.00000	0^+	GS	
	2	0.98352	2^+		1(100)
	3	2.29563	4^+		2(100)
	4	2.42102	2^+		1(5), 2(95)
	5	2.46500	3^-		3(75), 4(25)
	6	2.99719	0^+		2(100)
	7	3.06200	2^+		1(20), 2(80)
	8	3.22392	3^+		2(73), 3(23), 4(4)
	9	3.23974	4^+		3(100)
	10	3.33318	6^+		3(100)
	11	3.35880	3^-		2(92), 3(7), 4(1)
	12	3.37084	2^+		1(13), 2(87)
	13	3.50854	6^+		3(24), 10(76)
	14	3.61678	2^+		1(2), 2(90), 4(8)
	15	3.63300	2^+		2(100)
	16	3.69945	1^-		1(35), 2(65)

Table 23: (continued)

^{A}Z		Energy	J^{π}	M	Branching Ratios
	17	3.71100	2^+		2(100)
	18	3.73850	1^+		1(65), 2(27), 4(8)
	19	3.78244	3^-		3(24), 8(3), 11(73)
	20	3.80275	2^-		2(100)
	21	3.85200	0^+		2(100)
	22	3.85223	3^-		2(75), 3(20), 4(5)
	23	4.03511	2^+		4(69), 8(31)
	24	4.04600	5^-		3(85), 9(9), 10(6)
	25	4.07390	4^+		2(52), 3(10), 9(38)
	26	4.07448	2^+		1(9), 2(54), 9(37)
^{49}Ti	1	0.00000	3.5^-	GS	
	2	1.38177	1.5^-		1(100)
	3	1.54215	5.5^-		1(100)
	4	1.58597	1.5^-		1(100)
	5	1.61000	4.5^-		1(50), 3(50)
	6	1.62293	2.5^-		1(100)
	7	1.72347	0.5^-		2(98), 4(2)
	8	1.76201	2.5^-		1(100)
	9	2.26130	2.5^-		1(35), 6(48), 8(17)
	10	2.47140	2.5^-		1(32), 6(47), 8(21)
	11	2.50444	0.5^+		2(85), 6(15)
	12	2.50550	7.5^-		3(100)
	13	2.51337	5.5^-		1(100)
	14	2.52010	2.5^+		2(100)
	15	2.66434	1.5^+		6(35), 8(65)
	16	2.72060	6.5^+		3(100)
	17	2.72130	1.5^-		4(92), 9(8)
	18	2.98050	3.5^-		6(100)
	19	3.03868	2.5^+		7(100)
	20	3.04250	4.5^-		1(35), 3(25), 6(40)
	21	3.17529	0.5^-		2(68), 4(26), 7(6)
	22	3.26070	1.5^-		2(8), 4(7), 8(85)
	23	3.29030	8.5^-		12(100)
	24	3.42829	1.5^-		2(42), 4(50), 8(8)
	25	3.45100	3.5^-		6(75), 18(25)
	26	3.46899	0.5^-		4(100)
^{50}Ti	1	0.00000	0^+	GS	
	2	1.55378	2^+		1(100)
	3	2.67491	4^+		2(100)
	4	3.19871	6^+		3(100)
	5	3.86279	3^+		2(100)
	6	3.86820	0^+		2(100)
	7	3.97490	4^+		3(100)
	8	4.14700	3^-		2(75), 3(25)

Table 23: (continued)

^{A}Z		Energy	J^{π}	M	Branching Ratios
	9	4.14719	4^+		3(100)
	10	4.17197	3^-		2(68), 3(32)
	11	4.17250	2^-		2(100)
	12	4.30985	2^+		1(16), 2(84)
	13	4.40999	3^-		2(80), 3(20)
	14	4.48671	2^+		1(15), 2(85)
	15	4.53600	3^-		2(75), 3(25)
	16	4.57600	2^+		1(25), 2(75)
	17	4.78995	2^+		1(10), 2(90)
	18	4.88068	5^+		3(90), 4(8), 9(2)
	19	4.92800	1^-		1(50), 2(50)
	20	4.94000	1^+		1(50), 2(50)
	21	5.12500	4^-		2(75), 3(25)
	22	5.18607	4^+		2(29), 3(71)
	23	5.19100	4^-		1(50), 2(50)
	24	5.33600	3^-		2(75), 3(25)
	25	5.37991	4^+		2(8), 3(59), 10(33)
^{51}Ti	1	0.00000	1.5^-	GS	
	2	1.16670	0.5^-		1(100)
	3	1.43730	3.5^-		1(100)
	4	1.56750	2.5^-		1(100)
	5	2.14400	2.5^-		1(86), 2(2), 3(3), 4(9)
	6	2.19810	1.5^-		1(66), 2(14), 4(20)
	7	2.34460	5.5^-		3(100)
	8	2.69140	3.5^-		1(11), 3(19), 4(70)
	9	2.73120	3.5^-		3(74), 4(4), 7(22)
	10	2.75420	7.5^-		7(100)
	11	2.90580	0.5^-		1(25), 2(47), 6(28)
	12	2.91930	2.5^-		1(11), 3(55), 4(18), 5(16)
	13	3.06230	3.5^-		3(25), 7(54), 9(21)
	14	3.17380	1.5^-		1(81), 2(8), 6(11)
	15	3.23740	3.5^-		3(100)
	16	3.61850	2.5^-		3(15), 4(64), 5(15), 9(6)
	17	3.64410	6.5^-		10(100)
	18	3.77130	4.5^+		3(57), 7(43)
	19	4.02200	2.5^-		3(20), 4(60), 5(20)
	20	4.09500	3.5^-		7(35), 13(65)
	21	4.17200	2.5^+		1(60), 3(40)
	22	4.18660	2.5^-		4(100)
	23	4.47000	3.5^-		1(30), 3(30), 4(40)
	24	4.56900	1.5^-		1(30), 2(30), 4(40)
	25	4.60200	1.5^+		1(50), 4(50)
^{52}Ti	1	0.00000	0^+	GS	
	2	1.04973	2^+		1(100)

Table 23: (continued)

^{A}Z		Energy	J^{π}	M	Branching Ratios
	3	2.26420	2^+		1(12), 2(88)
	4	2.31765	4^+		2(100)
	5	2.43159	2^+		2(100)
	6	3.02770	6^+		4(100)
	7	3.14320	1^+		2(100)
	8	3.34990	4^+		4(100)
	9	3.45270	3^-		4(100)
	10	3.58870	2^+		1(8), 2(25), 3(55), 5(12)
^{53}Ti	1	0.00000	1.5^-	GS	
^{54}Ti	1	0.00000	0^+	GS	
^{45}V	1	0.00000	3.5^-	GS	
	2	0.05630	2.5^-		1(100)
^{46}V	1	0.00000	0^+	GS	
	2	0.80152	3^+	M1	
	3	0.91488	2^+		1(100)
	4	0.99370	2^+		1(100)
	5	1.17950	2^-		2(100)
	6	1.22502	5^+		2(100)
	7	1.23600	0^-		4(100)
	8	1.25400	3^-		2(60), 3(40)
	9	1.26300	3^-		2(80), 3(20)
	10	1.36700	3^+		3(28), 4(72)
	11	1.37600	3^+		3(100)
	12	1.43180	1^+		1(100)
	13	1.54070	6^+		6(100)
	14	1.60442	7^+		6(100)
	15	1.66560	1^+		3(100)
	16	1.73000	6^+		6(20), 11(80)
	17	1.79500	3^+		8(100)
	18	1.83300	2^+		3(100)
	19	1.94400	5^-		6(40), 13(30), 16(30)
	20	2.04900	2^-		3(20), 10(80)
	21	2.06250	3^-		2(100)
^{47}V	1	0.00000	1.5^-	GS	
	2	0.08753	2.5^-		1(100)
	3	0.14582	3.5^-		2(100)
	4	0.25949	1.5^+		1(93), 2(7)
	5	0.66036	2.5^+		1(38), 2(14), 3(18), 4(30)
	6	1.13855	3.5^+		2(38), 3(4), 4(33), 5(25)
	7	1.27180	4.5^-		2(18), 3(82)
	8	1.29496	5.5^-		3(100)
	9	1.66062	0.5^+		1(25), 4(74), 5(1)
	10	1.74696	4.5^+		3(36), 5(47), 6(17)

Table 23: (continued)

^{A}Z		Energy	J^{π}	M	Branching Ratios
	11	1.96892	1.5^{+}		1(3), 2(54), 4(9), 5(32), 6(1), 9(1)
	12	2.08272	1.5^{-}		1(28), 2(70), 3(2)
	13	2.17586	2.5^{-}		1(76), 2(22), 3(2)
	14	2.21175	0.5^{-}		1(81), 2(4), 4(14), 9(1)
	15	2.41600	5.5^{+}		6(86), 7(3), 10(11)
	16	2.43954	2.5^{+}		1(8), 2(2), 3(15), 4(36), 5(27), 9(1), 11(11)
	17	2.54600	3.5^{-}		1(60), 2(40)
	18	2.55800	6.5^{-}		7(62), 8(38)
	19	2.61410	7.5^{-}		8(98), 18(2)
	20	2.72263	2.5^{-}		1(55), 2(18), 3(20), 4(1), 6(5), 7(1)
	21	2.74712	4.5^{-}		2(7), 3(86), 7(5), 8(2)
	22	2.76732	0.5^{-}		1(100)
	23	2.81004	3.5^{+}		2(43), 4(3), 5(23), 6(3), 7(11), 10(12), 11(3), 16(1)
	24	2.98429	3.5^{-}		1(1), 2(12), 3(58), 7(29)
	25	3.00545	1.5^{-}		1(35), 2(65)
	26	3.05422	2.5^{-}		2(43), 3(57)
	27	3.24773	3.5^{-}		1(18), 2(19), 3(18), 7(10), 8(12), 13(23)
	28	3.27200	6.5^{+}		8(6), 10(79), 15(15)
	29	3.30353	1.5^{+}		2(71), 4(8), 5(9), 11(7), 12(5)
	30	3.35549	2.5^{+}		1(4), 4(78), 5(18)
^{48}V	1	0.00000	4^{+}	GS	
	2	0.30827	2^{+}		1(100)
	3	0.42065	1^{+}		2(100)
	4	0.42791	5^{+}		1(100)
	5	0.51866	1^{-}		2(66), 3(34)
	6	0.61338	4^{+}		1(89), 4(11)
	7	0.62729	6^{+}		1(59), 4(41)
	8	0.74498	2^{-}		2(5), 3(3), 5(92)
	9	0.76496	3^{+}		1(44), 2(54), 6(2)
	10	0.77620	5^{+}		1(100)
	11	1.05577	3^{-}		5(8), 8(91)
	12	1.09918	4^{-}		1(93), 6(7)
	13	1.12080	3^{+}		1(66), 2(34)
	14	1.25460	7^{+}		4(2), 7(98)
	15	1.26459	5^{+}		6(75), 7(25)
	16	1.52139	2^{+}		2(45), 3(35), 9(20)
	17	1.55755	4^{-}		8(19), 11(68), 12(14)
	18	1.68547	5^{-}		12(100)
	19	1.69150	2^{+}		1(69), 5(31)
	20	1.73000	6^{+}		1(60), 4(40)
	21	1.78098	3^{+}		1(15), 2(43), 6(42)
	22	1.99844	2^{-}		8(60), 12(40)
	23	2.06242	5^{-}		6(26), 11(22), 17(52)
^{49}V	1	0.00000	3.5^{-}	GS	

Table 23: (continued)

^{A}Z		Energy	J^{π}	M	Branching Ratios
	2	0.09064	2.5^-		1(100)
	3	0.15293	1.5^-		1(59), 2(41)
	4	0.74827	1.5^+		2(46), 3(54)
	5	1.02162	5.5^-		1(100)
	6	1.14053	2.5^+		1(53), 2(24), 3(17), 4(6)
	7	1.15532	4.5^-		1(75), 2(22), 5(3)
	8	1.51454	2.5^-		1(27), 2(9), 3(47), 4(17)
	9	1.60268	3.5^+		1(27), 2(56), 4(8), 6(8), 7(1)
	10	1.64319	1.5^-		3(100)
	11	1.64643	0.5^+		3(53), 4(47)
	12	1.66140	1.5^-		1(9), 2(52), 3(34), 4(5)
	13	1.99470	1.5^+		2(21), 3(34), 4(16), 6(29)
	14	2.17830	4.5^+		1(62), 5(10), 6(21), 9(7)
	15	2.18200	3.5^-		1(6), 2(71), 7(23)
	16	2.23400	2.5^+		1(5), 2(64), 3(17), 12(14)
	17	2.26330	7.5^-		5(100)
	18	2.26530	2.5^-		3(95), 10(5)
	19	2.30940	1.5^-		1(20), 2(40), 3(33), 4(7)
	20	2.35340	4.5^-		1(57), 2(6), 5(32), 7(5)
	21	2.38800	2.5^+		1(3), 2(8), 4(28), 6(3), 13(58)
	22	2.40830	3.5^-		1(57), 2(9), 5(4), 6(19), 7(11)
	23	2.67100	5.5^-		5(75), 7(25)
	24	2.67130	5.5^+		1(6), 2(4), 5(90)
	25	2.68000	3.5^+		5(50), 7(50)
	26	2.72750	7.5^-		5(50), 17(50)
	27	2.74100	5.5^+		7(39), 9(48), 14(13)
	28	2.78640	4.5^-		1(24), 2(4), 5(45), 7(24), 9(3)
	29	2.79660	4.5^+		1(62), 5(38)
	30	2.80830	2.5^+		1(35), 3(30), 4(18), 6(8), 9(9)
	31	2.81090	2.5^-		1(32), 2(43), 6(11), 15(14)
	32	2.86150	6.5^-		7(78), 17(22)
	33	3.01730	1.5^+		1(14), 2(37), 3(40), 9(9)
	34	3.13390	4.5^-		23(100)
	35	3.13400	4.5^+		1(41), 2(22), 4(7), 5(14), 7(16)
	36	3.15210	3.5^-		5(38), 6(62)
	37	3.22400	1.5^+		3(50), 12(50)
	38	3.23950	3.5^-		1(8), 2(61), 8(31)
^{50}V	1	0.00000	6^+	GS	
	2	0.22620	5^+		1(100)
	3	0.32016	4^+		1(1), 2(99)
	4	0.35540	3^+		2(1), 3(99)
	5	0.38840	2^+		4(100)
	6	0.83630	5^+		1(51), 3(49)
	7	0.91000	7^+		1(100)

Table 23: (continued)

^{A}Z		Energy	J^{π}	M	Branching Ratios
	8	0.91010	4^+		2(100)
	9	1.30140	2^+		4(33), 5(67)
	10	1.33150	1^+		5(100)
	11	1.40190	3^+		3(14), 4(16), 5(58), 8(12)
	12	1.49530	1^+		4(12), 5(88)
	13	1.51840	2^+		4(18), 5(82)
	14	1.56170	2^+		4(51), 5(49)
	15	1.67720	3^+		4(20), 5(15), 9(54), 11(11)
	16	1.70020	4^+		3(100)
	17	1.70310	3^+		8(100)
	18	1.71890	1^+		4(44), 5(56)
	19	1.72460	8^+		1(36), 7(64)
	20	1.72520	5^+		2(91), 3(9)
	21	1.75150	5^+		2(40), 3(30), 4(30)
	22	1.76150	6^+		1(60), 7(40)
	23	1.76230	3^-		6(100)
	24	1.81080	3^+		3(30), 4(25), 5(25), 9(20)
	25	1.88240	5^+		6(100)
^{51}V	1	0.00000	3.5^-	GS	
	2	0.32008	2.5^-		1(100)
	3	0.92866	1.5^-		1(86), 2(14)
	4	1.60923	5.5^-		1(100)
	5	1.81324	4.5^-		1(75), 2(24), 4(1)
	6	2.41078	1.5^-		1(19), 2(72), 3(9)
	7	2.54740	0.5^+		3(100)
	8	2.67743	1.5^+		3(100)
	9	2.69962	7.5^-		4(100)
	10	2.79000	2.5^-		1(100)
	11	3.08362	2.5^-		1(23), 2(40), 3(31), 6(6)
	12	3.15000	1.5^-		1(60), 2(40)
	13	3.21480	1.5^-		2(16), 3(54), 6(30)
	14	3.26403	2.5^-		2(89), 3(10), 6(1)
	15	3.27999	2.5^-		2(52), 3(34), 6(14)
	16	3.37200	1.5^-		1(100)
	17	3.37772	4.5^-		1(88), 2(12)
	18	3.38110	1.5^-		1(100)
	19	3.38320	4.5^+		1(61), 4(26), 5(13)
	20	3.38558	6.5^-		4(96), 5(1), 9(3)
	21	3.39502	6.5^-		4(44), 5(56)
	22	3.41220	3.5^+		2(100)
	23	3.44392	2.5^+		3(100)
	24	3.45409	4.5^-		1(38), 2(62)
	25	3.51702	4.5^-		1(71), 2(22), 5(7)
	26	3.55480	4.5^-		1(100)

Table 23: (continued)

^{A}Z		Energy	J^{π}	M	Branching Ratios
	27	3.56260	2.5^-		1(100)
	28	3.56820	3.5^-		2(100)
	29	3.57663	1.5^-		1(60), 2(40)
	30	3.61405	4.5^-		1(3), 4(75), 5(22)
	31	3.62370	2.5^+		1(16), 2(61), 3(23)
^{52}V	1	0.00000	3^+	GS	
	2	0.01716	3^+		1(100)
	3	0.02276	5^+		1(100)
	4	0.14161	1^+		2(100)
	5	0.14785	4^+		1(14), 3(86)
	6	0.43663	2^+		1(46), 2(32), 4(22)
	7	0.79355	3^+		1(21), 2(1), 5(77), 6(1)
	8	0.84594	4^+		1(41), 3(52), 5(7)
	9	0.88100	1^+		1(60), 2(40)
	10	1.28985	1^+		2(74), 4(26)
	11	1.41881	3^+		1(39), 2(40), 5(7), 6(11), 8(3)
	12	1.49306	7^+		3(100)
	13	1.55885	4^+		1(84), 3(1), 5(2), 8(13)
	14	1.57916	3^-		1(100)
	15	1.66400	1^+		1(60), 2(40)
	16	1.73257	5^+		1(32), 3(25), 4(1), 5(7), 8(35)
	17	1.75962	3^+		2(13), 4(2), 5(44), 6(40), 7(1)
	18	1.77017	3^+		3(18), 5(38), 6(44)
	19	1.79512	2^+		1(3), 2(42), 4(1), 6(38), 7(14), 10(2)
	20	1.84300	4^+		1(50), 3(50)
	21	2.10083	3^+		1(11), 2(14), 5(26), 6(20), 7(14), 8(9), 11(6)
	22	2.15100	6^+		12(50), 16(50)
	23	2.15200	1^+		1(60), 2(40)
	24	2.16864	4^+		1(5), 2(2), 3(69), 5(10), 7(4), 8(10)
	25	2.31803	3^+		1(26), 2(10), 5(23), 7(13), 8(12), 11(16)
^{53}V	1	0.00000	3.5^-	GS	
	2	0.12760	2.5^-		1(100)
	3	0.22841	1.5^-		1(66), 2(34)
	4	1.09124	5.5^-		1(100)
	5	1.26600	4.5^-		1(63), 2(28), 4(9)
	6	1.54960	1.5^-		2(64), 3(36)
	7	1.65300	4.5^-		1(100)
^{54}V	1	0.00000	3^+	GS	
^{55}V	1	0.00000	3.5^-	GS	
^{56}V	1	0.00000	2^+	GS	
^{57}V	1	0.00000	1.5^-	GS	
^{47}Cr	1	0.00000	1.5^-	GS	
	2	0.09940	0.5^-		1(100)

Table 23: (continued)

^{A}Z		Energy	J^{π}	M	Branching Ratios
	3	0.17510	0.5^-		$1(1), 2(99)$
^{48}Cr	1	0.00000	0^+	GS	
	2	0.75216	2^+		$1(100)$
	3	1.85839	4^+		$2(100)$
^{49}Cr	1	0.00000	2.5^-	GS	
	2	0.27193	3.5^-		$1(100)$
	3	1.08250	4.5^-		$1(6), 2(94)$
	4	1.56130	5.5^-		$2(49), 3(51)$
	5	1.70340	0.5^-		$1(100)$
	6	1.74140	1.5^-		$1(71), 2(29)$
	7	1.98220	1.5^+		$1(71), 2(11), 5(18)$
	8	2.16860	2.5^-		$1(55), 2(45)$
	9	2.43210	2.5^+		$1(40), 2(17), 7(43)$
	10	2.49810	6.5^-		$3(10), 4(90)$
	11	2.50400	3.5^-		$1(67), 2(33)$
	12	2.57830	0.5^+		$5(38), 6(62)$
	13	2.61320	1.5^-		$1(41), 2(59)$
^{50}Cr	1	0.00000	0^+	GS	
	2	0.78330	2^+		$1(100)$
	3	1.88129	4^+		$2(100)$
	4	2.92450	2^+		$1(8), 2(92)$
	5	3.16110	2^+		$2(100)$
	6	3.16369	6^+		$3(100)$
	7	3.32457	4^+		$3(100)$
	8	3.59455	4^+		$2(59), 3(41)$
^{51}Cr	1	0.00000	3.5^-	GS	
	2	0.74910	1.5^-		$1(100)$
	3	0.77695	0.5^-		$2(100)$
	4	1.16459	4.5^-		$1(100)$
	5	1.35265	2.5^-		$1(35), 2(56), 3(9)$
	6	1.48007	5.5^-		$1(52), 4(48)$
	7	1.55726	3.5^-		$1(15), 2(80), 5(5)$
	8	1.89920	1.5^-		$1(72), 2(21), 3(7)$
	9	2.00191	2.5^-		$1(100)$
	10	2.25550	7.5^-		$6(100)$
	11	2.31258	3.5^-		$1(14), 4(86)$
	12	2.37946	4.5^-		$1(28), 4(14), 5(26), 6(19), 7(13)$
	13	2.38540	6.5^-		$6(100)$
^{52}Cr	1	0.00000	0^+	GS	
	2	1.43409	2^+		$1(100)$
	3	2.36963	4^+		$2(100)$
	4	2.64690	0^+		$2(100)$
	5	2.76776	4^+		$2(98), 3(2)$
	6	2.96478	2^+		$1(1), 2(99)$

Table 23: (continued)

^{A}Z		Energy	J^{π}	M	Branching Ratios
	7	3.11386	6^+		3(99), 5(1)
	8	3.16174	2^+		1(9), 2(91)
	9	3.41531	4^+		2(7), 3(14), 5(79)
	10	3.47224	3^+		2(22), 5(78)
	11	3.61592	5^+		3(53), 5(43), 7(3), 9(1)
	12	3.77172	2^+		1(21), 2(79)
	13	3.94900	5^+		3(100)
	14	3.95120	2^+		1(100)
	15	4.01550	5^+		3(5), 5(36), 7(4), 9(38), 11(17)
	16	4.03920	4^+		10(100)
^{53}Cr	1	0.00000	1.5^-	GS	
	2	0.56403	0.5^-		1(100)
	3	1.00627	2.5^-		1(100)
	4	1.28952	3.5^-		1(94), 3(6)
	5	1.53662	3.5^-		1(9), 3(65), 4(26)
	6	1.97366	2.5^-		1(84), 4(16)
	7	2.17233	5.5^-		4(100)
	8	2.23316	4.5^-		5(100)
	9	2.32071	1.5^-		1(100)
	10	2.45310	0.5^-		3(60), 4(40)
	11	2.65640	2.5^-		1(5), 3(68), 4(27)
	12	2.66990	0.5^-		1(60), 2(40)
	13	2.70587	5.5^-		7(100)
	14	2.70850	1.5^-		1(11), 2(46), 3(29), 6(14)
^{54}Cr	1	0.00000	0^+	GS	
	2	0.83486	2^+		1(100)
	3	1.82392	4^+		2(100)
	4	2.61968	2^+		1(4), 2(96)
	5	2.82962	0^+		2(100)
	6	3.07407	2^+		1(1), 2(99)
	7	3.15956	4^+		2(47), 3(53)
	8	3.22228	6^+		3(100)
	9	3.39341	1^-		1(37), 2(63)
	10	3.43688	2^+		2(97), 4(3)
^{55}Cr	1	0.00000	1.5^-	GS	
	2	0.24191	0.5^-		1(100)
	3	0.51770	2.5^-		1(100)
	4	0.56591	1.5^-		1(88), 2(12)
	5	0.88071	2.5^-		1(88), 3(7), 4(5)
	6	1.13100	2.5^+		3(100)
	7	1.21475	2.5^-		1(65), 3(8), 5(27)
	8	1.43882	4.5^-		3(81), 7(19)
	9	1.47420	0.5^-		1(44), 2(6), 4(50)

Table 23: (continued)

^{A}Z		Energy	J^{π}	M	Branching Ratios
	10	1.47903	3.5^-		3(100)
^{56}Cr	1	0.00000	0^+	GS	
	2	1.00661	2^+		1(100)
	3	1.83160	2^+		1(15), 2(85)
	4	2.07660	1^+		2(100)
	5	2.32680	2^+		2(100)
	6	2.68170	4^+		3(100)
	7	3.16500	3^-		2(100)
	8	3.25200	4^-		4(100)
^{58}Cr	1	0.00000	0^+	GS	
^{60}Cr	1	0.00000	0^+	GS	
^{48}Mn	1	0.00000	4^+	GS	
^{49}Mn	1	0.00000	2.5^-	GS	
	2	0.26100	3.5^-		1(100)
	3	1.05890	4.5^-		2(100)
	4	1.54110	5.5^-		2(49), 3(51)
	5	2.48070	6.5^-		3(17), 4(83)
	6	3.18890	7.5^-		4(40), 5(60)
	7	4.24980	8.5^-		5(35), 6(65)
^{50}Mn	1	0.00000	0^+	GS	
	2	0.22900	5^+	M1	
^{51}Mn	1	0.00000	2.5^-	GS	
	2	0.23730	3.5^-		1(100)
	3	1.13980	4.5^-		1(14), 2(86)
	4	1.48800	5.5^-		1(1), 2(64), 3(35)
	5	1.81710	1.5^+		1(98), 2(2)
	6	1.82460	1.5^-		1(96), 2(4)
	7	1.95910	0.5^-		1(100)
	8	2.14040	1.5^-		1(98), 2(2)
	9	2.25570	2.5^-		1(31), 2(69)
	10	2.27590	0.5^+		1(2), 5(58), 6(10), 7(16), 8(14)
	11	2.31000	2.5^-		1(14), 2(76), 5(10)
	12	2.41590	3.5^-		1(6), 2(34), 3(37), 5(15), 8(8)
^{52}Mn	1	0.00000	6^+	GS	
	2	0.37775	2^+	M1	
	3	0.54644	1^+		2(100)
	4	0.73164	4^+		1(91), 2(9)
	5	0.82520	3^+		2(100)
	6	0.86990	7^+		1(100)
	7	0.88420	3^+		2(97), 4(3)
	8	0.88690	2^+		2(90), 3(10)
	9	1.23230	3^+		2(61), 4(27), 8(12)
	10	1.25360	5^+		1(81), 4(19)

Table 23: (continued)

^{A}Z		Energy	J^{π}	M	Branching Ratios
	11	1.27900	4^+		5(60), 7(40)
	12	1.68380	5^+		1(69), 4(21), 11(10)
	13	1.95600	6^+		1(100)
	14	2.04410	4^+		5(100)
	15	2.13000	3^+		2(50), 4(50)
	16	2.24000	7^+		1(50), 6(50)
	17	2.25260	4^+		4(50), 5(50)
	18	2.26100	2^+		2(50), 3(50)
	19	2.28598	8^+		1(4), 6(96)
	20	2.33720	3^+		5(51), 8(49)
	21	2.63120	1^+		3(100)
	22	2.67700	2^+		2(50), 3(50)
	23	2.71100	5^+		1(90), 4(10)
	24	2.78800	3^+		2(60), 3(30), 4(10)
	25	2.79600	1^+		2(50), 3(50)
	26	2.90770	9^+		6(29), 19(71)
	27	2.92600	0^+		3(100)
	28	2.97300	6^+		1(80), 6(20)
	29	3.02200	4^+		4(20), 12(80)
	30	3.08000	5^-		4(100)
	31	3.09700	3^+		4(20), 12(80)
	32	3.10600	2^+		3(70), 15(30)
	33	3.19900	6^+		1(40), 12(60)
^{53}Mn	1	0.00000	3.5^-	GS	
	2	0.37789	2.5^-		1(100)
	3	1.28967	1.5^-		1(54), 2(46)
	4	1.44112	5.5^-		1(100)
	5	1.62120	4.5^-		1(90), 2(10)
	6	2.27377	2.5^-		1(74), 2(22), 3(4)
	7	2.40700	1.5^-		1(40), 2(13), 3(47)
	8	2.44800	3.5^-		2(100)
	9	2.56285	6.5^-		4(100)
	10	2.57320	3.5^-		1(38), 2(62)
	11	2.67110	0.5^-		2(46), 3(31), 7(23)
	12	2.68650	3.5^-		1(78), 2(13), 3(9)
	13	2.69264	7.5^-		4(94), 9(6)
	14	2.69797	5.5^-		4(35), 5(65)
	15	2.70640	0.5^+		3(100)
	16	2.76100	4.5^+		2(100)
	17	2.87560	1.5^-		1(14), 2(83), 3(2), 7(1)
	18	2.91260	1.5^-		2(30), 3(70)
	19	2.94690	4.5^-		1(100)
	20	2.96730	2.5^+		1(100)
	21	2.97810	4.5^-		1(100)

Table 23: (continued)

^{A}Z		Energy	J^{π}	M	Branching Ratios
	22	3.00720	2.5^{+}		$1(14), 2(36), 3(50)$
^{54}Mn	1	0.00000	3^{+}	GS	
	2	0.05487	2^{+}		$1(100)$
	3	0.15630	4^{+}		$1(100)$
	4	0.36829	5^{+}		$1(1), 3(99)$
	5	0.40755	3^{+}		$1(29), 2(9), 3(62)$
	6	0.83891	4^{+}		$1(54), 3(10), 4(36)$
	7	1.00962	3^{+}		$2(56), 3(44)$
	8	1.07330	6^{+}		$3(1), 4(99)$
	9	1.13674	5^{+}		$3(34), 4(59), 6(7)$
	10	1.37499	2^{+}		$1(63), 2(17), 5(20)$
	11	1.37558	3^{+}		$1(94), 7(6)$
	12	1.39100	1^{+}		$2(100)$
	13	1.45440	1^{+}		$1(5), 2(95)$
	14	1.46080	4^{+}		$8(100)$
	15	1.50840	2^{+}		$1(67), 2(25), 6(8)$
	16	1.54400	2^{+}		$1(100)$
	17	1.63420	3^{+}		$2(49), 3(10), 5(41)$
	18	1.65110	1^{+}		$2(100)$
^{55}Mn	1	0.00000	2.5^{-}	GS	
	2	0.12595	3.5^{-}		$1(100)$
	3	0.98426	4.5^{-}		$1(5), 2(95)$
	4	1.28910	5.5^{-}		$2(10), 3(90)$
	5	1.29212	5.5^{-}		$2(75), 3(25)$
	6	1.29300	0.5^{-}		$1(100)$
	7	1.52836	1.5^{-}		$1(97), 2(3)$
	8	1.88408	3.5^{-}		$1(64), 2(36)$
	9	2.01520	3.5^{-}		$1(8), 3(92)$
	10	2.19843	3.5^{-}		$1(61), 2(6), 3(33)$
	11	2.21500	3.5^{-}		$1(100)$
	12	2.25245	1.5^{-}		$1(100)$
	13	2.26689	2.5^{-}		$1(73), 7(27)$
^{56}Mn	1	0.00000	3^{+}	GS	
	2	0.02661	2^{+}		$1(100)$
	3	0.11050	1^{+}		$2(100)$
	4	0.21203	4^{+}		$1(100)$
	5	0.21513	2^{+}		$1(8), 2(16), 3(76)$
	6	0.33553	5^{+}		$1(42), 4(58)$
	7	0.34099	3^{+}		$1(6), 2(93), 4(1)$
	8	0.45434	3^{+}		$1(96), 4(2), 7(2)$
	9	0.48631	3^{+}		$1(3), 2(20), 4(6), 5(71)$
^{57}Mn	1	0.00000	2.5^{-}	GS	
	2	0.08319	3.5^{-}		$1(100)$
	3	0.85007	1.5^{-}		$1(96), 2(4)$

Table 23: (continued)

^{A}Z		Energy	J^{π}	M	Branching Ratios
	4	1.05583	2.5^-		$1(20), 3(80)$
	5	1.07290	0.5^-		$1(6), 2(94)$
	6	1.22750	1.5^-		$2(92), 5(8)$
	7	1.37500	1.5^-		$2(72), 3(28)$
^{58}Mn	1	0.00000	1^+	GS	
	2	0.07178	4^+	M1	
^{60}Mn	1	0.00000	0^+	GS	
	2	0.27180	3^+	M1	
^{61}Mn	1	0.00000	2.5^-	GS	
^{51}Fe	1	0.00000	2.5^-	GS	
^{52}Fe	1	0.00000	0^+	GS	
	2	0.84960	2^+		$1(100)$
	3	2.38570	4^+		$2(100)$
	4	2.75980	2^+		$1(76), 2(24)$
	5	3.58670	4^+		$2(100)$
	6	4.14580	0^+		$2(100)$
^{53}Fe	1	0.00000	3.5^-	GS	
	2	0.74111	1.5^-		$1(100)$
	3	0.77442	0.5^-		$2(100)$
	4	1.32801	4.5^-		$1(100)$
	5	1.42350	2.5^-		$2(79), 3(21)$
	6	1.69632	3.5^-		$2(100)$
^{54}Fe	1	0.00000	0^+	GS	
	2	1.40819	2^+		$1(100)$
	3	2.53810	4^+		$2(100)$
	4	2.56130	0^+		$2(100)$
	5	2.94920	6^+		$3(100)$
	6	2.95900	2^+		$1(55), 2(45)$
	7	3.16600	2^+		$1(81), 2(19)$
	8	3.29480	4^+		$2(16), 3(84)$
	9	3.34480	3^+		$2(57), 3(43)$
	10	3.43740	4^+		$3(17), 5(83)$
	11	3.79380	5^-		$5(100)$
	12	3.83320	4^+		$2(89), 3(9), 8(2)$
	13	3.84100	4^-		$2(100)$
	14	4.03090	4^+		$3(16), 8(84)$
	15	4.04780	4^+		$2(17), 3(8), 6(3), 9(72)$
	16	4.07160	4^+		$2(92), 3(8)$
	17	4.09970	4^+		$8(100)$
	18	4.10340	6^+		$5(100)$
	19	4.26780	4^+		$2(20), 3(80)$
	20	4.29080	0^+		$2(100)$
	21	4.57850	2^+		$1(30), 2(70)$

Table 23: (continued)

^{A}Z		Energy	J^{π}	M	Branching Ratios
	22	4.65430	0^+		8(50), 15(50)
	23	4.69600	1^+		2(100)
	24	4.70010	3^-		2(15), 3(40), 9(45)
	25	4.78190	3^-		2(54), 3(17), 8(18), 9(11)
	26	4.94870	4^+		2(35), 3(55), 5(10)
^{55}Fe	1	0.00000	1.5^-	GS	
	2	0.41142	0.5^-		1(100)
	3	0.93129	2.5^-		1(98), 2(2)
	4	1.31654	3.5^-		1(93), 3(7)
	5	1.40845	3.5^-		1(44), 3(52), 4(4)
	6	1.91830	0.5^-		1(68), 2(32)
^{56}Fe	1	0.00000	0^+	GS	
	2	0.84678	2^+		1(100)
	3	2.08508	4^+		2(100)
	4	2.65756	2^+		1(3), 2(97)
	5	2.94170	0^+		2(100)
	6	2.95992	2^+		1(2), 2(98)
	7	3.07000	3^-		2(60), 3(40)
	8	3.11960	1^-		2(100)
	9	3.12293	4^+		2(1), 3(99)
	10	3.36974	2^+		1(15), 2(85)
	11	3.38849	6^+		3(99), 9(1)
	12	3.44531	3^+		2(79), 3(20), 4(1)
	13	3.44930	2^-		1(50), 2(50)
	14	3.59780	0^+		2(100)
	15	3.60200	2^+		1(65), 2(35)
	16	3.60700	0^-		2(100)
	17	3.74800	2^+		1(65), 2(35)
	18	3.75562	6^+		3(80), 9(2), 11(18)
	19	3.75960	4^+		2(65), 4(35)
	20	3.83200	2^+		1(11), 2(63), 4(26)
	21	3.85645	3^+		2(6), 3(92), 6(1), 9(1)
	22	4.04883	3^+		2(81), 3(18), 6(1)
	23	4.10031	4^+		2(62), 3(24), 4(1), 6(1), 9(12)
	24	4.11987	3^+		2(18), 3(79), 4(1), 6(1), 9(1)
	25	4.29804	4^+		2(25), 3(11), 4(2), 9(61), 12(1)
	26	4.30090	0^+		2(100)
	27	4.32000	2^+		1(65), 2(35)
	28	4.37000	3^-		2(60), 3(40)
	29	4.39483	3^+		2(88), 9(12)
	30	4.40110	2^+		2(78), 5(6), 12(16)
	31	4.44760	3^-		2(100)
	32	4.45853	4^+		2(4), 3(38), 9(58)
	33	4.51000	3^-		2(31), 3(16), 4(50), 12(3)

Table 23: (continued)

^{A}Z		Energy	J^{π}	M	Branching Ratios
	34	4.53950	2^{+}		1(13), 4(30), 6(57)
^{57}Fe	1	0.00000	0.5^{-}	GS	
	2	0.01441	1.5^{-}		1(100)
	3	0.13647	2.5^{-}		1(12), 2(88)
	4	0.36676	1.5^{-}		1(14), 2(79), 3(7)
	5	0.70642	2.5^{-}		1(5), 2(85), 3(9), 4(1)
	6	1.00713	3.5^{-}		2(33), 3(64), 4(3)
	7	1.13990	0.5^{-}		1(60), 2(40)
	8	1.19781	4.5^{-}		3(100)
	9	1.26552	0.5^{-}		1(3), 2(4), 4(93)
	10	1.35683	3.5^{-}		2(22), 4(23), 5(55)
	11	1.62726	1.5^{-}		1(2), 2(61), 4(28), 5(9)
	12	1.72538	1.5^{-}		1(68), 2(3), 4(10), 5(19), 9(100)
	13	1.97663	2.5^{-}		1(16), 3(67), 12(17)
	14	1.98966	4.5^{-}		5(41), 6(32), 8(27)
	15	1.99100	1.5^{-}		1(60), 2(40)
	16	2.11311	1.5^{-}		1(79), 9(21)
	17	2.11860	2.5^{-}		2(35), 5(50), 6(15)
	18	2.20688	2.5^{-}		1(36), 2(43), 6(18), 9(3)
	19	2.21766	2.5^{+}		2(44), 3(35), 4(21)
	20	2.22020	3.5^{-}		2(49), 3(46), 4(5)
	21	2.33041	1.5^{-}		11(100)
	22	2.35596	5.5^{-}		6(71), 8(29)
	23	2.45555	4.5^{-}		6(100)
	24	2.50529	2.5^{+}		2(10), 3(26), 4(55), 5(6), 12(3)
	25	2.56422	1.5^{-}		1(36), 12(64)
	26	2.57450	2.5^{-}		1(72), 4(28)
	27	2.59360	2.5^{-}		1(9), 5(50), 6(41)
	28	2.59940	1.5^{+}		1(30), 3(70)
	29	2.69717	0.5^{-}		1(35), 2(53), 4(8), 5(4)
	30	2.75830	2.5^{-}		4(79), 9(21)
	31	2.82107	1.5^{+}		6(31), 19(69)
	32	2.83589	1.5^{+}		1(15), 2(6), 4(36), 5(40), 6(2), 16(1)
^{58}Fe	1	0.00000	0^{+}	GS	
	2	0.81078	2^{+}		1(100)
	3	1.67475	2^{+}		1(43), 2(57)
	4	2.07654	4^{+}		2(100)
	5	2.13391	3^{+}		2(74), 3(26)
	6	2.25796	0^{+}		2(100)
	7	2.60042	4^{+}		2(30), 3(18), 4(39), 5(13)
	8	2.78214	1^{+}		1(22), 2(48), 3(22), 6(8)
	9	2.86472	2^{+}		7(100)
	10	2.87646	2^{+}		1(47), 2(53)
	11	2.96200	5^{-}		4(60), 7(40)

Table 23: (continued)

^{A}Z		Energy	J^{π}	M	Branching Ratios
	12	3.08371	2^+		2(100)
	13	3.13500	4^+		2(40), 3(20), 4(40)
	14	3.23328	2^+		2(35), 3(16), 4(32), 7(17)
	15	3.24411	0^+		2(100)
	16	3.38300	2^+		2(40), 3(20), 4(40)
	17	3.44980	4^+		5(31), 7(69)
	18	3.53799	1^+		1(17), 2(68), 3(15)
	19	3.59690	6^+		4(100)
	20	3.62960	2^+		1(8), 2(92)
	21	3.70300	4^+		5(30), 7(70)
	22	3.75430	4^+		4(100)
	23	3.78951	5^-		4(100)
	24	3.85400	2^+		2(40), 3(40), 4(20)
	25	3.86080	3^-		3(100)
	26	3.88010	1^+		1(41), 2(47), 8(12)
	27	3.88639	6^+		4(61), 7(5), 17(6), 19(28)
	28	3.90164	3^+		2(2), 3(7), 5(75), 7(16)
	29	4.00600	1^-		1(100)
	30	4.01080	2^+		1(10), 2(90)
	31	4.01500	1^+		2(100)
	32	4.08851	4^+		7(100)
	33	4.13938	1^+		1(100)
^{59}Fe	1	0.00000	1.5^-	GS	
	2	0.28702	0.5^-		1(100)
	3	0.47274	2.5^-		1(100)
	4	0.57087	2.5^-		1(100)
	5	0.61305	0.5^+		1(100)
	6	0.64280	3.5^-		1(100)
	7	0.72643	1.5^-		1(96), 2(4)
	8	1.02315	3.5^-		1(55), 3(5), 4(40)
	9	1.07781	1.5^-		5(100)
	10	1.16210	1.5^-		1(10), 2(20), 3(2), 4(68)
	11	1.21133	0.5^-		1(100)
	12	1.51724	4.5^+		8(100)
	13	1.56990	2.5^-		1(100)
	14	1.64800	2.5^+		1(100)
	15	1.74978	2.5^-		1(67), 11(33)
	16	1.91892	2.5^+		1(77), 7(10), 9(10), 10(3)
	17	1.96197	0.5^-		1(25), 5(7), 7(68)
	18	2.16190	0.5^+		5(100)
	19	2.27790	2.5^-		1(45), 7(55)
	20	2.31225	6.5^+		12(100)
	21	2.32240	1.5^+		1(100)
	22	2.34820	3.5^-		11(100)

Table 23: (continued)

^{A}Z		Energy	J^{π}	M	Branching Ratios
	23	2.39000	1.5^{+}		1(100)
	24	2.44727	1.5^{+}		1(7), 2(63), 7(19), 15(11)
	25	2.49380	3.5^{-}		1(100)
	26	2.56990	1.5^{-}		5(100)
	27	2.73500	1.5^{+}		1(100)
	28	2.75690	2.5^{+}		11(100)
	29	2.81028	0.5^{-}		7(19), 9(11), 11(60), 15(10)
^{60}Fe	1	0.00000	0^{+}	GS	
	2	0.82363	2^{+}		1(100)
	3	1.97380	0^{+}		2(100)
	4	2.11450	4^{+}		2(100)
	5	2.29940	2^{+}		1(55), 2(45)
	6	2.35800	0^{+}		2(100)
	7	2.67300	2^{+}		2(100)
	8	2.75600	2^{+}		2(100)
	9	2.79240	3^{+}		2(72), 4(3), 5(25)
	10	3.03900	2^{+}		2(100)
	11	3.07240	4^{+}		2(65), 4(35)
	12	3.29300	3^{-}		2(50), 4(25), 5(25)
	13	3.30800	3^{+}		2(50), 7(50)
	14	3.50200	4^{+}		2(65), 4(35)
	15	3.51610	5^{-}		4(100)
	16	3.52000	4^{+}		2(65), 5(35)
	17	3.56200	3^{-}		2(50), 4(25), 5(25)
	18	3.63500	2^{+}		2(100)
	19	3.64800	4^{+}		2(100)
	20	3.69800	0^{+}		2(100)
	21	3.71400	3^{+}		2(100)
	22	3.86700	3^{-}		2(50), 4(25), 5(25)
	23	3.87500	4^{-}		12(50), 15(50)
	24	3.92900	2^{+}		2(100)
	25	3.95440	6^{+}		15(100)
^{61}Fe	1	0.00000	1.5^{-}	GS	
	2	0.20676	2.5^{-}		1(100)
	3	0.39099	0.5^{-}		1(100)
	4	0.62866	1.5^{-}		1(93), 2(4), 3(3)
	5	0.86100	4.5^{+}		2(100)
	6	1.69000	2.5^{-}		1(50), 2(50)
	7	2.13000	3.5^{-}		2(100)
^{62}Fe	1	0.00000	0^{+}	GS	
	2	0.87680	2^{+}		1(100)
	3	1.81880	0^{+}		2(100)
	4	2.01600	2^{+}		1(100)
	5	2.17590	4^{+}		2(100)

Table 23: (continued)

^{A}Z		Energy	J^{π}	M	Branching Ratios
	6	3.63360	2^{+}		3(59), 5(41)
^{63}Fe	1	0.00000	2.5^{-}	GS	
^{53}Co	1	0.00000	3.5^{-}	GS	
	2	3.19000	9.5^{-}	M1	
^{54}Co	1	0.00000	0^{+}	GS	
	2	0.19900	7^{+}	M1	
	3	0.93720	1^{+}		1(100)
^{55}Co	1	0.00000	3.5^{-}	GS	
	2	2.16589	1.5^{-}		1(100)
	3	2.56585	1.5^{-}		1(100)
	4	2.65947	2.5^{-}		1(100)
	5	2.91857	3.5^{-}		1(100)
	6	2.92223	0.5^{+}		2(100)
	7	2.93909	0.5^{-}		2(74), 3(26)
	8	2.96010	1.5^{-}		1(38), 2(62)
	9	2.97310	5.5^{-}		1(100)
	10	2.97633	4.5^{-}		1(100)
^{56}Co	1	0.00000	4^{+}	GS	
	2	0.15838	3^{+}		1(100)
	3	0.57650	5^{+}		1(100)
	4	0.82961	4^{+}		1(25), 2(74), 3(1)
	5	0.97023	2^{+}		2(100)
	6	1.00913	5^{+}		1(89), 3(6), 4(5)
	7	1.11451	3^{+}		1(84), 2(5), 4(11)
	8	1.45068	0^{+}		5(100)
^{57}Co	1	0.00000	3.5^{-}	GS	
	2	1.22401	4.5^{-}		1(100)
	3	1.37765	1.5^{-}		1(100)
	4	1.50481	0.5^{-}		3(100)
	5	1.68940	5.5^{-}		1(46), 2(54)
	6	1.75758	1.5^{-}		1(99), 3(1)
	7	1.89745	3.5^{-}		1(47), 2(53)
	8	1.91955	2.5^{-}		1(100)
^{58}Co	1	0.00000	2^{+}	GS	
	2	0.02495	5^{+}	M1	
	3	0.05315	4^{+}	M2	
	4	0.11176	3^{+}		1(58), 3(42)
	5	0.36566	3^{+}		1(99), 4(1)
	6	0.37393	5^{+}		2(6), 3(94)
	7	0.45750	4^{+}		2(82), 3(1), 4(16), 5(1)
	8	0.88563	3^{+}		2(16), 3(6), 4(53), 5(25)
	9	1.04012	3^{+}		1(30), 5(23), 7(47)
	10	1.04426	3^{+}		1(82), 4(18)

Table 23: (continued)

^{A}Z		Energy	J^{π}	M	Branching Ratios
	11	1.05019	1^{+}		1(61), 4(36), 5(3)
	12	1.07550	6^{+}		6(100)
^{59}Co	1	0.00000	3.5^{-}	GS	
	2	1.09926	1.5^{-}		1(100)
	3	1.19045	4.5^{-}		1(100)
	4	1.29161	1.5^{-}		1(93), 2(7)
	5	1.43426	0.5^{-}		2(21), 4(79)
	6	1.45952	5.5^{-}		1(93), 3(7)
	7	1.48173	2.5^{-}		1(76), 2(23), 4(1)
	8	1.74469	3.5^{-}		1(55), 3(34), 7(11)
	9	2.06176	3.5^{-}		1(8), 3(47), 7(41), 8(4)
	10	2.08720	2.5^{-}		1(45), 4(39), 8(16)
	11	2.15362	4.5^{-}		6(100)
	12	2.18350	5.5^{-}		1(10), 3(90)
	13	2.20478	2.5^{-}		1(7), 3(22), 4(26), 5(9), 7(36)
	14	2.39480	4.5^{-}		1(33), 6(18), 8(44), 9(5)
	15	2.47870	2.5^{-}		1(87), 13(13)
	16	2.54040	3.5^{+}		1(14), 3(14), 8(72)
	17	2.58171	3.5^{-}		1(100)
	18	2.58580	3.5^{-}		1(58), 3(42)
	19	2.71310	0.5^{+}		2(100)
	20	2.72240	4.5^{+}		12(100)
	21	2.77020	1.5^{-}		1(80), 8(10), 9(10)
	22	2.78170	2.5^{-}		1(85), 2(15)
	23	2.81680	2.5^{-}		1(100)
	24	2.82420	6.5^{+}		1(56), 10(24), 11(20)
	25	2.82620	3.5^{-}		1(32), 2(62), 3(6)
	26	2.82910	2.5^{-}		2(100)
	27	2.91200	1.5^{-}		1(71), 9(29)
	28	2.91460	3.5^{+}		3(47), 10(25), 14(28)
	29	2.95790	1.5^{-}		2(50), 13(17), 18(33)
	30	2.96310	5.5^{+}		1(50), 3(25), 6(25)
	31	2.96590	1.5^{-}		1(61), 2(8), 5(8), 12(23)
	32	2.97300	1.5^{+}		8(100)
^{60}Co	1	0.00000	5^{+}	GS	
	2	0.05859	2^{+}	M1	
	3	0.27720	4^{+}		1(100)
	4	0.28840	3^{+}		2(100)
	5	0.43571	5^{+}		1(39), 3(61)
	6	0.50620	3^{+}		2(99), 4(1)
	7	0.54282	2^{+}		2(38), 4(62)
	8	0.61455	3^{+}		2(96), 3(4)
	9	0.73880	1^{+}		2(58), 7(42)
	10	0.78571	4^{+}		1(53), 4(44), 5(2), 8(1)

Table 23: (continued)

^{A}Z		Energy	J^{π}	M	Branching Ratios
	11	0.94000	3^-		2(60), 3(40)
	12	1.00391	3^+		2(49), 3(23), 4(2), 7(26)
	13	1.00580	4^+		1(6), 4(40), 8(52), 10(2)
	14	1.13198	2^+		9(100)
	15	1.15070	2^+		4(100)
	16	1.20783	5^+		1(29), 3(71)
	17	1.21645	6^+		1(74), 5(26)
	18	1.21685	4^-		4(19), 6(81)
	19	1.34186	3^+		1(4), 2(62), 7(34)
	20	1.37974	6^+		5(84), 16(16)
	21	1.38097	3^+		3(100)
	22	1.45121	4^+		7(58), 10(42)
	23	1.50830	2^+		6(100)
	24	1.51000	7^+		1(50), 5(25), 17(25)
	25	1.51580	4^+		1(78), 3(9), 8(13)
	26	1.56594	2^-		2(70), 4(20), 19(10)
	27	1.63984	4^+		3(30), 10(70)
	28	1.66900	6^+		1(50), 5(25), 16(25)
	29	1.68621	1^+		9(100)
	30	1.70968	1^-		2(100)
	31	1.74929	3^+		2(36), 3(33), 7(12), 10(19)
	32	1.78762	5^+		1(30), 13(70)
	33	1.80022	6^-		1(93), 17(6), 20(1)
	34	1.80863	3^-		1(100)
	35	1.83080	4^+		1(93), 3(7)
	36	1.83323	3^+		2(100)
	37	1.85271	4^+		1(100)
	38	1.87715	2^+		2(100)
	39	1.88890	4^+		1(27), 8(53), 13(20)
	40	1.92429	5^+		3(100)
	41	1.98120	4^-		4(100)
	42	1.98352	2^-		34(100)
	43	2.03271	3^+		16(100)
	44	2.04542	5^-		6(65), 16(35)
	45	2.08077	2^+		2(100)
	46	2.12182	3^+		1(21), 12(79)
	47	2.13223	7^-		17(18), 33(82)
	48	2.13344	3^+		2(59), 4(41)
	49	2.15190	3^-		13(100)
	50	2.18310	3^+		26(100)
^{61}Co	1	0.00000	3.5^-	GS	
	2	1.02748	1.5^-		1(100)
	3	1.20509	1.5^-		1(96), 2(4)
^{62}Co	1	0.00000	2^+	GS	

Table 23: (continued)

^{A}Z		Energy	J^{π}	M	Branching Ratios
	2	0.02200	5^{+}	M1	
^{63}Co	1	0.00000	3.5^{-}	GS	
	2	0.99492	1.5^{-}		1(100)
^{64}Co	1	0.00000	1^{+}	GS	
^{55}Ni	1	0.00000	3.5^{-}	GS	
^{56}Ni	1	0.00000	0^{+}	GS	
	2	2.70060	2^{+}		1(100)
	3	3.92360	4^{+}		2(100)
	4	3.95660	0^{+}		2(100)
	5	4.93200	5^{-}		3(100)
	6	5.00370	0^{+}		2(100)
	7	5.31570	6^{+}		3(100)
	8	5.35250	2^{+}		1(90), 2(10)
	9	5.48370	3^{+}		2(100)
	10	5.66800	3^{+}		3(100)
	11	5.67900	6^{+}		3(100)
	12	5.79900	3^{+}		2(50), 3(50)
	13	5.98500	4^{+}		2(75), 3(25)
	14	6.00000	0^{+}		2(100)
	15	6.01100	1^{-}		2(100)
	16	6.23600	2^{+}		1(75), 2(25)
	17	6.31970	2^{+}		2(100)
	18	6.32700	3^{-}		2(75), 3(25)
	19	6.40580	2^{+}		2(100)
	20	6.43600	4^{+}		2(75), 3(25)
	21	6.51700	2^{+}		2(100)
	22	6.55460	2^{+}		2(100)
	23	6.57200	2^{+}		2(100)
	24	6.65480	0^{+}		2(100)
^{57}Ni	1	0.00000	1.5^{-}	GS	
	2	0.76850	2.5^{-}		1(100)
	3	1.11260	0.5^{-}		1(100)
	4	2.44310	2.5^{-}		1(100)
	5	2.57760	3.5^{-}		1(100)
	6	3.00710	1.5^{-}		1(100)
	7	3.00900	3.5^{+}		2(50), 4(50)
	8	3.23400	3.5^{-}		1(40), 2(60)
	9	3.31100	2.5^{-}		1(100)
	10	3.37000	3.5^{-}		2(50), 5(50)
	11	3.70000	2.5^{-}		2(70), 5(30)
	12	3.71500	1.5^{+}		4(40), 5(30), 8(30)
	13	3.72600	2.5^{+}		1(100)
	14	3.84000	1.5^{-}		1(80), 3(10), 5(10)

Table 23: (continued)

^{A}Z		Energy	J^{π}	M	Branching Ratios
	15	3.86500	5.5^{-}		5(100)
	16	3.88200	2.5^{-}		2(70), 5(30)
	17	4.02100	4.5^{+}		2(100)
	18	4.04400	2.5^{-}		2(70), 5(30)
	19	4.07300	4.5^{-}		5(100)
	20	4.23000	3.5^{-}		1(2), 2(64), 5(34)
	21	4.37200	1.5^{+}		2(50), 4(50)
	22	4.37400	2.5^{-}		1(70), 2(30)
	23	4.46100	1.5^{-}		1(70), 2(30)
	24	4.54400	2.5^{+}		1(100)
	25	4.57600	3.5^{-}		1(65), 2(35)
^{58}Ni	1	0.00000	0^{+}	GS	
	2	1.45400	2^{+}		1(100)
	3	2.45910	4^{+}		2(100)
	4	2.77520	2^{+}		1(4), 2(96)
	5	2.90180	1^{+}		1(6), 2(94)
	6	2.94240	0^{+}		2(10), 4(10), 5(80)
	7	3.03760	2^{+}		1(40), 2(59), 4(1)
	8	3.26340	2^{+}		1(60), 2(39), 3(1)
	9	3.42030	3^{+}		2(2), 3(90), 4(1), 5(1), 6(1), 7(5)
	10	3.52400	4^{+}		2(60), 4(40)
	11	3.53090	0^{+}		2(92), 3(3), 4(2), 5(1), 6(1), 7(1)
	12	3.55800	3^{-}		2(40), 3(30), 4(30)
	13	3.59340	2^{+}		1(63), 2(11), 3(2), 4(17), 6(5), 7(1), 8(1)
	14	3.62000	4^{+}		2(20), 3(80)
	15	3.77440	3^{+}		2(14), 3(58), 7(9), 9(19)
	16	3.87000	2^{-}		2(40), 4(30), 5(30)
	17	3.89830	2^{+}		1(24), 2(76)
	18	3.93210	6^{+}		3(100)
	19	4.02000	3^{+}		2(40), 3(30), 4(30)
	20	4.10770	2^{+}		1(47), 2(40), 4(6), 5(5), 9(2)
	21	4.26000	2^{+}		1(50), 2(50)
	22	4.29400	4^{+}		2(50), 3(50)
	23	4.34800	1^{-}		2(100)
	24	4.35500	2^{+}		1(50), 2(50)
	25	4.38000	5^{+}		3(29), 14(71)
	26	4.40480	4^{+}		2(100)
	27	4.45000	2^{+}		4(10), 5(9), 13(81)
	28	4.47530	3^{-}		2(80), 4(20)
	29	4.51800	4^{+}		2(50), 3(50)
	30	4.53830	0^{+}		2(100)
^{59}Ni	1	0.00000	1.5^{-}	GS	
	2	0.33942	2.5^{-}		1(100)
	3	0.46498	0.5^{-}		1(100)

Table 23: (continued)

^{A}Z		Energy	J^{π}	M	Branching Ratios
	4	0.87795	1.5^-		$1(99), 2(1)$
	5	1.18879	2.5^-		$1(90), 2(4), 3(1), 4(5)$
	6	1.30141	0.5^-		$1(75), 3(11), 4(14)$
	7	1.33789	3.5^-		$1(29), 2(71)$
	8	1.67970	2.5^-		$1(14), 2(82), 3(2), 4(2)$
	9	1.69500	1.5^-		$1(50), 2(50)$
	10	1.73472	1.5^-		$1(58), 2(18), 3(12), 5(12)$
	11	1.73924	4.5^-		$2(100)$
	12	1.74610	3.5^-		$1(100)$
	13	1.76745	4.5^-		$2(91), 7(9)$
	14	1.94793	3.5^-		$1(49), 2(31), 4(2), 5(12), 7(6)$
	15	2.33000	3.5^-		$1(50), 2(50)$
	16	2.41497	1.5^-		$1(14), 2(2), 3(49), 4(21), 5(13), 6(1)$
	17	2.42800	4.5^+		$2(50), 5(50)$
	18	2.48000	1.5^+		$1(60), 2(40)$
	19	2.53040	4.5^-		$2(22), 5(54), 7(24)$
	20	2.53550	5.5^-		$11(100)$
	21	2.55340	0.5^+		$2(100)$
	22	2.62707	3.5^-		$1(57), 2(43)$
	23	2.64000	0.5^-		$1(40), 3(30), 4(30)$
	24	2.68140	1.5^-		$1(57), 4(43)$
	25	2.69200	1.5^-		$1(60), 4(40)$
	26	2.70502	5.5^-		$7(90), 13(10)$
	27	2.71300	3.5^+		$4(100)$
	28	2.89362	1.5^-		$2(61), 3(11), 4(19), 5(4), 6(2), 8(3)$
	29	3.02583	1.5^-		$1(49), 3(2), 4(47), 5(2)$
	30	3.03750	3.5^-		$2(100)$
	31	3.05433	4.5^+		$7(34), 14(65), 26(1)$
	32	3.06100	3.5^-		$2(100)$
	33	3.12543	3.5^-		$1(14), 2(86)$
^{60}Ni	1	0.00000	0^+	GS	
	2	1.33252	2^+		$1(100)$
	3	2.15864	2^+		$1(15), 2(85)$
	4	2.28487	0^+		$2(100)$
	5	2.50577	4^+		$2(100)$
	6	2.62608	3^+		$2(33), 3(63), 5(4)$
	7	3.11970	4^+		$2(92), 6(8)$
	8	3.12402	2^+		$1(9), 2(86), 3(1), 4(1), 6(3)$
	9	3.18602	3^-		$2(33), 3(36), 5(31)$
	10	3.19402	1^+		$1(16), 2(38), 3(30), 4(16)$
	11	3.26938	2^+		$1(15), 2(43), 3(21), 4(2), 6(19)$
	12	3.31870	0^+		$2(100)$
	13	3.38100	3^-		$3(100)$
	14	3.39350	2^+		$1(6), 2(83), 3(11)$

Table 23: (continued)

^{A}Z		Energy	J^{π}	M	Branching Ratios
	15	3.58810	0^+		2(26), 3(57), 10(17)
	16	3.61955	3^-		5(30), 6(70)
	17	3.62290	1^-		1(100)
	18	3.67071	4^+		5(100)
	19	3.70000	4^+		7(100)
	20	3.73067	2^-		2(60), 5(40)
	21	3.73610	2^+		1(3), 2(78), 4(17), 8(2)
	22	3.87500	2^+		2(33), 3(27), 6(14), 8(16), 13(10)
	23	3.88780	3^+		2(100)
	24	3.89500	1^-		2(60), 6(40)
	25	3.92580	3^+		3(32), 5(40), 9(28)
	26	4.00790	2^+		1(34), 2(56), 14(10)
	27	4.02045	2^+		1(56), 2(31), 4(4), 8(9)
	28	4.03500	0^+		1(50), 2(50)
	29	4.03967	3^-		2(70), 3(30)
	30	4.07854	2^+		1(3), 2(59), 3(38)
	31	4.11600	2^+		1(25), 2(26), 5(25), 8(24)
	32	4.16541	5^+		5(80), 6(20)
	33	4.19100	2^+		6(57), 16(43)
	34	4.26513	6^+		5(95), 7(5)
	35	4.29450	2^-		2(60), 5(40)
^{61}Ni	1	0.00000	1.5^-	GS	
	2	0.06741	2.5^-		1(100)
	3	0.28296	0.5^-		1(100)
	4	0.65601	0.5^-		1(77), 2(8), 3(15)
	5	0.90862	2.5^-		1(81), 2(16), 3(3)
	6	1.01517	3.5^-		1(24), 2(73), 4(3)
	7	1.09962	1.5^-		1(41), 2(7), 3(52)
	8	1.13233	2.5^-		1(61), 2(32), 6(7)
	9	1.18524	1.5^-		1(88), 2(1), 3(2), 4(9)
	10	1.45460	3.5^-		1(71), 2(23), 6(6)
	11	1.60964	2.5^-		1(42), 2(49), 5(5), 8(4)
	12	1.72947	1.5^-		1(27), 2(27), 3(23), 4(16), 5(1), 9(6)
	13	1.80770	4.5^-		2(89), 6(11)
	14	1.98799	4.5^-		2(57), 5(18), 6(12), 10(13)
	15	1.99760	2.5^-		1(68), 2(5), 5(16), 6(11)
	16	2.01800	3.5^-		2(90), 5(10)
	17	2.12000	1.5^-		1(100)
	18	2.12163	4.5^+		6(100)
	19	2.12348	0.5^-		1(100)
	20	2.12923	5.5^-		6(100)
	21	2.40970	4.5^-		2(62), 6(9), 8(12), 10(17)
	22	2.41000	1.5^-		1(100)
	23	2.46400	3.5^-		2(75), 5(25)

Table 23: (continued)

^{A}Z		Energy	J^{π}	M	Branching Ratios
	24	2.52600	2.5^{-}		1(50), 2(50)
	25	2.59200	3.5^{-}		2(75), 5(25)
	26	2.63990	1.5^{-}		1(100)
	27	2.69700	2.5^{+}		1(100)
	28	2.71700	1.5^{-}		1(100)
	29	2.76500	1.5^{-}		1(100)
^{62}Ni	1	0.00000	0^{+}	GS	
	2	1.17291	2^{+}		1(100)
	3	2.04860	0^{+}		2(100)
	4	2.30180	2^{+}		1(61), 2(39)
	5	2.33635	4^{+}		2(100)
	6	2.89120	0^{+}		2(100)
	7	3.05851	2^{+}		1(11), 2(39), 4(35), 5(15)
	8	3.15798	2^{+}		1(27), 2(65), 4(8)
	9	3.17650	4^{+}		2(93), 4(7)
	10	3.25768	2^{+}		1(3), 2(97)
	11	3.26200	2^{+}		2(75), 4(25)
	12	3.26992	1^{+}		1(11), 2(50), 3(36), 4(3)
	13	3.27746	4^{+}		2(100)
	14	3.37026	2^{+}		1(59), 3(11), 4(14), 6(16)
	15	3.37800	4^{-}		2(100)
	16	3.46200	3^{+}		2(100)
	17	3.48600	1^{+}		4(100)
	18	3.50000	2^{+}		2(75), 4(25)
	19	3.51850	2^{+}		1(6), 2(80), 3(8), 7(6)
	20	3.52287	2^{+}		4(56), 5(27), 7(16), 10(1)
	21	3.75700	3^{-}		2(56), 4(44)
	22	3.84400	2^{+}		2(75), 4(25)
	23	3.84934	0^{+}		4(48), 12(52)
	24	3.85300	2^{+}		2(75), 4(25)
	25	3.86000	2^{+}		1(75), 6(25)
	26	3.96700	2^{+}		4(100)
	27	3.97290	2^{+}		1(37), 2(56), 12(6), 20(1)
	28	3.99700	4^{+}		2(100)
	29	4.01871	6^{+}		5(100)
	30	4.03500	2^{+}		2(75), 4(25)
	31	4.05508	4^{+}		2(11), 4(6), 5(66), 13(17)
	32	4.06250	1^{+}		1(47), 4(53)
	33	4.14400	2^{-}		4(100)
	34	4.15120	2^{+}		4(31), 5(21), 7(48)
	35	4.15410	4^{+}		5(100)
	36	4.16007	5^{-}		5(78), 11(22)
	37	4.17900	3^{+}		9(100)

Table 23: (continued)

^{A}Z		Energy	J^{π}	M	Branching Ratios
	38	4.20140	3^-		20(100)
^{63}Ni	1	0.00000	0.5^-	GS	
	2	0.08715	2.5^-		1(100)
	3	0.15555	1.5^-		1(100)
	4	0.51755	1.5^-		1(10), 2(2), 3(88)
	5	1.00110	0.5^-		1(3), 3(51), 4(46)
	6	1.06899	2.5^-		1(29), 2(57), 3(14)
	7	1.25110	2.5^+		2(70), 3(30)
	8	1.29183	4.5^+		2(100)
	9	1.32404	1.5^-		1(25), 2(16), 3(59)
	10	1.45170	2.5^-		2(100)
	11	1.65700	1.5^+		1(50), 2(50)
	12	1.67700	2.5^-		2(100)
	13	1.78700	3.5^-		2(100)
	14	1.89900	2.5^-		2(100)
	15	2.14900	1.5^-		1(50), 2(25), 3(25)
	16	2.18350	5.5^+		8(100)
	17	2.26170	2.5^-		2(61), 3(39)
	18	2.29700	2.5^+		3(50), 4(50)
	19	2.35310	0.5^+		1(81), 2(19)
	20	2.51900	4.5^+		2(100)
	21	2.57300	4.5^+		2(100)
	22	2.67500	2.5^+		3(50), 4(50)
	23	2.69660	0.5^-		1(32), 3(68)
	24	2.81450	5.5^+		8(61), 16(39)
^{64}Ni	1	0.00000	0^+	GS	
	2	1.34575	2^+		1(100)
	3	2.27656	2^+		2(100)
	4	2.48500	2^+		1(25), 2(75)
	5	2.61010	4^+		2(100)
	6	2.86730	0^+		2(100)
	7	2.97208	2^+		1(41), 2(59)
	8	3.02583	0^+		2(96), 3(4)
	9	3.16610	4^+		2(100)
	10	3.27598	2^+		1(74), 2(26)
	11	3.39570	4^+		2(55), 5(45)
	12	3.46361	2^-		2(16), 3(84)
	13	3.48200	2^+		1(25), 2(75)
	14	3.56040	3^-		1(8), 2(72), 3(20)
	15	3.64798	1^+		1(35), 2(65)
	16	3.74900	2^+		1(23), 2(77)
	17	3.74940	4^+		9(25), 14(75)
	18	3.79700	1^+		1(40), 2(60)
	19	3.80800	1^+		1(40), 2(60)

Table 23: (continued)

^{A}Z		Energy	J^{π}	M	Branching Ratios
	20	3.84890	5^-		5(86), 11(10), 17(4)
	21	3.96500	2^-		2(50), 3(50)
	22	4.08520	4^+		5(67), 20(33)
	23	4.13700	2^-		2(50), 3(50)
	24	4.17230	6^-		20(100)
^{65}Ni	1	0.00000	2.5^-	GS	
	2	0.06337	0.5^-	M1	
	3	0.31008	1.5^-		1(98), 2(2)
	4	0.69323	1.5^-		1(10), 2(81), 3(9)
	5	1.01701	4.5^+		1(100)
	6	1.14170	2.5^-		1(100)
	7	1.27410	0.5^-		1(27), 2(28), 3(45)
	8	1.41760	0.5^-		1(24), 3(43), 4(33)
	9	1.55600	3.5^+		1(100)
	10	1.59400	3.5^-		1(40), 3(30), 4(30)
	11	1.77200	1.5^-		1(60), 2(40)
	12	1.92040	2.5^+		3(100)
	13	2.09600	2.5^+		1(50), 3(50)
	14	2.14680	1.5^-		1(51), 2(49)
	15	2.16300	0.5^+		1(40), 2(40), 3(10), 4(10)
	16	2.18574	5.5^+		5(100)
	17	2.30200	1.5^+		1(50), 2(50)
	18	2.32470	3.5^-		1(40), 3(30), 4(30)
	19	2.33600	3.5^+		1(40), 5(40), 6(20)
	20	2.51000	3.5^+		1(40), 5(40), 6(20)
	21	2.51934	6.5^+		5(100)
	22	2.52000	2.5^+		1(50), 3(50)
	23	2.57400	0.5^-		1(40), 2(30), 3(30)
	24	2.69800	3.5^-		1(40), 3(30), 4(30)
	25	2.71150	1.5^+		2(28), 3(72)
^{56}Cu	1	0.00000	3^+	GS	
^{57}Cu	1	0.00000	1.5^-	GS	
^{58}Cu	1	0.00000	1^+	GS	
	2	0.20300	0^+		1(100)
	3	0.44468	3^+		1(100)
	4	1.05152	1^+		2(100)
	5	1.42780	2^+		1(100)
	6	1.55010	4^+		3(100)
^{59}Cu	1	0.00000	1.5^-	GS	
	2	0.49109	0.5^-		1(100)
	3	0.91398	2.5^-		1(99), 2(1)
	4	1.39851	3.5^-		1(88), 3(12)
	5	1.86524	3.5^-		1(30), 3(55), 4(15)

Table 23: (continued)

^{A}Z		Energy	J^{π}	M	Branching Ratios
	6	1.98780	2.5^{+}		1(100)
	7	2.26630	1.5^{+}		1(52), 2(48)
	8	2.31810	2.5^{-}		1(83), 2(17)
	9	2.32385	1.5^{+}		1(90), 3(10)
^{60}Cu	1	0.00000	2^{+}	GS	
	2	0.06220	1^{+}		1(100)
	3	0.28720	2^{+}		1(30), 2(70)
	4	0.33580	2^{-}		2(100)
	5	0.36460	1^{+}		1(100)
	6	0.45380	3^{+}		1(99), 3(1)
	7	0.55750	4^{+}		1(57), 3(11), 6(32)
^{61}Cu	1	0.00000	1.5^{-}	GS	
	2	0.47510	0.5^{-}		1(100)
	3	0.97006	2.5^{-}		1(99), 2(1)
	4	1.31055	3.5^{-}		1(94), 3(6)
	5	1.39420	2.5^{-}		1(85), 2(12), 3(3)
	6	1.66046	1.5^{-}		1(65), 2(14), 3(16), 5(5)
	7	1.73261	3.5^{-}		1(62), 3(14), 4(22), 5(2)
	8	1.90418	2.5^{-}		1(36), 3(42), 4(22)
	9	1.93266	1.5^{-}		1(67), 2(25), 3(8)
	10	1.94249	3.5^{-}		1(10), 3(61), 4(19), 7(10)
	11	2.08886	0.5^{-}		1(68), 2(32)
	12	2.20340	2.5^{-}		2(23), 3(47), 4(19), 7(11)
	13	2.29509	4.5^{-}		3(12), 4(34), 5(26), 7(20), 10(8)
	14	2.33646	4.5^{-}		3(75), 4(22), 5(1), 10(2)
	15	2.35819	1.5^{-}		1(24), 2(34), 6(31), 9(11)
	16	2.39902	3.5^{-}		3(58), 4(42)
	17	2.47246	1.5^{-}		1(6), 2(84), 3(10)
	18	2.58375	2.5^{+}		7(82), 10(18)
	19	2.58460	2.5^{+}		1(100)
	20	2.61175	4.5^{-}		4(10), 7(59), 10(30), 13(1)
	21	2.62715	3.5^{-}		4(95), 13(3), 14(2)
	22	2.68413	1.5^{-}		1(43), 2(54), 5(3)
	23	2.72077	4.5^{+}		4(56), 7(37), 10(1), 16(1), 20(5)
	24	2.72834	3.5^{-}		3(60), 4(33), 12(4), 16(3)
	25	2.79263	2.5^{-}		1(45), 4(45), 6(10)
	26	2.84049	1.5^{-}		1(44), 11(56)
	27	2.85710	1.5^{-}		1(80), 2(20)
	28	2.92420	2.5^{-}		7(78), 10(9), 13(3), 16(4), 20(2), 21(4)
	29	2.93274	1.5^{-}		1(11), 2(79), 5(10)
	30	3.00161	2.5^{-}		1(60), 5(26), 12(14)
	31	3.01569	3.5^{-}		4(73), 13(13), 14(14)
	32	3.01930	1.5^{-}		1(29), 2(71)
^{62}Cu	1	0.00000	1^{+}	GS	

Table 23: (continued)

^{A}Z		Energy	J^{π}	M	Branching Ratios
	2	0.04084	2^+		1(100)
	3	0.24345	2^+		1(100)
	4	0.28782	2^+		2(100)
	5	0.39021	4^+		2(96), 3(4)
	6	0.42614	3^+		2(100)
	7	0.54832	1^+		1(48), 2(47), 3(1), 4(4)
	8	0.63747	1^+		1(1), 2(89), 3(8), 4(2)
	9	0.64450	2^+		1(100)
	10	0.67508	3^+		2(37), 3(44), 5(19)
	11	0.69831	2^+		2(39), 3(36), 6(25)
	12	0.72773	2^+		2(36), 3(54), 4(10)
	13	0.75584	2^+		1(100)
	14	0.91537	2^+		1(42), 3(12), 4(2), 6(44)
	15	0.98273	3^+		2(45), 5(35), 6(20)
	16	1.02303	2^+		1(50), 2(10), 3(40)
	17	1.05170	3^+		10(100)
	18	1.07724	2^+		2(40), 5(60)
	19	1.14168	2^+		3(20), 5(50), 6(30)
^{63}Cu	1	0.00000	1.5^-	GS	
	2	0.66967	0.5^-		1(100)
	3	0.96210	2.5^-		1(100)
	4	1.32701	3.5^-		1(84), 3(16)
	5	1.41205	2.5^-		1(71), 2(7), 3(22)
	6	1.54705	1.5^-		1(76), 2(2), 3(22)
	7	1.86116	3.5^-		1(55), 3(45)
	8	2.01125	1.5^-		1(49), 2(22), 3(25), 5(2), 6(2)
	9	2.06223	0.5^-		1(16), 2(48), 6(36)
	10	2.08139	2.5^-		1(39), 3(24), 4(27), 6(10)
	11	2.09260	3.5^-		1(9), 3(51), 4(40)
	12	2.20788	4.5^-		3(43), 4(57)
	13	2.33658	2.5^-		1(70), 3(22), 5(8)
^{64}Cu	1	0.00000	1^+	GS	
	2	0.15928	2^+		1(100)
	3	0.27826	2^+		1(100)
	4	0.34390	1^+		1(96), 2(4)
	5	0.36223	3^+		1(2), 2(98)
	6	0.57463	4^+		2(6), 5(94)
	7	0.60878	2^+		1(82), 2(8), 3(4), 4(6)
	8	0.66300	1^+		1(32), 2(27), 3(35), 4(6)
	9	0.73905	2^+		1(7), 2(62), 3(10), 4(3), 5(18)
	10	0.74625	3^+		3(70), 5(21), 7(9)
	11	0.87828	0^+		1(57), 2(3), 4(40)
	12	0.89571	3^+		1(14), 2(6), 3(65), 6(15)
	13	0.92708	1^+		1(8), 2(16), 3(67), 5(9)

Table 23: (continued)

^{A}Z		Energy	J^{π}	M	Branching Ratios
	14	1.24109	2^{+}		$2(19), 3(26), 7(15), 10(40)$
	15	1.24265	1^{+}		$1(100)$
	16	1.28715	2^{+}		$5(100)$
	17	1.28860	3^{+}		$2(54), 3(22), 8(24)$
^{65}Cu	1	0.00000	1.5^{-}	GS	
	2	0.77064	0.5^{-}		$1(100)$
	3	1.11556	2.5^{-}		$1(100)$
	4	1.48183	3.5^{-}		$1(83), 3(17)$
	5	1.62343	2.5^{-}		$1(56), 2(11), 3(33)$
	6	1.72500	1.5^{-}		$1(72), 3(28)$
	7	2.09434	3.5^{-}		$1(29), 3(53), 4(13), 5(5)$
	8	2.10744	2.5^{-}		$1(17), 2(10), 3(35), 4(32), 6(6)$
	9	2.21284	0.5^{-}		$1(37), 2(55), 6(8)$
	10	2.27850	3.5^{-}		$1(2), 3(98)$
	11	2.32905	1.5^{-}		$1(48), 2(29), 3(23)$
	12	2.40660	4.5^{+}		$3(27), 4(56), 7(17)$
	13	2.52574	4.5^{+}		$4(100)$
	14	2.53304	1.5^{+}		$1(41), 2(50), 6(9)$
	15	2.53390	3.5^{+}		$4(43), 7(42), 10(15)$

C Neutron Resonance Data

In this table we list the neutron resonance data used in the development of our level density and photon strength function systematics. This data is taken from the Reference Input Parameter Library, as explained in the text. Note that this table lists the data by target nucleus, though the data applies to the structure of the compound nucleus (target plus neutron).

Table 24: Experimental neutron resonance data

Target	D_0 (keV)	$\langle\Gamma_\gamma\rangle_0$ (meV)
^{40}Ca	32.6 ± 4.30	1500 ± 1000
^{42}Ca	20.0 ± 5.00	1100 ± 200
^{43}Ca	1.80 ± 0.30	750 ± 40
^{44}Ca	24.1 ± 3.20	1300 ± 400
^{45}Sc	1.30 ± 0.10	840 ± 460
^{46}Ti	25.0 ± 4.40	1400 ± 400
^{47}Ti	1.75 ± 0.25	1200 ± 400
^{48}Ti	18.3 ± 2.90	1400 ± 400
^{49}Ti	4.00 ± 0.80	810 ± 240
^{50}Ti	125. ± 70.0	1100 ± 300
^{50}V	2.30 ± 0.60	600 ± 80
^{51}V	4.10 ± 0.60	1500 ± 300
^{50}Cr	13.3 ± 1.30	1500 ± 500
^{52}Cr	43.4 ± 4.37	1850 ± 550
^{53}Cr	7.80 ± 0.80	2100 ± 800
^{54}Cr	62.0 ± 8.00	2500 ± 700
^{55}Mn	2.30 ± 0.40	750 ± 150
^{54}Fe	18.0 ± 2.40	1800 ± 500
^{56}Fe	25.4 ± 2.20	920 ± 410
^{57}Fe	6.50 ± 1.00	1900 ± 600
^{58}Fe	25.4 ± 4.90	3000 ± 900
^{59}Co	1.25 ± 0.15	560 ± 100
^{58}Ni	13.4 ± 0.90	2600 ± 800
^{59}Ni	2.00 ± 0.70	2200 ± 700
^{60}Ni	13.8 ± 0.90	1700 ± 500
^{61}Ni	2.10 ± 0.15	2200 ± 700
^{62}Ni	16.0 ± 3.00	910 ± 270
^{64}Ni	19.6 ± 3.00	2400 ± 700
^{63}Cu	0.95 ± 0.09	490 ± 30

Table 24: (continued)

Target	D_0 (keV)	$\langle\Gamma_\gamma\rangle_0$ (meV)
^{65}Cu	1.30 ± 0.11	385 ± 20

D Experimental GDR Parameters

In this table we list the measured GDR parameters used in the development of our local GDR systematics. This data is taken from the Reference Input Parameter Library, as explained in the text.

Table 25: Experimental GDR parameters

Target	$E_{E1,1}$	$\sigma_{E1,1}$	$\Gamma_{E1,1}$	$E_{E1,2}$	$\sigma_{E1,2}$	$\Gamma_{E1,2}$
^{51}V	17.93	53.3	3.62	20.95	40.7	7.15
^{51}V	17.86	58.8	4.42	21.22	28.8	5.10
^{54}Cr	17.80	88.0	6.50			
^{55}Mn	16.82	51.4	4.33	20.09	45.2	4.09
^{59}Co	16.43	28.3	2.73	18.66	58.4	7.38
^{60}Ni	16.30	34.1	2.44	18.51	55.2	6.37
^{63}Cu	16.72	66.1	4.19	19.10	30.1	3.56
^{63}Cu	16.24	60.8	4.65	19.65	26.8	4.59
^{65}Cu	16.70	75.2	6.89			

E Level Density Parameters

The following table lists our Fermi gas and constant temperature level density parameters. The parameters listed correspond to those discussed in Section 4. The column labeled "N" indicates how many of the discrete levels listed in Appendix B were included in the constant temperature fit and subsequent Hauser-Feshbach calculations. In the last column, an "x" indicates that the asymptotic level density parameter $\tilde{a}$ was derived from a measured average resonance spacing. An "s" indicates that $\tilde{a}$ is drawn from our systematic (see Section 4.3). All quantities listed are in units of MeV, with the exception of $\tilde{a}$ (units of MeV^{-1}) and $\sigma(E_x)$ (unitless).

Table 26: Local systematic level density parameters

Nucleus	$\tilde{a}$	Δ	δW	E_x	E_0	T	$\sigma(E_x)$	N	x/s
^{43}Ca	5.277	0.195	3.000	5.292	-3.782	1.279	2.674	16	x
^{44}Ca	5.725	2.248	2.620	7.818	-2.051	1.262	2.745	14	x
^{45}Ca	5.668	0.269	2.340	2.000	-1.391	0.941	2.092	3	x
^{46}Ca	5.631	2.112	1.480	5.600	-0.568	1.130	2.579	6	s
^{47}Ca	5.725	0.524	0.670	2.000	-1.127	1.008	2.132	0	s
^{45}Sc	5.536	-0.223	2.670	7.008	-5.900	1.425	3.014	35	s
^{46}Sc	5.675	-1.029	2.280	4.680	-5.400	1.291	2.885	25	x
^{47}Sc	5.725	-0.137	1.320	5.868	-4.604	1.335	3.007	26	s
^{48}Sc	5.819	-0.950	0.950	1.700	-3.080	1.050	2.492	6	s
^{49}Sc	5.912	0.384	0.210	2.000	-1.281	1.004	2.257	0	s
^{50}Sc	6.005	-0.660	0.330	6.578	-5.865	1.412	3.323	2	s
^{44}Ti	5.441	3.450	3.040	11.608	-3.098	1.504	3.052	16	s
^{45}Ti	5.536	-0.135	3.430	3.300	-2.854	1.071	2.467	13	s
^{46}Ti	5.631	2.371	3.020	10.316	-3.988	1.456	3.119	26	s
^{47}Ti	4.982	0.222	2.680	8.231	-6.114	1.589	3.294	25	x
^{48}Ti	5.745	2.043	1.690	9.470	-3.603	1.431	3.212	25	x
^{49}Ti	6.128	0.151	0.630	3.800	-2.560	1.107	2.725	16	x
^{50}Ti	5.965	2.167	0.240	5.430	-0.295	1.111	2.729	24	x
^{51}Ti	5.874	0.510	0.260	4.000	-2.098	1.142	2.832	14	x
^{52}Ti	6.190	1.559	1.030	3.981	-0.402	0.977	2.562	9	s
^{53}Ti	6.282	0.502	1.730	5.400	-3.168	1.156	3.066	0	s
^{54}Ti	6.373	1.776	2.370	6.800	-2.052	1.137	3.097	0	s
^{45}V	5.536	-0.173	3.460	5.660	-4.791	1.289	2.825	1	s
^{46}V	5.631	0.212	3.850	6.155	-4.544	1.273	2.866	20	s

Table 26: (continued)

Nucleus	$\tilde{a}$	Δ	δW	E_x	E_0	T	$\sigma(E_x)$	N	x/s
^{47}V	5.725	-0.121	3.360	2.600	-2.325	0.979	2.393	9	s
^{48}V	5.819	-0.580	1.880	4.551	-4.454	1.233	2.906	22	s
^{49}V	5.912	-0.154	1.990	2.000	-1.993	0.953	2.361	37	s
^{50}V	6.005	-0.820	0.810	5.720	-5.604	1.349	3.218	24	s
^{51}V	5.748	0.325	0.540	5.878	-3.698	1.320	3.186	30	x
^{52}V	6.239	-0.824	0.540	1.871	-2.933	1.014	2.646	24	x
^{53}V	6.282	-0.084	1.360	2.189	-1.951	0.940	2.539	6	s
^{54}V	6.373	-0.843	2.120	4.435	-4.844	1.165	3.147	0	s
^{55}V	6.465	-0.060	2.530	5.167	-4.064	1.139	3.159	0	s
^{56}V	6.556	-0.804	3.260	4.375	-4.840	1.105	3.159	0	s
^{57}V	6.646	-0.076	3.490	5.055	-4.094	1.086	3.179	0	s
^{47}Cr	5.725	-0.114	3.560	8.459	-7.157	1.476	3.206	2	s
^{48}Cr	5.819	2.943	3.100	9.231	-2.008	1.294	3.015	2	s
^{49}Cr	5.912	0.285	1.400	3.258	-2.036	1.047	2.582	12	s
^{50}Cr	6.005	2.015	1.760	5.155	-0.416	1.037	2.639	7	s
^{51}Cr	5.953	0.048	0.360	4.718	-3.332	1.225	3.032	12	x
^{52}Cr	6.190	2.011	0.120	8.101	-2.322	1.309	3.272	15	s
^{53}Cr	6.016	0.448	0.070	6.039	-3.528	1.298	3.280	13	x
^{54}Cr	6.080	1.945	0.740	7.490	-2.094	1.264	3.285	9	x
^{55}Cr	6.233	0.354	1.570	7.141	-4.761	1.315	3.450	9	x
^{56}Cr	6.556	1.714	1.980	4.189	-0.251	0.905	2.663	7	s
^{57}Cr	6.646	0.248	2.670	5.300	-3.627	1.100	3.198	0	s
^{58}Cr	6.736	1.814	2.900	6.900	-2.111	1.087	3.230	0	s
^{59}Cr	6.826	-0.040	3.340	4.100	-3.236	0.987	3.081	0	s
^{60}Cr	6.916	1.830	3.250	6.600	-1.865	1.034	3.233	0	s
^{48}Mn	5.819	-0.431	2.150	5.194	-4.717	1.266	2.965	0	s
^{49}Mn	5.912	0.304	1.330	2.000	-1.335	0.949	2.244	3	s
^{50}Mn	6.005	-0.226	1.170	5.274	-4.289	1.258	3.065	1	s
^{51}Mn	6.098	0.261	0.370	4.780	-3.013	1.192	2.988	11	s
^{52}Mn	6.190	-0.625	0.020	3.200	-3.409	1.136	2.917	19	s
^{53}Mn	6.282	0.205	-0.270	5.542	-3.543	1.253	3.223	21	s
^{54}Mn	6.373	-0.735	-0.210	6.115	-5.546	1.347	3.468	17	s
^{55}Mn	6.465	0.210	0.680	4.615	-3.000	1.126	3.102	12	s
^{56}Mn	6.617	-0.712	1.500	7.620	-7.069	1.374	3.638	8	x
^{57}Mn	6.646	-0.076	1.960	3.098	-2.496	0.959	2.869	6	s
^{58}Mn	6.736	-0.632	2.560	4.455	-4.523	1.096	3.244	1	s
^{59}Mn	6.826	-0.103	2.800	4.939	-3.982	1.077	3.263	0	s
^{60}Mn	6.916	-0.284	3.160	4.716	-4.161	1.055	3.276	1	s
^{61}Mn	7.006	-0.100	3.340	4.859	-3.958	1.038	3.296	0	s
^{51}Fe	6.098	0.385	0.640	5.826	-3.564	1.257	3.119	0	s
^{52}Fe	6.190	2.818	0.530	6.222	0.274	1.081	2.811	5	s

Table 26: (continued)

Nucleus	$\tilde{a}$	Δ	δW	E_x	E_0	T	$\sigma(E_x)$	N	x/s
^{53}Fe	6.282	0.121	-0.730	4.763	-3.114	1.216	3.135	5	s
^{54}Fe	6.373	1.967	-1.010	8.021	-2.135	1.315	3.403	25	s
^{55}Fe	6.428	0.366	-0.970	4.922	-2.781	1.199	3.212	5	x
^{56}Fe	6.556	1.927	0.050	8.893	-3.026	1.324	3.552	33	s
^{57}Fe	6.486	0.302	0.720	7.054	-4.629	1.300	3.554	31	x
^{58}Fe	6.551	2.014	1.220	9.192	-3.347	1.310	3.629	32	x
^{59}Fe	6.880	0.383	1.940	4.674	-2.836	1.032	3.161	28	x
^{60}Fe	6.916	1.921	2.070	6.777	-1.739	1.071	3.297	24	s
^{61}Fe	7.006	0.191	2.380	4.900	-3.382	1.042	3.293	4	s
^{62}Fe	7.095	1.935	2.590	6.400	-1.463	1.008	3.274	4	s
^{63}Fe	7.184	0.170	3.100	4.700	-3.316	0.992	3.298	0	s
^{52}Co	6.190	-0.962	0.120	4.423	-4.799	1.256	3.173	0	s
^{53}Co	6.282	0.278	-0.860	5.608	-3.380	1.272	3.251	1	s
^{54}Co	6.373	-0.229	-1.170	3.513	-2.869	1.151	3.029	2	s
^{55}Co	6.465	0.476	-2.180	4.728	-2.355	1.218	3.218	9	s
^{56}Co	6.556	-0.694	-1.540	4.295	-4.032	1.234	3.349	7	s
^{57}Co	6.646	0.165	-0.890	5.072	-3.210	1.194	3.338	7	s
^{58}Co	6.736	-0.881	0.110	5.390	-5.344	1.251	3.535	11	s
^{59}Co	6.826	0.198	0.770	4.955	-3.261	1.109	3.304	31	s
^{60}Co	7.022	-0.854	1.390	4.032	-4.469	1.081	3.320	49	x
^{61}Co	7.006	0.089	1.750	1.000	-1.185	0.783	2.195	2	s
^{62}Co	7.095	-0.862	2.350	4.058	-4.597	1.051	3.366	1	s
^{63}Co	7.184	0.034	2.410	4.915	-3.676	1.038	3.391	1	s
^{64}Co	7.272	-0.628	2.890	4.216	-4.351	1.015	3.398	0	s
^{55}Ni	6.465	0.404	-2.170	5.632	-2.980	1.285	3.384	0	s
^{56}Ni	6.556	3.215	-2.740	9.275	-0.532	1.346	3.582	23	s
^{57}Ni	6.646	0.624	-2.670	3.000	-1.256	1.092	2.880	15	s
^{58}Ni	6.736	1.993	-1.580	10.652	-3.691	1.445	3.922	29	s
^{59}Ni	6.909	0.433	-0.680	7.495	-4.430	1.305	3.712	32	x
^{60}Ni	6.872	2.075	-0.160	10.171	-3.664	1.362	3.872	34	x
^{61}Ni	7.111	0.305	0.590	5.581	-3.509	1.124	3.460	28	x
^{62}Ni	6.954	2.193	1.100	9.664	-3.384	1.284	3.824	37	x
^{63}Ni	7.378	0.337	1.580	3.200	-1.826	0.873	2.976	20	x
^{64}Ni	7.272	2.164	1.630	6.816	-1.296	1.032	3.419	23	s
^{65}Ni	7.785	0.337	1.760	2.000	-1.064	0.730	2.622	22	x
^{56}Cu	6.556	-0.666	-0.940	4.512	-4.210	1.227	3.348	0	s
^{57}Cu	6.646	0.693	-2.310	5.825	-2.610	1.260	3.454	0	s
^{58}Cu	6.736	-0.090	-1.210	4.332	-3.119	1.159	3.307	5	s
^{59}Cu	6.826	0.252	-0.650	3.219	-1.939	1.014	3.000	8	s
^{60}Cu	6.916	-0.616	0.350	7.061	-6.178	1.319	3.788	6	s
^{61}Cu	7.006	0.287	0.880	4.660	-2.904	1.057	3.299	31	s

Table 26: (continued)

Nucleus	$\tilde{a}$	Δ	δW	E_x	E_0	T	$\sigma(E_x)$	N	x/s
^{62}Cu	7.095	-0.702	1.530	5.539	-5.385	1.172	3.615	18	s
^{63}Cu	7.184	0.337	1.860	1.000	-1.052	0.817	2.066	12	s
^{64}Cu	7.131	-0.643	2.420	3.673	-3.910	0.997	3.336	16	x
^{65}Cu	7.360	0.343	2.330	1.000	-0.941	0.764	2.088	2	s

F Initial Solar Seeds for Hydrogen Burning

Table 27: Initial composition for hydrogen burning

^{A}Z	$X_{^{A}Z}$	^{A}Z	$X_{^{A}Z}$	^{A}Z	$X_{^{A}Z}$
^{1}H	7.0573×10^{-1}	^{2}H	4.8010×10^{-5}	^{3}He	2.9291×10^{-5}
^{4}He	2.7521×10^{-1}	^{6}Li	6.4957×10^{-10}	^{7}Li	9.3525×10^{-9}
^{9}Be	1.6619×10^{-10}	^{10}B	1.0674×10^{-9}	^{11}B	4.7246×10^{-9}
^{12}C	3.0323×10^{-3}	^{13}C	3.6500×10^{-5}	^{14}N	1.1049×10^{-3}
^{15}N	4.3634×10^{-6}	^{16}O	9.5918×10^{-3}	^{17}O	3.8873×10^{-6}
^{18}O	2.1673×10^{-5}	^{19}F	4.0515×10^{-7}	^{20}Ne	1.6189×10^{-3}
^{21}Ne	4.1274×10^{-6}	^{22}Ne	1.3022×10^{-4}	^{23}Na	3.3394×10^{-5}
^{24}Mg	5.1480×10^{-4}	^{25}Mg	6.7664×10^{-5}	^{26}Mg	7.7605×10^{-5}
^{27}Al	5.8052×10^{-5}	^{28}Si	6.5301×10^{-4}	^{29}Si	3.4257×10^{-5}
^{30}Si	2.3524×10^{-5}	^{31}P	8.1551×10^{-6}	^{32}S	3.9581×10^{-4}
^{33}S	3.2221×10^{-6}	^{34}S	1.8663×10^{-5}	^{36}S	9.3793×10^{-8}
^{35}Cl	3.5147×10^{-6}	^{37}Cl	1.1886×10^{-6}	^{36}Ar	7.7402×10^{-5}
^{38}Ar	1.5379×10^{-5}	^{40}Ar	2.5295×10^{-8}	^{39}K	3.4685×10^{-6}
^{40}K	5.5446×10^{-9}	^{41}K	2.6311×10^{-7}	^{40}Ca	5.9898×10^{-5}
^{42}Ca	4.1964×10^{-7}	^{43}Ca	8.9734×10^{-8}	^{44}Ca	1.4190×10^{-6}
^{46}Ca	2.7926×10^{-9}	^{48}Ca	1.3841×10^{-7}	^{45}Sc	3.8929×10^{-8}
^{46}Ti	2.2340×10^{-7}	^{47}Ti	2.0805×10^{-7}	^{48}Ti	2.1503×10^{-6}
^{49}Ti	1.6361×10^{-7}	^{50}Ti	1.6442×10^{-7}	^{50}V	9.2579×10^{-10}
^{51}V	3.7669×10^{-7}	^{50}Cr	7.4240×10^{-7}	^{52}Cr	1.4876×10^{-5}
^{53}Cr	1.7200×10^{-6}	^{54}Cr	4.3573×10^{-7}	^{55}Mn	1.3286×10^{-5}
^{54}Fe	7.1301×10^{-5}	^{56}Fe	1.1686×10^{-3}	^{57}Fe	2.8548×10^{-5}
^{58}Fe	3.6971×10^{-6}	^{59}Co	3.3579×10^{-6}	^{58}Ni	4.9441×10^{-5}
^{60}Ni	1.9578×10^{-5}	^{61}Ni	8.5944×10^{-7}	^{62}Ni	2.7759×10^{-6}
^{64}Ni	7.2687×10^{-7}	^{63}Cu	5.7528×10^{-7}	^{65}Cu	2.6471×10^{-7}
^{64}Zn	9.9237×10^{-7}	^{66}Zn	5.8765×10^{-7}	^{67}Zn	8.7619×10^{-8}
^{68}Zn	4.0593×10^{-7}	^{70}Zn	1.3811×10^{-8}	^{69}Ga	3.9619×10^{-8}
^{71}Ga	2.7119×10^{-8}	^{70}Ge	4.3204×10^{-8}	^{72}Ge	5.9372×10^{-8}
^{73}Ge	1.7136×10^{-8}	^{74}Ge	8.1237×10^{-8}	^{76}Ge	1.7840×10^{-8}
^{75}As	1.2445×10^{-8}	^{74}Se	1.0295×10^{-9}	^{76}Se	1.0765×10^{-8}
^{77}Se	9.1542×10^{-9}	^{78}Se	2.9003×10^{-8}	^{80}Se	6.2529×10^{-8}
^{82}Se	1.1823×10^{-8}	^{79}Br	1.1950×10^{-8}	^{81}Br	1.1925×10^{-8}
^{78}Kr	3.0187×10^{-10}	^{80}Kr	2.0216×10^{-9}	^{82}Kr	1.0682×10^{-8}
^{83}Kr	1.0833×10^{-8}	^{84}Kr	5.4607×10^{-8}	^{86}Kr	1.7055×10^{-8}
^{85}Rb	1.1008×10^{-8}	^{87}Rb	4.6434×10^{-9}	^{84}Sr	2.8047×10^{-10}
^{86}Sr	5.0468×10^{-9}	^{87}Sr	3.3230×10^{-9}	^{88}Sr	4.3206×10^{-8}
^{89}Y	1.0446×10^{-8}	^{90}Zr	1.3363×10^{-8}	^{91}Zr	2.9463×10^{-9}
^{92}Zr	4.5612×10^{-9}	^{94}Zr	4.7079×10^{-9}	^{96}Zr	7.7706×10^{-10}

Table 27: (continued)

^{A}Z	$X_{^{A}Z}$	^{A}Z	$X_{^{A}Z}$	^{A}Z	$X_{^{A}Z}$
^{93}Nb	1.6420×10^{-9}	^{92}Mo	8.7965×10^{-10}	^{94}Mo	5.6114×10^{-10}
^{95}Mo	9.7562×10^{-10}	^{96}Mo	1.0320×10^{-9}	^{97}Mo	5.9868×10^{-10}
^{98}Mo	1.5245×10^{-9}	^{100}Mo	6.2225×10^{-10}	^{96}Ru	2.5012×10^{-10}
^{98}Ru	8.6761×10^{-11}	^{99}Ru	5.9099×10^{-10}	^{100}Ru	5.9190×10^{-10}
^{101}Ru	8.0731×10^{-10}	^{102}Ru	1.5171×10^{-9}	^{104}Ru	9.1547×10^{-10}
^{103}Rh	8.9625×10^{-10}	^{102}Pd	3.6637×10^{-11}	^{104}Pd	4.0775×10^{-10}
^{105}Pd	8.2335×10^{-10}	^{106}Pd	1.0189×10^{-9}	^{108}Pd	1.0053×10^{-9}
^{110}Pd	4.5354×10^{-10}	^{107}Ag	6.8205×10^{-10}	^{109}Ag	6.4517×10^{-10}
^{106}Cd	5.3893×10^{-11}	^{108}Cd	3.9065×10^{-11}	^{110}Cd	5.5927×10^{-10}
^{111}Cd	5.7839×10^{-10}	^{112}Cd	1.0992×10^{-9}	^{113}Cd	5.6309×10^{-10}
^{114}Cd	1.3351×10^{-9}	^{116}Cd	3.5504×10^{-10}	^{113}In	2.2581×10^{-11}
^{115}In	5.1197×10^{-10}	^{112}Sn	1.0539×10^{-10}	^{114}Sn	7.1802×10^{-11}
^{115}Sn	3.9852×10^{-11}	^{116}Sn	1.6285×10^{-9}	^{117}Sn	8.6713×10^{-10}
^{118}Sn	2.7609×10^{-9}	^{119}Sn	9.8731×10^{-10}	^{120}Sn	3.7791×10^{-9}
^{122}Sn	5.4622×10^{-10}	^{124}Sn	6.9318×10^{-10}	^{121}Sb	5.4174×10^{-10}
^{123}Sb	4.1069×10^{-10}	^{120}Te	1.3052×10^{-11}	^{122}Te	3.8266×10^{-10}
^{123}Te	1.3316×10^{-10}	^{124}Te	7.1827×10^{-10}	^{125}Te	1.0814×10^{-9}
^{126}Te	3.1553×10^{-9}	^{128}Te	4.9408×10^{-9}	^{130}Te	5.3731×10^{-9}
^{127}I	2.8912×10^{-9}	^{124}Xe	1.7910×10^{-11}	^{126}Xe	1.6223×10^{-11}
^{128}Xe	3.3349×10^{-10}	^{129}Xe	4.1767×10^{-9}	^{130}Xe	6.7411×10^{-10}
^{131}Xe	3.3799×10^{-9}	^{132}Xe	4.1403×10^{-9}	^{134}Xe	1.5558×10^{-9}
^{136}Xe	1.2832×10^{-9}	^{133}Cs	1.2515×10^{-9}	^{130}Ba	1.5652×10^{-11}
^{132}Ba	1.5125×10^{-11}	^{134}Ba	3.6946×10^{-10}	^{135}Ba	1.0108×10^{-9}
^{136}Ba	1.2144×10^{-9}	^{137}Ba	1.7466×10^{-9}	^{138}Ba	1.1240×10^{-8}
^{138}La	1.4277×10^{-12}	^{139}La	1.5681×10^{-9}	^{136}Ce	7.4306×10^{-12}
^{138}Ce	9.8787×10^{-12}	^{140}Ce	3.5590×10^{-9}	^{142}Ce	4.5258×10^{-10}
^{141}Pr	5.9562×10^{-10}	^{142}Nd	8.0817×10^{-10}	^{143}Nd	3.6172×10^{-10}
^{144}Nd	7.1756×10^{-10}	^{145}Nd	2.5197×10^{-10}	^{146}Nd	5.2441×10^{-10}
^{148}Nd	1.7857×10^{-10}	^{150}Nd	1.7719×10^{-10}	^{144}Sm	2.9140×10^{-11}
^{147}Sm	1.4836×10^{-10}	^{148}Sm	1.0931×10^{-10}	^{149}Sm	1.3417×10^{-10}
^{150}Sm	7.2470×10^{-11}	^{152}Sm	2.6491×10^{-10}	^{154}Sm	2.2827×10^{-10}
^{151}Eu	1.7761×10^{-10}	^{153}Eu	1.9660×10^{-10}	^{152}Gd	2.5376×10^{-12}
^{154}Gd	2.8008×10^{-11}	^{155}Gd	1.9133×10^{-10}	^{156}Gd	2.6675×10^{-10}
^{157}Gd	2.0492×10^{-10}	^{158}Gd	3.2772×10^{-10}	^{160}Gd	2.9180×10^{-10}
^{159}Tb	2.4252×10^{-10}	^{156}Dy	8.6812×10^{-13}	^{158}Dy	1.4787×10^{-12}
^{160}Dy	3.7315×10^{-11}	^{161}Dy	3.0340×10^{-10}	^{162}Dy	4.1387×10^{-10}
^{163}Dy	4.0488×10^{-10}	^{164}Dy	4.6047×10^{-10}	^{165}Ho	3.7104×10^{-10}
^{162}Er	1.4342×10^{-12}	^{164}Er	1.6759×10^{-11}	^{166}Er	3.5397×10^{-10}
^{167}Er	2.4332×10^{-10}	^{168}Er	2.8557×10^{-10}	^{170}Er	1.6082×10^{-10}
^{169}Tm	1.6159×10^{-10}	^{168}Yb	1.3599×10^{-12}	^{170}Yb	3.2509×10^{-11}
^{171}Yb	1.5312×10^{-10}	^{172}Yb	2.3624×10^{-10}	^{173}Yb	1.7504×10^{-10}

Table 27: (continued)

${}^{A}Z$	$X_{{}^{A}Z}$	${}^{A}Z$	$X_{{}^{A}Z}$	${}^{A}Z$	$X_{{}^{A}Z}$
^{174}Yb	3.4682×10^{-10}	^{176}Yb	1.4023×10^{-10}	^{175}Lu	1.5803×10^{-10}
^{176}Lu	4.5855×10^{-12}	^{174}Hf	1.0783×10^{-12}	^{176}Hf	3.4636×10^{-11}
^{177}Hf	1.2581×10^{-10}	^{178}Hf	1.8550×10^{-10}	^{179}Hf	9.3272×10^{-11}
^{180}Hf	2.4131×10^{-10}	^{180}Ta	1.1292×10^{-14}	^{181}Ta	9.4772×10^{-11}
^{180}W	7.8768×10^{-13}	^{182}W	1.6113×10^{-10}	^{183}W	8.7950×10^{-11}
^{184}W	1.8989×10^{-10}	^{186}W	1.7878×10^{-10}	^{185}Re	9.0315×10^{-11}
^{187}Re	1.6603×10^{-10}	^{184}Os	5.6782×10^{-13}	^{186}Os	5.0342×10^{-11}
^{187}Os	3.8172×10^{-11}	^{188}Os	4.2704×10^{-10}	^{189}Os	5.2110×10^{-10}
^{190}Os	8.5547×10^{-10}	^{192}Os	1.3453×10^{-9}	^{191}Ir	1.1933×10^{-9}
^{193}Ir	2.0211×10^{-9}	^{190}Pt	8.1702×10^{-13}	^{192}Pt	5.0994×10^{-11}
^{194}Pt	2.1641×10^{-9}	^{195}Pt	2.2344×10^{-9}	^{196}Pt	1.6757×10^{-9}
^{198}Pt	4.8231×10^{-10}	^{197}Au	9.3184×10^{-10}	^{196}Hg	2.3797×10^{-12}
^{198}Hg	1.7079×10^{-10}	^{199}Hg	2.8843×10^{-10}	^{200}Hg	3.9764×10^{-10}
^{201}Hg	2.2828×10^{-10}	^{202}Hg	5.1607×10^{-10}	^{204}Hg	1.2023×10^{-10}
^{203}Tl	2.7882×10^{-10}	^{205}Tl	6.7255×10^{-10}	^{204}Pb	3.1529×10^{-10}
^{206}Pb	3.0900×10^{-9}	^{207}Pb	3.3720×10^{-9}	^{208}Pb	9.6177×10^{-9}
^{209}Bi	7.6127×10^{-10}	^{232}Th	2.4647×10^{-10}	^{235}U	3.4061×10^{-11}
^{238}U	1.0897×10^{-10}				